DOE Grant Number DE-FG02-05ER54810

Formation of Imploding Plasma Liners for HEDP and MIF Application

Final Report for the Period March 1, 2005 - December 14, 2012

November 11, 2014

PREPARED FOR THE UNITED STATES
DEPARTMENT OF ENERGY
OFFICE OF FUSION ENERGY SCIENCES

F. Douglas Witherspoon, Andrew Case, Samuel Brockington, Sarah Messer
Richard Bomgardner, Mike Phillips, Linchun Wu, Ray Elton

HyperV Technologies Corp.
Chantilly, VA 20151

Contents

Contents 2

1 Abstract 5

2 Overview of Program 7
2.1 Background 7
2.2 Coax Gun Background 8
2.3 The Plasma Liner Experiment (PLX) Background 9
2.4 Report Structure 11

3 Contoured-Gap Coaxial Plasma Accelerators 12
3.1 Dense Injected Plasma Armatures 12
3.2 The Blow-by Instability 13
3.3 Coaxial Accelerators with Tailored Electrode Geometries 14
3.4 The MHD Code 17
3.5 The Wasp Profile 18
3.6 Systematic Tuning of Profile Curvature 18
3.7 Prototype Coax Gun Development 23
3.7.1 Experimental Facility 23
3.7.2 Plasma Injection 24
3.7.3 Parallel Operation of Capillaries 26
3.7.4 Sparkgap Gun 28
3.7.5 TwoPi Test Fixture 30
3.8 Experimental Results 30
3.8.1 Gun Electrical 30
3.8.2 Visible Light Imaging 30
3.8.3 Spectrometry 32
3.8.4 Ballistic Pendulum Tests 33
3.8.5 Interferometry 34
3.8.6 Pressure probe 35
3.8.7 Magnetic probes 35
3.9 Gun Efficiency 37
3.10 Gas Injection 37

4 MiniRailgun Parallel Plate Plasma Accelerators 38
4.1 MiniRailguns as Plasma Injectors 38
4.2 A Heuristic Model 38
4.3 Two Basic Configurations 40
4.4 Gas Fed Minirailguns Make Good Plasma Accelerators 43
4.5 Fast Gas Valve - Early Version 43
4.6 Performance of Gas Fed 1cm Minirailgun 46

5 Pulsed Power Systems 50
5.1 Introduction 50
5.2 High Voltage Switches for Rail Guns 50
5.3 MAF Design 51
5.4 FEMM Modeling of Trigger Fields 52
5.5 Aster Modeling of Switch Stress 52
5.6 Capillary Load Results 55
5.7 Railgun Load Results 55
5.8 Coatings, Wear, and Lifetime 58
5.9 Comments 61
5.10 Linear Spark Gap Switches 61

6 Mark 1 MiniRailgun Development 66
6.1 Introduction 66
6.2 Railgun design 66
6.3 Gas Valve - Later Version 68
6.4 Plasma Capillary Pre-Ionizer 76
6.5 Accelerator section design 77
6.6 Railgun Model with Ablation 78
6.7 Railgun Testing 79
6.8 Railgun Driver Circuits 81
6.9 Experimental Results 82
6.10 Conclusions 88

7 PLX Experiment 89
7.1 Introduction 89
7.2 Motivations 89
7.3 PLX facility construction at LANL 91
7.4 Single jet propagation experiments on PLX 93
7.5 Plasma gun and pulsed power development 95
7.6 Plasma gun design 95
7.7 Pulsed power components 96

8 Plasma Jet Merge Experiments at HyperV 98
8.1 Recap of Three Jet Merging Experiments 98
8.2 Recap of Six Jet Merging Experiments 103

9 Mark 2 MiniRailgun - PLX Gun Performance Goal Achieved 109
9.1 Railgun and Driver Circuit Changes 110
9.2 Experimental Results 111
9.3 Mark2 Summary 114

10 Directions for Future Experiments 117
10.1 Coaxial vs. MiniRailguns 117
10.2 Coax Gun 118
10.3 The Full Scale Coax Gun 121
10.4 Injection Approaches 124
  10.4.1 Central Gas Valve 124
  10.4.2 Single-Coil Annular Gas Valve 124

10.4.3 Multi-Coil Annular Gas Valve 125
10.4.4 Multiple Small Gas Valves 125

11 Acknowledgments 128

References 129

APPENDIX 136

A Ballistic Pendulum 137

1 Abstract

Plasma jets with high density and velocity have a number of important applications in fusion energy and elsewhere, including plasma refueling, disruption mitigation in tokamaks, magnetized target fusion, injection of momentum into centrifugally confined mirrors, plasma thrusters, and high energy density plasmas (HEDP). In Magneto-Inertial Fusion (MIF), for example, an imploding material liner is used to compress a magnetized plasma to fusion conditions and to confine the resulting burning plasma inertially to obtain the necessary energy gain. The imploding shell may be solid, liquid, gaseous, or a combination of these states. The presence of the magnetic field in the target plasma suppresses thermal transport to the plasma shell, thus lowering the imploding power needed to compress the target to fusion conditions. This allows the required imploding momentum flux to be generated electromagnetically using off-the-shelf pulsed power technology. Practical schemes for standoff delivery of the imploding momentum flux are required and are open topics for research. One approach for accomplishing this, called plasma jet driven magneto-inertial fusion (PJMIF), uses a spherical array of pulsed plasma guns to create a spherically imploding shell of very high velocity, high momentum flux plasma. This approach requires development of plasma jet accelerators capable of achieving velocities of 50-200 km/s with very precise timing and density profiles, and with high total mass and density. Low-Z plasma jets would require the higher velocities, whereas very dense high-Z plasma shells could achieve the goal at velocities of only 50-100 km/s.

In this report, we describe our work to develop the pulsed plasma gun technology needed for an experimental scientific exploration of the PJMIF concept, and also for the other applications mentioned earlier. The initial goal of a few hundred of hydrogen at 200 km/s was eventually replaced with accelerating 8000 μg of argon or xenon to 50 km/s for the Plasma Liner Experiment (PLX) at Los Alamos National Laboratory (LANL).

Initial work used existing computational and analytical tools to develop and refine a specific plasma gun concept having a novel tapered coaxial electromagnetic accelerator contour with an array of symmetric ablative plasma injectors. The profile is designed to suppress the main barrier to success in coaxial guns, namely the blow-by instability in which the arc slips past and outruns the bulk of the plasma mass. Efforts to begin developing a set of annular non-ablative plasma injectors for the coaxial gun, in order to accelerate pure gases, resulted in development of linear parallel-plate MiniRailguns that turned out to work well as plasma guns in their own right and we subsequently chose them for an initial plasma liner experiment on the PLX facility at LANL. This choice was mainly driven by cost and schedule for that particular experiment, while longer term goals still projected use of coaxial guns for reactor-relevant applications for reasons of better symmetry, lower impurities, more compact plasma jet formation, and higher gun efficiency.

Our efforts have focused mainly on 1) developing various plasma injection systems for both coax and linear railguns and ensuring they work reliably with the accelerator section, 2) developing a suite of plasma and gun diagnostics, 3) performing computational modeling to design and refine the plasma guns, 4) establishing a research facility dedicated to plasma gun development, and finally, 5) developing plasma guns and associated pulse power systems capable of achieving these goals and installing and testing the first two gun sets on the PLX facility at LANL.

During the second funding cycle for this program, HyperV joined in a collaborative effort with LANL, the University of Alabama at Huntsville, and the University of New Mexico to perform a plasma liner experiment (PLX) to investigate the physics and technology of forming spherically imploding plasma liners. HyperV's tasks focused on developing the plasma guns and associated pulse power systems required for the 30 gun experiment at LANL. Unfortunately, funding for the entire PLX collaborative project was terminated after only two years of the four year project due to program funding realignments which necessitated recompeting the project in midstream. Despite

the loss of funding, HyperV installed two Mark1 guns and pulsed power systems on PLX, and jet characterization and merging experiments were subsequently successfully performed at LANL by the PLX Team. In parallel with those PLX experiments, HyperV continued its efforts to develop a plasma gun capable of meeting the PLX goal of 8 mg of argon at 50 km/s. HyperV was ultimately successful in this effort, demonstrating 10.8 mg at 52.8 km/s and 7.5 mg at 62.4 km/s with the Mark2 MiniRailgun.

2 Overview of Program

2.1 Background

Plasma jets with high density and velocity have a number of important applications in fusion energy and elsewhere, including plasma refueling, disruption mitigation in tokamaks, magnetized target fusion, injection of momentum into centrifugally confined mirrors, plasma thrusters, and high energy density plasmas (HEDP).

In Magneto-Inertial Fusion (MIF) [1, 2, 3, 4, 5], for example, an imploding material liner is used to compress a magnetized plasma to fusion conditions and to confine the resulting burning plasma inertially to obtain the necessary energy gain. The imploding shell may be solid, liquid, gaseous, or a combination of these states. The presence of the magnetic field in the target plasma suppresses thermal transport to the plasma shell, thus lowering the imploding power needed to compress the target to fusion conditions. This allows the required imploding momentum flux to be generated electromagnetically using off-the-shelf pulsed power technology. Practical schemes for standoff delivery of the imploding momentum flux are required and are open topics for research. One approach for accomplishing this, called plasma jet driven magneto-inertial fusion (PJMIF), uses a spherical array of pulsed plasma guns to create a spherically imploding shell of very high velocity, high momentum flux plasma [6]. This approach requires development of plasma jet accelerators capable of achieving velocities of 50-200 km/s with very precise timing and density profiles, and with high total mass and density. Low-Z plasma jets would require the higher velocities, whereas some calculations [7, 10, 11, 12] have indicated the possibility of using high-Z plasma shells at velocities of only 50-100 km/s.

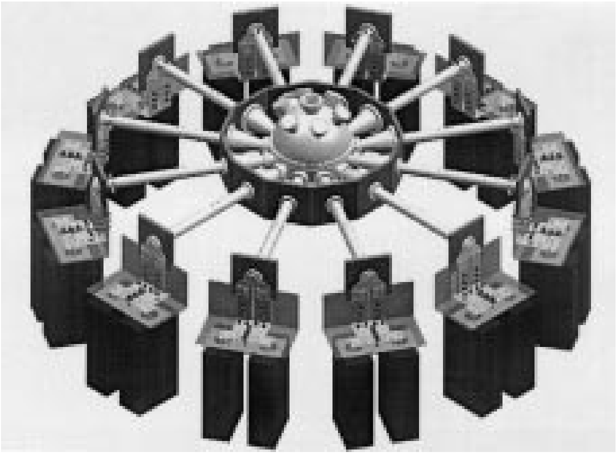

Figure 1 *The original conceptual Plasma Liner Exploratory Experiment (PLX) consisted of 12 merging plasma jets launched by 12 coaxial plasma guns. From Reference [1].*

Thio *et al.* [1, 6] recognized that coaxial railgun accelerators were potentially capable of meeting this challenge, noting that spheromaks and field reversed configurations had already achieved velocities in excess of 200 km/s, albeit with lower densities and total mass. They projected that it would be possible to accelerate $200 - 400\ \mu g$ of plasma to ~ 200 km/s in a plasma gun with a length of no more than 1 m and a muzzle diameter of less than 0.2 m, with timing precision of better than 100 ns. Given these parameters, the density of the plasma jets would need to be approximately 10^{17} cm^{-3}.

We describe our work to develop the pulsed plasma gun technology needed for an experimental exploration of the PJMIF concept, and also for the other applications mentioned earlier. The parameters in the previous paragraph were taken as initial experimental goals, but which were later updated to accelerating 8000 μg to 50 km/s for the Plasma Liner Experiment (PLX) [13] to be described in Section 2.3 further below. Initial work used existing computational and analytical tools to develop and refine a specific plasma gun concept having a novel tapered coaxial electromagnetic accelerator profile (originally suggested by Thio [14]) with an array of symmetric ablative plasma injectors. The profile is designed to suppress the main barrier to success in coaxial guns, namely the blow-by instability in which the arc slips past and outruns the bulk of the plasma mass [15, 16, 17]. The first generation half-scale prototype gun is illustrated schematically in Figure 2.

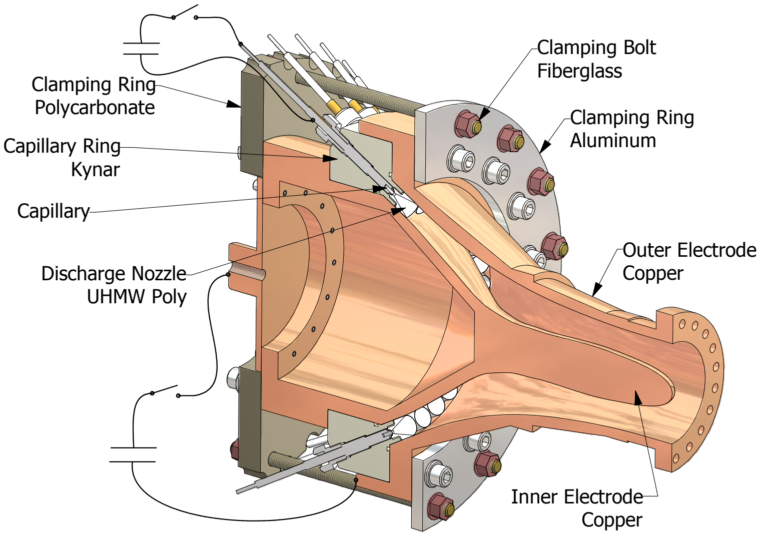

Figure 2 *Cutaway view of a first-generation half-scale prototype plasma jet accelerator module which uses tailored electrode profiles to suppress the occurrence of the blow-by instability. Two separate high voltage circuits power the electrothermal injectors and the main electromagnetic accelerator.*

Initial efforts to begin developing a set of annular non-ablative plasma injectors for the coaxial gun resulted in development of linear parallel-plate MiniRailguns that turned out to work so well that we chose them for an initial plasma liner experiment on the PLX facility at Los Alamos National Laboratory [13].

Our efforts have focused mainly on 1) developing various plasma injection systems for both coax and linear railguns and ensuring they work reliably with the accelerator section, 2) developing a suite of plasma and gun diagnostics, 3) performing computational modeling to design and refine the plasma guns, 4) establishing a research facility dedicated to plasma gun development, and finally, 5) developing plasma guns and associated pulse power systems capable of achieving these goals and installing and testing the first two gun sets on the PLX facility at Los Alamos National Laboratory.

In the following report, we first describe the development and testing of the coaxial guns. The bulk of the report then details the development and testing of the parallel-plate linear MiniRailguns and associated subsystems that were eventually partially deployed on the PLX experiment at Los Alamos National Laboratory. After two of the Minirailguns (Mark1) were deployed on PLX, HyperV continued its development efforts to successfully demonstrate a gun (Mark2) meeting the full PLX requirements of 8000 μg at 50 km/s.

2.2 Coax Gun Background

Pulsed coaxial plasma accelerators (or "guns") [18, 19] have been researched since the 1950's for various applications. Except for the work during the 1950's and 1960's when the research was associated with applications to fusion, most of the research on these accelerators in the last four decades has been associated with applications to space propulsion. During the 1980's and 1990's, plasma accelerators were encountered in several other applications, including dense plasma focus and the acceleration of relatively large compact toroids (MARAUDER of the Air Force Research Laboratory [20], RACE of Lawrence Livermore Laboratory [21], CTIX of UC-Davis [22]) for fusion and x-ray generation, and in accelerating solid projectiles to hypervelocity for impact fusion and a variety of defense applications.

For space propulsion, these accelerators are called pulsed plasma thrusters (PPTs). Small PPT devices have been successfully fielded on orbiting satellites for station keeping purposes. In these devices, and in the larger plasma guns studied in the 1950’s and 1960’s, the plasma densities are typically low ($< 10^{15}$ cm^{-3}) and collisionless. Their development was in part inspired by the 1954 paper of Rosenbluth [23] which provided the theoretical underpinning for the collisionless acceleration in these guns. Coaxial versions of these guns typically consist of a pair of concentric straight cylindrical conducting pipes serving as the electrodes. Before a shot, the bore of the gun (the region between the electrodes) is first pre-filled with the desired propellant gas. By closing a switch that connects a capacitor bank to the electrodes, a current sheet is then initiated near the breech, usually with the help of one or more sparks. This current sheet is essentially a collisionless magnetoplasmadynamic shock. The collisionless shock then propagates down the bore of the gun. The scheme relies on the shock ionizing the cold pre-filled gas, and on the advancing magnetic field sweeping up the resulting ions and electrons. This is known as the snow-plow mode [18, 24] of acceleration.

Although there has been some notable success with this approach, culminating in the flying of some devices in practical satellites, the performance of PPTs has been found to be limited by the complexity of the physical phenomena. The complexity arises from the particle kinetic effects coupled to the magnetoplasmadynamic (MPD) shocks, and their interactions with neutral particles. An example of the effects that can lead to detrimental performance is the leakage of the particles past the current sheet. These leaked particles lead to low utilization of the propellant, resulting in low mean plasma velocity and efficiency. Further, they are a source of restrike behind the main current sheet, causing further detriment to the performance by drawing drive current from the main current sheet.

2.3 The Plasma Liner Experiment (PLX) Background

Imploding plasma liners are an innovative, potentially high-payoff research area of HEDLP and particularly MIF [7]. The key idea is to create HED-relevant plasma conditions (~ 0.1 Mbar) in a unique new way. We proposed to use an array of 30 plasma guns mounted on a spherical vacuum chamber to shoot dense ($\sim 10^{17}$ cm^{-3}), high Mach number (10–35) plasma jets in a spherically convergent geometry. The jets would merge at an intermediate merging radius r_m, forming an imploding spherical plasma shell or “liner,” which would subsequently reach high ram pressure ($\rho v^2/2$) before stagnating at the center of the vacuum chamber. The overall concept and the vacuum chamber are shown in Figure 3. We can also vary the situation by placing a hard spherical “target” or a “balloon” of hydrogen gas in the center of the chamber. Three-dimensional hydrodynamic simulations in support of this project indicate that the imploding plasma liner can reach peak pressures $\gtrsim 0.1$ Mbar based on 1.5 MJ of total initial stored energy and plasma gun performance expected within the program. The plan was to study scientific issues of jet propagation/merging and liner formation/implosion at lower energy levels ($\sim$ 150–300 kJ) before proceeding to high pressure (~ 0.1 Mbar) implosion experiments (requiring ~ 1.5 MJ). If the liner formation, implosion, and pressure amplification are successfully demonstrated, then the approach could be scaled up to > 1 Mbar in follow-on work using more guns and higher power. It is of interest to mention two related recent research efforts within the past decade. First, the operation of a cylindrical array of 24 plasma guns [8] at up to 1 MJ of total energy has shown via fast photography that the separate gun discharges combine into a single, symmetric, cylindrically converging discharge with neutron yields up to 6×10^9 in pure deuterium experiments. Second, imploding solid aluminum liner experiments

[9] have compressed a dense unmagnetized H plasma to Mbar pressures, as inferred from radiographs showing the radius versus time history of the target surface. Our work uses plasma guns to form imploding plasma liners in spherical geometry and focus on the physics of liner formation and implosion via detailed experimental measurements and theoretical/computational analysis.

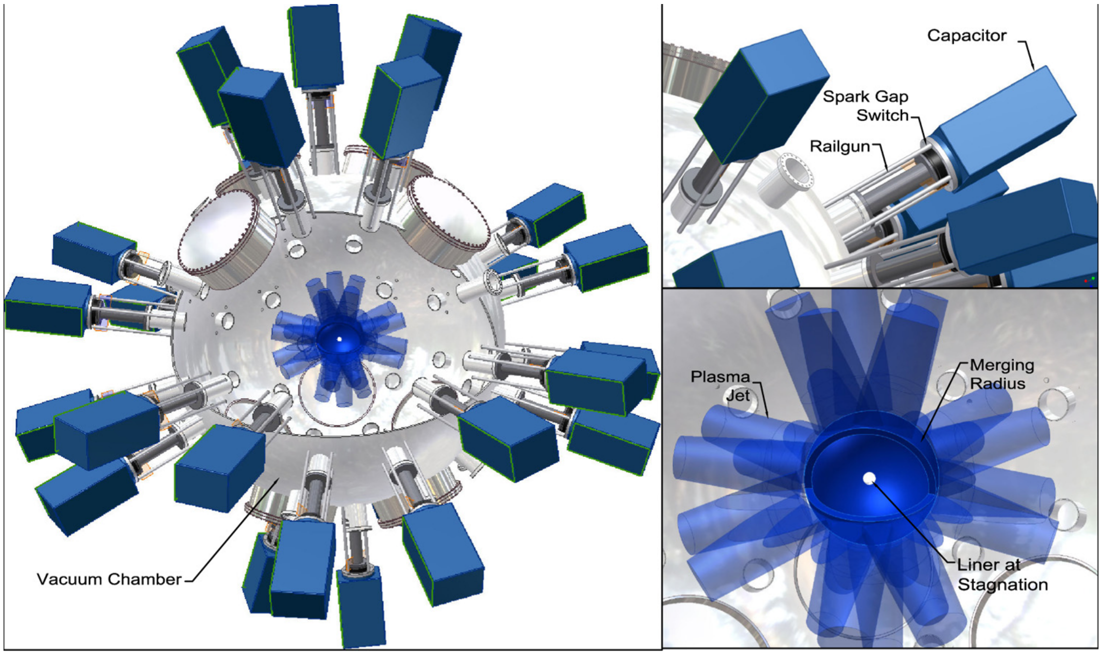

Figure 3 *Illustration of the envisioned imploding plasma liner experiment with 30 guns (and their capacitors) mounted on a 9 ft. (2.74 m) spherical vacuum chamber. Also shown are a moment in time when all the jets have reached the merging radius, and a later moment in time when the liner stagnates at the center of the chamber. (For the highest energy shots, four capacitors per gun will be needed, and the capacitors will be mounted in frames next to the chamber.)*

The project is motivated by two key future applications of importance to the HEDLP program. First, as a nearer-term goal (5–10 years), this approach scaled up to 1–10 Mbar can lead to a unique low-cost HEDLP science facility well-suited for fundamental HEDP studies. Each shot would cost hundreds of dollars rather than tens-to-hundreds of thousands of dollars on laser and large pulsed-power facilities. The cm-scale and μs-scale plasmas that this technique creates would be much easier to diagnose, which could allow for rapid scientific progress in developing fundamental understanding of HED plasmas and phenomena. Such a facility could focus on clarifying the basic plasma physics of equilibrium, stability, and transport in an HED plasma, with or without magnetic fields. In addition, co-location of the facility with a short-pulse laser (such as Trident at LANL) could lead to unprecedented abilities to study laser-plasma interactions, which are important to the mainline ICF program. Finally, such a facility could also be utilized for exciting laboratory astrophysics experiments and high pressure material property studies, which would both be of tremendous value for connecting HEDLP to other scientific disciplines.

Secondly and even more importantly, our primary longer-term (10–20 years) goal is to enable an attractive path toward inertial fusion energy (IFE) via MIF, with an imploding plasma liner serving as an elegant standoff driver to compress magnetized target plasmas to fusion conditions *without any hardware destruction* (see Figure 3) [1, 6]. MIF is an approach to IFE that makes use of a magnetic field in the fusion fuel to reduce thermal losses and enhance α-particle energy deposition within the fusing fuel. The MIF parameter space in terms of density and implosion velocity is quite large, ranging from $n \sim 10^{20}$–10^{22} cm^{-3} and 10–100 km/s, respectively, for magnetized target fusion (MTF) [*e.g.*, [5] to $n \sim 10^{26}$ cm^{-3} and $\sim$ 350 km/s for magnetized ICF [26]. Plasma liners may significantly improve the attractiveness of the MTF approach by directly addressing two issues for MTF. First, plasma liners solve the "standoff problem," *i.e.*, the implosion driver sources can be positioned far enough away from the location of fusion burn such that they survive each shot. Second, the use of plasma liners facilitates amplifying the fusion energy gain by a factor of 2 or more by either re-fueling the fusing target or surrounding the target with additional cold fuel. Over the next 5 years, if the ongoing solid liner MIF program (AFRL/LANL collaboration) [27] can demonstrate favorable results with regards to compressional heating of magnetized target plasmas to fusion conditions, and if over the next 10 years, we can make significant progress in creating suitable imploding plasma liners up to 50 Mbar, then MIF could claim a legitimate pathway toward attractive IFE. A scientific workshop on plasma jets [Hsu, 2008] emphasizing MIF applications was held at LANL in January, 2008. with $\sim$ 35 participants from around the country. Since then, the concept of plasma liner driven MIF has received renewed interest with several groups around the country engaged in evaluating the concept. There are uncertainties associated with plasma liner implosion dynamics in the theoretical models [6, 28] used for estimating the fusion energy gain of plasma liner driven MIF; this project is timely and necessary for helping to address these uncertainties. The workshop and subsequent interactions among interested researchers helped crystallize the ideas and team subsequently formed for PLX. There are also other related ideas for plasma liner driven MIF, e.g. Ryutov [29] that warrant further study. However, the most urgent scientific questions relate to the formation of imploding plasma liners, what limits their peak pressures at stagnation, and hydrodynamic efficiencies of magnetized target compression. Resolving the first two scientific issues through coordinated experiments and theory is the primary focus of the PLX effort.

2.4 Report Structure

In the following report, we first describe the contour-gap coaxial and then parallel-plate railguns we have developed over the period of this project. Along the way, we describe the supporting systems, such as controls, diagnostics, fast gas valves, pulse forming networks, and high current switches. We then briefly describe our input to the PLX experiment and the Mark 1 guns that were installed there. The experiments with those guns are briefly described along with a description of multi-gun merging experiments at HyperV. We then conclude with a description of the successful work to develop the Mark2 gun at HyperV, which achieved the performance goal of 8000 μg at 50 km/s needed for a full up PLX experiment. The appendix contains a description of the ballistic pendulum diagnostic.

3 Contoured-Gap Coaxial Plasma Accelerators

3.1 Dense Injected Plasma Armatures

Consideration of the shortcomings of existing coaxial pulsed plasma thrusters led Thio *et al.* [25] to propose an innovative new approach to the plasma dynamics in these accelerators. The main features of their proposed approach were:

(1) No pre-fill is used. The plasma to be accelerated is preformed and injected impulsively at high density and nearly fully ionized with an initially high electrical conductivity.

(2) The main body of the plasma is sufficiently collisional that the plasma behaves more like a fluid, in order to suppress undesirable particle kinetic effects.

They essentially laid out a new microphysics approach and basis for plasma accelerators, where microphysics refers here mainly to localized particle effects. The new approach traded the microphysics problems of conventional PPT's with the engineering challenge of creating the new pulsed plasma feeds (injectors) that would be needed to inject the dense plasmas that meet the requirements of the new microphysics proposed. One of the objectives of our research is to demonstrate the potential of this new microphysics approach to plasma acceleration.

However, having a plausible microphysics approach is only half the challenge. The microphysics also needs to be implemented in a practical macrodynamic scheme, where macrodynamic refers mainly to bulk MHD fluid type behavior and the associated flow geometries. Several challenges remain to be overcome once this highly collisional, no pre-fill, microphysics approach is adopted. Firstly, the approach requires new plasma injectors to be developed that can deliver the dense plasma that meets the microphysics specifications. Secondly, in the main plasma accelerator, the notable MHD instabilities and the issues of restrike, skin friction, and electrode ablation and erosion will need to be addressed and overcome.

Thio *et al.* [1] proposed an accelerator concept as a possible implementation of this new approach. The accelerator consisted of a pair of coaxial electrodes, both electrodes having a gradual conical taper and an electromagnetic focusing section much like a plasma focus device. The conical taper induces a small component of radially inward velocity at the muzzle exit which tends to focus the jet for a short distance before collisional effects cause subsequent rebound and expansion further downstream. Whether the focusing provides a net gain in the performance of the jet during its flight to the target remains to be determined, since the induced compressional heating may take back whatever gains were made by focusing.

The acceleration chamber would be thoroughly flushed with helium and evacuated (i.e. no gas pre-fill). The two electrodes are electrically connected to the two terminals of a capacitor bank or pulse forming network (PFN). Before a shot, the capacitor bank (or PFN) is charged to the desired voltage, which appears simultaneously on the electrodes. The required plasma mass is introduced into the acceleration chamber by a set of extremely low-jitter (< 10 ns) pulsed plasma injector feeds arranged annularly near the breech. The plasma is then launched in the form of a plasma "fan" (or "plume") radially inwards toward the axis of the inner electrode. The plasma fans join to form a dense plasma sheet that closes the external circuit and initiates the main current pulse to accelerate the plasma sheet down the accelerator. A somewhat similar technique was used by Kohno *et al.* in a plasma opening switch experiment [30].

The requisite amount of plasma is injected into the accelerator using pulsed electrothermal capillary discharges with ablative polyethylene walls. Ablative capillaries have been used successfully for large electrothermal guns [31], injectors to high energy railguns [32], plasma thrusters [33], and in experiments involving laser propagation through long plasma channels [34, 35, 36, 37], to name just a few applications. Ultimately the ablative walls will be replaced with nonablative refractory

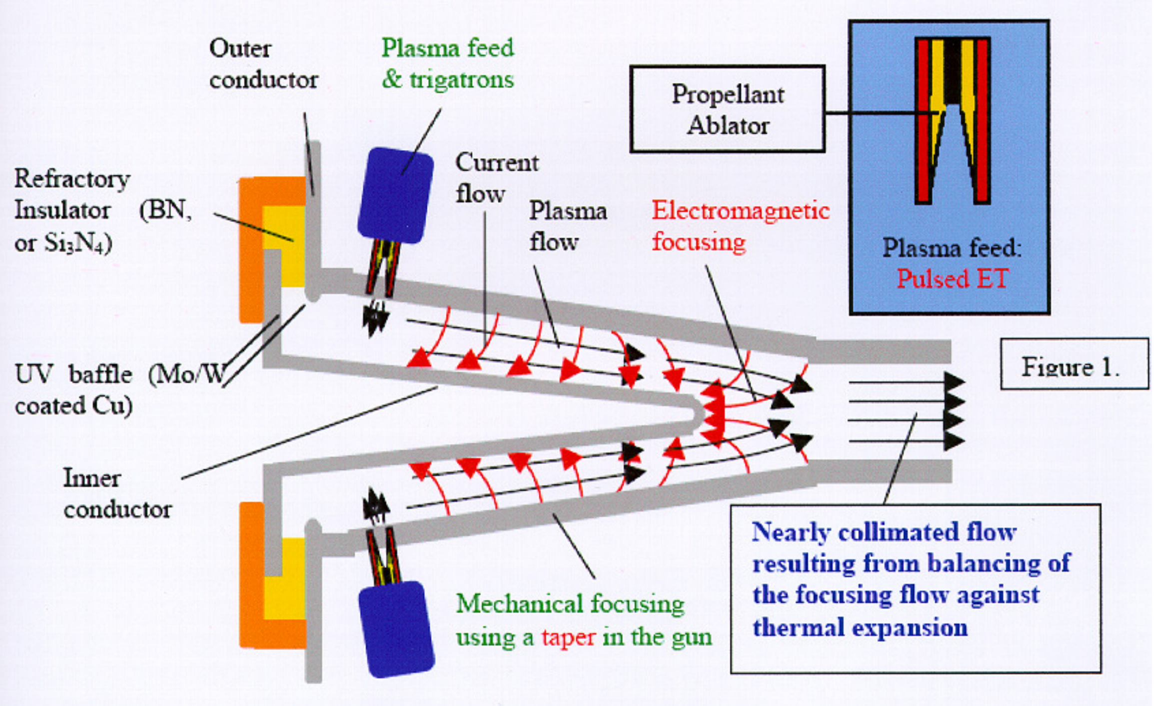

Figure 4 *Original coaxial accelerator proposed by Thio et al.[1] Our approach uses this concept as a baseline and makes important modifications to suppress the blowby instability and improve axisymmetry of the plasma injection.*

ceramics, as has been accomplished for pulsed soft x-ray sources [38, 39, 40, 41] and for high energy pulsed thermal spray devices [42]. This will allow clean and repetitive operation. The H_2 or D_2 (or other, higher-Z gases) in this case are introduced by other means.

3.2 The Blow-by Instability

Plasma acceleration techniques which depend on Lorentz $\mathbf{J} \times \mathbf{B}$ forces are generally susceptible to MHD instabilities that can deteriorate the plasma jet acceleration process significantly, induce restriking and secondary arcs, and even terminate plasma jets. Therefore, it is crucial to understand the MHD instabilities and optimize the design of the accelerator to avoid them in order to achieve the desired plasma jet acceleration. The major instabilities include the blow-by and Rayleigh-Taylor instabilities. The Rayleigh-Taylor instability encompasses filamentation and interchange instabilities.

The main macrodynamic problem in coaxial plasma jet acceleration is the blow-by instability that develops during the acceleration phase. The blow-by instability has its origin in the r^{-2} radial dependence of the magnetic pressure. If the plasma has an initially uniform density and thickness (uniform mass distribution), its acceleration will be higher along the inner electrode than along the outer one. The faster movement along the inner electrode produces a "backward canting" of the current-carrying plasma. The canting current sheet then develops a large axial component which produces a Lorentz force with a radial outward component. This radial acceleration causes a runaway effect in which increasingly more plasma mass is removed from the high velocity region, making the imbalance of the magnetic field pressure against the adverse density profile more severe. As can be seen in Figure 5, the blow-by instability accelerates a small piece of plasma to a disproportionately high velocity, while leaning most of the plasma mass against the outer electrode where it eventually exits at much lower velocity.

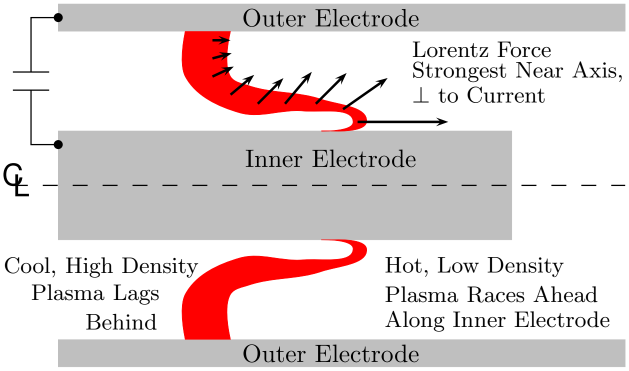

Figure 5 *Illustration of blow-by in a straight coax accelerator driven by a high voltage capacitor. The larger magnetic field and higher current density at smaller radii causes an imbalance in the nominally axially directed Lorentz force, resulting in a faster acceleration of plasma near the inner electrode, which runs away from the bulk of the plasma.*

Blow-by was previously investigated by Baker *et al.* [15, 16]. More recently, Cassibry [43] performed a detailed computational study of the blow-by instability in straight coax accelerators and found that for straight coax guns, the principal acceleration phase must be limited to no more than about 1 μs and the electrode radius ratio should be no more than about 2:1. These constraints are too severe to achieve the goals of this project, but Thio and Cassibry [43] also began investigating the possibility of combining pulsed injection along with shaping of the electrode profiles as a means to suppress the blowby instability and thus achieve higher performance.

3.3 Coaxial Accelerators with Tailored Electrode Geometries

Cassibry and Thio [43] had looked at a curved-profile coaxial configuration, which showed some promise but was not investigated experimentally. Our approach to addressing the blow-by problem uses a novel shaping of the electrodes originally suggested by Thio [14]. This is basically a further evolution of his straight conical tapered gun mentioned in the last section and the curved profile investigated by Cassibry. Our initial modeling effort focused on analyzing this approach and identifying geometries and parameters which would avoid the blow-by. Although some minor modifications to Thio's original suggestion were found to be necessary, the simulations supported the basic concept.

We thus adopt Thio's microphysics approach that uses highly collisional plasma in a shaped coaxial plasma gun, along with plasma sources that impulsively inject a dense fast-moving preformed plasma armature into a coaxial gun having no initial pre-fill. Ideally, no external switch would be required, letting the injected plasma itself act as a closing switch, but in practice one may be required.

Assuming an impulsively injected plasma armature, we now consider the physics issues and challenges of controlling the macrodynamics of the plasma slab so that the global characteristics of the plasma acceleration can be achieved.

The Injection and Transition Regions Figure 6 shows the baseline geometry for the accelerator based on Thio's earlier suggestion. This electrode geometry provides for a breech section (between A and B) that is orthogonal to the gun axis. It was later found to be necessary to change this to an oblique angle, but the following discussion remains essentially unchanged. In this section of the gun, the injected plasma initially flows radially inward towards the gun axis. The initial discharge, initiated by the injected plasma, is axial between the electrodes (and mostly so for the angled injector case), thus forming a fat z-pinch that rapidly accelerates the plasma radially inwards in the region between A and B to supersonic speeds. As the plasma enters the transitional region between B and C, its leading edge is at the outer electrode. Having the leading edge of the plasma at the outer electrode is the preferred inclination for the plasma to counter the blow-by instability. Thio and Cassibry call this the "forward canting" of the plasma sheet. Furthermore, the plasma sees a convex curvature at the outer electrode, versus a concave curvature at the inner electrode. The convex curvature produces an expanding fan of the Mach lines (characteristics) for the flow at the outer electrode, giving rise to an expansion of the flow at the outer electrode.

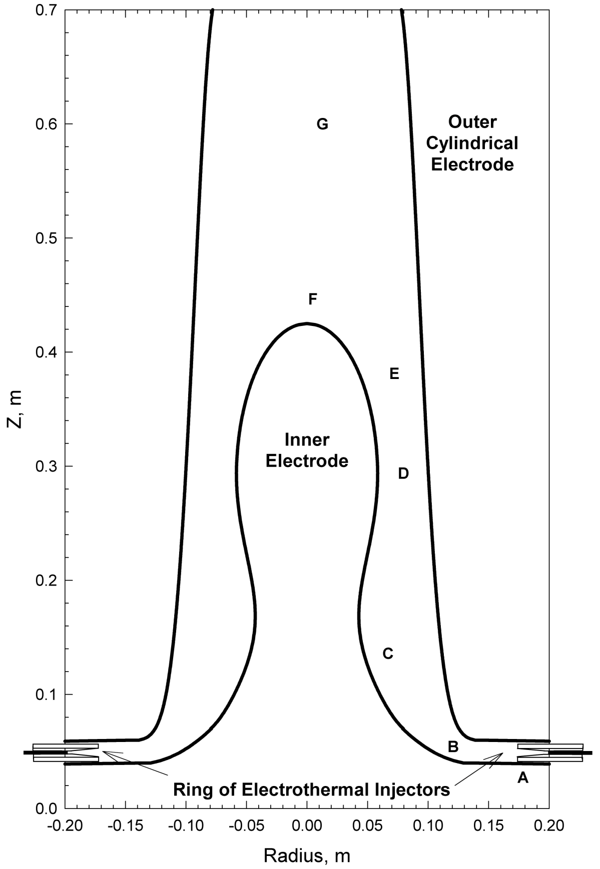

Figure 6 *Baseline plasma jet accelerator geometry for simulations. The right angle turn in this drawing turns out to be too large, and an angle closer to 45 degrees is much better. See Figs. 7 and 12 for examples of simulated plasma flow in this geometry.*

The flow expansion helps accelerate the plasma along the outer electrode, reducing the density of the plasma near the outer electrode. On the other hand, the concave curvature relative to the flow at the inner electrode produces convergence of the Mach lines for the flow at the inner electrode between B and C, making the flow bend into itself, giving rise to compression of the flow at the inner electrode. The increased plasma density near the inner electrode tends to reduce the acceleration produced by the greater Lorentz force there. A favorable density profile, monotonic with respect to the magnetic pressure, is thus created by the way the plasma is injected and by the chosen curvatures of the entry and transition regions. These features help to suppress (or at least delay) the occurrence of the blow-by. The electrode profiles are chosen so that the bends produce smooth transitions in the flow, making the compression or expansion as isentropic (shockless) as possible. Our studies showed that the right angle turn is too sharp, while 45 degrees is about right, as discussed later in Sec. 3.5.

In the above discussion, we have borrowed fluid dynamics concepts established for steady flow, even though the flow in our accelerator is unsteady. However, just as is common experience in similar cases, the qualitative descriptions remain essentially correct, while the deviations from the steady-flow results lie in the quantitative details. The 2-D MHD modeling validated this expectation and the qualitative behavior of the flow as described above is observed in the simulations.

The Intermediate Acceleration Stage The section of the accelerator between C and D is called the intermediate acceleration stage. As the plasma enters this stage, the driving current reaches its peak, and the full Lorentz force is brought to bear on the plasma.

A taper is maintained in the outer electrode to mechanically induce a focusing of the flow towards the axis, the idea being that after the flow exits from the accelerator, the radially inward velocity component of the flow could help counter the thermal expansion of the jet radially, to produce a focusing flow or at least a collimated flow over the required distance.

A gradually decreasing concave curvature is maintained along the inner electrode to continue to reduce the risk of any blow-by instability, seeking to maintain an organized and compact acceleration of the plasma. This is done at the expense of some constriction of the flow and thus some reduction in the acceleration of the plasma through the constriction. This is compensated, however, by the final acceleration stage, in which the concavity in the curvature becomes convex at point D, beyond which the supersonic flow expands along the inner electrode.

The Final Accelerating and Focusing Stage The region indicated by points D, E, F and G represents the final accelerating and focusing stage. The driving current is maintained as close as possible to a flat top equaling its peak value at the point C until the plasma first reaches near the top of the inner electrode (point F). The driving current is ultimately allowed to fall to zero after that as the plasma reaches the point G close to the muzzle.

In addition to the Lorentz acceleration, the supersonic expansion around the inner electrode beyond the point D contributes to the total acceleration of the flow. The convex curvature of the inner electrode also bends the flow towards the axis. Because of the cylindrical geometry, the flow expansion soon ceases and gives in to compression due to convergence of the flow towards the axis. Nevertheless, further acceleration of the flow occurs due to the increasing Lorentz force.

Beyond point D, the plasma at the outer electrode makes gains on the axial position of the plasma at the inner electrode, producing a forward tilting of the current flow. The forward tilting of the current produces a force that accelerates the plasma towards the axis, as well as axially, thus focusing the flow electromagnetically, similar to a dense plasma focus device. The forward tilting of the current increases as the plasma moves towards the point G, producing a conical z-pinch with the tip of the inner electrode as the vertex. The radial pinching of the flow intensifies as the vertex angle of the conical z-pinch decreases, and leads to forward electrothermal acceleration of the plasma axially supported by the intense magnetic pressure due to the z-pinch at the top of the inner electrode. To further enhance the nearly isentropic compression of the flow, a small concave curvature is provided on the outer electrode in this region. The combination of the electromagnetic and electrothermal acceleration propels the plasma forward as a relatively focused jet. The outer electrode has an extended section at the muzzle to provide a guided drift of the accelerated plasma jet to allow it to cool radiatively and convectively in contact with the wall. This lowers the sound speed of the jet and increases its Mach number rapidly as it exits from the muzzle of the accelerator. The high Mach number then maintains the collimation of the focused jet.

A series of simulations were performed to find a suitable geometrical configuration and set of parameters that suppresses plasma blow-by and allows at least 100 μg of plasma to be accelerated to 200 km/s. We will briefly summarize the initial modeling results in this section. The simulations validated the basic conceptual approach with the restriction that the right angle injection needed to be reduced.

3.4 The MHD Code

To understand the dynamics of contoured coaxial plasma guns and the effect electrode shape has on performance, preliminary design simulations were carried out using the MACH2 code [44, 45]. MACH2 is a 2.5-dimensional single-fluid MHD simulation code. The code follows the non-linear evolution of density, velocity, and magnetic field, as well as the electron and ion specific internal energies. The code solves equations for mass continuity, fluid momentum, electron and ion specific internal energies, radiation energy density, and magnetic induction. Quantities are solved on a 2-dimensional Cartesian or cylindrical mesh; for the coaxial geometries studied here, a cylindrical mesh was used. The equations are coupled through equation of state (EOS) and transport coefficients. MACH2 features a range of EOS and transport models including table look-up that can utilize the Los Alamos National Laboratory SESAME Equation of State database [46]. Our calculations used the ideal gas equation of state, Spitzer resistivity, and Braginskii transport coefficients. The magnetic induction equation can optionally include a Hall effect term in certain geometries, which unfortunately did not include the geometry of interest here. The Hall effect is thought to have an influence on the particle dynamics on the trailing edge of the plasma blob, which may lead, in certain circumstances, to detachment of the current armature. Other than the possibility of detachment, it is not expected to appreciably change the acceleration of the plasma blob. The Hall effect will be left for future study.

A multi-block grid with arbitrary quadrilateral cells and boundary-fitted coordinates is used, which makes possible the simulation of a large variety of complex geometries and boundary conditions. Perfectly conducting walls are assumed on the electrode surfaces. Blocks are connected by overlapping ghost cells. An insulating boundary is assumed at the breech of the gun. For cylindrical geometry, the quantity rB_θ is computed on the insulating surface using Ampere's law. These computations used both an LRC circuit model and a prescribed current profile of a shape that can be generated by a PFN. At the beginning of the computation, initial plasma conditions are prescribed on the blocks. For these simulations, an initial annular slug of constant density with an initial velocity directed down the bore of the gun is assumed. This mimics the initial plasma produced by capillary injection. Though these initial conditions may seem highly simplified, the initial density profile was not found to have an appreciable effect on the outcome: during the first microsecond or two, the plasma tends to thermally expand to fill the breech before acceleration gets underway.

3.5 The Wasp Profile

Initial simulations used a “Wasp” profile for the center electrode (so called because of its similarity to a wasp’s body) with 90 degree injection of the plasma, as illustrated earlier in Figure 6. After running a number of test cases with this configuration, it was observed that this design overcorrects for blow-by. The problem lies with the sharp right angle turn the plasma must make going around the initial corner, where it transitions from the z-pinch into the main accelerator section. This is illustrated in Figure 7. The momentum of the plasma causes formation of a pocket of very low density plasma just around the corner which rapidly accelerates under both electrothermal and electromagnetic forces up along the outer electrode. Meanwhile the main bulk of the plasma continues forward curving around along the inner electrode, generating the very steep density gradient seen in the figure.

The current density peaks in the regions of high conductivity, i.e. where the temperature and charge carrier density are high, as seen in the joule heating contours in Figure 8. As the plasma accelerates around the curve, it necessarily takes the current attachment point on the outer electrode with it. This stretches out the current channel very rapidly. The resulting $\mathbf{J} \times \mathbf{B}$ forces then act to further compress the plasma radially inwards against the inner wall. The result is a “blow-by” that occurs on the outside rather than on the inside as in a straight coax.

A set of initial conditions could not be found that circumvents this problem for this specific injection geometry. In this particular configuration, the curvature is excessive and over-corrects, causing the blow-by to occur on the outside. This suggests that the convexity of the outer electrode and the concavity of the inner electrode in the transition from the z-pinch to the main acceleration section needs to be reduced.

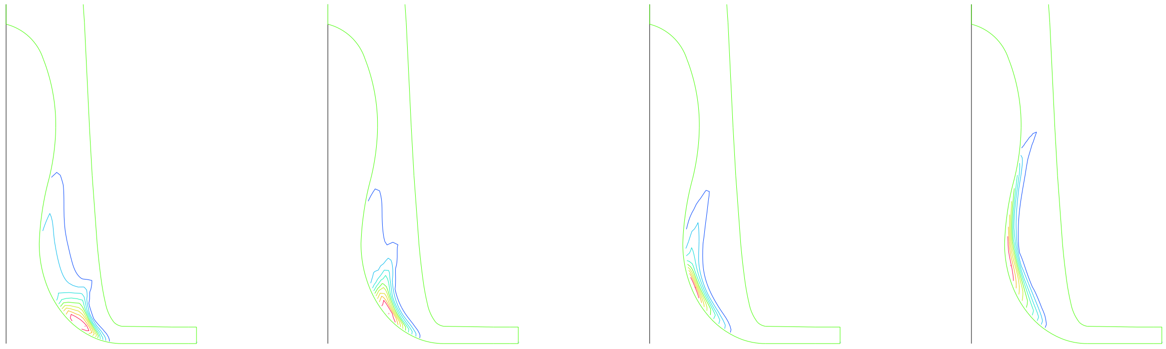
(a) 11.5 μs (b) 12 μs (c) 12.5 μs (d) 13 μs

Figure 7 *Density contours for baseline wasp profile run hyperv37. Highest density is the red contour, lowest the outer dark blue contour. Velocity plots show the plasma rapidly accelerating around the corner, leaving a virtual vacuum there which prevents significant current flow. We were unable to find a set of parameters which worked with 90 degree injection as shown here.*

3.6 Systematic Tuning of Profile Curvature

Based on the simulations described above, a new series of simulations were performed to test the original Wasp electrode profile, but with an angled injector to provide the correct curvature. The best angle seemed to be around 45 degrees, as was also indicated by another series of simulations using simple circular arc profiles to study armature dynamics. The detailed behavior of the flow from a well performing simulation of the Wasp electrode profile is shown in Figure 12, which shows contours of the kinetic energy density $\frac{1}{2}\rho v^2$. As can be seen from these figures, a compact, well-

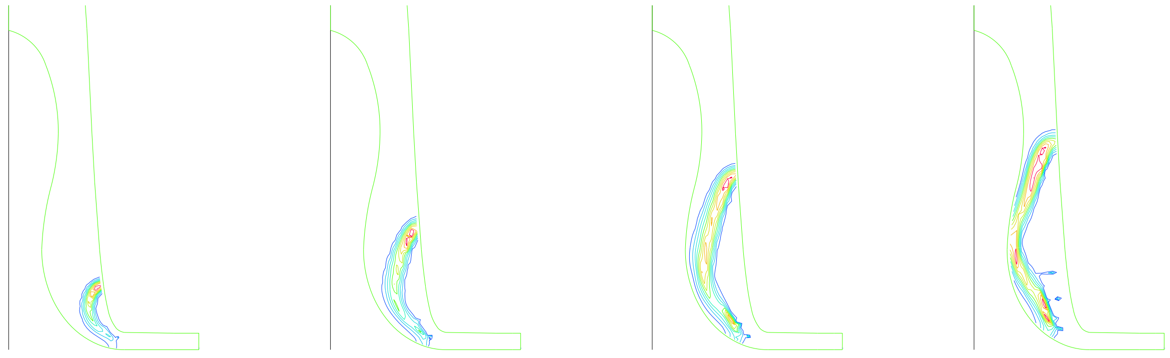

(a) 11.5 μs (b) 12 μs (c) 12.5 μs (d) 13 μs

Figure 8 *Joule heating contours for run hyperv37. As a result of the strong density gradients, current density tends to follow the region of high plasma density as reflected by the joule heating profiles. A proper armature cannot form in this case.*

organized plasma slug is formed early in time. The curvature of the electrode profile continues to maintain a compact plasma as it accelerates up the annular channel, very much as expected theoretically and described above. A number of runs were made with a range of parameters for the initial conditions (injection velocity, density, temperature and plasma mass). The current density is confined primarily to the compact plasma armature for these best runs. This successful profile, and the range of parameters determining the initial conditions, were later used as the baseline for the design and development of the prototype plasma accelerator.

The plasma is injected at the correct angle to allow the armature to hold together as it accelerates down bore. The $\mathbf{J}\times\mathbf{B}$ forces on each end of the armature are balanced so that the extra distance the inner attach point has to travel around the convex curve of the inner electrode (region C in Figure 6) just allows it to maintain pace with the attach point on the outer electrode. As the armature starts to compress near the throat (region D in Figure 6), the plasma compresses and a hint of blow-by can be seen near the outer wall, but the compressing plasma prevents it from growing. As the plasma travels through the throat and emerges on the other side it rapidly accelerates toward the axis where it compresses to very high density and then rapidly exits through the muzzle. The bulk flow velocity in the muzzle region of these simulations was about 200 km/s with densities in the range of $10^{16} - 10^{17}$ cm^{-3} with total mass on the order of 200-400 μg. The bulk flow velocity is defined as $V_{bulk} = (2E_{kinetic}/M_{total})^{\frac{1}{2}}$. The plasma jet takes on a "smoke-ring-like" structure in most of these simulations with a low density core near the axis, as seen in Figure 12.

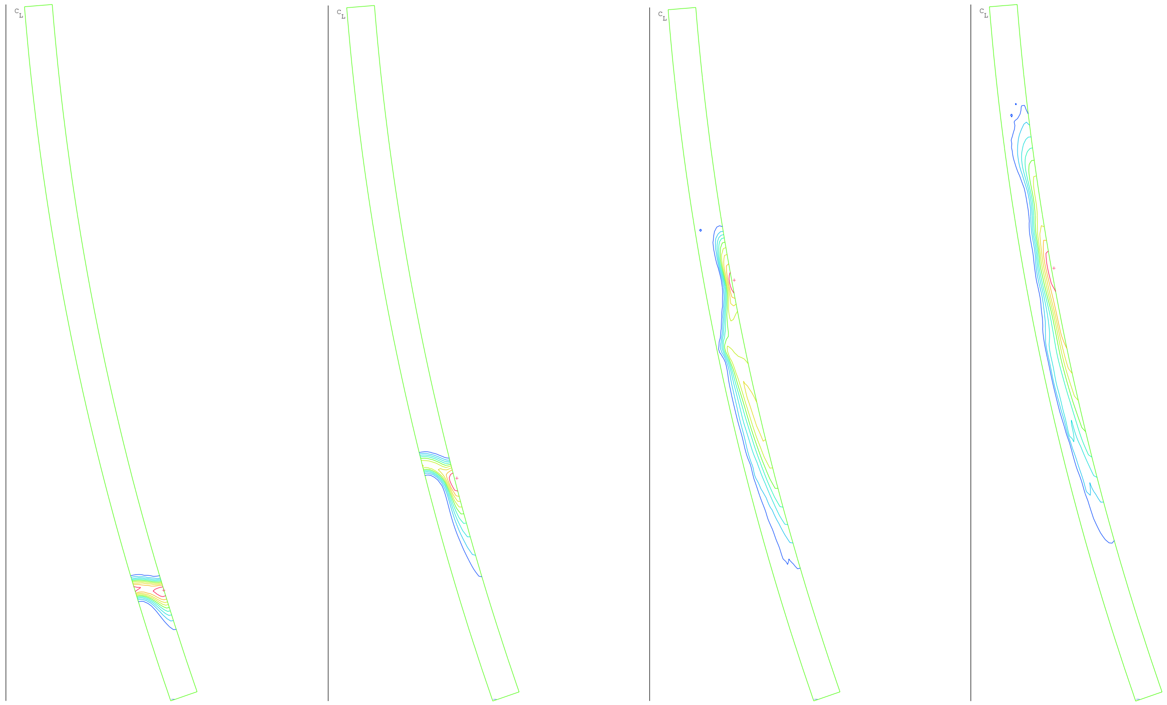

(a) 5 μs (b) 6 μs (c) 7 μs (d) 8 μs

Figure 9 *Kinetic energy density contours for run circular06 illustrating a classic case of blowby. Plasma density is pushed aside to the outer wall while current races ahead along the inner electrode, eventually leaving the plasma mass behind.*

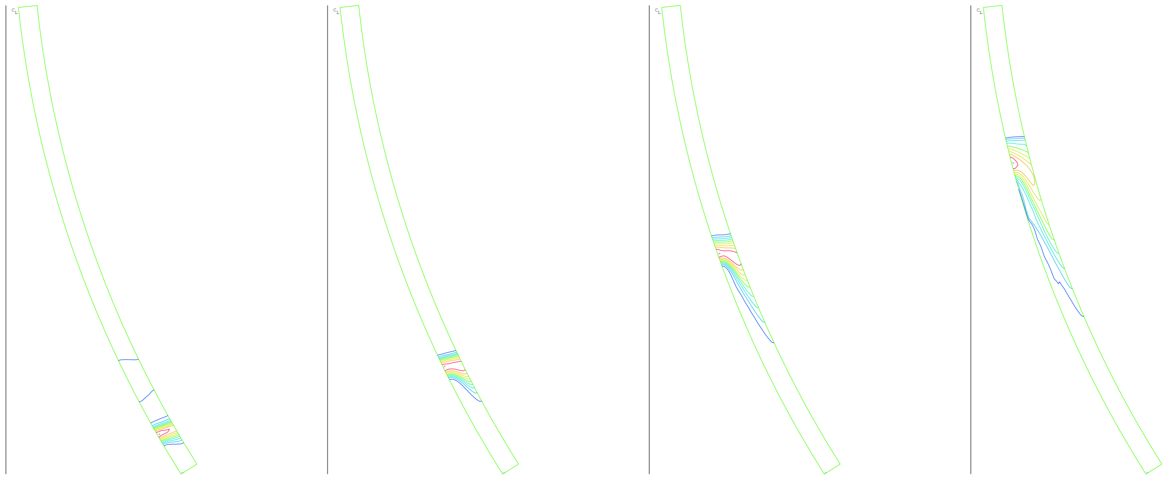

(a) 5 μs (b) 6 μs (c) 7 μs (d) 8 μs

Figure 10 *Kinetic energy density contours for run circular09 show that plasma armature holds together almost long enough to reach the end, but plasma mass is still trailing out along the outer electrode.*

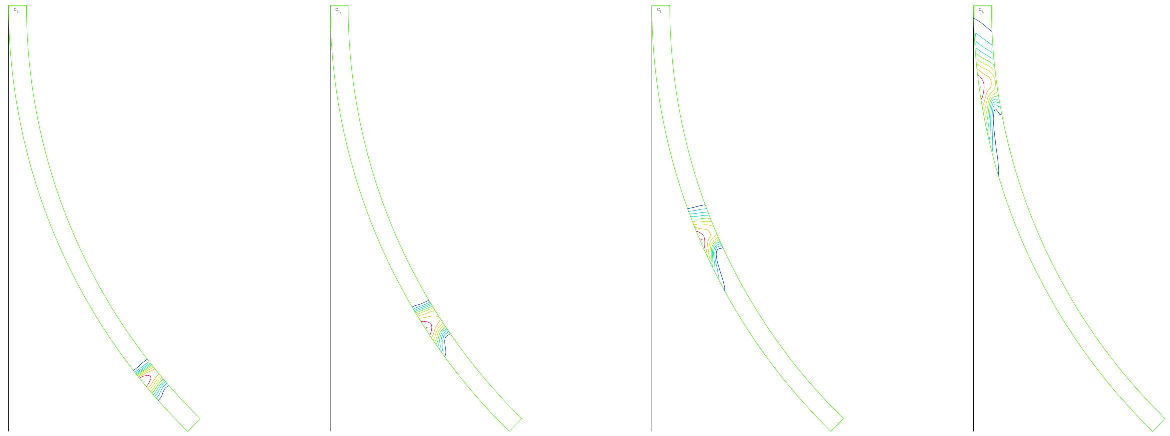

(a) 5 μs (b) 6 μs (c) 7 μs (d) 8 μs

Figure 11 *Kinetic energy density contours for run circular10. Even more curvature now provides a radial density profile sufficient to suppress blowby and allow a compact well-formed armature to reach the end of the accelerator. Additional runs with even higher curvature show that conditions similar to that for the 90 degree injection turn are approached and blowby begins occurring along the outer electrode with increasing strength as the curvature is increased.*

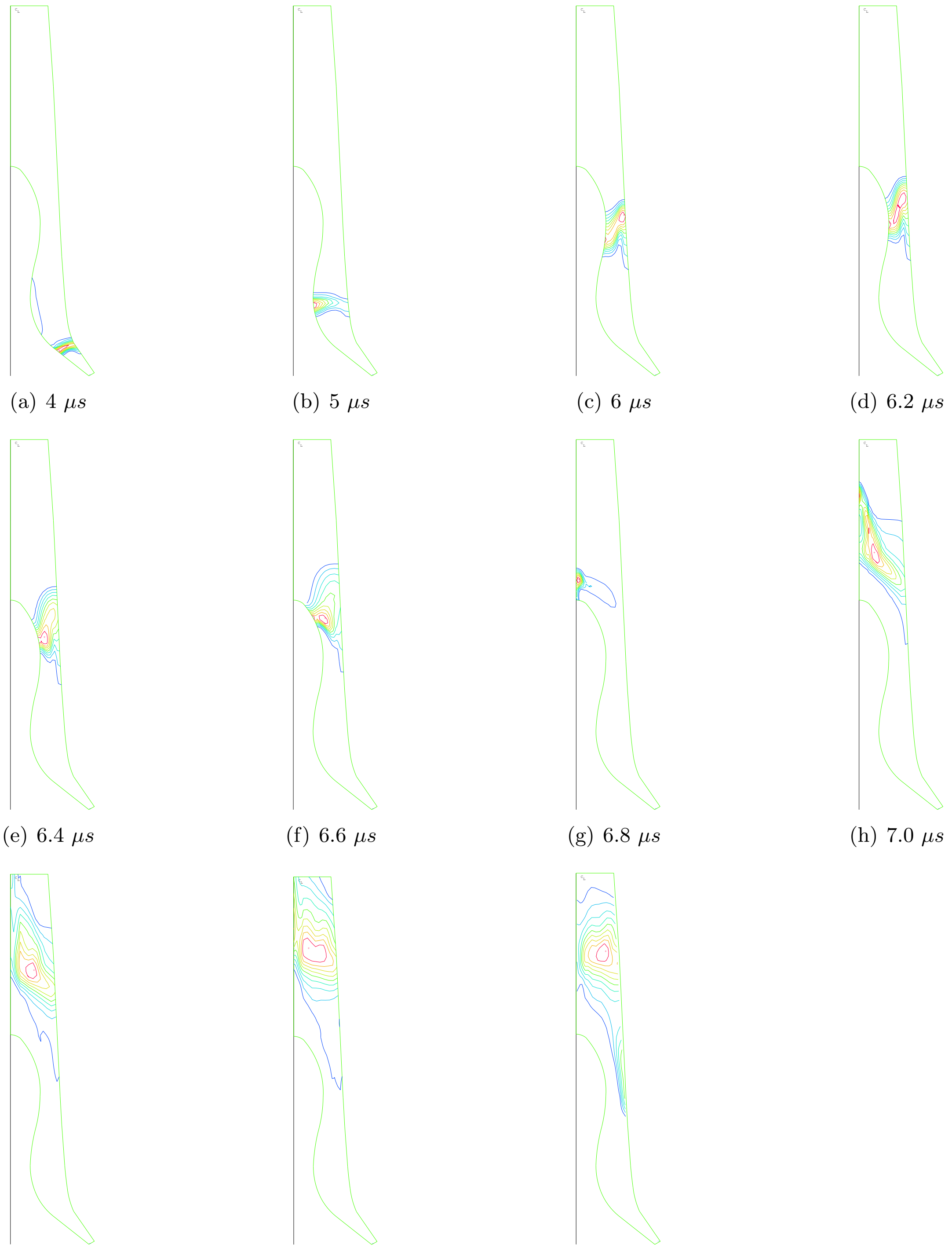

(a) 4 μs (b) 5 μs (c) 6 μs (d) 6.2 μs

(e) 6.4 μs (f) 6.6 μs (g) 6.8 μs (h) 7.0 μs

(i) 7.2 μs (j) 7.4 μs (k) Density at 7.4 μs

Figure 12 *Kinetic energy density contours for case extwasp31 with angled injection. An angle of about 45 degrees seems optimal. The plasma is injected at the correct angle to allow the armature to hold together as it accelerates down bore. The* $\boldsymbol{J} \times \boldsymbol{B}$ *forces on each end of the armature are balanced just right so that the extra distance the inner attach point has to travel around the convex curve of the inner electrode just allows it to keep up with the attach point on the outer electrode. As the armature starts to compress near the throat, the plasma compresses and a hint of blowby can be seen near the outer wall, but the compressing plasma prevent it from growing. As the plasma travels through the throat and emerges on the other side it rapidly accelerates toward the axis where it compresses to very high density and then accelerates down the bore. The velocity in the muzzle region of these simulations was about 200 km/s with densities in the range of* $10^{16} - 10^{17}$ *and total mass on the order of 100* μ *gm. The plasma jets takes on a smoke ring like appearance in these simulations, while others have a more centered blob of plasma.*

3.7 Prototype Coax Gun Development

A cutaway view of the first-generation half-scale prototype plasma accelerator was shown earlier in Figure 2. The design is based on the Wasp profile and MACH2 simulations described earlier, but the half-scale conforms to the physical constraints of installation onto the MCX vacuum chamber at the University of Maryland, where it was intended as a driver of rotations in a centrifugally confined mirror plasma [47]. Modeling similar to that of the last section predicted the half-scale gun could accelerate 80-100 μg of polyethylene plasma to ~90 km/s with a 9 μs current pulse of ~190 kA. The experimental results described below confirm these performance predictions.

The accelerator [48] consists of two main copper alloy electrodes with a ring of 32 equally spaced capillary discharge injector units. The capillaries are mounted in an insulating block of Kynar so that they float electrically with respect to the two main electrodes. The tungsten exit nozzle of each capillary is recessed behind a polyethylene nozzle, which provides a tapered transition to the breech of the main coaxial accelerator. The two main electrodes are held together by two stiff ring structures using 32 insulating fiberglass studs. The Kynar ring also provides HV insulator standoff between the inner and outer electrodes. Attempts to operate without an external switch have been generally unsuccessful to date. Even at an ambient pressure of 10^{-5} Torr, the structure does not hold off more than about 6 kV after the first shot. It is currently unknown whether this is a fundamental limitation, or whether it could be avoided with a modified design, perhaps using a ceramic insulator instead of plastic. This will be readdressed in the future.

The main electrodes were machined from solid cylindrical "logs" of copper alloy. The inner wall profiles were machined with numerically controlled lathes using profile data from the MHD simulations.

3.7.1 Experimental Facility

The experimental facility is shown in Figure 13. The gun is mounted on a support stand and connected to an octagonally shaped vacuum chamber (with an inner diameter of 18 inches) through a so-called pinch section (corresponding to region G in Figure 6). The pinch section consists of a copper tube that carries the final pinching current of the main discharge. Several small ports have been drilled through the wall, which allow insertion of optical and magnetic field probes. A turbopump assembly provides base pressures below 10^{-5} Torr.

We have developed a suite of diagnostics including magnetic and pressure probes as well as time-resolved HeNe interferometry, optical spectroscopy, and fast imaging. There is also an assortment of Rogowski coils and Pearson current monitors to measure the current and voltage supplied to the capillaries and the center electrode. Two cameras were used to obtain both fast and time-integrated signals. These diagnostics and typical results are described in detail in Sec. 3.8. We have also constructed a fast 16 channel PMT diagnostic based on a Hamamatsu R5900U-00-L16 multichannel photomultiplier array. Time resolution is better than 50 nanoseconds, but optical crosstalk between channels creates a practical limit of 4 channels of well-resolved data. Those diagnostics that produce voltage traces on experimental timescales are recorded by 24 Tektronix TDS2000-series oscilloscopes. Each of these four-channel digitizers has a sampling rate up to 1 Gb/sec and 100 MHz bandwidth. A screen room shields the oscilloscopes from electrical interference during the high-voltage shots. The oscilloscopes are controlled and read by custom Python-based software.

The 20 kV, 96 μF capacitor bank supplying the main discharge current is typically charged to 18 kV. The PFN is configured as two parallel legs of four 12 μF Maxwell capacitors in each leg as illustrated in Figure 14. An adjustable ballast resistance of 30-60 milliohms roughly matches the PFN to the discharge in order to reduce ringing (although it is never entirely eliminated). The

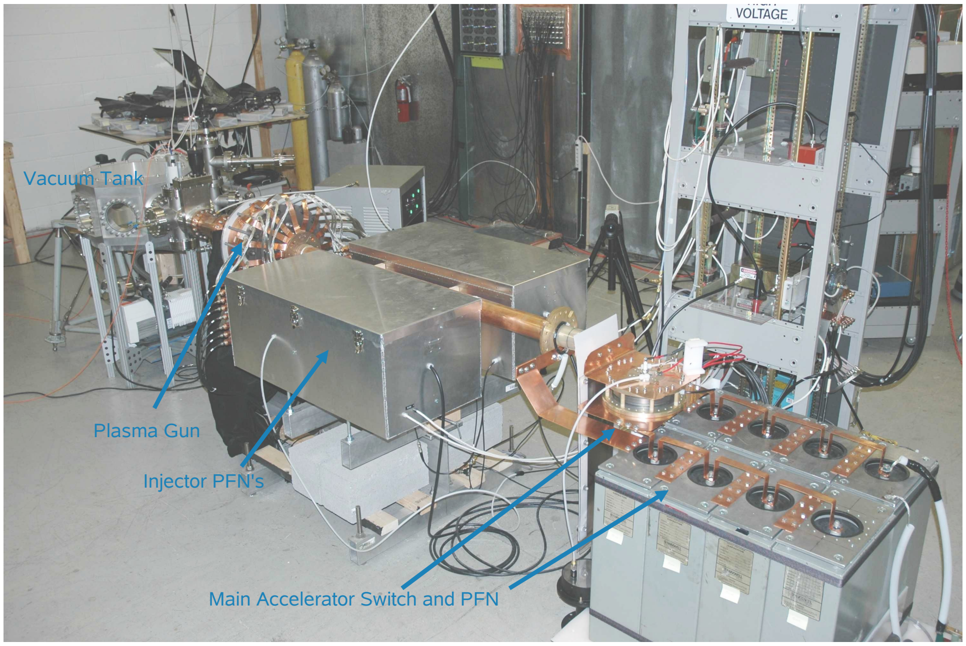

Figure 13 *Gun testing facility with the main accelerating PFN in foreground and target vacuum tank in background. The two large boxes in the center contain the capacitors and switches for the 32 capillary injectors.*

capillaries draw current from a set of eight 40 kV, 0.15 μF capacitors. Charge and dump operations are controlled with a set of 120 VAC drop hammers. A pair of Titan 40264 spark-gap switches discharges the capillary capacitors. A single Beverly III Associates SG-172CM2 spark-gap switch discharges the main PFN.

3.7.2 Plasma Injection

Plasma injection is accomplished using a large number of small capillary discharge units. Each of the capillaries is a high-voltage coaxial unit. The output end of the capillaries provides an axial discharge path across the ablative plastic insulation. A surface discharge across this insulation connects the inner and outer electrodes, heating and vaporizing the polyethylene insulation. The resulting plasma expands to fill the interior tube. Ohmic heating of the plasma combines with magnetic forces to eject a hot, dense plume past the tungsten nozzle. Plumes from neighboring capillaries combine to form a uniform ring of plasma connecting the inner and outer electrodes of the main gun.

The electrical energy input to the capillaries must be split between heating, ablating, and ionizing the polyethylene surface. Thermal pressures dominate the resulting plasma. As a result, the injection velocity is near Mach 1, typically 10-14 km/s for these polyethylene plasmas.

Initial designs for the capillary injectors used a series of sealing O-rings and was both expensive and complex to assemble. Later designs moved toward press-fit and glued seals. The components are cheaper, assembly is faster, and both vacuum and high-voltage performance are just as good as for the original design. The center, high-voltage electrode is an off-the-shelf 1/8” (3.18 mm) diameter tungsten welding rod. The grounded outer conductor is a brass cylinder. The nozzle electrode is tungsten. A high-density polyethylene (HDPE) tube provides the high-voltage insulation and ablative mass. An assembly drawing of the final design is shown in Figure 15. The capillaries can

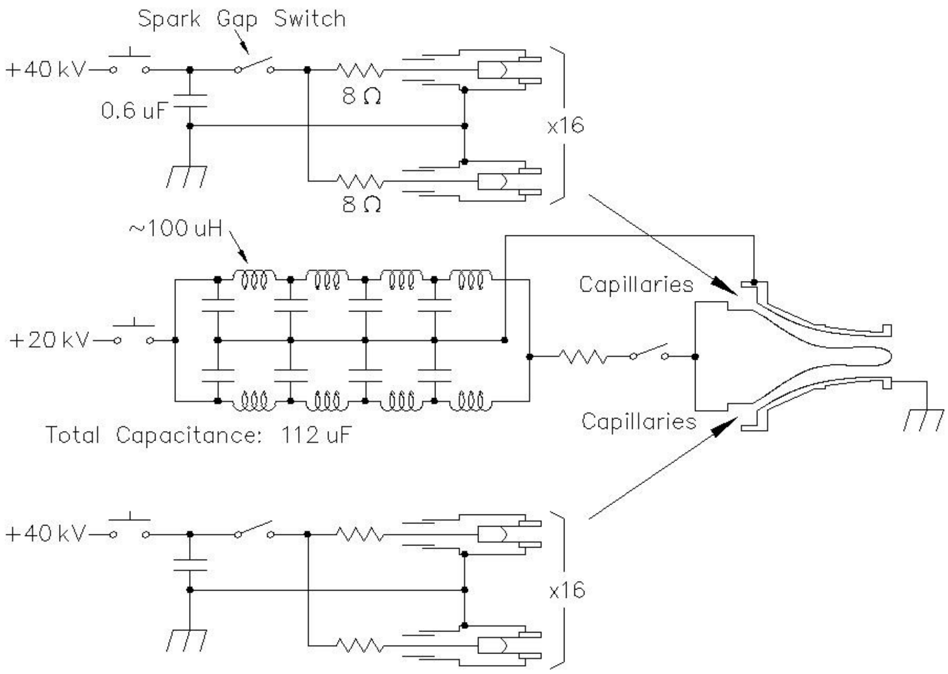

Figure 14 *Schematic of accelerator system showing two separate high voltage circuits for the capillary injectors and the main accelerator respectively.*

be seen protruding from the rear of the accelerator in Figure 16, with the internal mounting details in the annular breech of the accelerator illustrated in Figure 17.

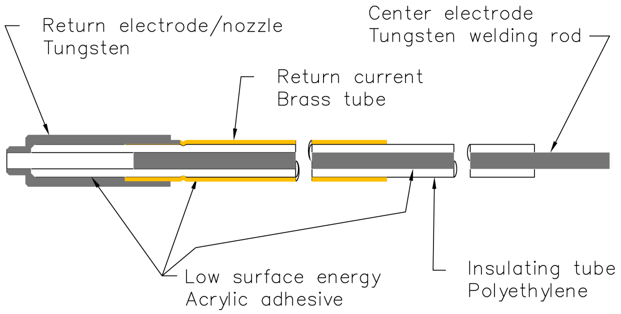

Figure 15 *Detailed view of internal structure of capillary used in main accelerator. Except for the tungsten nozzle which requires machining, all components are commercial-off-the-shelf items simply cut to length. Internal vacuum seals are achieved using acrylic adhesives.*

Once a capillary establishes a surface discharge, its resistance drops as the increasing capillary current heats the plasma. Initially, this led to the concern that the capillary array would operate unevenly, i.e. the voltage would drop too low to complete the discharge initiation of the remaining capillaries once the first one went. This would result in a highly asymmetric injection into the main gun. Such high asymmetry would accelerate the development of the Rayleigh-Taylor instability and sharply limit gun performance. To avoid this situation, early designs placed a ballast resistor in series with each capillary, but the explicit ballast resistors ultimately turned out to be unnecessary, since the stray (inductive) impedances in the circuit were found to be sufficient to maintain balance.

We have established reliable symmetric operation of 32 capillaries (and 64 in the TwoPi device discussed later) by connecting each capillary to the switch through a single cable. There are two

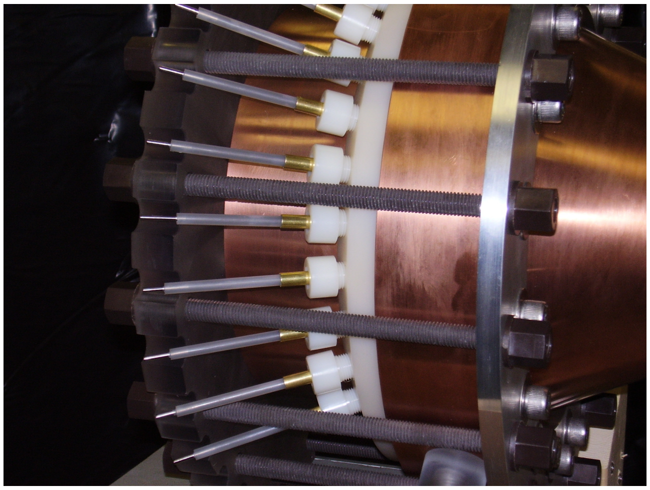

Figure 16 *Closeup view of capillary high voltage connections extending out the back of the gun from their insulating carrier bolts. Current enters through the center tungsten electrode and returns via the coaxial brass tube. An external coaxial braid (not shown) keeps the current coaxial to reduce noise generation in diagnostics and other circuitry. See also Figs. 15 and 17.*

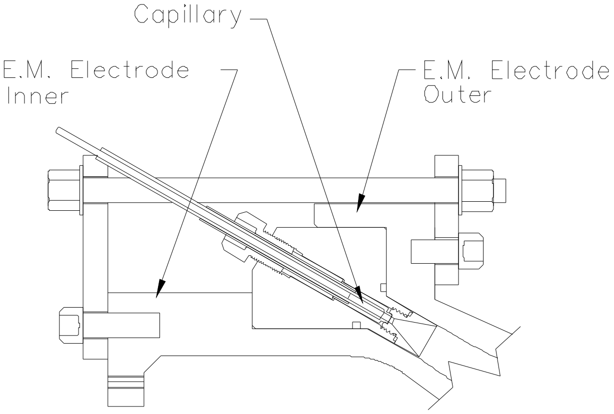

Figure 17 *The capillaries are mounted in a plastic Kynar ring with individual polyethylene nozzles.*

Titan switches in parallel, each of which controls the current to 16 capillaries. Each Titan switch gates the current from four 0.15 μF capacitors typically charged to 35 kV. Eliminating the ballast resistors allowed more of the capacitor energy to be used in ablation and heating of the polyethylene, which produced higher-density and higher-temperature capillary discharges. The capillaries all fire within about 25 ns, as shown in Figure 18. Typical capillaries currents are 3-5 kA, with a ~1.54 μs period, and a subsequent 1/e decay time of ~3.2 μs.

3.7.3 Parallel Operation of Capillaries

As a general rule, it is not possible to run capillary discharges in parallel because of two main reasons 1) instability in the I,V characteristics, and 2) HV breakdown. In the first case, a small perturbation in the capillary parameters of one relative to the other usually leads to an instability in which one capillary draws all of the available current and the other one extinguishes. This results from Spitzer resistivity in that a positive perturbation in the current in a capillary leads to

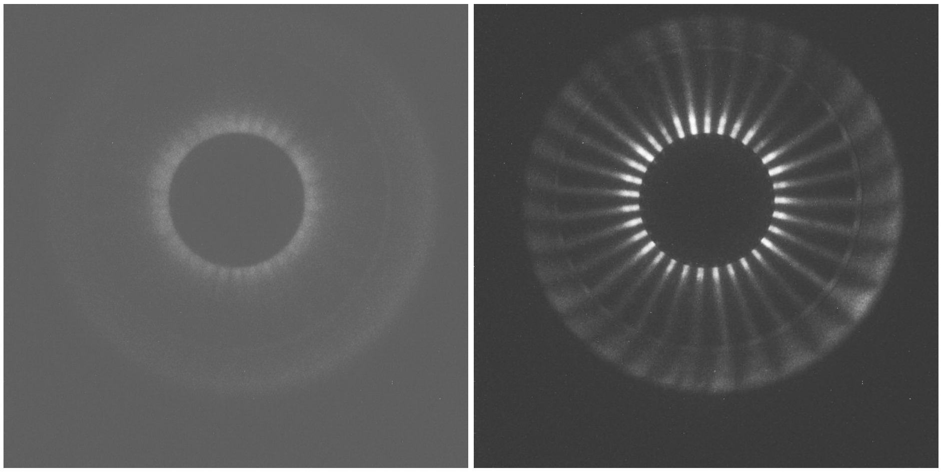

Figure 18 *Left) Fast PI*MAX *image of capillaries firing. Gate is 25 ns wide triggered at t=0. Right) Gate of 1 μs. Capillary discharge fully established. Both images looking back up through the muzzle. Dark central circle is the center electrode.*

increased temperature, and lower resistance, which in turn leads to more current, and so on. The reverse occurs for a negative perturbation, so that two capillaries in parallel are naturally unstable.

In the second case, it is usually not possible to get more than one capillary to even breakdown. What happens is that as soon as one capillary breaks down, the voltage seen by the rest of the capillaries is suddenly very small, well below the Paschen limit in most cases, so that in general, only one capillary can break down at all. At first glance, we thought this might require a separate capacitor and switch for each capillary, but further analysis and experiment revealed this is fortunately not the case at all.

We plan to run the capillaries using the parallel circuit illustrated in Figure 19. In this schematic, r represents the small impedance of the capillary, while R represents a larger ballast resistor placed in series with each capillary. For sufficiently large R/r, the circuit remains stable to small perturbations in any individual r, for much longer than the time scales of interest in these experiments. For example, for a typical value of $r = 0.1\ \Omega$ a ballast resistance of about $7 \times r = 0.7\ \Omega$ should be sufficient for a circuit with 8 parallel capillaries.

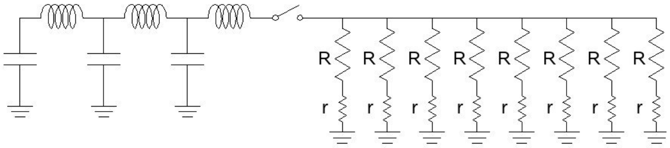

Figure 19 *Representative parallel circuit. r is the capillary resistance and R the ballast resistance*

Consider the following. For a given capillary geometry, assume the voltage across the capillary is given by $v_0 = i_0 r$ where i_0 is the measured current. The charging voltage for a matched pfn would thus be $2v_0$. Now place a ballast resistor R in series with r of value $R = 7r$. In order to maintain the same current through the capillary discharge, the pfn charging voltage needs to increase to $2(r + R)v_0 = 16v_0$, i.e. 8 times the original voltage. Place 8 such series combinations of r and R in a parallel arrangement as shown in the figure, and the total impedance seen by the pfn is just r and 1/8 of the total current flows in each leg. If the pfn voltage is $8v_0$, then the current in each leg equals that in the original capillary by itself. Thus total current is now $8i_0$. The same analysis holds true for any number of parallel circuits. The required pfn charge voltage scales linearly with the number of capillaries placed in parallel.

This is a very attractive scaling. We already know (and our experimental testing confirms) that the desired capillary current is on the order of 2-4 kA, and that the capillary impedance is of order 0.1 Ω. We see the voltage drop across the capillary will be a few hundred volts. Placing 16 units in parallel will drive the pfn charging voltage to 2×16 times a few hundred volts, or only about 12-13 kV. Total current through the switch would then be about 32-48 kA, well within the 65 kA limit of the switches we have selected (described in a later section). This implies that we should be able to easily run 16 capillaries in parallel. In principle, we could drive even more in parallel by simply operating at higher voltage.

Operating at higher voltage has real advantages, both in the speed at which the switch operates, and in reducing jitter in the Paschen breakdown time of each capillary [49, 50]. In fact, it may be desirable to increase the ballast resistance even further, thus increasing the charging voltage and hence the voltage used for initial breakdown. The initial voltage available for Paschen breakdown in the capillary can be driven almost arbitrarily high, in principle limited only by HV breakdown elsewhere, and the higher cost of capacitors (which scale roughly as the square of the voltage). Values of 20-30 kV are readily achievable, but probably not necessary until we operate the accelerator at 10^{-7} Torr. Further experimental testing will determine what voltage level is optimal.

Now what about HV breakdown as mentioned a few paragraphs above? With the ballast resistor in place, as soon as the first capillary breaks down, the voltage seen by the other capillaries no longer plummets, but only drops a small amount since they will still see the voltage on the high side of the ballast resistors, which drops only by the ratio r/R, which for 16 parallel capillaries is only a 6.25% drop. The jitter between capillary breakdowns is expected to be smaller than the switches at the voltages we expect to operate.

The only operational price that is paid for these advantages is that most of the stored energy in the capacitors is "wasted" in the ballast resistors. However, this is irrelevant, since the value in absolute terms is relatively small and precision high voltage resistors are readily available that can handle the voltage and energy dissipation for this application at modest cost [51, 52, 53].

3.7.4 Sparkgap Gun

As an alternative to the capillary injector approach, a second approach using sparkgap injectors was also built and tested. This configuration uses a much larger number of small tungsten electrodes mounted with their tips roughly flush with the inside surface of an annular insulator ring at the breech of the gun. This is illustrated in Figure 20. The external HV circuit is arranged so that the electrode tips alternate in polarity: Ground-HV-Ground-HV-Ground . . . . Surface arc discharges along the insulator, with alternating current direction, then ablate the local polyethylene surface, ejecting plasma into the gap between the coaxial electrodes. Due to the much larger number of plasma sources, 112 sparkgap electrodes vs. 32 capillaries, a higher degree of symmetry in the injected plasma can be achieved. The electrodes consist of off-the-shelf tungsten welding rods with a diameter of 1/16" (1.6 mm) by 6" (15.2 cm) long. They are carefully press fit into a slightly undersize hole in the polyethylene, forming a tight vacuum seal that allows base pressures into the 10^{-6} Torr range. Figure 21 shows the HV connections surrounding the gun. There are 7 switches, each of which connects two 0.15 μF capacitors to 16 electrodes. A combined total of almost 0.7 MA is driven through the 112 sparkgaps generating the injected plasma.

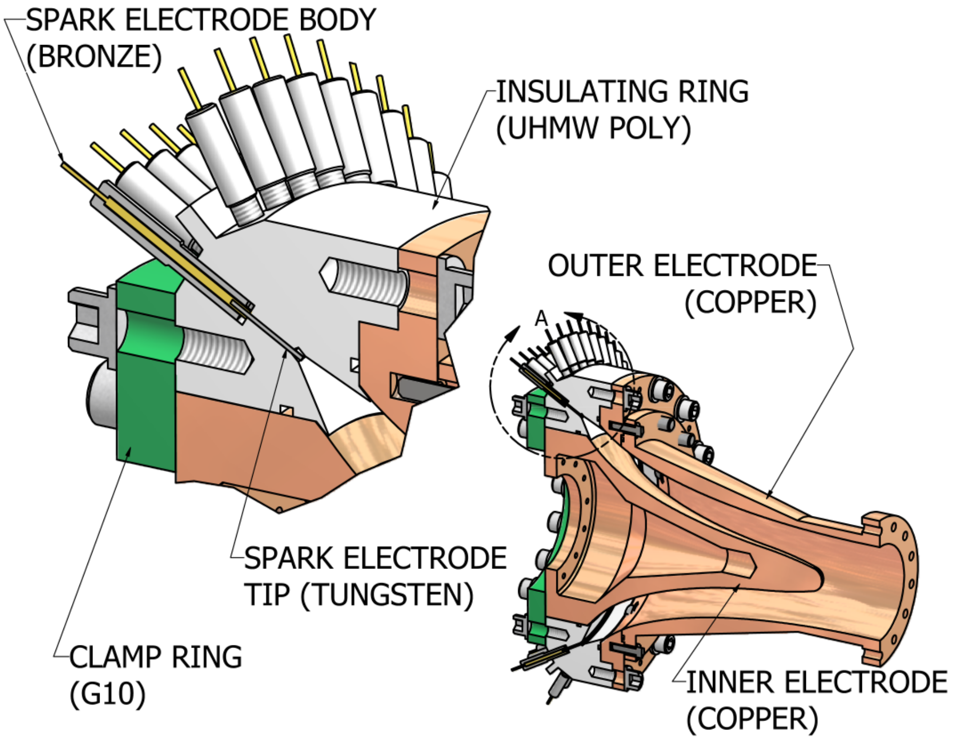

Figure 20 *Sparkgap gun configuration with 112 tungsten electrodes and a center electrode with a smooth circular arc profile instead of the "wasp" profile of the first prototype gun shown in Figure 2.*

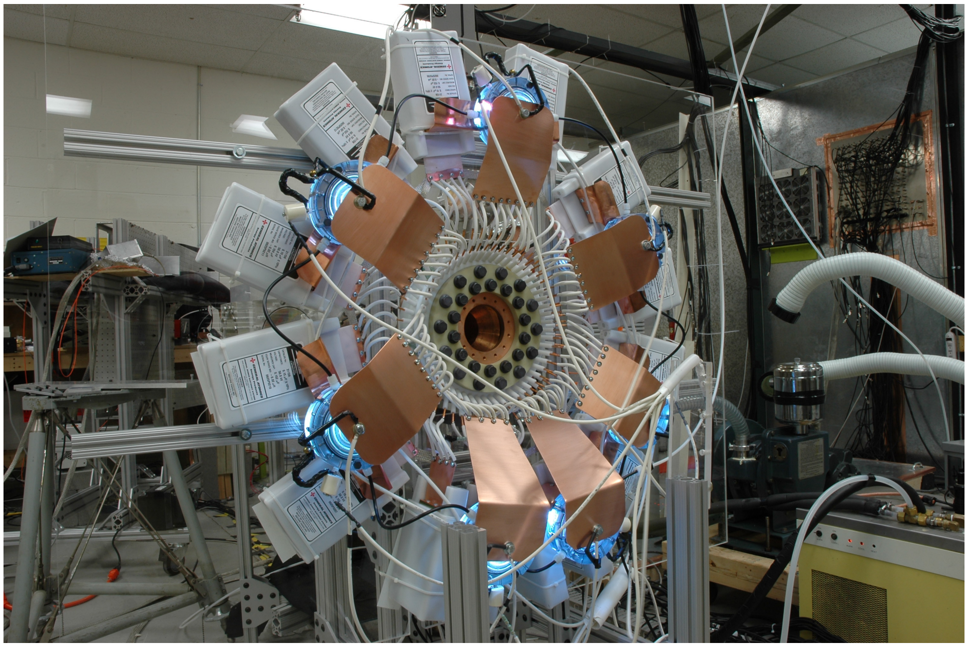

Figure 21 *Rear view of sparkgap gun with main bank disconnected to show only the 112 sparkgap injectors firing.*

3.7.5 TwoPi Test Fixture

The "TwoPi" test fixture was built to allow development testing of large capillary arrays and their associated HV circuitry. The initial version used a disc-shaped vacuum chamber with an inner diameter of 19.5" (49.5 cm) and inner height of 2" (5.1 cm). Sixty-four radially inward pointing capillaries (essentially identical to those used on the gun) are arranged uniformly around the periphery as seen in Figure 22. Large top and bottom acrylic viewing flanges allow optical probing and imaging of the plasma as it emerges from the capillaries and propagates toward the center.

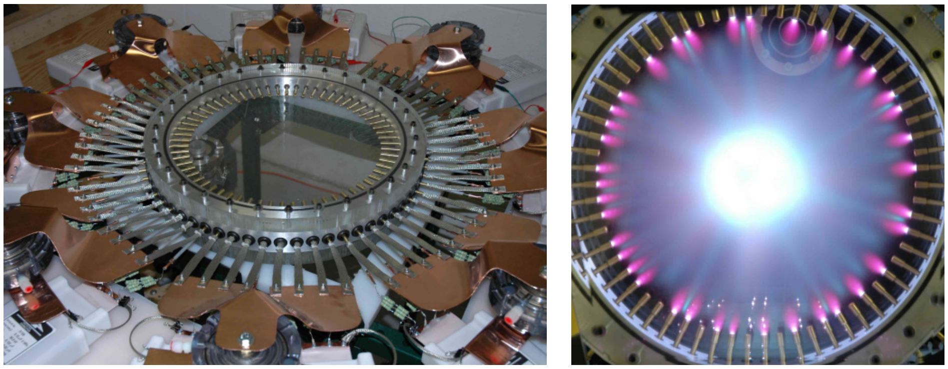

Figure 22 *Left) Arrangement of the original TwoPi test fixture showing copper bus plates, ballast resistors, capacitors, switches, and vacuum vessel. Right) Nikon open shutter photograph of a test shot in original TwoPi test fixture.*

3.8 Experimental Results

We discuss below typical characteristics for the half-scale prototype gun used on MCX. Variations in the ballast resistances, fill pressure, and other machine parameters were observed to shift these numbers. For example, the electron density was found to increase from $4\times10^{14}\text{cm}^{-3}$ to $6\times10^{14}\text{cm}^{-3}$ when the ballast resistor was decreased from 8 Ω to 0. For purposes of definiteness and direct comparisons, all measurements quoted below are made with 0 Ω ballast resistance on the capillary plasma injectors and a 1 μs delay between firing the capillaries and the main PFN. The background pressure is less than 10^{-5} Torr of air (i.e. no separate gas filling).

3.8.1 Gun Electrical

The main gun's current and voltage waveforms are routinely measured. A Rogowski coil records peak currents of about 174 kA on each shot. The first half-cycle of the current ring lasts 22.8 μs, and the reverse current is 44% of the peak current. (See Figure 23.) Voltage is obtained by a Pearson monitor measuring current through a 1 kΩ resistor across the gun's breech. The current waveform varies smoothly over the course of the shot, suggesting that any restrikes or filamentation provide only gradual changes to the gun impedance. Additional Rogowski coils measure the current to individual capillaries. These Rogowski coils show 5 kA per capillary.

3.8.2 Visible Light Imaging

A Nikon D70s digital camera routinely gives time-integrated color pictures of the plasma discharge from various angles. These typically show a bright blue-white plasma flowing from the gun muzzle

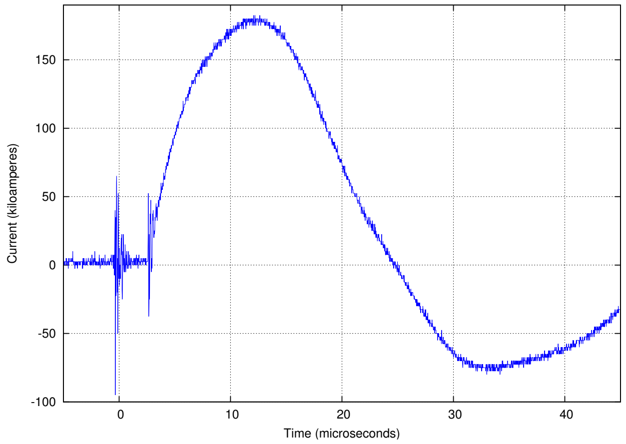

Figure 23 *Main accelerating current rings due to impedance mismatch.*

and gradually expanding downstream as seen in Figure 24. A pink plasma fills the target chamber, and a dimmer blue plasma rebounds off the back wall of the chamber. The interior of the gun is filled with a bright blue plasma, and there is often evidence for distinct bright-white filaments between the inner and outer electrodes (future work will attempt to determine when and where these occur within the gun). Photographs of the capillary plasma plumes taken without firing the main PFN confirm that all capillaries fire on virtually every shot (Figure 18).

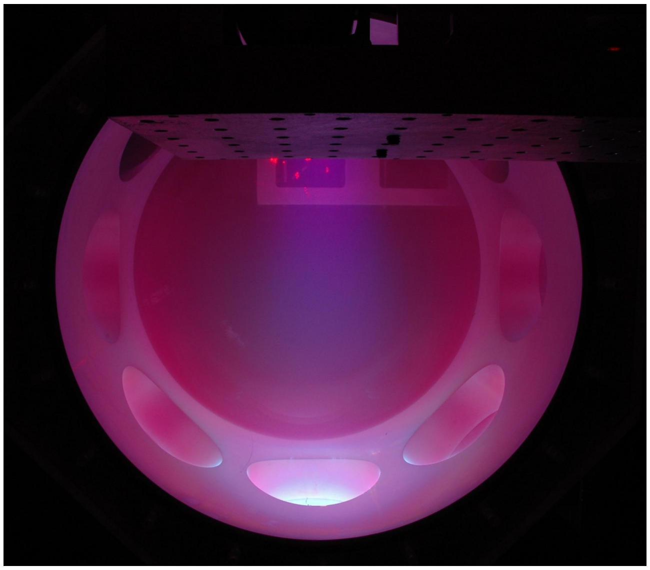

Figure 24 *Nikon open shutter photograph of bright jet plume in vacuum tank. One arm of the interferometer and the interferometer probe beam are visible at the top of the image. Plasma jet travels towards the bottom where it stagnates on one of the 8 side port windows.*

A fast PIMAX camera (model 7489-0004) is used to image the gun plasma on sub-microsecond time scales. It confirms that the capillaries fire simultaneously within 25 ns. The PIMAX shows the gun produces a dense bright stream of plasma (Figure 25.) If the background pressure is raised to the vicinity of 1 mTorr, the stream of plasma condenses into a discrete blob.

Photodiodes have been positioned to look across the plasma flow. These measure speeds of the luminous front ranging up to $\sim$ 143 km/s for some gun configurations.

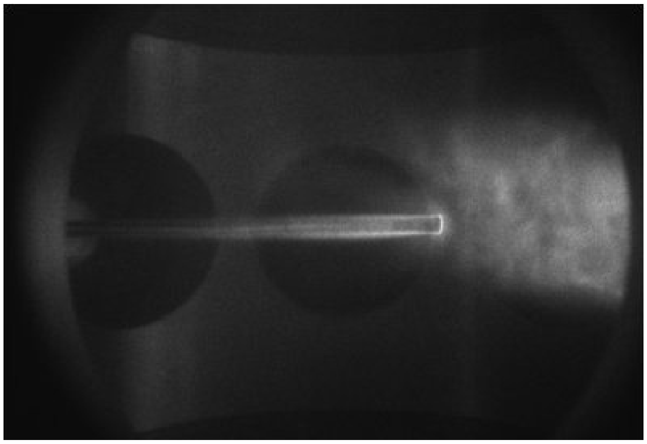

Figure 25 *PIMax image of plasma stream incident on the pressure probe. This image coincides with an increase in the measured pressure. The bright spot at the probe tip and the dim arc upstream of it are reproducible features of the bow shock.*

3.8.3 Spectrometry

We used a compact Ocean Optics, Inc. survey spectrograph to identify interesting regions in the plasma spectrum, time-integrated over the event. It showed spectra consistent with a 2:1 hydrogen-to-carbon ratio, as expected for the ablative polyethylene capillaries used for plasma injection. Interesting regions identified by the spectrograph were further examined using a 1-m stigmatic Czerny/Turner spectrometer (Acton Model 410) with the PIMAX camera previously mentioned used for capturing the spectra. It was coupled to the experiment by two 100 μm diameter fiber-optic cables aligned along the entrance slit, thus permitting two simultaneous views of the plasma, e.g. axial and radial. The monochromator was equipped with an 1800 grooves/mm grating for a nominal reciprocal linear dispersion at the exit of 0.5 nm/mm. With a pixel size of 0.011 mm at the charge coupled device (CCD), this dispersion translates to nominally 0.006 nm/pixel at the detector output. Hence, a detector coverage of 1024 pixels yields a wavelength span of nominally 6.1 nm at any one wavelength setting. A spectral resolution of 6 pixels (as determined from spectral lamps) results both from the selection of a 50-μm wide entrance slit and from a somewhat larger pixel size (16 μm) for the image intensifier in front of the CCD.

Spectral lines from neutral hydrogen (Balmer series), as well as carbon atoms up to 3-times ionized (C IV spectra) are recorded and analyzed. The intensity ratio of carbon-ion lines yields an electron temperature in the slug as high as 4-5 eV, and 5-6 eV in the gun itself when viewed axially. These are based upon calculations [54] of ionization balance (see Figure 26). Interestingly, neutral C I emission is *not* observed, implying an electron temperature greater than $\sim$ 2 eV.

Doppler shift measurements along the axis of the gun indicate a mean C^+ velocity of 80-90 km/s, with a lesser component exceeding 100 km/s (see Figure 27). There is also a somewhat stationary component (arising either at the gun or at the output window) that at times distinctly shows a portion moving with a velocity of $\sim$ 12 km/s. For the same shots on which photodiodes measured 143 km/s, the Doppler shift of the fastest H-α component corresponds to a speed of 147 km/s. (See Sec. 3.8.2.)

The widths of hydrogen Balmer-β and -γ lines observed radially indicate [55] an electron density $\sim 5 \times 10^{14}\text{cm}^{-3}$, averaged across the column (Figure 28). This is likely a slight overestimate of the electron density after correcting for a small Doppler broadening contribution. Other configurations have shown higher electron densities, ranging up to $\sim 5 \times 10^{15}\text{cm}^{-3}$, depending primarily on the fill

(a) Viewed radially

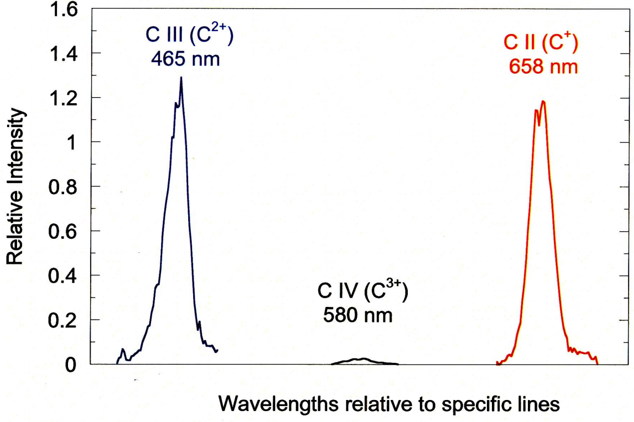

(b) Viewed axially

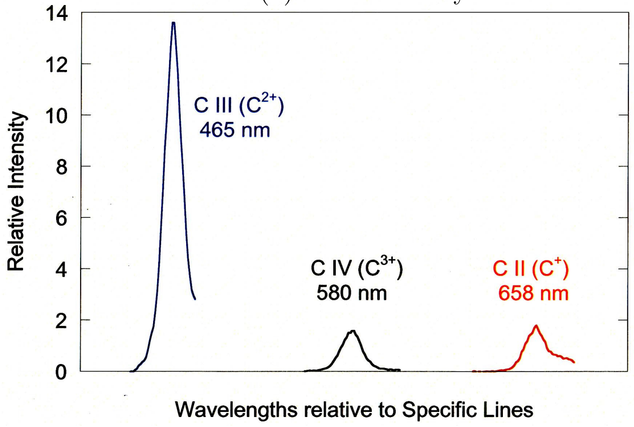

Figure 26 *Relative line intensities for carbon ions. (a) Viewed radially from the gun, implying an electron temperature in the blob from ionization balance of* kT_e *~4-5 eV. (b) Viewed axially inside the gun, implying an electron temperature internal to the gun from ionization balance of* kT_e *~5-6 eV, higher than in the expanding blob.*

pressure. (See also Sections 3.8.5 and 3.8.6.)

3.8.4 Ballistic Pendulum Tests

Initial measurements of the plasma slug momentum were made using a fast camera and a low mass ballistic pendulum consisting of a plastic petri dish suspended by a tungsten wire. A PIMAX fast camera recorded the image at multiple time delays. The pendulum mass and maximum vertical rise give the change in its potential energy ($\Delta E_P = m_{dish} g \Delta h$). From this we calculated the pendulum initial kinetic energy ($\Delta(E_K + E_P) = 0$) and momentum ($p_{dish} = \sqrt{2 m_{dish} E_K}$). If all this momentum is transferred from the plasma, the plasma momentum p_{slug} is not less than the initial momentum of the dish, p_{dish}. (We equate the momenta of the dish and plasma slug rather than using the kinetic energies. This accounts for the likelihood of an inelastic collision involving heating and radiation.) The chamber was evacuated, so the momentum lost to drag is negligible. In addition, the dish is wider and much more massive than the plasma, so the amount it moves during the impact event is tiny, and it blocks the entire plasma throughout impact. We confirmed that this momentum transfer results from the main accelerated plasma jet by firing the injector

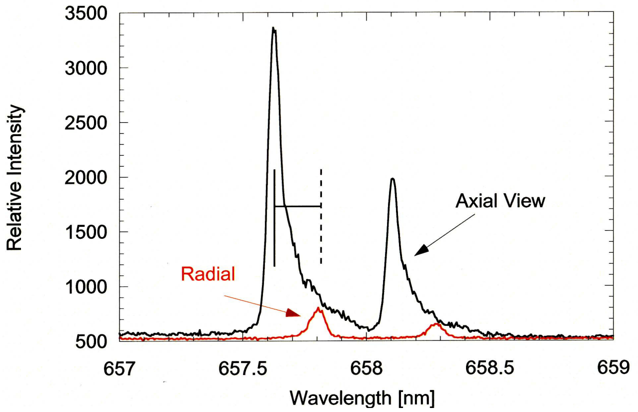

Figure 27 *Velocity for C^+ ions from the Doppler shift of two C II spectral lines viewed along the axis compared to the unshifted radial view. A shift of 0.18 nm here is equivalent to a velocity of ~82 km/s.*

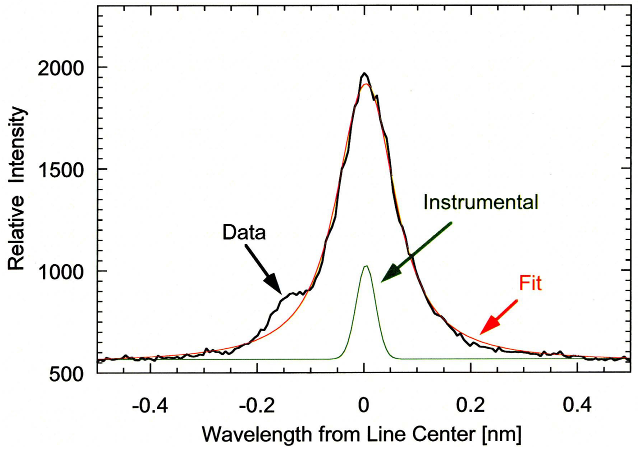

Figure 28 *Stark broadened H-β Balmer line of neutral hydrogen with a Lorentzian fit at an electron density of N_e=5×10^{14} cm^{-3}. The lack of a central dip is attributed to integration along the radial line of sight.*

capillaries without the main gun. In this case, no pendulum motion was detected. Typical direct measurements are: $m_{dish} = 28.9$ g, 21 degree displacement, and $v_{slug} = 90$ km/s (from spectroscopy, Sec. 3.8.3). From the measured angular displacement, the dish undergoes a vertical displacement of 9.7 mm. The measurements imply a plasma momentum of 13 g-m/s and a mass of 140 μg. Raising the background pressure to $\sim$ 1 mTorr has been observed to lower the momentum to 11 g-m/s. The pendulum measures a somewhat higher total momentum (and mass) than the value estimated from other diagnostics. (See Sections 3.8.3 and 3.8.5.) This is probably due to a "rocket" effect of material ablated from the dish surface by the plasma.

3.8.5 Interferometry

The HyperV interferometry system is a 632nm HeNe laser quadrature heterodyne interferometer using a single pass through an Acousto-Optic modulator at 110 MHz which serves as both the modulation source for the reference beam and the beam splitter. The unmodulated scene beam makes two passes through the plasma before recombining with the modulated reference beam on a polarizing beam splitter. The scene beam makes two passes through a quarter wave plate, rotating the direction of polarization through 90 degrees so that the scene and reference beams have orthogonal polarization when recombined on the beamsplitter. The combined beam is passed through a polarizer at 45 degrees to the polarization direction of the beams, projecting the sense of polarization onto the same axis. Detection is via a fiber coupled reverse biased PIN diode, and the signal is demodulated using a quadrature heterodyne detection circuit. This arrangement measures the line-integrated electron density across the output plasma blob 17 cm downstream from the muzzle. If we estimate the path length from PIMAX photographs (10 cm at the position of the interferometer), we find a typical density is 5×10^{14} cm^{-3}. This density is comparable to that obtained by Stark broadening, as described above. The 90 km/s speed of the plasma and the observed duration give an estimated plasma slug length of about 1 m. A 10 cm diameter column 1 m in length with this electron density and an average ion mass of 5 amu will have a mass of about 33 μg. (Compare measurements in Sections 3.8.3, 3.8.4 and 3.8.6.)

Optical spectroscopy (Sec. 3.8.3) on the spark gap gun has routinely measured Doppler-shift velocities of 100 km/s for carbon and hydrogen lines. The HeNe interferometer shows that the plasma is produced in multiple pulses (due to current ringing). To obtain a mass estimate, we assume an average ion mass of 5.5 amu per free electron, and use the 100 km/s speed to convert the time history into a spatial profile. With these assumptions, integration of the first pulse alone gives a mass of 200 μg from the interferometer traces.

3.8.6 Pressure probe

We have constructed a fast pressure probe incorporating a commercial piezoelectric pressure sensor from PCB Piezotronics (Model number 113A21, used in combination with a Model 480D06 bias and amplifier unit.) The stainless-steel sensor is epoxied inside the end of a 9.5 mm outer-diameter quartz tube and is protected from the plasma by a 0.5-mm thick polished quartz disc. Shock tube calibrations indicate the probe has a nominal 0.8 μs rise time, although there is an acoustic resonance near 160 kHz. For pressures lasting longer than 2 μs, the probe generates a signal of about 2.3 mV/kPa.

When this probe is aligned for head-on collision with the plasma slug, it measures an increase in pressure coincident with the arrival of the luminous plasma stream described in Sec. 3.8.2. At a distance of 15 cm downstream from the muzzle, this signal shows a flattop pulse of ~ 150 kPa and has a full-width, half-maximum duration near 10 μs. This is approximately the adiabatic stagnation pressure of the plasma flow. We combine this pressure with the 90 km/s velocity from spectroscopy, the electron density from interferometry and Stark widths, and with estimates of $Z = 1$, $T = 3$ eV and $\gamma = 5/3$ to estimate the mass per ion as 5.8×10^{-27}kg $= 3.5$ amu.

We can estimate the plasma momentum density by multiplying this mass by the density and velocity from optical diagnostics. This gives 0.26 kg-m^{-2}s^{-1}. If we take the diameter of the plasma column as 10 cm and the duration as 12 μs, this gives a total momentum of 2.2 g-m/s and a mass of 24 μg. Measurements taken in combination with the interferometer show that the electron density increases by about a factor of 6 when crossing the shock structure upstream of the pressure probe. (See Figure 25 and compare measurements in Sections 3.8.2, 3.8.3 and 3.8.5.)

3.8.7 Magnetic probes

Several passive magnetic induction probes have been constructed and inserted into the plasma accelerator. These are protected by 3 mm diameter quartz tubes with a half-mm thick wall. The probe heads are constructed of magnet wire, with 12-14 turns at a 1 mm nominal diameter. These probes are placed just inside the outer electrode and are aligned to measure the azimuthal component of dB/dt. Two probes are inserted into the main accelerator section, at about the same axial position as the inner electrode's neck. Except for the earliest times, these two probes are strongly correlated with the current. Since the sign of B_ϕ/I is constant, the main current paths are downstream from these probes during most of the shot. In particular, there is no sign of restrikes upstream of this position. From these data, we conclude that the dominant current sheet passes the neck 2-4 μs after the switch closes. Additional magnetic induction probes have been constructed and installed downstream of the inner electrode's nose. These will also be just inside the outer electrode's wall. These have been individually calibrated *in situ* with a 24 μs current oscillation. At that frequency, typical sensitivities are about 1×10^{-5} Volt-seconds/Tesla. These produce waveforms similar to that of the main gun's current (Sec. 3.8.1), but with much more structure and time-delays dependent on their axial position. From this, we conclude that the dominant current sheet passes the neck in about 3 μs and has formed a plasma focus structure by 10 μs.

3.9 Gun Efficiency

Of particular interest is the potential efficiency of these guns. An estimate is provided by the simulation, which outputs total plasma kinetic energy $E_{kinetic} = \int \frac{1}{2}\rho v^2 d^3x$, energy stored in the magnetic field $E_{magnetic} = \int \frac{B^2}{2\mu_0} d^3x$, and the energy dissipated as joule heating $E_{joule} = \int I^2 R dt$. We define the overall gun efficiency as:

$$\eta = \frac{E_{kinetic}}{\frac{1}{2}CV_i^2 - \frac{1}{2}CV_f^2} \qquad (1)$$

where the final capacitor voltage is taken as the peak negative voltage on the capacitor bank at the time of current zero as it rings down. This is essentially equivalent to assuming that all stored magnetic field energy can be recovered in the external circuit. If we further assume an external resistance of 1 $m\Omega$, then the gun efficiency is roughly 59% for the case in Figure 29(a) and 75% for the case in Figure 29(b). In all cases we looked at, the total joule heating in the plasma was small compared to the kinetic energy or the magnetic field energy, being typically only 10-15% of the former, and the simulation gun efficiencies ranged between 35% and 75%. Higher efficiencies are seen for the more massive armatures at lower velocity (such as 50 km/s), as would be expected. This is good news since just these types of plasma jets appear to have promise for PJMIF. These simulations have not included various other effects (such as skin friction drag) which will tend to depress the overall efficiency, and higher external circuit resistance which will need to be kept to 1 or 2 $m\Omega$ (skin effect in the rails themselves however is negligible). In any case, efficiencies in the range 40-60% appear to be possible and are consistent with reported railgun efficiencies using inductive recapture [56] and in Pulsed Inductive Thrusters (PIT) [57]. This will require additional work to clarify.

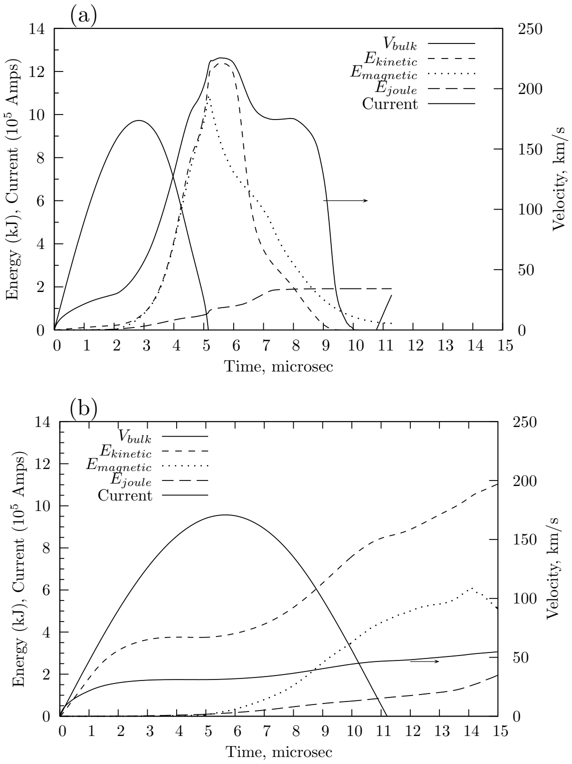

Figure 29 *Mach2 simulations show performance capability of coax gun for (a) low mass (400 μg) and (b) high mass ($\sim$ 8000 μg) armatures. Curves peak and then drop off in (a) as plasma leaves computational zone at muzzle exit.*

3.10 Gas Injection

The PJMIF concept evolved towards the use of heavier plasma liners using gases such as argon or xenon or similar. These much heavier liners allowed operating at lower velocity, typically 50-100 km/s instead of the 200 km/s originally envisioned, while still maintaining high total jet energy. In order for the coaxial guns to accomplish this and to be more generally useful and flexible in the types of plasma accelerated, they needed to be able to inject heavy gases such as argon, xenon, etc. The following sections describe MiniRailgun injectors that could accomplish this.

4 MiniRailgun Parallel Plate Plasma Accelerators

4.1 MiniRailguns as Plasma Injectors

The Minirailguns were originally conceived as high velocity plasma injectors for the shaped coaxial gun described in [48] that could inject various gases instead of only ablative materials. After some initial experimentation and development, it was realized that these guns could provide a useful high density plasma jet in their own right for many applications of interest. This ultimately led to their use in the original PLX experiment at LANL.

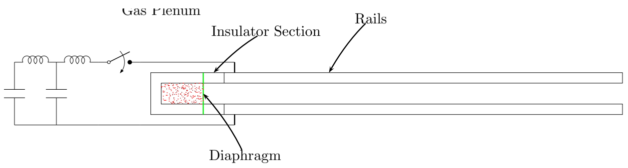

(a) Initial conditions

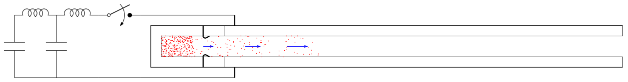

(b) Diaphragm bursts as a result of pulsed arc from two electrodes inside plenum (not shown here). The sudden pressure increase bursts the diaphragm allowing gas/plasma to freely expand down the bore.

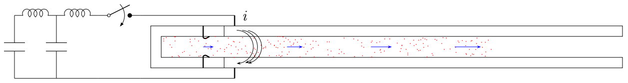

(c) Main plasma armature is initiated by a trigger when gas/plasma fills much of bore.

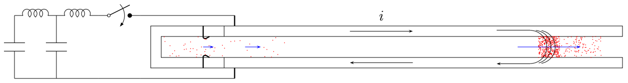

(d) A compact armature nears end of bore after snowplowing initial gas/plasma mass.

Figure 30 *A heuristic model for minirailgun operation. Original basic MiniRailgun injection scheme. A more advanced version will use a very fast gas valve to inject high-Z gas followed by a pre-ionizer to provide sufficient conductivity to initiate armature formation.*

4.2 A Heuristic Model

A heuristic model of the original basic concept is illustrated in Figure 30. Consider a small plenum located at the breech of a small railgun pressurized with a working gas (H_2, D_2, Ar, N_2, He, Xe, Kr, etc.) and constrained by an imaginary burst diaphragm such that when the diaphragm bursts, the gas is rapidly injected into the breech of the railgun. The axial length of the plenum is kept small and its cross section area large, so that outflow time, roughly given by $2\ell_{plenum}/c_{sound}$, into the railgun breech is minimized. A small sparkgap located within the plenum is connected to a switch and capacitor (not shown in the figure) and is used to suddenly heat the gas and burst the diaphragm, ejecting the partially ionized plasma into the railgun, where after a short delay, another capacitor (or pfn) is switched across the rails to form an armature which accelerates and sweeps up the plasma in the bore. Representative plots of gas flows for hydrogen and argon are shown in Figure 31.

The total mass of injected gas is determined by the volume of the plenum and the pre-fill pressure. In practice, the volume can range from a small fraction of a cubic centimeter to one or more cubic centimeters, and the pre-fill pressure can range from one atmosphere to 10 or more, yielding anywhere from tens to thousands of micrograms of gas depending on the type of gas.

The length of the MiniRailgun is adjusted to provide a compromise between gas/plasma expansion speed down the bore and the total mass of injected gas, but in any case is expected to be ∼5-30 cm long, depending on the application. Flow dynamics will yield an essentially exponentially decaying density profile with a scale height which is dependent on the sound speed of the gas, i.e. the higher the sound speed the longer the scale height so that low molecular weight gases like H_2 expand quite rapidly down the bore. When the bulk gas flow has substantially filled the bore, but not yet exited the muzzle, or when some other preselected condition is met, the railgun is triggered,

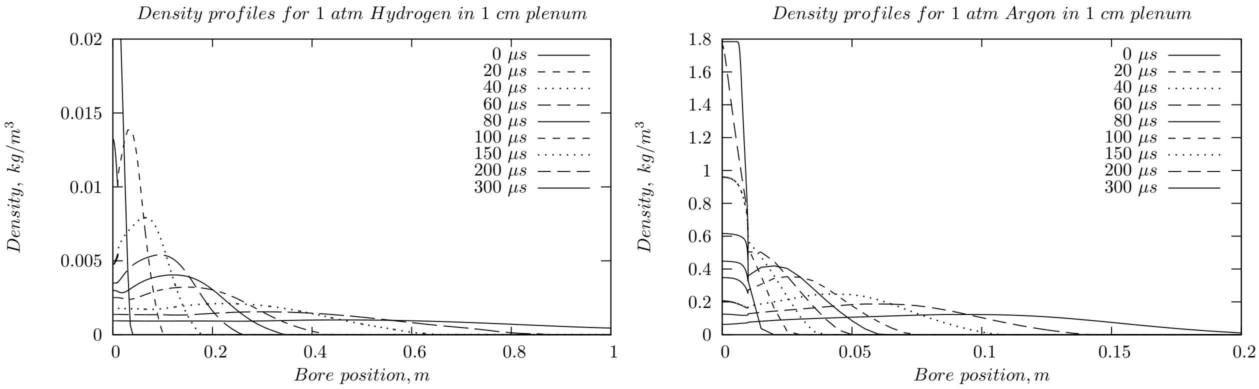

Figure 31 *Density profiles vs. time after release from 1 cm long plenum. Note the vastly different horizontal and vertical scales for the Hydrogen (left) and Argon (right) cases. The time scale for flow down the gun bore is long enough for high-Z gases that fast gas valves are feasible. Profiles from MACH2 simulations.*

resulting in formation of a plasma armature at the back end of the railgun which moves forward under the usual **J** × **B** forces. Under the proper conditions, this plasma armature will ionize and “sweep” up the gas ahead of it in the bore (hence the term “snowplow”) [18]. The high acceleration of the plasma armature is sufficient to overtake the free expansion of the gas ahead of it in the bore, hopefully arriving at the muzzle well before the expanding gas front. When configured properly, the swept up plasma armature should then eject a compact pulse of plasma at the end of the railgun, which can be used for various applications such as for injecting a fast moving plasma armature into a coaxial railgun or acting as a plasma gun in its own right.

The equation of motion for the plasma armature in the snowplow approximation is given by Jahn [18]

$$m\ddot{x} + \dot{m}\dot{x} = \frac{1}{2}L'I^2 \tag{2}$$

where L' is the inductance gradient and m is the mass of the armature at time t or position x. If we assume a constant mass density along the axis (not a good approximation!) then the armature mass as a function of position is given by

$$m(x) = m_0 + d^2\int_0^{t(x)} \rho(x)\dot{x}dt = m_0 + d^2\rho x. \tag{3}$$

The equation of motion thus becomes

$$(m_0 + d^2\rho x)\ddot{x} + d^2\rho\dot{x}^2 = \frac{1}{2}L'I^2 \tag{4}$$

An interesting operating mode is one in which the driving force is exactly counterbalanced by the drag force and the armature maintains a constant speed while sweeping up mass. This speed is determined by setting $\ddot{x}$ equal to zero in the above equation, which yields

$$d^2\rho\dot{x}^2 = \frac{1}{2}L'I^2 \tag{5}$$

or

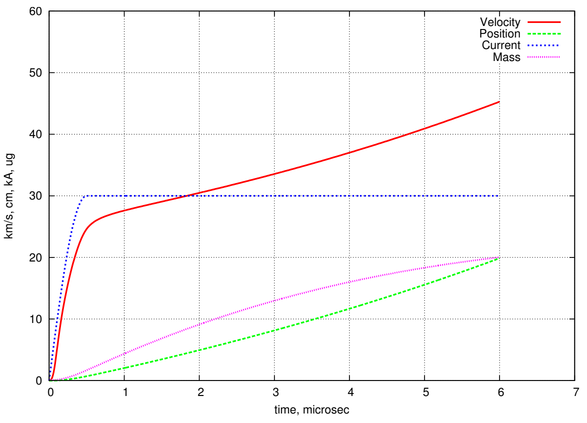

Figure 32 *Minirailgun simulation for Helium. L′=0.35 µg, mass = 20 µg.*

$$\dot{x}^2 = \frac{1}{2}L'I^2/\rho d^2 \qquad (6)$$

For L'=0.35 $\mu H, I = 30kA, \rho = 8\ \mu g/cm^3$ (equivalent to total of 20 μg), and 5 mm cross section, the limiting speed is about 20 km/s.

In reality, the density profile will be a decreasing function of distance along the bore as the gas expands downstream, with a scale height dependent on the sound speed, and the equation of motion must, in general, be solved numerically. As an example, Figure 32 illustrates a solution for Equation (3) for an exponentially decaying density profile and a roughly square current pulse with 30 kA flat top, and 20 μg of total plasma mass. In this case, the current sheet continues to accelerate to the end of the 20 cm rails and achieves almost 45 km/s. This is an example of a small low performance minirailgun suitable (perhaps in even smaller size) as an injector o a coaxial gun.

HyperV embarked on developing variations of this basic MiniRailgun concept to pulse feed plasma into larger coaxial plasma guns [48] and also to directly drive plasma jets to the >50 km/s range for use in MTF.

Table 1 *Target Railgun Parameters*

Bore size	1-2 cm square
Length	30-50 cm
L'	$\sim 0.5\ \mu H/m$
Rails	Cu, W, Ta, GlidCop
Insulator	BN, Si_3N_4
Current	400-600 kA
Pulsewidth	10-15 μs
PFN	4 sections
Capacitance	40 μF (total)
Bank energy	50 kJ
Voltage	up to 50 kV
Armature mass	8000 μg of Xe
$V_{injection}$	$\sim 1-2\ km/s$ for xenon $\sim 2-3\ km/s$ for argon
V_{jet}	50 km/s

4.3 Two Basic Configurations

The basic MiniRailgun is illustrated in Figure 33. The simple railgun [18] itself consists of two parallel metallic rails top and bottom separated by ceramic insulators forming the side walls of the bore. The cross section is slightly off-square to maximize L', the inductance gradient of the railgun, since the accelerating force is $\frac{1}{2}L'I^2$. The effective L' of the railgun assembly can be estimated using the algorithm developed in [58]. It is to our advantage to maximize L' within the other constraints so as to reduce the peak current and total coulomb transfer required. This reduces requirements on the pfn, the switch, and the wear and tear on the railgun itself. Typical values for L' range from 0.35-0.5 μH/m. Although it is possible to increase the effective railgun inductance gradient by almost a factor of two using augmentation [59, 60], we decided not to follow this approach in this effort in order to minimize design complexity and reduce cost. Future systems might observe gains by using augmentation.

The nominal parameters for a MiniRailgun for application to the Los Alamos National Laboratory PLX jet merging experiment are listed in Table 1. Early work used a smaller, lower energy unit for testing. The rails and insulator assembly are contained inside a supporting structure to provide both mechanical stiffness and vacuum sealing.

The plasma armature is injected at 1-20 km/s into the breech of the railgun by one of several methods. Our original work had concentrated on using small plenums filled with atmospheric pressure gas contained by a diaphragm at the entrance to the railgun. A small arc discharge in the plenum heated and pressurized the gas bursting the diaphragm and forming a plasma which then flows into the breech of the railgun. Switch S2 is then activated and current flows through the rails and the plasma armature between the rails, accelerating down the bore via the $\mathbf{J} \times \mathbf{B}$ force. Additional experiments have used a very thin aluminized mylar foil which initially shorts out

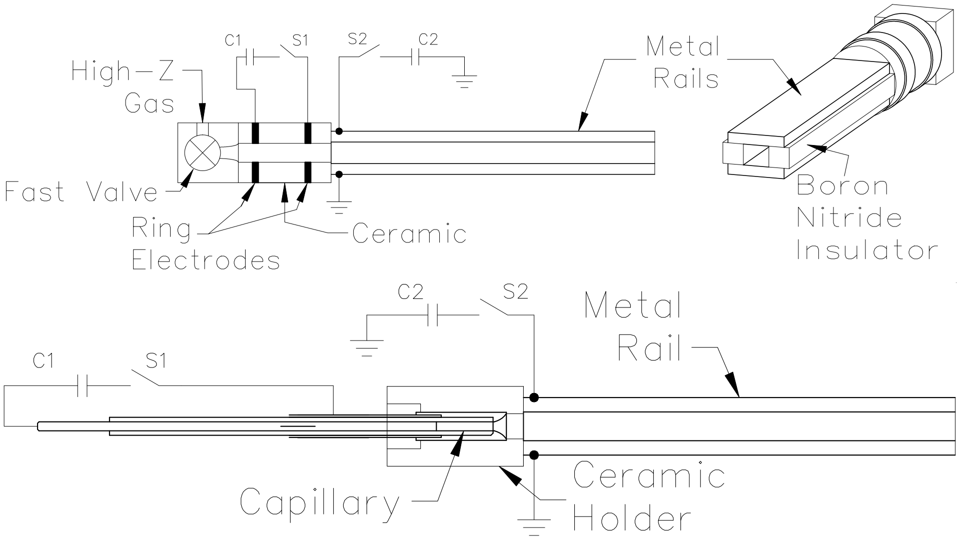

Figure 33 *Railgun with two versions of plasma injector - (top) ceramic capillary with fast valve gas injection, (bottom) polyethylene ablative capillary. The dimensions of the railgun relative to the injectors are not quite to scale here. The fast gas valve version (top) could also use other techniques for establishing initial ionization.*

the breech of the railgun and rapidly vaporizes as current rises forming a thin plasma sheet which accelerates down the bore. It is easy to get a few hundred or even a few thousand micrograms of plasma in this manner. However, although simple, this approach tends to cause some electrode damage near the breech due to the low speed at arc initiation and also requires the replacement of the diaphragm after each test firing. Since we wish to establish a gun system for plasma liner experiments, it is highly desirable to be able to have a reasonable shot rate to generate data rapidly, and not have to replace foils or burst diaphragms after each shot on 30 or more guns, or have to come up to air after each shot to do so. Therefore we needed an approach which provides repetitive operation with only occasional maintenance.

The configuration illustrated in Figure 33 shows two generic ways to accomplish this. The lower figure uses one of our standard ablative capillary units acting as an injector. It fires a very short ($\sim 1\ \mu s$) pulse of plasma into the breech of the railgun, where, after a few microseconds to give the capillary time to empty out, a switch then closes and railgun operation commences. The bulk of early testing used this approach since it is very simple and reliable. A very similar approach was taken by Witherspoon et al. [61, 62, 63, 64] for injection of very large plasma masses into the bore of megajoule level railgun experiments. This allowed quick testing of the concept and generation of initial performance data at high velocity with the relatively low molecular weight of polyethylene. Figure 34 shows one of these capillary injectors operating at 100 kA for a 1 μs pulse and generating a compact plasma plume with $n_e \sim 10^{17} cm^{-3}$ and velocity of 63 km/s. For the early testing we generally did not operate the capillary at this level, but at the lower velocity of 10-20 km/s to make timing easier and allow the capillaries to last essentially indefinitely.

The configuration shown in the upper half of Figure 33 illustrate a better longer term approach which provides the capability of accelerating high-Z gases such as argon and xenon for the implosion experiments. In this configuration, the ablative capillary is replaced with a similar capillary geometry but with BN ceramic insulator walls. Ring shaped electrodes at each end provide a means of initiating the discharge, while a very fast gated valve at the rear admits a burst of high pressure

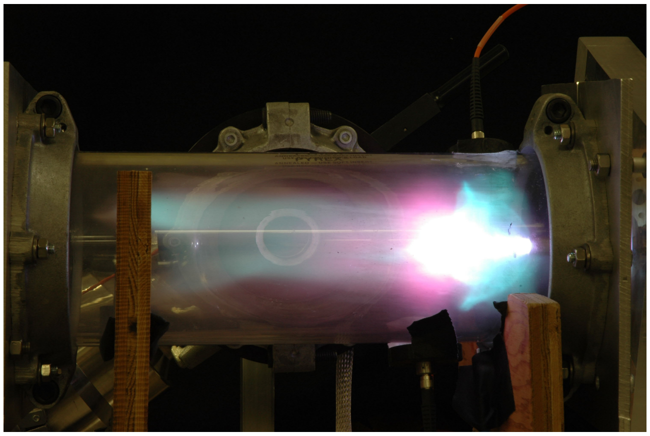

Figure 34 *Plume of 100 kA capillary test at 63 km/s and* $10^{17}cm^{-3}$. *A reduced energy version provided a good injector for MiniRailgun testing.*

gas into the capillary volume. For the case of high-Z gases such as argon or xenon, the sound speed of the gas is so slow (e.g. 180 m/s for xenon) that in the 100 μs it takes for the valve to open and close, the gas will move less than 2 cm downstream. Most of the gas is still within the capillary by the time the valve closes. A very fast (sub-microsecond) current discharge then heats the gas, forming a few eV plasma, which jets out the capillary nozzle into the railgun. By timing the firing of the railgun switch, essentially all of the plasma mass can be captured and accelerated by the railgun discharge. This then provides a repetitively operating high density high velocity injection system into the breech of the railgun.

The plenum behind the valve can be at relatively high pressure (1-10 bar for instance) so that a very large mass of xenon can be injected into the gun. At one bar pressure, xenon has a density of about 5000 $\mu g/\text{cm}^3$, and a number density of roughly $2.5 \times 10^{19} cm^{-3}$. This provides the means by which extremely dense and massive plasmas can be injected into the railgun. We next address the potential performance of such a railgun.

Plasma armature railguns have a well demonstrated capability to operate in the 50-70 km/s range. Markusic [65] performed an important series of tests with a large bore railgun (5cm x 10cm x 60cm) at currents of only 60 kA in a background fill gas of 75-400 mTorr of H_2, D_2, He, Ne, Ar, Kr, and Xe. He measured velocities of almost 70 km/s for H and somewhat lower velocities for the heavier gases, down to 20 km/s for Xe. His accelerating pressures were quite low, however. Using $F = \frac{1}{2}L'I^2 = pA$, where A = bore height h times bore width w for his experiment yields an effective accelerating pressure of only 1.8×10^5 Pa, or 1.8 bar.

We plan to use a much higher effective pressure, in the kilobar range. We do this by operating at 100's kA in a 1-2 cm square bore cross-section. The parameters were summarized earlier in Table 1. We will also operate at much higher plasma armature densities, eventually above 10^{19} cm^{-3}. For a bore size of 1 cm square, our effective pressure would then be

$$p = \frac{L'I^2}{2hw} = \frac{0.5 \cdot 10^{-6}(300 \cdot 10^3)^2}{2(0.01)^2} \backsimeq 4.5 \times 10^8 \ Pa = 4.5 \ kbar. \tag{7}$$

This may be a little too much current for a 1 cm bore. A bore size of 2 cm would be 1/4 that, or about 1.1 kbar.

The ideal performance of a parallel plate railgun is much easier to analyze than a coax gun with curved electrodes, since L' is a constant. For a constant current drive, the velocity attained for a railgun length x is given simply by $v^2 = 2ax$, or

$$v = \sqrt{\frac{L'x}{m}} I = \sqrt{\frac{0.5 \cdot 10^{-6} \cdot 0.5}{8000 \cdot 10^{-9}}}\, 300 \cdot 10^3 = 53\ km/s. \tag{8}$$

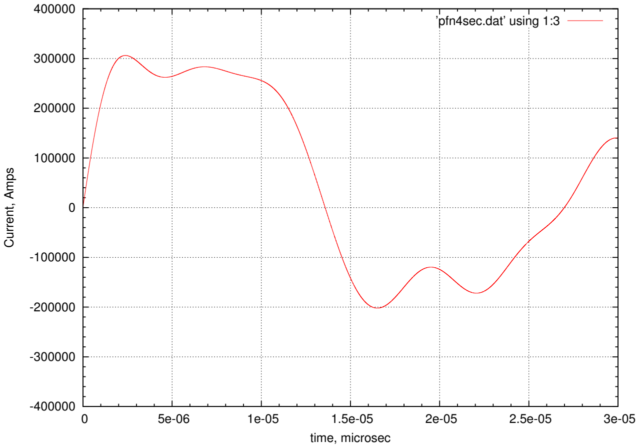

Figure 35 *Simulation of railgun circuit with 4 section pfn at 50 kV.*

In reality the pulse shape will not be a square wave but more like a sinusoid, so that the peak current will need to go up to perhaps twice the flat top value or about 600 k. A MACH2 simulation is shown in a later section.

4.4 Gas Fed Minirailguns Make Good Plasma Accelerators

4.5 Fast Gas Valve - Early Version

Mach2 runs investigating gas flow down the bore for an ideal burst diaphragm released case, showed the time scales that we needed to work with. The code output is shown in Figure 31 for hydrogen and argon initially stored in a plenum 1 cm long and pressurized to 1 atmosphere. The initial conditions are similar in nature to that of a conventional shock tube, with a pre-filled plenum separated from the bore by an imaginary zero mass burst diaphragm. At t=0 the diaphragm bursts, allowing the gas to freely expand down the bore. The density is then plotted as a function of position along the bore at various times. The background gas pressure was 10−6 Torr of air. For hydrogen, it can be seen that the gas quickly accelerates to down bore, with the front reaching about 7 km/s in rough agreement with back of the envelope estimates. The bulk of the gas, however, flows at much lower velocity, as expected. After 80 μs, the rarefaction moving back into the plenum has propagated about 10 cm. The front of the gas has moved about 20 cm down the bore. The velocity at the diaphragm location maintains a sonic flow, i.e. about 2000 m/s and increases to 7000 m/s at 20 cm downbore. The higher Z argon, however, takes much longer to propagate down bore.

A very fast opening gas valve is being adapted from existing fast valve designs to inject high-Z gas into the breech of the MiniRailgun. Poppet valves with ≈ 25 μs opening times have been employed on spheromaks as fast-high density ($n \approx 10^{19} cm^{-3}$) gas sources for plasma generation [66]. The valve shown in Figure 37 consists of a small annular gas plenum housed in a plastic body which is fed from a rear port and stoppered by an aluminum poppet flyer plate. An O-ring spring is used to return the poppet to the closed position. Channels cut in the rear wall of the plenum allow gas to flow around the return spring and pressurize the plenum. At rest the vacuum of the rail gun breech holds the poppet against an O-ring seal. The poppet is actuated by a flat solenoid. By keeping the poppet mass <1 gram, a driving coil current of only several kiloamperes is sufficient

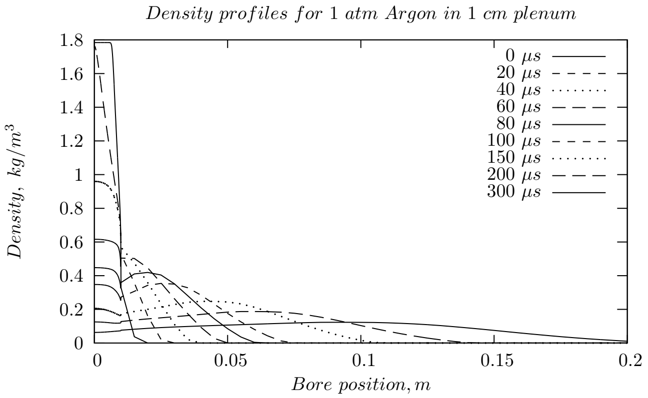

Figure 36 *MACH2 simulation of argon flow after burst disk. This is the best you could do with a valve that opens instantaneously.*

to drive the valve open in order to exhaust the annular pressurized plenum into the breech of the rail gun. An O-ring spring is used to return the poppet to the closed position. The efficiency of gas injection will be driven by the ratio of the outer diameter of the poppet to the outer diameter of the solenoid, and the ratio of the outer diameter of the plenum to the diameter of the outlet. We will need to determine exact dimensions and drive currents experimentally. Similar devices at CTIX developed by Robert Horton at CTIX open and close in less than 100 μs. Our valve just needs to open extremely quickly and does not necessarily need to close on that time scale, although that would provide an additional control knob for the gas injection. Our initial valve design has been developed after several conversations with Robert Horton who has designed, constructed, and deployed a similar device for CTIX. Our design diverges a little from his due to our unique gun configuration, but he has been very helpful getting us started on the right track [67, 68, 69].

The previously developed 1cm diameter fast gas valve (20-25 μs opening time) worked well, but flow dynamic calculations and experimental data raised concerns about possible choked flow at the valve orifice. A 2nd generation fast gas valve was designed with a 2cm diameter orifice and testing began. However, in the initial physical testing phase of the new 2cm diameter valve, several scientific and engineering issues were encountered and addressed.

The first issue was the theoretical determination and experimental validation of the magnetic force required to actuate the new larger valve in 20us (100m/s peak velocity). Various capacitance and voltages were investigated to achieved valve disk velocities in the relevant range. Final RLC circuit tuning was performed to maximize coil performance in the short time available. Design parameter achieved, but further development is necessary.

Next, practical design elements such as gas plenum geometry were considered and plenum designed to allow for the full mass of gas (up to 8000 μg) to be released from the valve within 1mm of physical valve disk travel. Design parameter achieved.

During initial physical testing many valves blew apart due to materials limitations. Materials limitations were in this case overcome by redesigning the valve body, valve plenum and valve mount to more robust flange and mount thickness. Plenum mounts required redesigning and it was advantageous to move the metallic plenum mounting studs farther away from the magnetic coil. Valve disk life is now about 50 shots before disk ruptures. A mechanically sound and relatively robust working valve was achieved, though further development is necessary for long life operation.

The final major issue encountered in new fast valve development was corona and arcing of coil leads inside the vacuum chamber. The final solution to this was simply to move the valve outside the vacuum, something we had planned to do later, but dealing with it now was indicated. The

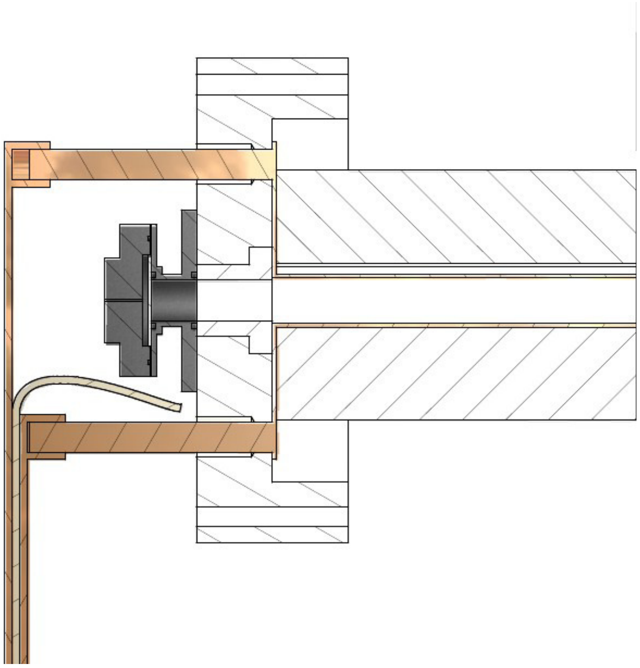

Figure 37 *Minirailgun configuration with gas valve and no pre-ionizer.*

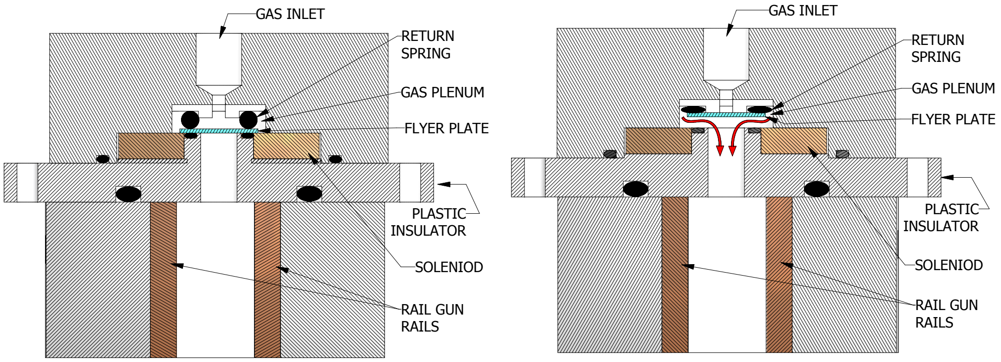

Figure 38 *A fast opening gas valve is being adapted to inject high-Z gas into the breech of a rail gun. An aluminum poppet (mass$<$ 1 g) is actuated by a flat solenoid to open the valve on a time scale less than 100 μs. Channels cut in the rear wall of the plenum (not shown) allow gas to flow around the return spring and pressurize the plenum.*

minirail mounting, vacuum window and valve mount were redesigned to accommodate the new valve mounted externally to the vacuum. The necessity of mounting the gas valve externally provided a good opportunity to begin redesigning the minirail transmission line to lower the circuit inductance.

4.6 Performance of Gas Fed 1cm Minirailgun

Recent interferometer measurements have revealed compact plasma slugs, only 4 cm long. The HyperV HeNe quadrature heterodyne interferometer is broadly based on the design used by the Compact Toroid Injection Experiment (CTIX) [70] and is described in detail in Case et al. [71]. The optical components are mounted on an aluminum structure with two extension arms which allow the system to straddle the vacuum chamber. The laser beam is modulated using an Acousto-Optic Modulator (Intra-Action ATM-A1) operating at 110 MHz, which also serves as a beam splitter. The undeflected beam is used as the scene beam, and the deflected beam (modulated at 110MHz) is the reference beam. The scene beam passes through a polarizing beamsplitter (the beam polarization is aligned with the beamsplitter so as to pass undeflected), makes a double pass through the plasma and also through a quarter wave plate, rotating the angle of polarization by $\pi/2$, so that on returning to the beamsplitter it is deflected onto a second beamsplitter where it is recombined with the reference beam. The combined beam is then passed through a polarizer which projects the polarization of the two beams onto a common axis intermediate between the polarization of the two component beams. Detection of the modulated interference signal is via a reverse biased PIN diode.

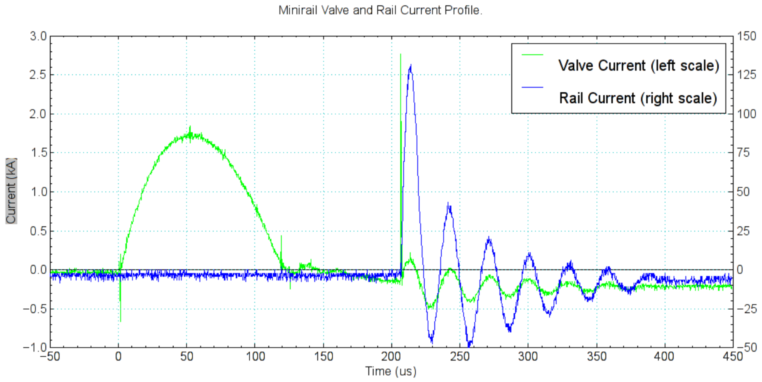

Figure 39 *Current profiles showing timing.*

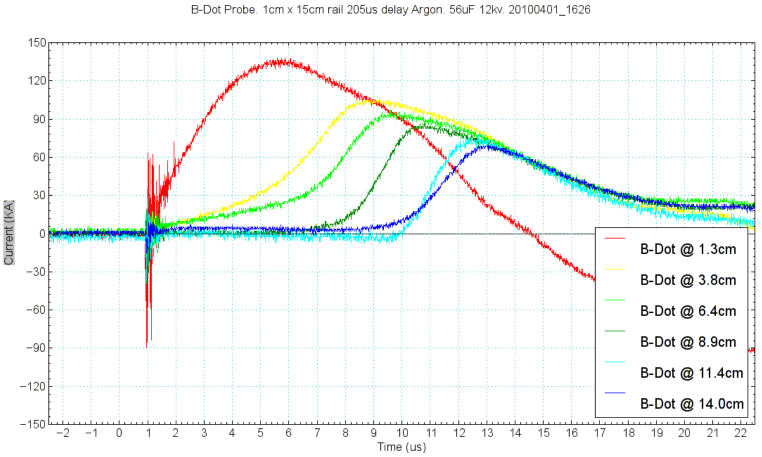

Figure 40 *Typical magnetic field profile traveling from breech to muzzle.*

The signal from the PIN diode is passed to a quadrature heterodyne detector where it is resolved into two components proportional to the sine and cosine of the phase difference between the scene and reference beams. These signals are digitized at 25 MHz with a total record length of 2500 points, giving a time window of 100 μs. Prior to analysis the raw data was filtered using an FFT cutoff frequency of 1 MHz. All data presented here has a time resolution of 1 μs.

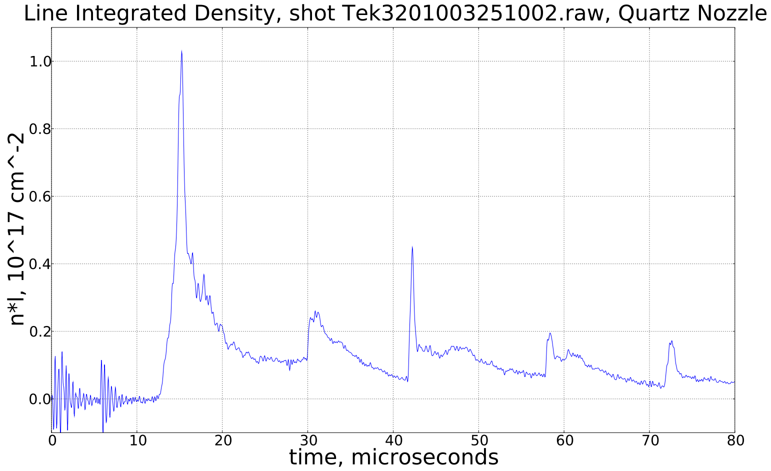

Figure 41 *Quartz nozzle*

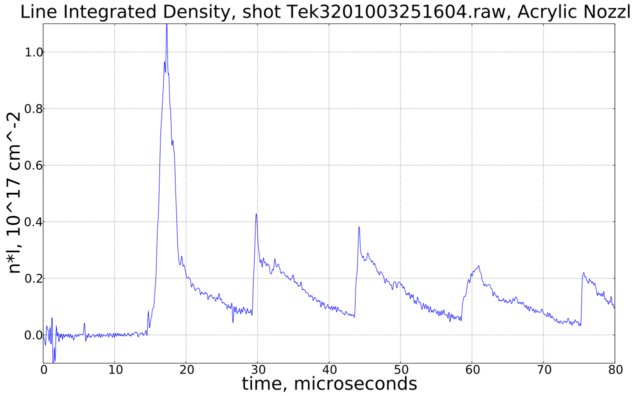

Figure 42 *Acrylic nozzle*

For the nozzle test series only a single beam was used, so as to maximize signal to noise ratio. The scene beam passed through the plasma 10 cm from the end of the rails of the MiniRailgun. This means that with the 7.5 cm nozzles in place the observation volume was 2.5 cm from the end of the nozzle. A photodiode was placed so as to observe the plasma immediately on exiting the nozzle, and two others were placed downstream, with a separation of 10 cm between each photodiode pair. This allows for a fairly straightforward measurement of plasmoid velocity.

The data presented here is two shots using nozzles that are as close as practicable to identical in physical dimensions, with the only difference being the nozzle materials: Quartz and Acrylic Polycarbonate. The results are presented in Figures 41 and 42. Despite near identical conditions the differences between the two signals is considerable. The quartz nozzle produces a faster and substantially more compact plasmoid, with much less plasma in the trailing plasmoids. This result suggests that ablation of the nozzle leads to significant amounts of material in the trailing portion of the plasmoid. The additional plasmoids trailing the main one are due to ringing of the capacitor bank producing secondary plasmoids.

The difference in velocities is only 10%, which is at the limit of our ability to distinguish velocities. The difference in plasmoid length is much more striking, as the quartz nozzle produces a plasmoid that is only 40% the length of the Acrylic nozzle plasmoid. This is almost certainly due to ablation of the acrylic nozzle injecting material into the plasmoid, increasing drag at the plasmoid edge and thus broadening it. The slightly greater peak density ($1.1 \times 10^{17}\text{cm}^{-3}$ for the acrylic vs. $1.0 \times 10^{17}\text{cm}^{-3}$ for quartz) of the acrylic nozzle plasmoid supports this conclusion. The higher peak density and longer plasmoid indicate that the total mass of the acrylic nozzle plasmoid is higher than that of the quartz nozzle plasmoid by a factor of at least two. We therefore conclude that material ablated from the acrylic nozzle is a significant fraction of total plasmoid mass.

Additional nozzle geometries have been studied using interferometry, and analysis of the data is ongoing. Preliminary investigations show that a straight nozzle provides a substantial improvement in plasmoid velocity and compactness compared to no nozzle at all, and quartz is a good nozzle material from the standpoint of minimizing ablation and creating a compact plasmoid. Figure 43 shows a MACH2 simulation of a test shot in which about 1200 μg of argon was accelerated to 42 km/s.

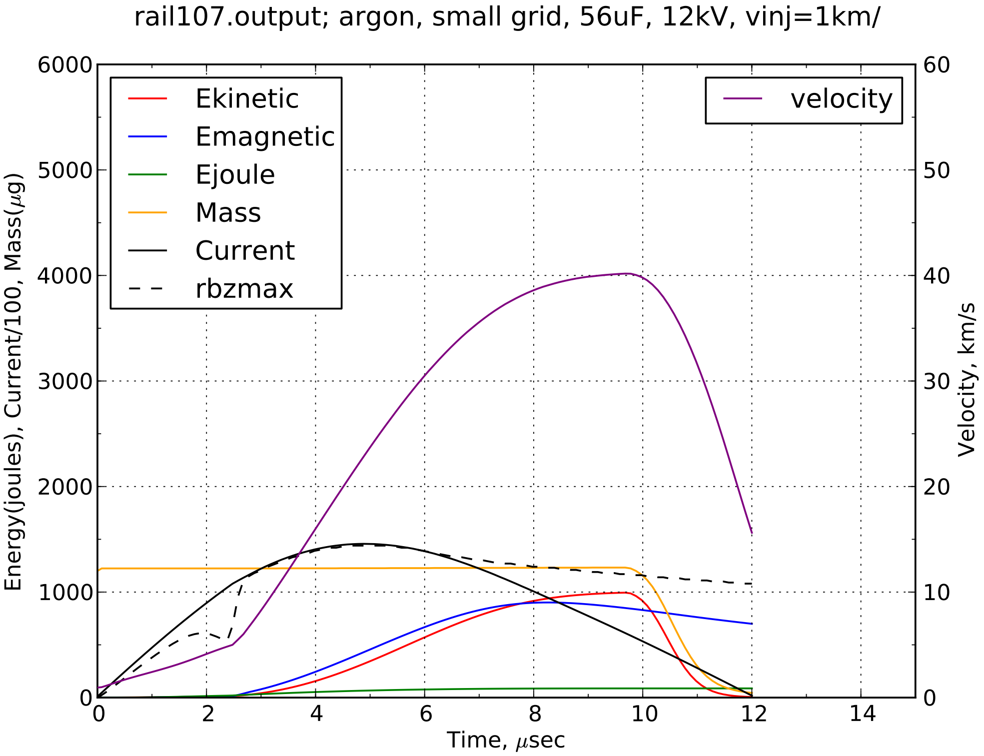

Figure 43 *MACH2 simulation of test shot in which about 1200 μg of argon is accelerated to about 42 km/s with about 150 kA peak current.*

Nozzle R was a proof of principle test to demonstrate the ability to deliver a high density plasma jet via a relatively long nozzle tube extension. In order to achieve a longer drift zone for the plasma jet, a 10in diameter drift tube was mounted to the octagon vacuum chamber. The adapter flange for the new drift tube had a 4in diameter opening. In order to get the total mass of the plasma jet into the tube, using a very long tube nozzle was considered.

The tests were successful. Nozzle R produced the highest velocity jet measured during nozzle testing at 44 km/s. Pressure of 8.8 bar was measure at 1.1 meters from the muzzle (60cm from the end of the nozzle). Density, $n_i = 2.0 \times 10^{16}$ cm^{-3} was measured at 61cm from the MiniRail Muzzle. Density, $n_i = 1.4 \times 10^{15}$ cm^{-3} was measured at 81cm from the MiniRail Muzzle. These are exciting numbers.

A test was performed to observe propagation of the jet over a distance comparable to that to be seen on PLX. Using the vacuum hardware at hand we set up the configuration shown in Figure 44. The photodiode traces shown in Figure 44(g) shows the expansion of the jet length as it propagates about one meter.

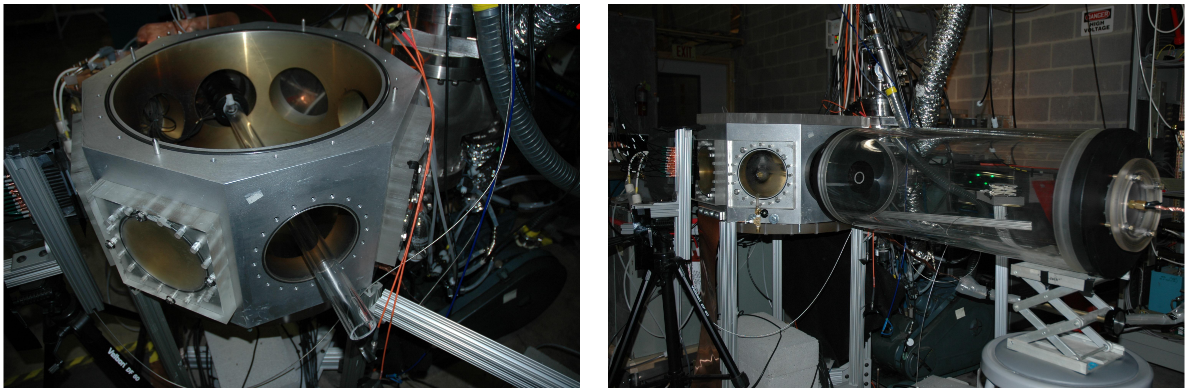

(a) 2.9cm ID x 61cm Long Acrylic Nozzle. Nozzle protrudes through octagon into a 10in diameter drift tube, extending total transit distance from muzzle to 1.4 meters.

(b) 1.4 meter plasma transit distance from muzzle

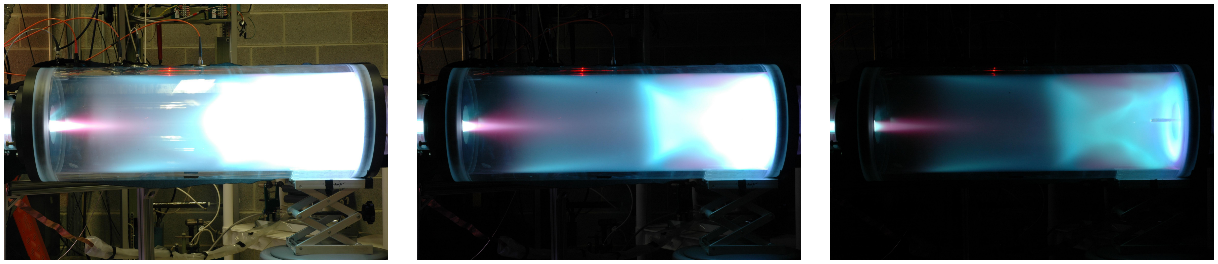

(c) Nikon f-18 open shutter exposure.

(d) Nikon f-29 open shutter exposure.

(e) Nikon f-29 open shutter exposure with 2 neutral density filters.

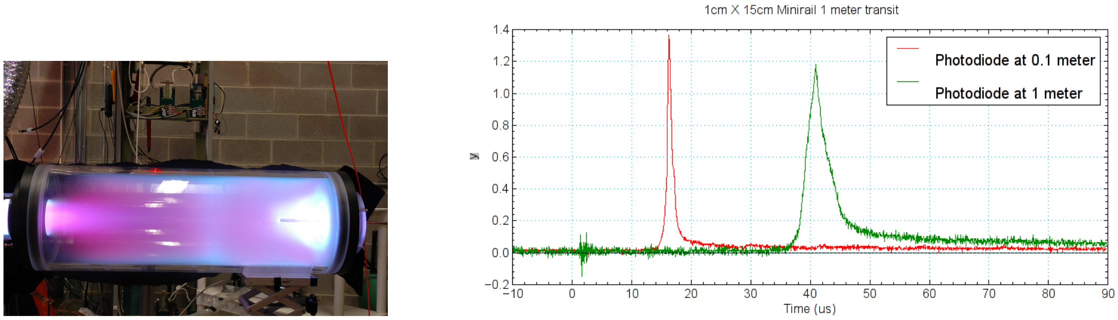

(f) Nikon open shutter photo of 1200 μg of argon through a straight quartz nozzle impinging onto pressure probe over 1 meter downstream. Plasma jet travels from left to right.

(g) Photodiodes at 0.1 meter (red) and 1.0 meter (green) from minirail muzzle with 3.3cm dia. x 7.5cm Quartz nozzle. Photodiode half widths are 1.2 μs and 4.5 μs respectively. Average velocity over 1 meter = 36 km/s, corresponding to a 5cm long jet at 10cm and a 16cm long jet at 1 meter.

Figure 44 *Various plumes from Nozzle R*

5 Pulsed Power Systems

5.1 Introduction

Both the coaxial and linear plasma railguns under development at HyperV require high-voltage, high current switches to accelerate plasma armatures. Present railgun driver banks can be as large as 29 kJ to 44 kJ. These banks required low-inductance switches with at least 60 kV stand off, and could source currents of up to 1.0 MA. A single channel, axially symmetric switch was constructed and tested with a rail gun load at moderate power and a capillary load at high peak power. Switch jitter time was measured to be about 550 ns, and mean time to failure was also evaluated.

5.2 High Voltage Switches for Rail Guns

HyperV rail-gun plasma accelerators [48] can be considered two stage plasma rail guns. The first stage, or formation stage, forms a plasma armature and injects it into a linear or coaxial railgun electrode gap. The second stage, or acceleration stage, employs a Pulse Forming Network (PFN) to drive a large current through the railgun electrodes and plasma armature, accelerating the armature to high velocity. Regardless of rail geometry and armature formation method, rail gun performance will be influenced considerably by the pulse shape and peak value of the PFN accelerator current. Present HyperV railgun designs call for peak accelerator currents of 0.5 MA to 1.0 MA and pulse widths as long as 15 μs. As these railguns are primarily an inductive load of 100 - 200 nH, it is necessary to minimize inductance of PFN switches and transmission lines in order to maximize peak PFN current. In order to repeatably generate large currents from a single PFN capacitor bank, a robust, low jitter, low inductance switch must be designed for high repeatability and high mean-time-to-repair.

A switch can be modeled as a pair of electrodes separated by a gap filled with a controllable dielectric medium. The choice of dielectric medium and width of the gap determine the internal voltage stand off or self breakdown voltage of the switch. Gas dielectric switches are very common [72, 73]. Water dielectric switches have also been constructed [74]. Solid dielectrics [75] and semiconductor switches [76, 77] are also possible, but can be cost prohibitive at the Mega-amp current level. Gas filled dielectric switching was selected for simplicity of design.

When closing a gas dielectric switch, a conducting channel must be created through the gas by means of a trigger mechanism. Several trigger mechanisms were considered: Laser [78, 79, 80, 81], Spark[82, 83], Field Distortion [84], Magnetic [85] and Glow Discharge [86]. Magnetic triggers complicate arrayed switch deployments as manufacturing coils with several nanosecond uniformity in rise time can be challenging. The glow discharge designs considered employed small orifices that might have been damaged by high currents. Laser triggering produces low jitter times because the laser actively ionizes a channel between the switch electrodes instead of waiting for an induced current step leader to propagate through the dielectric medium. However, laser trigger methods required for similar switch designs can "require a peak intensity at focus of $> 10^{12}$ W/cm^2 of laser output" to close each switch [87], necessitating a laser of significant power for operation, and N times more laser power to trigger an array of N switches. Also steps must be taken to preserve the optics in high power laser switching. However, existing spark gap and field distortion switches can be constructed with jitters on the order of tens of nano seconds which was deemed acceptable for initial experimentation.

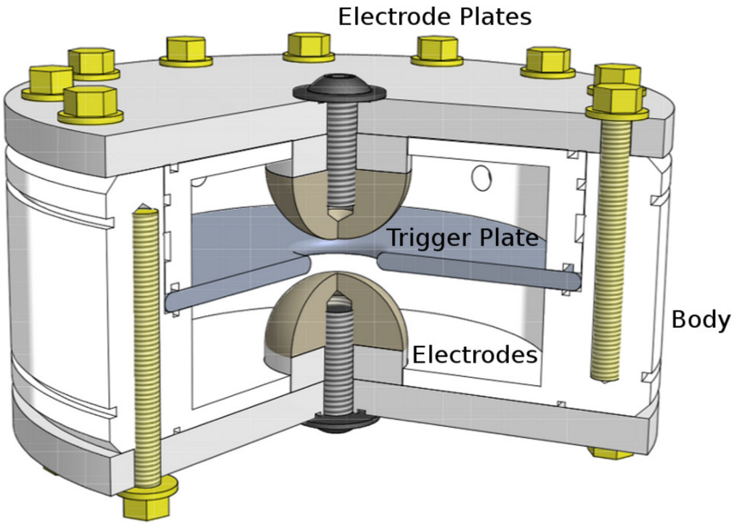

Figure 45 *A Mega Amp Field Distortion (MAF) switch was designed with the goal of switching peak currents of up to 1 MA from banks as large as 44 kJ. The switch designed consists of a pair of hemispherical electrodes mounted on cylindrical metal plates clamped to a plastic housing. An annular trigger plate is suspended halfway between the electrodes.*

5.3 MAF Design

To meet HyperV’s switching requirements, a Mega Amp Field Distortion (MAF) switch was designed with the goal of switching peak currents of up to 1 MA from banks as large as 44 kJ. Shown in Figure 45, the switch designed consists of a pair of hemispherical electrodes mounted on cylindrical metal plates clamped to a plastic housing. An annular trigger plate is suspended equidistant between the electrodes. An internal spacer holds the trigger plate in place. The internal volume of the switch can be pressurized with a dielectric gas to set the voltage stand off. For operation, the trigger plate is DC biased to half the bank voltage, while the switched plate is held at ground potential by a pull down resistor. The switch can then be triggered by applying an externally trigger voltage signal of 10-30 kV or more to the trigger plate. This causes the voltage over the switch gap to exceed the hold off of the gas dielectric, initiating discharge, and closing the switch. Assuming the switch materials and components can handle the total energy dissipated in the switch for the amount of coulombs being transferred, the three critical parameters in this switch design become the electrode gap width, the trigger gap width, and the forces on the body.

The electrode gap width is set by the desired pressure operating range. A maximum voltage stand-off of 60 kV was deemed necessary to achieve experimental goals, and a maximum working pressure of 450 kPa was selected to allow the use of plastic tubing and fittings for gas distribution. Because the current channel of the closed switch is formed in the gas dielectric by a combination of the switch and trigger voltages, the jitter in the closing time will increase as the electrode gap width is increased. However, the working pressure necessary to prevent self breakdown of the switch increases as the electrode gap decreases [88, 89]. Nitrogen and argon were selected as dielectric gases to allow operation below 450 kPa at 60 kV without requiring exotic fill gases. At 450 kPa the dielectric strength of nitrogen is about 50 kV/cm, requiring a voltage gap of about 1.2 cm to hold off 60 kV [88]. Using argon allows lower voltage operation (5 kV to 8 kV). It may be possible to operate these switches in between these regions with argon/nitrogen gas mixtures, but no tests of this were performed as part of this work.

Similarly, the trigger gap width is determined by the strength of trigger voltage and the gas pressure. However, since the trigger plate can be DC biased to any voltage, small electrode gaps are possible. The trigger voltage need only exceed the stand-off of the trigger gap at operating pressure. Otherwise, as the trigger gap distance approaches the voltage gap distance, it becomes necessary to employ trigger voltages larger than the bank voltage in order to close the switch. Other switch designs use small diameter trigger pins to initiate the spark to close the switch [90]. While small pins reduce the parasitic capacitance of the trigger pin, allowing faster trigger rise times, switching currents as high as 1 MA could erode or deform small diameter trigger pins. Thus, a stainless steel trigger plate was employed instead. The inner diameter of the trigger plate was selected such that the distance from the edge of the trigger plate to the edge of the hemispherical electrode was 1/2 the distance of the voltage gap.

The overall height and diameter of the switch pieces will determine the inductance of the switch. Switch inductance can be estimated by considering the switch to be a stack of rod inductors. This not only implies the height of the switch should be minimized, as inductance of a rod grows with rod length, but also implies that length of the voltage gap should be minimized, as this is the smallest diameter section of the stack. The overall switch diameter contributes to the inductance as well, as it sets the minimum distance between the arc channel and the transmission line ground return plate. MAF switch inductance is estimated to be $\sim$ 15 to 30 nH depending on the diameter of the arc channel. As the switch height and radius will also limit the internal gas volume of the switch, a trade-off exists between this switch's inductance and peak internal gas pressure rise.

5.4 FEMM Modeling of Trigger Fields

The MAF trigger circuit, shown in Figure 46, was adapted from the Titan spark gap switch trigger designs [90]. However, while the titan switches employ a ceramically isolated trigger pin with their central plate to generate their spark, repeated breakage of this trigger pin and ceramic insulator was observed to be a common fault. Hence the MAF switch employs no trigger pin, and is triggered by the central plate directly. The base plate of the switch is attached to the high voltage plate of the PFN capacitor bank. The switched plate is held at ground potential via a pull-down resistor. The trigger plate of the switch is then biased to half the bank voltage via a resistor divider and pull-down resistor, but allowed to rise with capacitively coupled trigger pulse. A R.E. Beverly and Associates THD-001B trigger generator [91] was used to create a 35 kV trigger pulse in order to close the switch. Trigger plate capacitance to a switch plate was calculated to be $\sim$ 3.5 pF. Trigger impulses can be simulated by modeling the gaps between the trigger plate and switch electrodes as 3.5 pF capacitors. Use of the trigger plate of this capacitance are acceptable, because the bandwidth of the trigger circuit is set by the RC time constant of the 50 Ω and 440 pF, which is about 7 MHz in this design.

The electric field of the untriggered and triggered states of the switch were simulated with FEMM and are shown in Figure 47 [92]. The peak voltage over the trigger gap at the time of closing is $V_{bank}/2 + V_{trig}$. Since rail guns are a spark-gap-like load, a pull-down resistor on the switch plate is necessary to drain off any residual voltage on the switched plate after the capacitor bank discharge. Omitting this resistor would allow the final voltage of the switched plate to become undetermined and invites the possibility for self-break-down and misfires on the next charging cycle as the switched plate may not have returned to ground potential.

5.5 Aster Modeling of Switch Stress

Finally, the switch body design must be constructed to house the electrodes in a gas cell, while still holding off the working voltage in atmosphere, and survive both acoustic and magnetic concussive

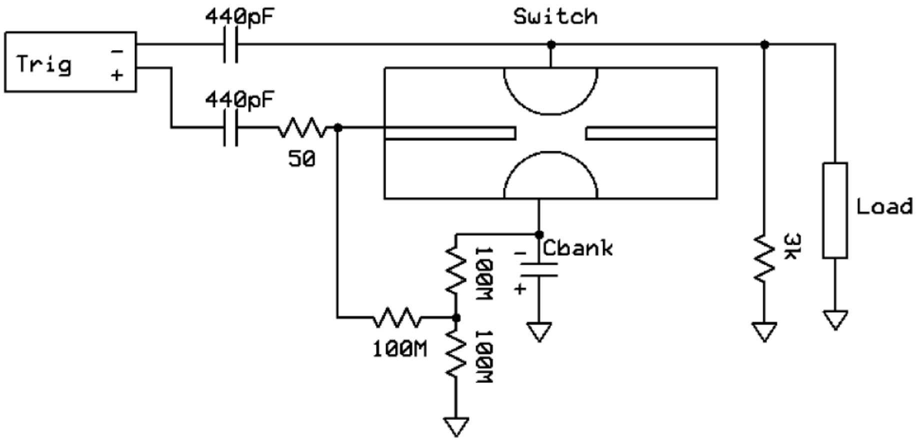

Figure 46 *MAF Trigger Circuit. Trigger impulses can be simulated by modeling the gaps between the trigger plate and switch electrodes as 3.5 pF capacitors. The bandwidth of the trigger circuit is set by the RC time constant of the 50 Ω and 440 pF, which is about 7 MHz in this design*

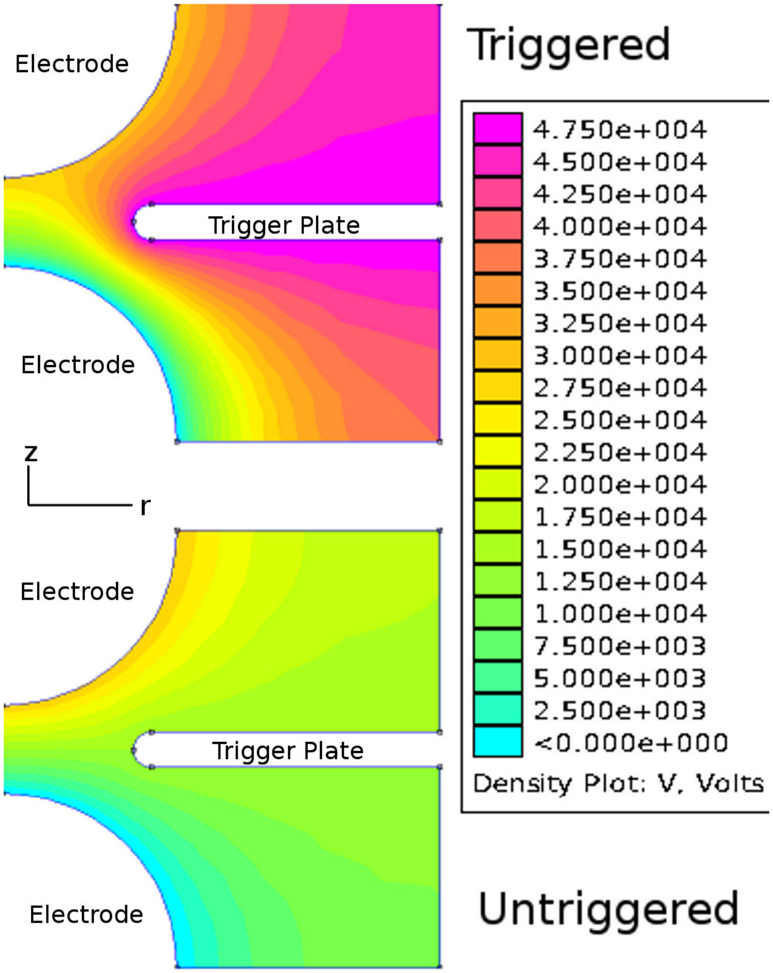

Figure 47 *Finite Element analysis of switch trigger fields with FEMM. The inner diameter of the trigger plate was selected so the trigger gap is 1/2 distance of the voltage gap.*

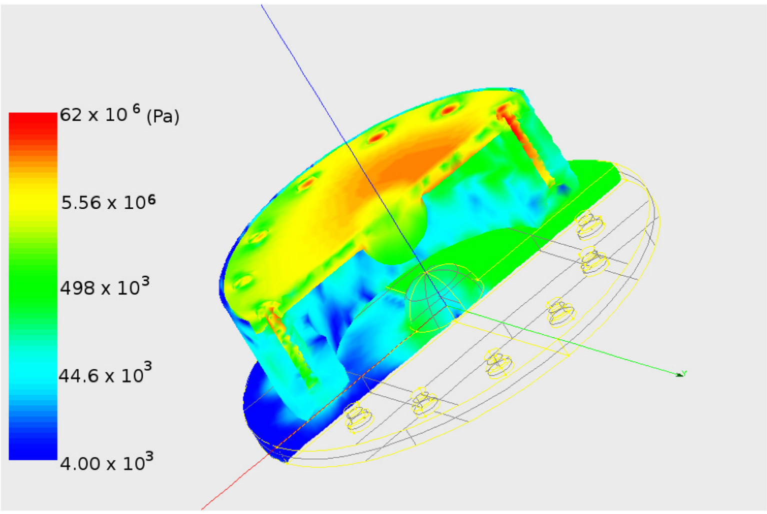

Figure 48 *Finite Element analysis of stresses (Pa) on switch from magnetic forces with Code Aster.*

forces while minimizing switch inductance. Plates were originally composed of stainless steel, but 6061 aluminum was selected to lower switch resistance. Electrodes were constructed out of HD17, a 90% tungsten alloy [93]. Delrin [94] was selected for the plastic housing because it is a strong hydrocarbon plastic with good UV resistance. Polycarbonate was considered for the body material because its shock resistance is about an order of magnitude better than Delrin, but exposure to UV can degrade the material properties of polycarbonate unless special coating/resins are employed [95, 94].

The principle dynamic forces at work on the switch during a shot are the concussion from the heating of the internal gas volume and the $J \times B$ concussion due to PFN current flow through the switch. The rise in gas pressure due to heating can be bounded by examining the "worst-case" effect of dissipating all of the capacitor bank energy in the switch gas volume. For a gas cell at pressure P_0 composed of a gas with molar mass M and isovolumetric specific heat c_v experiencing a change in energy ΔE, the final pressure is:

$$P_f = P_0 + \Delta E \frac{R}{M V c_v} \tag{9}$$

The internal volume of the switch allows for $\sim$ 1000 cm^3 of gas. Nitrogen gas fills of about 450 kPa are necessary to stand off bank voltages of 60 kV. If the entire 44 kJ of bank energy were discharged in the switch gas cell, gas pressure would be expected to rise to about 18 MPa.

Magnetic forces were estimated by approximating the switch installation as a current loop comprised of parallel plates. The $J \times B$ force on the opposing loop segments is a function of the plate current I, width w and separation s.

$$F_{mag} = I^2 \frac{\mu_0 s}{w} \tag{10}$$

If the switch base is assumed to be firmly rooted, at $I = 1$ MA the switch lid experiences an estimated $|F_z| = 400$ kN on the lid faces and $|F_y| = 200$ kN on the switch knobs.

These magnetic force approximations were used to estimate the peak stresses on the switch using the finite element Code Aster [96]. A model of the bolted switch, shown in Figure 48, was constructed in order to simulate the effect of magnetic forces on the switch arising from 1 MA currents. Static forces were used for the computation. Peak stresses from magnetic forces on the

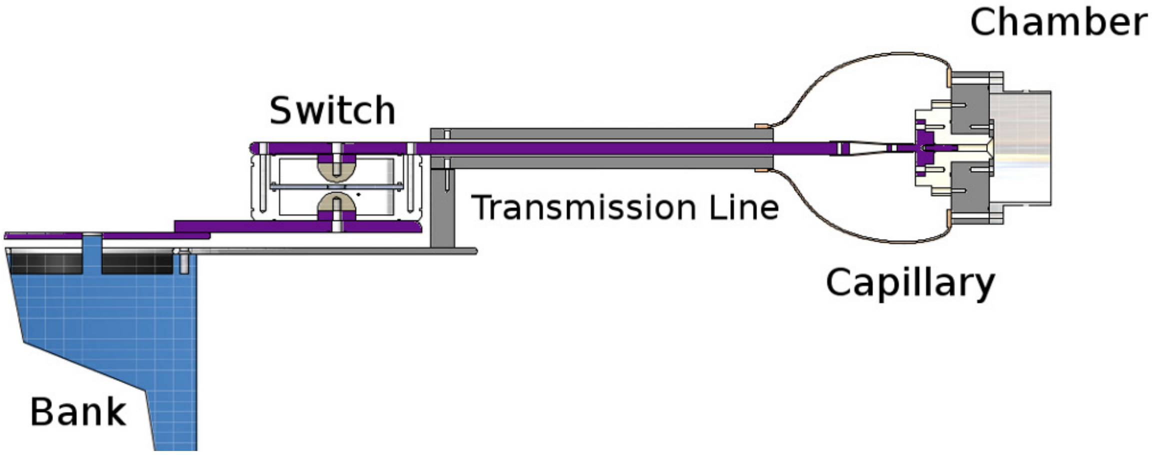

Figure 49 *MAF switch installed on Capillary PFN. Transmission line is a Tri-plate stack.*

body were found to be near the bolt threads and estimated to be 5 MPa. This is within the tensile stress of Delrin of about 69 MPa [94].

5.6 Capillary Load Results

Two MAF switches were constructed using this design. External hold off voltages were tested with a Hipotronics hi-potter to 60 kV. Switch internal self-breakdown voltages were also measured for ultra high purity argon and nitrogen gas fills, and are shown in Figure 50. Argon gas fills were necessary for voltages below 10 kV. Nitrogen gas fills were used for operating at 19 kV higher. Argon/Nitrogen mixtures for intermediate voltage operation were not tested. Static gas fills were used for experimentation. The switch gas was purged at the end of each shot with additional fill gas fed at the operating pressure.

A MAF switch was installed on a 54 μF bank and attached to a high current ablative plasma capillary [97, 98] via a low-inductance, parallel-plate transmission line, shown in Figure 49. Buswork was constructed from 1/2 in thick aluminum plate. The transmission line was constructed with 5/8 in thick aluminum plate. Ten layers of 0.010 in thick Mylar sheets were used as insulation between plates. A copper jumper plate connected the high voltage to the capillary. An array of 12 AWG 40 kV wires was used to create the ground return.

A total of 27 shots were taken with the high current capillary using PFN voltages ranging from -4 kV to -40 kV. PFN current traces can be approximated by a lumped element series LC model. This estimates system inductance to be 155 nH. The largest peak current, shown in Figure 51, was measured to be $\sim$ 0.995 MA [1].

5.7 Railgun Load Results

A MAF switch was installed on a 36 μF bank and attached to a high current plasma railgun via a low inductance coaxial transmission line network, as shown in Figure 52. A second MAF switch was mounted as a crowbar switch for damping of PFN circuit ringing. Buswork was constructed

---

[1] Shot was recorded when an air arc short circuited the capillary load

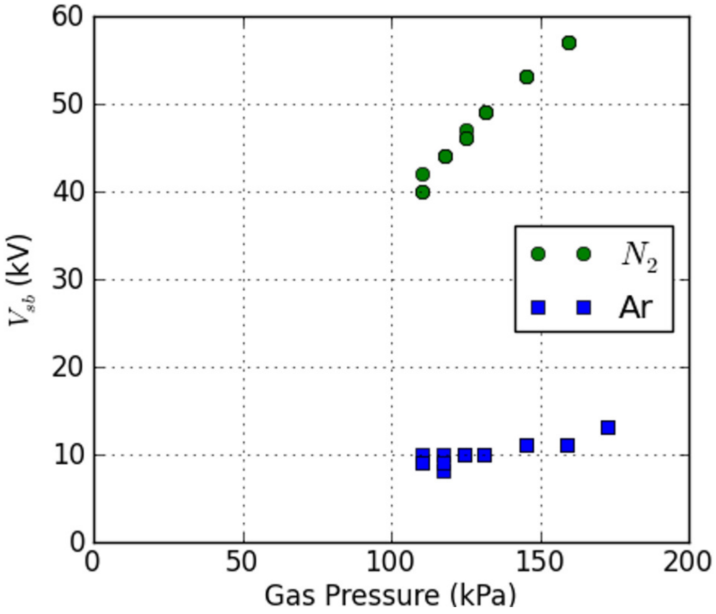

Figure 50 *Switch self-breakdown voltage V_{sb} for static gas fills of dry Nitrogen and Argon vs switch fill pressure. Argon is used for low voltage operation (4-8 kV). Nitrogen is used for high voltage operation. (19-40 kV)*

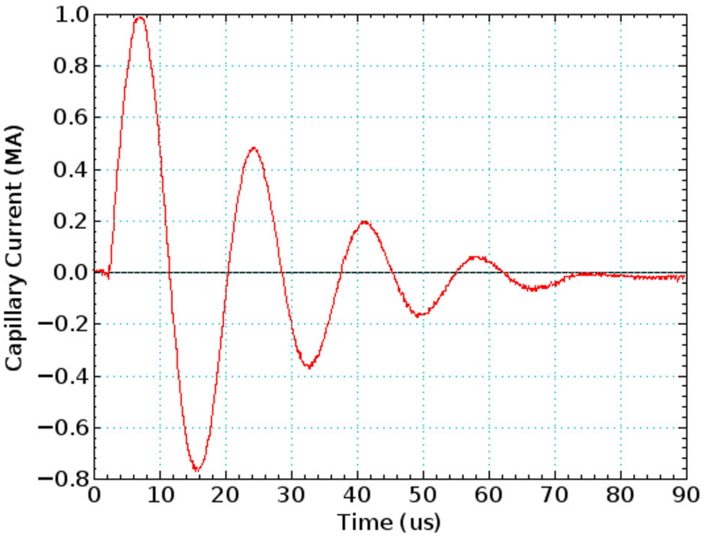

Figure 51 *Peak current sourced by the switch was measured to ∼ 0.995 MA with a capillary load.*

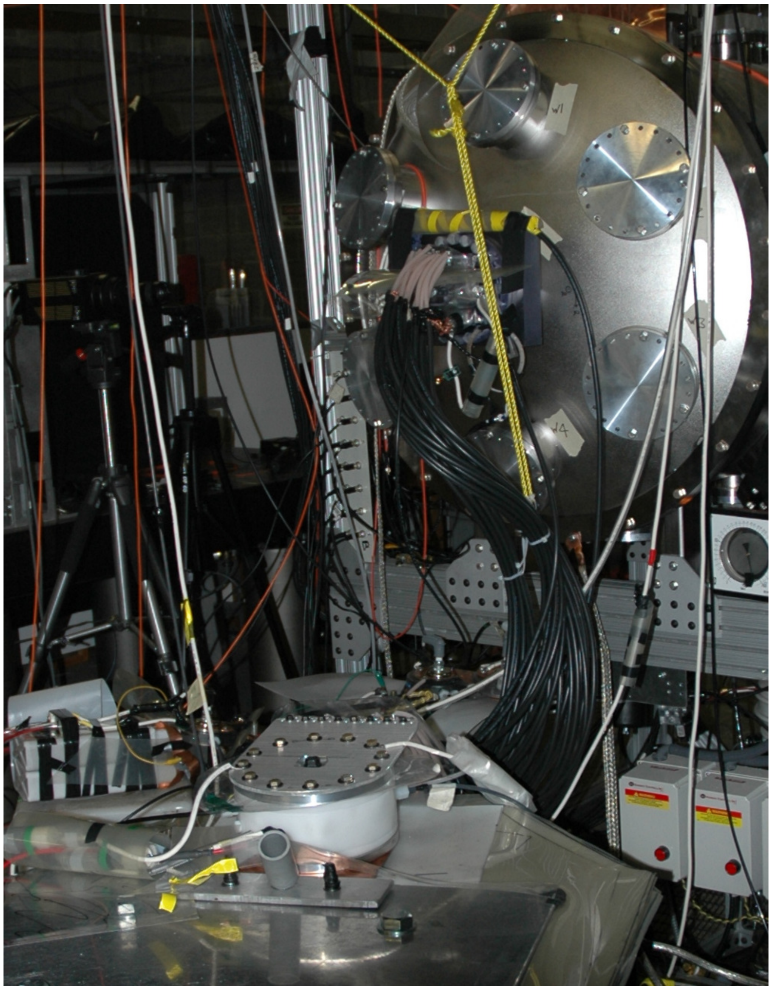

Figure 52 *A MAF switch installed as the PFN switch on a 2.5 cm bore plasma railgun. A transmission line comprised of RG-8 cables connects the railgun to the switch. A second MAF switch (not shown) was mounted as a crowbar switch for damping of PFN circuit ringing.*

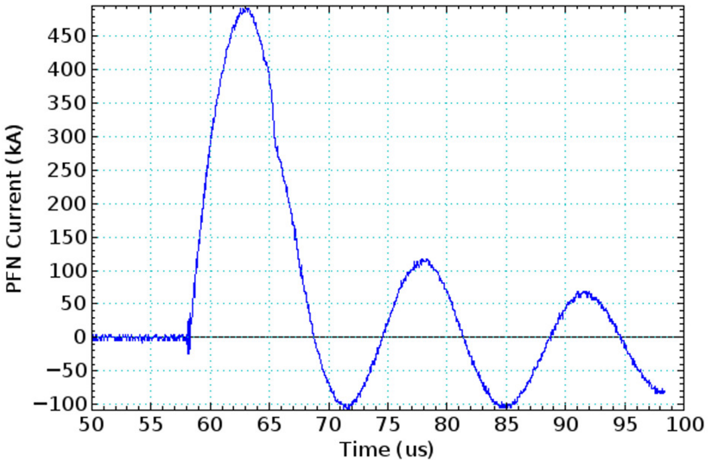

Figure 53 *A MAF switch was employed to switch the PFN current for a HyperV railgun. Peak Current for this shot was measured to be 0.495 Mega-amps.*

from aluminum plate. Ten layers of 0.010 in thick Mylar sheets were used as insulation between plates. A ∼2 m long transmission line was constructed with 30 RG-8/U cables.

A total of 126 shots were taken with a high current plasma railgun using PFN voltages ranging from -22 kV to -38 kV. PFN current traces can be approximated by a lumped element series LC model. This estimates system inductance to be 240 nH. The largest peak current, shown in Figure 53, was measured to be 0.495 MA. A histogram of peak currents from all shots taken with the switches is shown in Figure 55. Variation in time between the trigger and the onset of PFN current was measured to be 550 ns for these shots.

5.8 Coatings, Wear, and Lifetime

In an effort to reduce the over-all cost of the switch, an attempt was made at substituting 6061 aluminum electrode knobs coated with a layer of 25 μm to 38 μm hard chrome in place of the solid tungsten alloy electrodes. An electroless nickel binder layer was employed. A pair of coated and un-coated aluminum knobs were exposed to one 16 kJ, 550 kA peak shot. As seen in Figure 56, a single shot was enough energy to damage the hard chrome coating layer and cause heavy pitting to the aluminum in both the coated (B) and un-coated (A) cases. The HD-17 knobs shown (C) perform much better, displaying mostly discoloration after about 10 shots.

The trigger plate also exhibits signs of pitting and wear. Stainless is not an ideal choice for the trigger plate material because of erosion. However, the stainless trigger plates were often re-manufactured and returned to service. Moving to an alternative material for the plate may reduce wear, but could increase cost because of the size of the part.

The switch has a maintenance cycle of ∼50 shots or less. After this, the switch will begin misfiring as black conductive debris will have built up on the internal surfaces. This material is the result of ablation of electrode, wall, trigger plate, and air supply tube-fitting materials due to PFN current discharge and UV illumination. Lightly sanding and scrubbing the internal surfaces clean with alcohol restores operation of the switch.

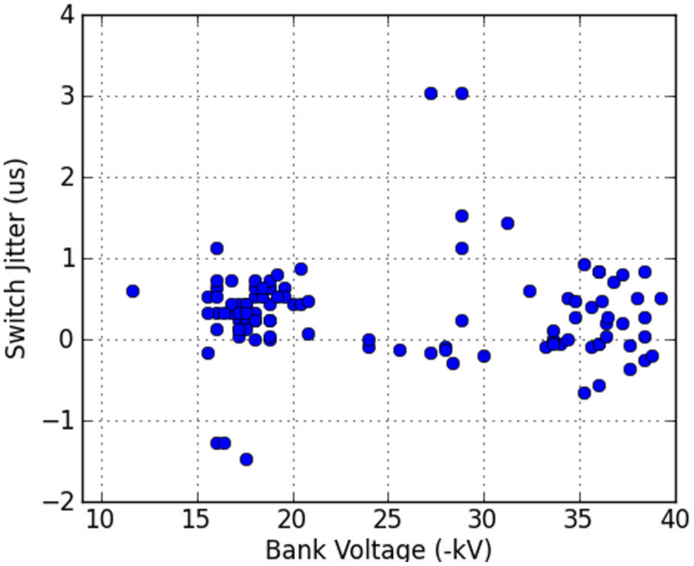

Figure 54 *Variation in time between the trigger and the onset of PFN current was measured to be 550 ns for railgun shots taken.*

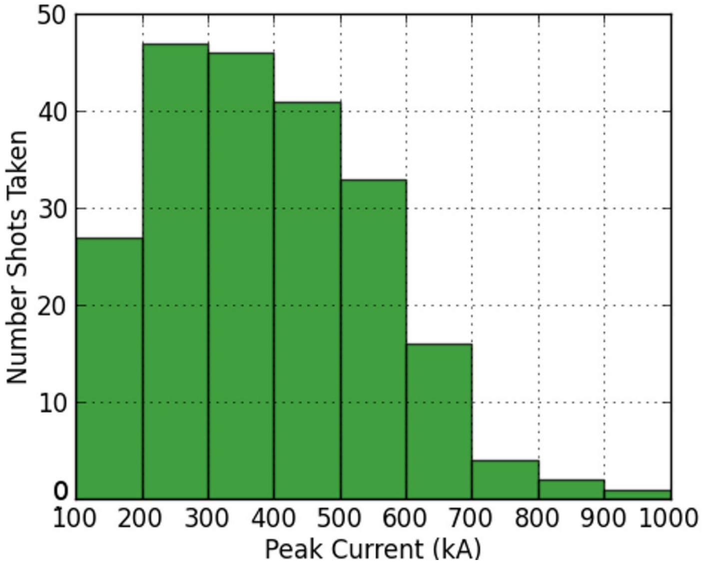

Figure 55 *251 shots were taken with high current plasma railguns or capillary loads using PFN voltages ranging from -4 kV to -40 kV.*

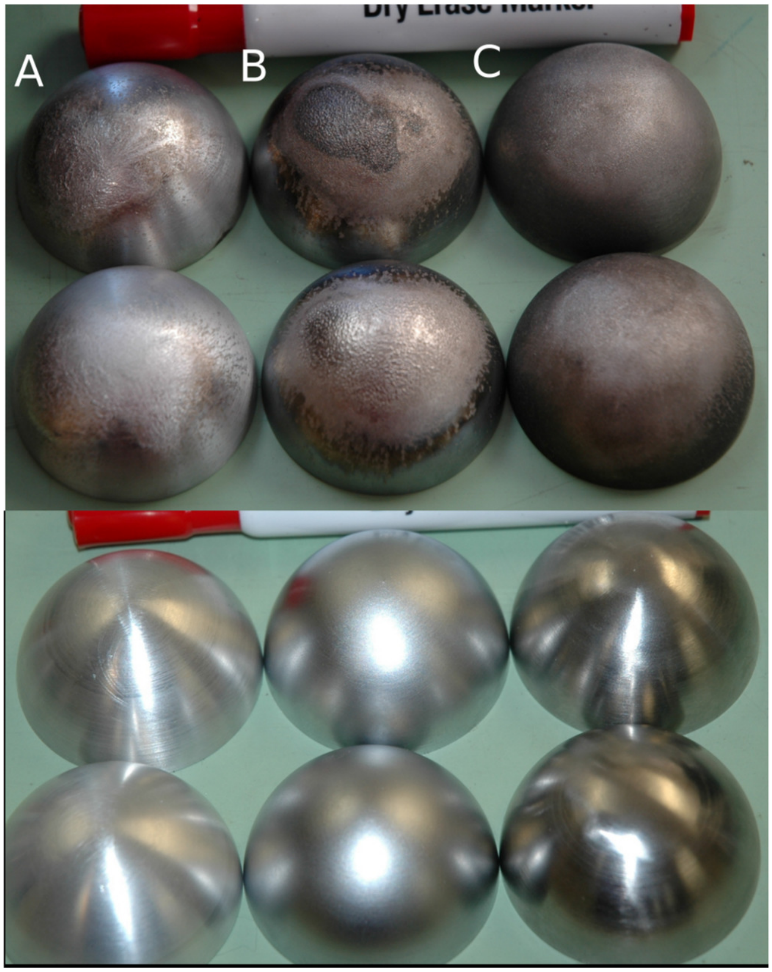

Figure 56 *An attempt was made at substituting 5 cm diameter 6061 aluminum electrode knobs coated with a layer of 25 μm to 38 μm hard chrome in place of the solid tungsten alloy electrodes. A single 16 kJ shot was enough energy to damage the hard chrome coating layer and cause heavy pitting to the aluminum in both the coated (B) and un-coated (A) cases. The HD-17 knobs (C) displayed mostly discoloration after about 10 shots.*

5.9 Comments

The principle advantages of the MAF switch design are its performance and its cost. Peak current of up to 0.995 MA were switched for banks sourcing as much as 1.4 Coulombs. with an estimated inductance of ∼ 15 to 30 nH. Switch lifetime was low at ∼125 shots per switch, but each switch's material cost was about an order of magnitude less than existing commercial solutions for 1 MA at the time.

The chief disadvantage of this design is its susceptibility to material fatigue. The current design places all stresses from firing on the plastic body of the switch. While the design is strong enough to survive high current shots, the repeated loading and unloading of forces on the body can fatigue the Delrin plastic[99]. The impact strength of Delrin is also only about 200 $\mathrm{kJ/m^2}$. After about 120 shots, cracks form in the walls of the plastic body of the switch. This is a run-away failure mode as a crack can expose the two bolt patterns to each other. This results in the formation of an arc channel inside the wall of the switch causing the switch to fail. Future designs will require an insulator material with fatigue and shock resistance superior to Delrin or an alternate method of clamping the upper and lower plates that does not load the switch body. Increasing the internal volume of the switch would reduce the pressure rise from gas heating. The trigger plate also needs better heat management for repeated high current operation. Repeated high current operation of the switch causes the central plate to store heat, raising the temperature of the gas cell, and reducing the dielectric hold-off of the switch at a given pressure. This leads to misfires until the switch cools. Heating could be corrected in part by using higher operating pressure for the gas cell, or by continuously flowing the gas in addition to heat sinking the trigger plate.

5.10 Linear Spark Gap Switches

For the Mark 1 gun and the Mark 2 gun we eventually transitioned to linear spark gap switches to address the issues described above. The goal was to design linear spark gap switches that could be easily machined, were relatively inexpensive, and could handle currents above 500 kA routinely and reliably.

Early versions of the linear spark gap switch utilized a linear array of current conduction electrodes separated by a small adjustable gap. Triggering was accomplished using a row of trigger pins situated slightly above the midpoint of each pair. The geometry is illustrated in Figure 57. A 12 inch long version is shown in Figure 60. Construction uses off-the-shelf angle aluminum. The central insulator body is machined from a single block of Delrin for strength and to make gas pressure sealing easier. The top and bottom compression plates are constructed from thick G-10 sheet for strength.

Electrical connections are made through numerous RG-8 cables all connected in a wide array in order to reduce lead inductance. The ground return is underneath the bottom plate and not visible in the photo. The o-ring seal allows the central cavity to be pressurized with a working gas, typically argon or nitrogen at a couple of atmospheres, sufficient to hold off the working voltage, but easy to trigger a brealdown. Early versions used Lexan for the central cavity, but that led to too much residual dust after firing. Delrin (or Noryl) plastics solved that problem and was also cheaper.

This design approach worked satisfactorily for relatively low current discharges (i.e.$<$200 kA) but had some difficulty with reliable triggering and uniform current distribution among the current electrodes. It could not handle high current reliably without over-pressuring and blowing out cracks in the end plates. This was solved by lengthening the cavity, increasing the number of electrodes to distribute the coulomb transfer among a larger surface area, changing the triggering method, and

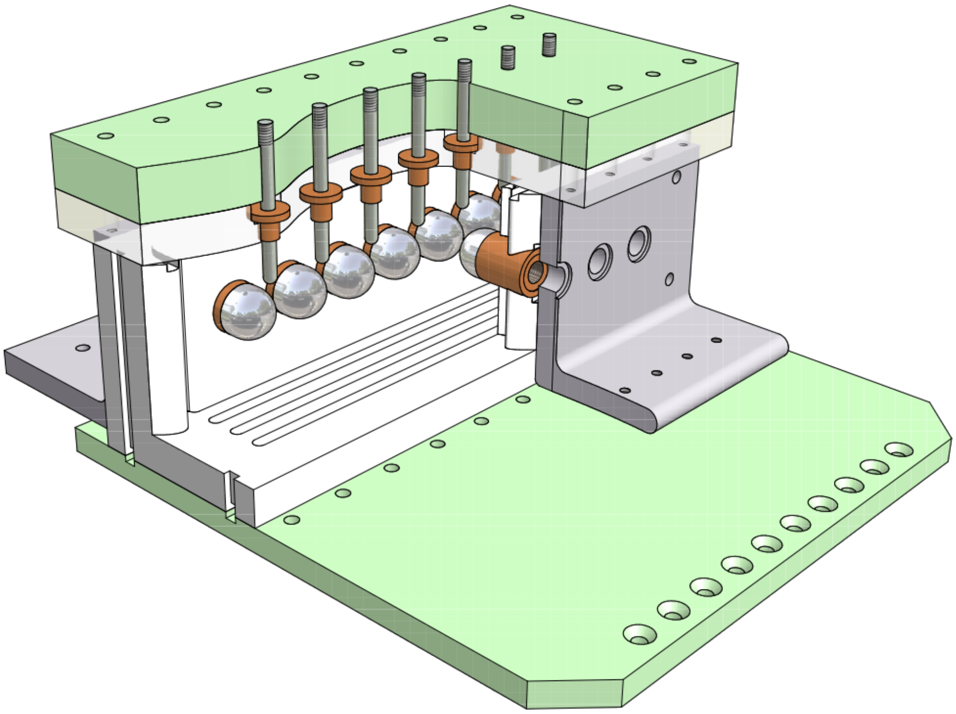

Figure 57 *Early version of linear spark gap switch.*

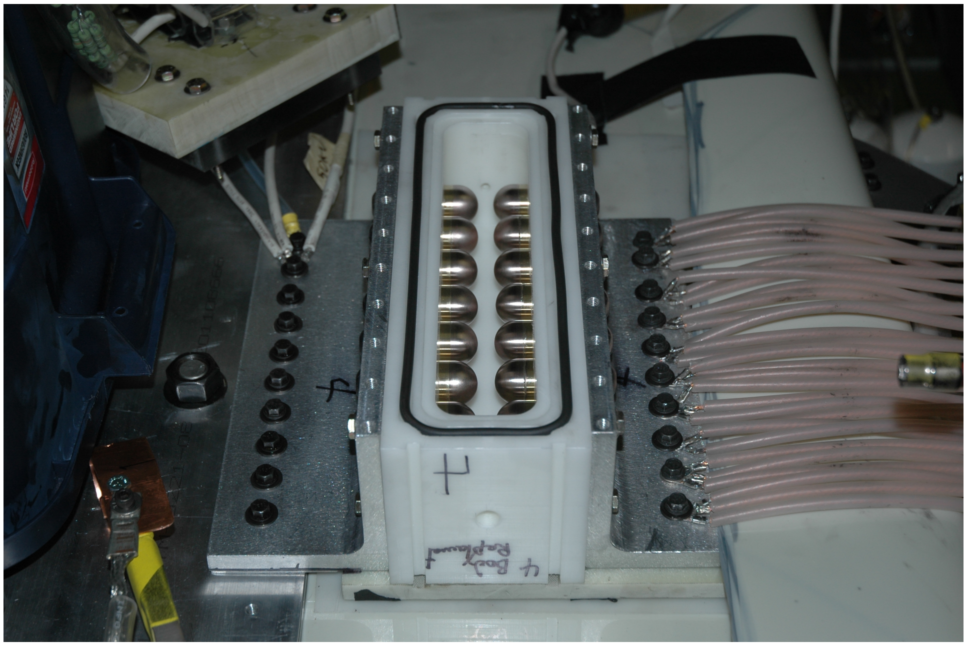

Figure 58 *A 12 inch long version of early top trig linear spark gap switch.*

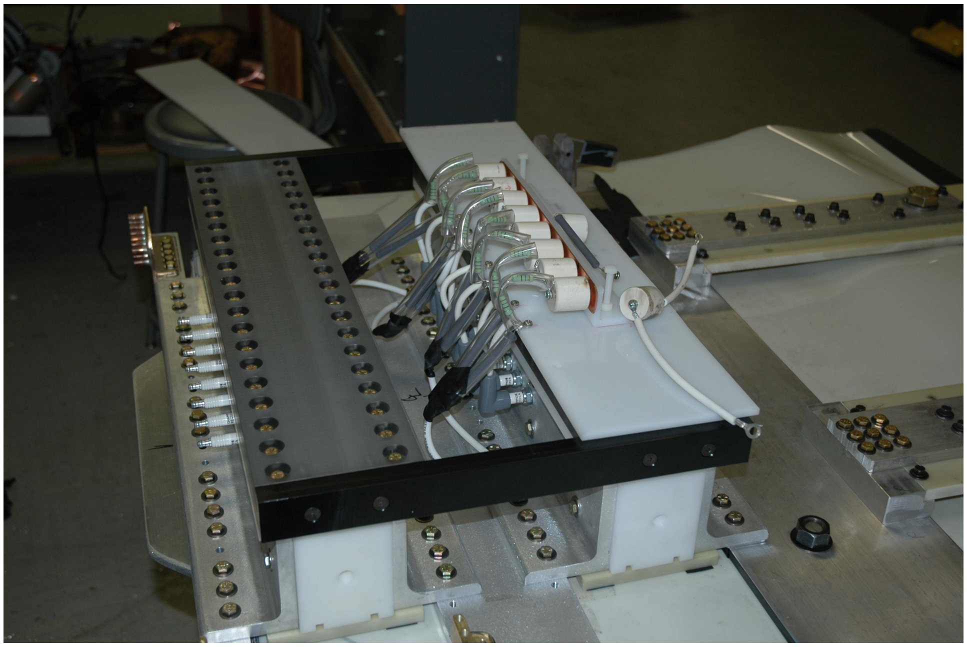

Figure 59 *A 12 inch long version of early top trig linear spark gap switch.*

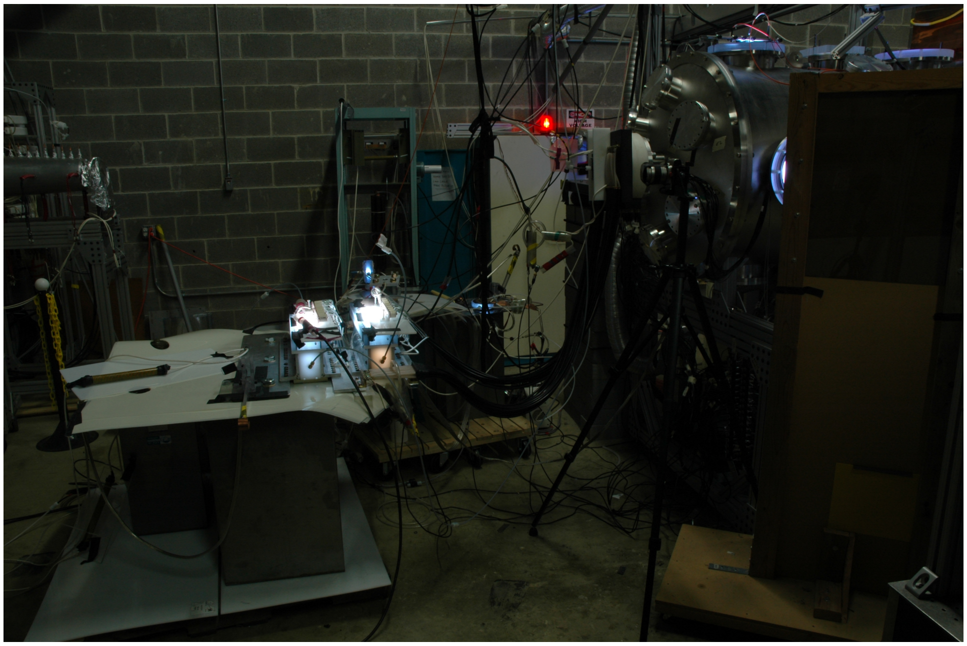

Figure 60 *A 12 inch long version of early top trig linear spark gap switch.*

Figure 61 *24 inch Linear switch with crowbar.*

strengthening the supporting external structure. The trigger electrodes were moved from the central mid-plane to integral spark plugs in the center of each electrode knob. This provided much more reliable and uniform breakdown of the electrodes. With these changes, we were able to routinely run at 600 kA for about 10-20 μs using 24 inch wide switches.

Because of ringing in the pfn, we decided to implement crowbar switches to cut off current to the gun when current reverses. The purpose for this was primarily to reduce wear and tear on the gun components and the main switch. Two sets of switch with integral crowbar, as shown in Figures 61-63 were constructed and tested. Although the crowbar worked, it was decided later that the system became too complex, too expensive, and physically too unwieldy to implement for a large number of guns, and so we ultimately abandoned that approach. A far simpler and more effective approach would be to properly match the gun and pfn and avoid the ringing problem in the first place, although we did not have sufficient capacitors to do that.

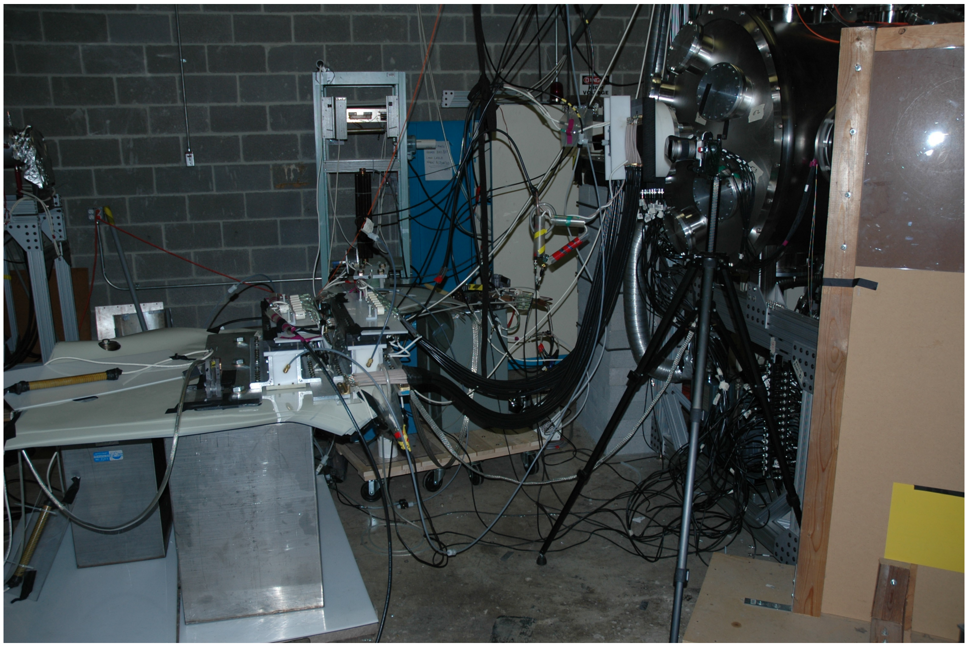

Figure 62 *Side view of testing of 24 inch switch with gun.*

Figure 63 *Closeup of the internal switch cavity showing electrodes and spark plug ignitors.*

6 Mark 1 MiniRailgun Development

6.1 Introduction

A plasma railgun is a device with uses Lorentz force to accelerate a plasma slug that is both railgun armature and projectile. Because they can produce high exhaust velocities and momentums, plasma railguns are already being evaluated for applications in tokamak refueling, ELM pacing, and disruption mitigation [100, 101, 102]. Plasma railguns are also being considered as rotation drivers for magnetically confined fusion reactors, implosion liner drivers for plasma-jet magneto-inertia fusion reactors, and fuel injectors for magnetized target fusion reactors [13, 103, 104]. This is in addition to their applications in laboratory astrophysics and satellite electric propulsion. While the topologies of these plasma railguns show similarities, the parallel plate electrode geometry employed in HyperV's linear plasma accelerators [105] retains several distinct advantages over coaxial devices. Parallel plate, or linear railguns, have higher inductance per unit length, L', for increased power efficiency. The parallel plate geometry also creates a more uniform pushing field, mitigating the blow-by instability which is inherent in coaxial designs [106]. Additionally, linear railguns can also be augmented with external fields for further increased performance [107]. In order to meet the design specification for the PLX experiment of 8 mg of argon plasma jets ejected at 50 km/s, HyperV has been focusing on advancing the performance of it's linear plasma railguns by maximizing the momentum of ejected plasmas.

6.2 Railgun design

HyperV linear plasma railguns, show in Figure 113, are three stage linear plasma accelerators. In the first stage, or gas injection stage, neutral gas is injection into the rear of an electrothermal capillary channel via an electromechanical fast gas valve (GV). In the next stage or pre-ionization stage (PI), a current of tens of kiloamps is discharged though the capillary channel. This pre-ionizes the injected gas which will form the plasma armature, and injects this plasma into the breech of the railgun electrode gap. Finally, the acceleration stage employs a Pulse Forming Network (PFN) to drive a large current (as much as 500 kA) through the armature via the rail electrodes. As the armature current moving through the plasma is also moving normal to its self-generated magnetic field, the plasma armature experiences a Lorentz force, accelerating it down the length of the bore to be ejected as a high velocity plasma jet. Since the goal of this design is to meet or exceed the PLX plasma jet specifications, these specifications determine the performance requirements for the various subsections of the railgun. The gas valve must be fast opening, and inject sufficient gas to produce the required plasma jet mass. The pre-ionizer must not only ionize the gas, but also inject a localize plasma pulse with some initial velocity to reduce the dwell time of the armature at the breech of the accelerator [105]. Finally, the accelerator must supply the necessary energy and withstand the forces required to repeatedly accelerate 8 mg of plasma to 50 km/s. Since the desired plasma jet kinetic energy for PLX is about 10 kJ, even a railgun operating with an assumed efficiency of 20% would still require a PFN bank energy of 50 kJ.

The Cartesian coordinate system will be used to describe railgun features. Axes are defined as x being the lateral axis of the railgun across the electrode face, y being changes in height, and z being locations along the length of the railgun. The foot of the accelerator rail is defined as z=0. Unless indicated otherwise, time events are referenced from the time of accelerator current onset at t=0.

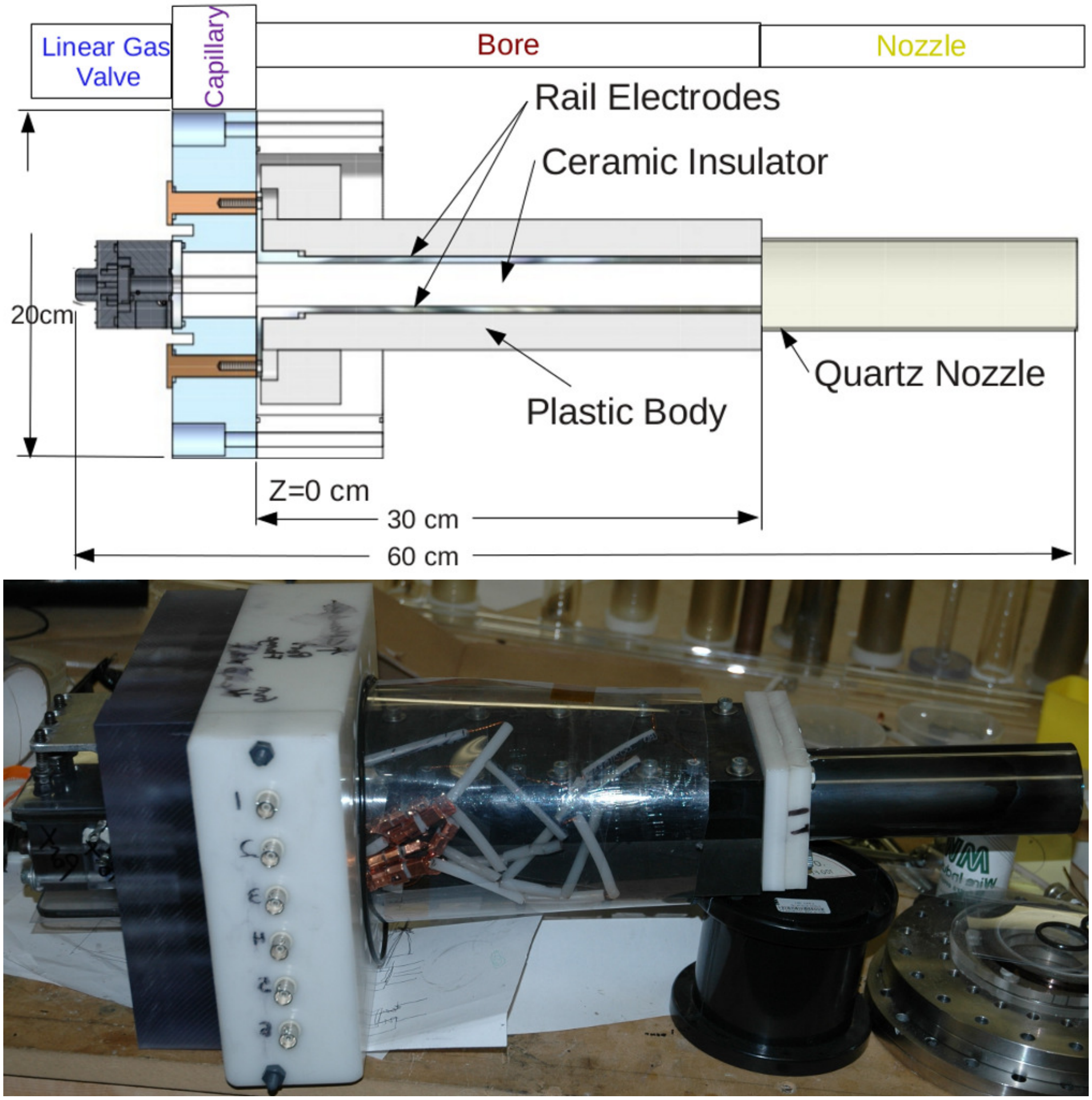

Figure 64 *HyperV plasma railguns are three stage linear plasma accelerators. First Neutral gas is injected with an electromechanical fast gas valve (GV). Next the pre-ionization stage (PI) ionizes the gas electrothermally using a capillary discharge channel. This injects a plasma armature into the final railgun acceleration stage. Here the plasma armature is accelerated via a Lorentz force, generated by current from a Pulse Forming Network (PFN), and ejected as a high velocity plasma jet.*

6.3 Gas Valve - Later Version

The use of high speed gas valves is common in plasma physics. The typical high speed gas valve uses magnetic pressure to move a conductive poppet, opening a path through which gas can flow. The use of magnetic pressure allows for very high forces (100's of Newtons) to be generated over very short time intervals (10's of μs). This in turn gives the lightweight poppet a very high initial acceleration, opening the valve rapidly. Valve closing is effected by a return spring, often simply an o-ring resting against the back of the poppet. The magnetic field is generated by a coil of wire (sometimes just a single turn), with the current driven by a capacitor switched by a high current switch, forming a simple RLC circuit.

The HyperV Linear Gas Valve (LGV) represents a step forward in high speed high mass puff valve technology. Previous high speed puff valves using the principle of magnetic pressure to rapidly move a poppet (or flyer plate) wrapped the magnetic field coil around the exit orifice[108, 109, 110, 111]. This limits the peak central field due to the requirement that the coil not impinge on the orifice. As the orifice is enlarged the central field drops, requiring ever higher currents in order to drive the flyer plate. In addition the requirement that the flyer plate be thin in order to be light means that it potentially suffers from distortion due to the high forces applied both by the magnetic field and by impact with the return spring.

The HyperV linear gas valve is innovative in two ways: first the driving coil is split into two coils placed on either side of the orifice, decoupling coil geometry from orifice size. Second, the flyer plate is extended linearly over the coils and has vertical tangs to resist distortion. An exploded view is shown in figure 65, showing the coils inserted from the side of the base block (which is not possible with coaxial designs), the tanged flyer plate, and the linear arrangement of coils and orifice. Insertion of the coils from the side allows for the necessary voltage standoff from the pre-ionizer plate during operation of the MiniRailgun. The coils are vacuum potted in epoxy once in place.

The valve is designed to operate mounted on the breech of a MiniRailgun[48, 105] plasma accelerator, which requires that it mount directly to a pre-ionizer plate which is switched to voltages as high as 30 kV. This means that the coils must be protected from arcing from the pre-ionizer plate. This is complicated by the fact that the pre-ionizer generates plasma which electrically connects the flyer plate to the pre-ionizer, potentially exposing the coils to high voltage from both above and below. Previous experiments indicated that epoxy was incapable of standing off the voltages directly, especially due to the fact that the shock of the coils firing tends to cause small scale cracking of the epoxy. The pre-ionizer also leads to the requirement for a Delrin insert in the orifice, as this reduces ablation of body material due to exposure to the plasma. The body is polycarbonate for shock resistance: the shock of firing had lead to weakening of Delrin bodies in previous iterations of the valve design, leading to failure by arcing between the coils and the pre-ionizer. However polycarbonate has poor plasma ablation properties leading to contamination of the plasma with significant quantities of hydrogen and carbon.

The placement of the gas valve on the breech of the railgun puts it in between the two high voltage leads. In order to minimize railgun inductance (to maximize driving current) the valve has to be as narrow as possible so as to reduce the spacing between the high voltage leads. This requirement, along with the high mass flow requirement to feed the railgun, leads to the low profile design presented here.

Construction The main body (base) of the valve is machined out of a single block of polycarbonate, chosen for shock resistance. The coils are wound on a special winding jig and inserted into position. Once the coils are in place a screw connection is made to a set of HV leads (the white leads on the left in figure 67). The coils are then potted into the base using Duralco 4461 epoxy

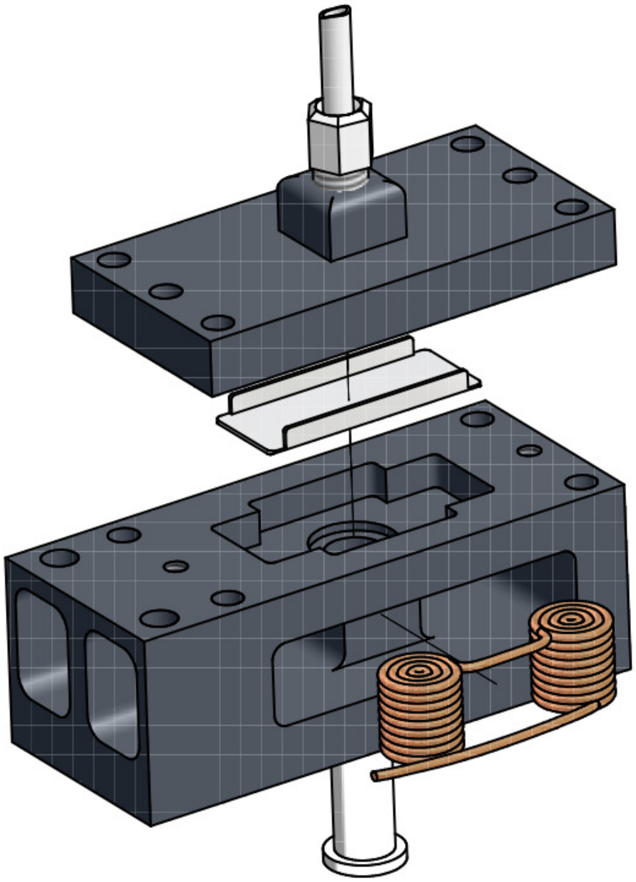

Figure 65 *Exploded view of linear gas valve assembly, showing base, coils, flyer plate, and top.*

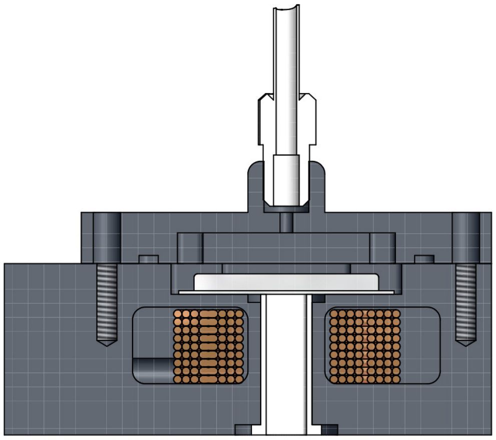

Figure 66 *Cutaway view of linear gas valve assembly, showing how the various elements fit together. Not shown are the return springs, which consist of two rubber o-rings mounted on edge (in the plane of the cutaway) bearing on the flyer plate on one side and restrained in a groove in the top piece on the other.*

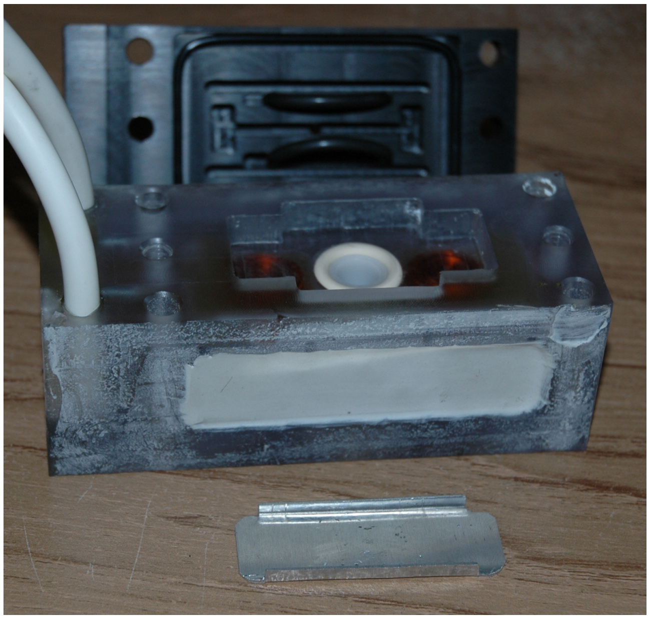

Figure 67 *The three main elements of the gas valve, disassembled. From bottom to top: Flyer plate, Base, Top*

Valve	Wire	Turns (radial x axial)	Voltage	Capacitor	Ballast Resistance
LGV 3	0.075“ x 0.012“	14 x 7	5 kV	28 μF	1.4 Ω
LGV 5	14 gauge	4 x 9	8.5 kV	28 μF	0.6 Ω
LGV 6	18 gauge	6 x 14	5.3 kV	14 μF	1.2 Ω

Table 2 *Table I: Parameters for three generations of valve design. Iterations not shown (LGV1, 2 and 4) differ from the other valves in body materials and orifice insert rather than coil design.*

(a formulation designed for high voltage standoff). Once the epoxy has been poured the entire assembly is placed under low vacuum to draw out trapped air bubbles. Once the epoxy is set the base is sanded to remove drips and high points on the casting.

Three types of coil were used: a 14 gauge wire coil with 4 radial turns and 9 axial turns, and a 18 gauge coil with 6 radial turns and 14 axial turns, and a 0.075” by 0.013” flat wire coil of 14 radial by 7 axial turns. In all cases the wire was insulated to 6 kV standoff voltage. Three generations of valve were used, all using the same basic geometry but differing in coil design. The parameters of the circuits used to drive them are shown in table I.

The top is machined from a single block of delrin. The hole through which the valve is fed is kept small (˜1/16“) so as to decouple the valve dynamics from the gas feed lines as much as possible. The top has two slots to hold the o-rings that serve as return springs and is relieved to allow the maximum volume behind the flyer plate.

The flyer plate is constructed from 1/32” aluminum plate (6061-T6) which is cut into shape using a bandsaw and filed to final dimensions. The tabs are bend up by hand using a vice to hold the workpiece, and the whole thing is filed and sanded again to reduce the height of the tabs for minimum weight. The tabs provide rigidity to the plate so as to prevent distortion by the large forces experienced during operation.

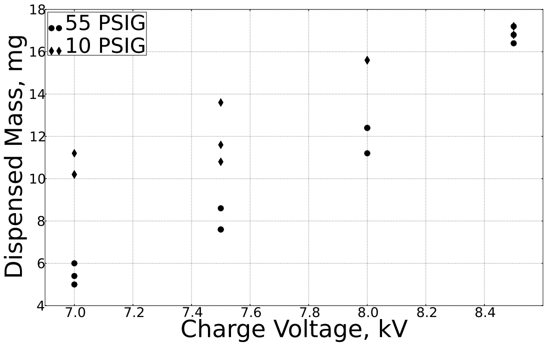

Figure 68 *Dispensed volume as a function of charge voltage for two feed pressures, 55 PSI (blue) and 10 PSI (red).*

Operation The final version (LGV 6) of the valve is driven by a 14 μF capacitor in series with a 1.2 Ohm resistor, forming a simple series RLC circuit. The capacitor is switched using a spark gap switch (R. E. Beverly and Associates SG-111M-75C). For the 6 × 14 turn (18 gauge) coils charge voltages between 4.5 and 6 kV have been tested, and the valve should be able to function at up to 8 kV, though performance below this point is satisfactory. Typical peak currents are 2.4 kA at 5.5 kV, and the system is slightly underdamped, with a ring of about 30% of the first peak. The 18 gauge wire coils (4 × 9 turns) charge voltages are in the range 7 to 8.5 kV, with currents 5.6 to 7 kA, giving roughly the same number of amp-turns in each case. Operating pressures of 15 to 60 PSIG have been tested. Below 30 PSIG operation has poor repeatability: the ideal operating point appears to be 45-60 PSIG and 5.5-6 kV charge voltage for the 18 gauge coils.

Performance and Testing In order to gauge the amount of gas dispensed per shot the valve (LGV4) was mounted on the HyperV 1128 liter vacuum chamber. The chamber was pumped down to a base pressure of 7×10^{-6} Torr. The procedure followed was to close the gate valve to the diffusion pump, fire the valve, wait one minute for the pressure to stabilize, and record the final pressure in the chamber, from which the total dispensed mass is calculated. The base pressure was measured using an ion gauge, and the final pressures with a Thermocouple gauge. The valve used in this series of tests had the 14 gauge (4 × 9 turn) coils. Voltages were scanned from 7 kV to 8.5 kV, and two valve feed pressures were used, 10 PSIG and 55 PSIG. Results are shown in figure 68.

From the figure it is clear that increasing voltage and feed pressure both increase the mass dispensed, as expected. The unexpected result is the convergence of the two trends for different feed pressures as voltage is increased. We hypothesize that the closing of the valve is accelerated at higher feed pressures due to the gas itself forcing the poppet closed, in effect forming a gas spring behind the poppet which is stiffer at the higher pressure.

A second approach to valve characterization was to use deflectometry to analyze the plume emitted by the valve. Deflectometry is a technique to measure line integrated density gradients by measuring the deflection of a laser beam passed perpendicular to the gradient[112]. By integrating the measured density gradient a time history of density can be built up. The time history can in turn be integrated to give an estimated total mass, though multiple integrations can lead to accumulated errors due to baseline offsets associated with vibration of the instrument.

Figure 69 shows the results of a set of deflectometry measurements on the plume emitted by the gas valve, The deflectometer was set up so that the beam passed 1.3 cm from the exit of the gas valve. Shots were taken at gauge pressures of 15, 30, 45, and 60 PSI, and drive voltages were

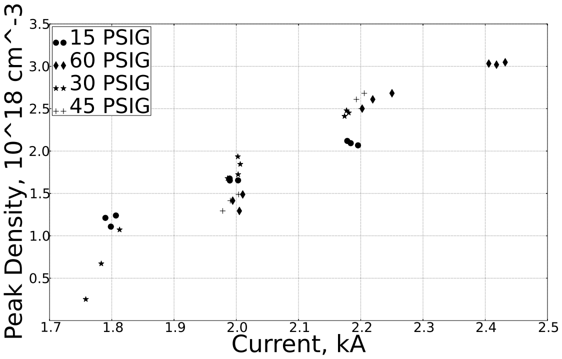

Figure 69 *Peak density in emitted plume as a function of coil current at four pressures, 15, 30, 45, and 60 PSIG.*

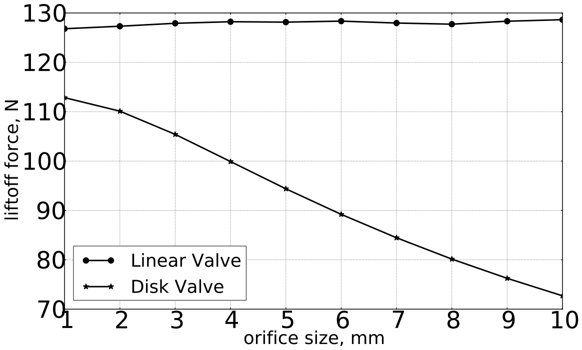

Figure 70 *Poppet liftoff force scaling with orifice size for linear valve and annular (disk) valve designs. Linear valve has 3 radial turns and 6 axial turns per solenoid, disk valve has 4 radial turns and 6 annular turns. Both are run at 2000 amps.*

scanned so as to give currents ranging from 1.8 to 2.4 kA. It is notable that the change in pressure seems to have very little impact on the peak emitted densities, most likely due to the gas spring effect discussed previously. The parameter that does impact dispensed mass is the drive current, which gives nearly linear performance over the range tested.

Discussion One of the features of this design that is most promising is scalability. Figure 70 shows the scaling of poppet liftoff force for two comparable valves, a linear valve of the type discussed here and the traditional circular (disk) design with the magnetic field coil wrapped around the orifice. The simulation used equal area poppets and the number of turns for the two sets of coils was chosen to roughly match the maximum liftoff force for each case. As the orifice size increases the linear valve liftoff force varies only slightly. The disk valve design has a significant decline in liftoff force at larger orifice sizes. This decline of liftoff force with orifice size for the disk valve is consistent across a wide range of coil geometries. The slow variation of liftoff force for the linear valve design is similarly robust over a wide range of coil geometries.

HyperV linear railguns employ custom-designed, electromagnetic-solenoid actuated, fast Linear Gas Valves (LGV) described more extensively by Case et al. [113]. The linear gas valve employed for these experiments consists of an aluminum flyer plate actuated by a pair of solenoids. The chief advantage of the linear design over concentric designs [114, 115] is it allows the diameter of the gas throat to be set independently of the inner diameter of the actuating solenoid. This allows smaller

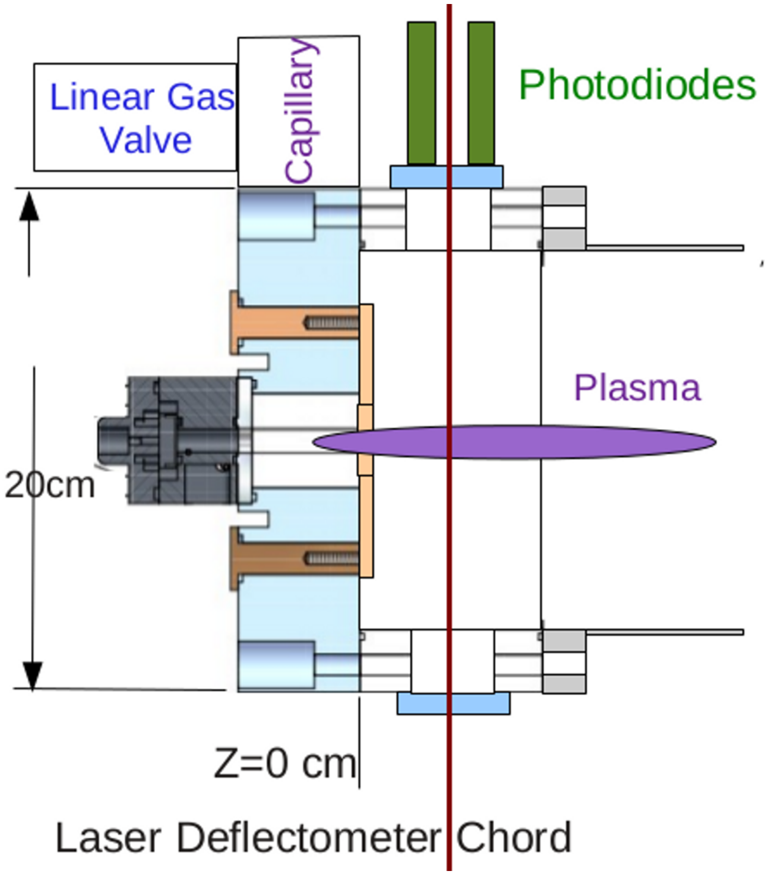

Figure 71 *To inspect injected neutral gas profiles and initial pre-ionizer plasma armature distributions, a breech only configuration of the railgun was mounted with a special plastic flange to provide diagnostic access at z=2 cm. This allowed neutral gas (or the plasma pulse if the pre-ionizer was activated) to be inspected as it emerged from the pre-ionizer and enter the bore. A single chord laser deflectometer was used for gas measurements. A pair of collimated photodiodes were used for pre-ionizer emission profile measurements.*

solenoids to actuate large throat openings, reducing driver bank energy[113]. Characteristics of the gas pulse are determined by the shape of the gas valve current pulse, the gas species, and gas valve feed pressure, p_{feed} as well as gas valve geometry.

The gas valve exhaust port throat can be modeled as a pipe of diameter d and length l with an inlet area at the back that changes with time as the flyerplate opens. Since pipe conductance goes with the quartic of diameter, gas valve throat diameter must be maximized to increase mass injection rate. Throat length must be minimized to not only reduce conductance but also increase gas efficiency, as any volume of gas remaining in the throat after the PI has fired would emerge after the shot as waste.

In order to quantify produced gas profiles and timings, an LGV5 linear gas valve was mounted to a modified pre-ionizer section built with a mock rail electrode as a ground. This breech only configuration of the railgun, shown in Figure 71, was mounted with a special plastic flange to provide diagnostic access at z=2 cm, where neutral gas (or the plasma pulse if the pre-ionizer were activated) would emerge from the pre-ionizer and enter the bore. A series RLC lumped element model of driver circuits can be used to model driver currents tested. Values are shown in Table 3.

To proceed with analysis, let us make the following assumptions. First the gas valve does not launch gas shocks because it does not open supersonically. Furthermore, as $p_{feed} \gg p_{vacuum}$, the gas injected is in “choked flow” where increasing p_{feed} will not increase the flow velocity, but will increase the mass flow rate. Thus, the gas will diffuse with some sort of profile $n_{Ar}(x, y, z, t)$ into the vacuum of the pre-ionizer channel at it’s sound speed, which for argon is about 319 m/s for Temp = 0^{o}C [116]. This implies that if a laser deflector were used to measure the lead edge of the gas profile [112, 117], the axial line integrated density gradient (LIDG) of the density profile can be determined as

$$\frac{\partial}{\partial z}\int n_{Ar}(x,y,z,t)dx = \frac{\Delta\theta_z \rho_0}{(n_0 - 1)} \tag{11}$$

where $\Delta\theta_z$ is the angle of axial laser deflection and n_0 is the index of refraction of the gas at number density ρ_0 given in pp/cm^3. While the present gas profile is expected to be insensitive to radial deflection at the point of measurement due to symmetry, axial LIDG measurements for a single shot are shown in Figure 72. After a burst of trigger noise, Argon gas pulses measured by laser deflectometry, shown in Figure 72, were seen to arrive about 200 μs after the gas valve was triggered. The lack of large negative axial density gradients following the initial peak suggests that the gas valve remains sourcing gas for the entire duration of the shot. Signals indicate density gradient remain positive as late as 1000 μs. The valve does not appear to open a second time, as this would be expected to cause a second axial density gradient peak. This suggests that for the shot timescale, the peak density of neutral gas feeding the capillary increases to some maximum and then remains high for remainder of the shot. The total volume of gas dispersed is expected to be approximately the plenum volume of the gas valve, or about 10.6 cm^3 for the gas valves employed. This implies a pressure of at least 47.1 kPa of argon at STP would be required in order to inject 8 mg of argon into the railgun.

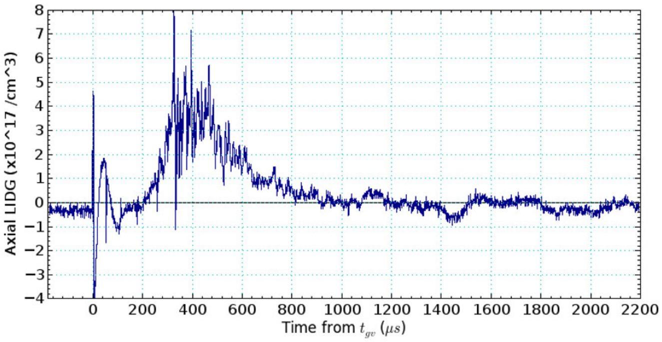

Figure 72 *Gas valve performance was measured via laser deflection to determine the axial line integrated density gradient (LIDG) of injected argon gas profiles. The lead edge of the density profile in this shot arrives at about 200* μs.

The mass of argon present in the capillary at time of firing is expected to be the integral of the density profile accumulated in the capillary (and the railgun bore for long delays) at time of capillary trigger. This can be estimate by integrating axial deflectometry data over the delay time between gas valve and pre-ionizer triggers using an assumed radial density profile. For a normalized Gaussian radial distribution with the the full width half maximum of the radial distribution equal to half the path length l_p, Argon mass is then estimated by

$$m = \int_{t_{gv}}^{t_{pi}} \int_{0}^{l_p} 2\pi \frac{\partial}{\partial z}\frac{n(z,r,t)}{k} v_z dt r dr. \tag{12}$$

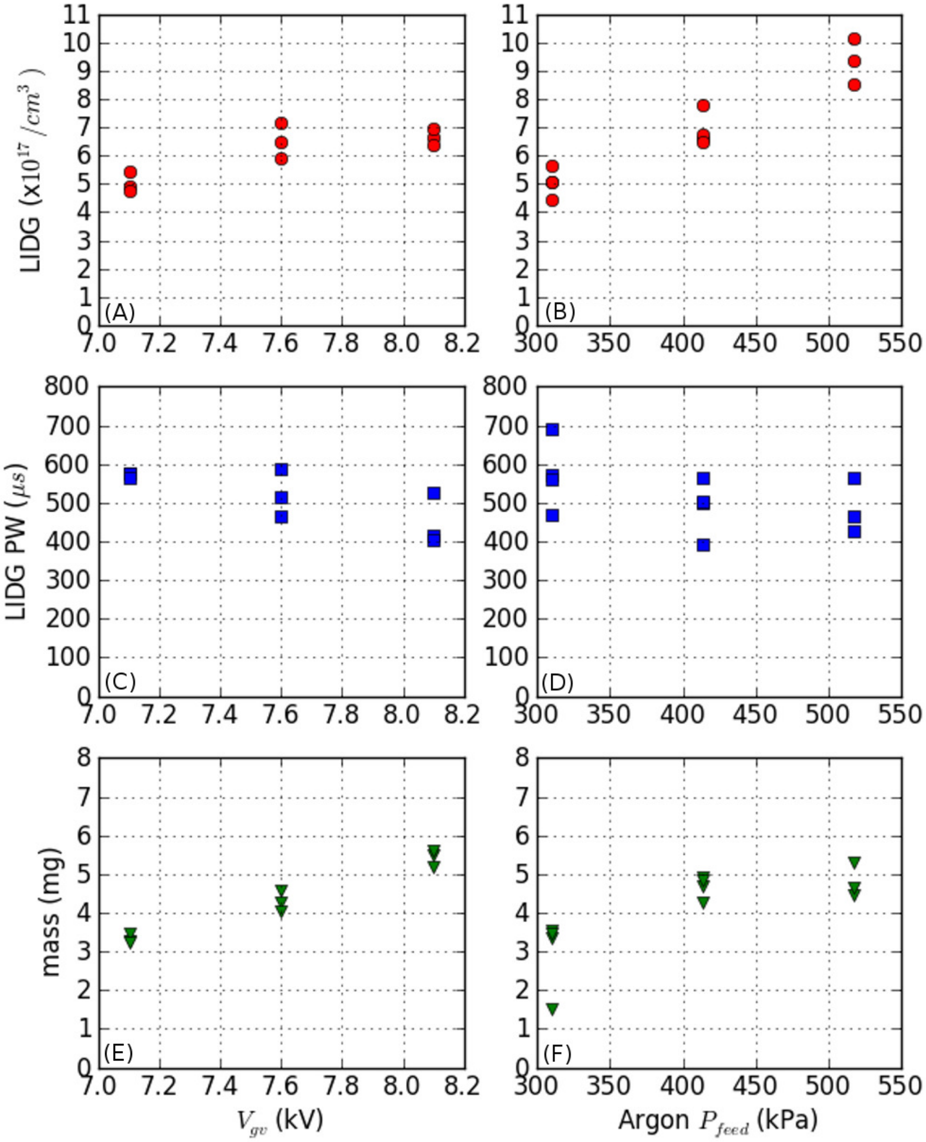

Figure 73 *Gas valve performance was measured via laser deflection to determine the axial line integrated density gradient (LIDG) of injected argon gas profiles. The peak of axial LIDG or maximum axial slope of the incoming line-integrated argon density distribution was found to increase with both increased feed pressure (A) and gas valve bank voltage (B). Meanwhile, the rise time of the incoming line-integrated argon density distribution, indicated by the the width of Axial LIDG pulse, was found to decrease when either gas valve parameter was increased (C and D). The total mass and resultant gas profile in the gun was seen to increase with the gas valve driver current (E) and the feed pressure of neutral gas to be injected (F).*

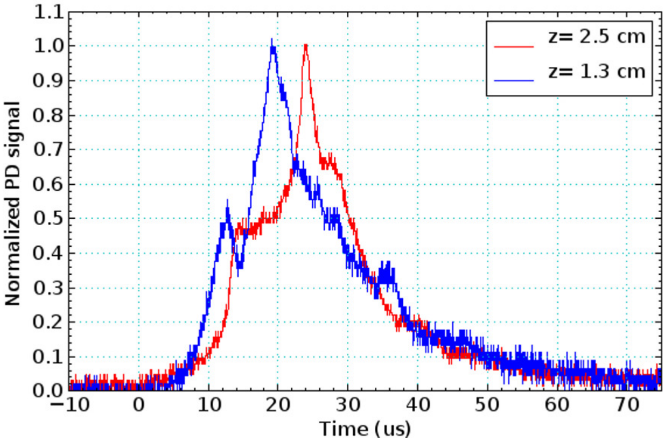

Figure 74 *Pre-ionizer plasma emission profile was observed emerging from the breech at z= 2.5 cm by a pair of photodiodes. Mean plasma velocity estimated from photodiodes over all 19 shots was found to be 2.9 km/s. This implies a pre-ionizer ion temperature of about 3.5 eV.*

Results, shown in Figure 73, indicate the injected mass of argon can be augmented by changing the gas valve feed pressure and driver current. The peak of axial LIDG or maximum axial slope of the incoming line-integrated argon density distribution was found to increase with both increased feed pressure and gas valve bank voltage. Meanwhile, the rise time of the incoming line-integrated argon density distribution, indicated by the the width of Axial LIDG pulse, was found to decrease when either gas valve parameter was increased. The total mass and resultant gas profile in the gun was seen to increase with the gas valve driver current and the feed pressure of neutral gas to be injected. Increasing delay time between the PI and GV triggers would allow a denser portion of the argon profile to diffuse into the pre-ionizer before activation. Delays of several milliseconds would allow the entire bore to be flooded with argon before activation of the remainder of the accelerator.

6.4 Plasma Capillary Pre-Ionizer

The pre-ionization section consist of a ceramic capillary channel with length ℓ and diameter D [98]. The rear end of the capillary channel is capped with an annular electrode of refractory alloys. The bore side of the channel opens directly into the bore with the ground rail of the accelerator section acting as the ground electrode of the pre-ionizer. Gas present at the time of fire is then electrothermally ionized with a current of 10 kA - 20 kA. The capillary dimensions were selected to maintain an ℓ/D ratio of at least 5 in order to prevent current filamentation so that the capillary will act as a cylindrical plasma resistor instead of an arc [97]. Capillary diameter D was set equal to the gas valve diameter d to avoid producing turbulence in the gas valve throat.

The breach-only railgun configuration was also used to evaluate the plasma pulse ejected by the pre-ionizer. A plastic DC break was employed to prevent the pre-ionized plasma armatures from electrically connecting to the vacuum vessel over the shot lifetime. A pair of photodiodes mounted at about z= 2.5 cm were used to measure the ejected pre-ionizer plasma optical emission profiles. An Argon feed pressure p_{feed} of $\sim$ 517 kPa, gas valve voltage V_{gv} = 8.5 kV and a pre-ionizer energy of 1.6 kJ were used to produce emission profiles shown in Figure 74. Mean pre-ionizer plasma velocity estimated from photodiodes over all 19 shots was found to be 2.9 km/s. This implies a pre-ionizer ion temperature of about 3.5 eV. This is consistent with spectroscopic measurements of breach-only plumes which bound temperature at < 5 eV.

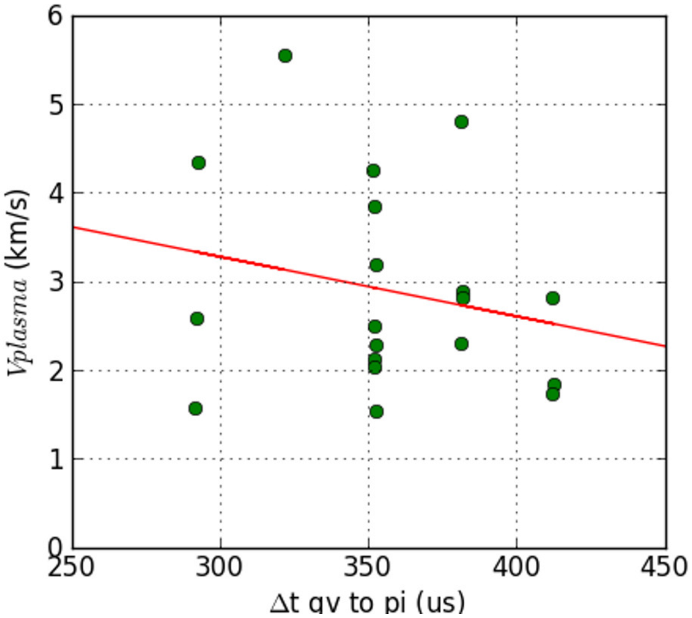

Figure 75 *Pre-ionizer plasma velocity was found to decrease with additional delay between gas valve and pre-ionizer triggers. Since PI energy was held constant for experimentation, the increased the delay allows the total mass of gas to be ionized to increase as the gas profile diffuses further down the axis of the gun.*

Pre-ionizer plasma velocity was found to decrease with additional delay between gas valve and pre-ionizer triggers, shown in Figure 75. This is to be expected as PI energy was held constant for experimentation as the increased the delay allows the total mass of gas to be ionized to increase as the gas profile diffuses further down the z-axis of the gun. Plasma light emission profiles were measured to be about 11.9 μs FWHM in duration. This implies the percentage of the pre-ionizer plasma profile injected into the breach could be adjusted by changing is velocity by changing the delay time between the PI and PFN triggers, t_{pi} and t_{pfn}.

6.5 Accelerator section design

Finally, the acceleration section is comprised chiefly of a 30 cm long bore channel with a 2.5 cm x 2.5 cm square cross-section. Noryl was selected for the shell for its machinability and shock resistance. The acceleration electrodes are on the top and bottom faces, and ceramic insulators comprise the wall faces. Advanced materials were employed because components must withstand the forces and energies necessary to produce 10 kJ plasma jets for PLX. Refractory metal electrodes comprised of 90% tungsten were used as rail electrodes [93] Surface finish and parallelocity were tightly controlled in order to guaranty bore joints could be clamped to seal against plasma leaks. The principle difference in accelerator configurations evaluated was the choice of material employed to seal the triple joints at the ends of the bore and the choice of ceramic comprising the insulators. A complex triple joint seal exists at the breech of the bore where the acceleration section meet the pre-ionizer, and again where the nozzle attaches to the bore. Seals here are paramount as plasma leaks at these locations would allow PFN currents to connect to the vacuum vessel and bypass the bore. It was necessary to add gaskets to prevent plasma leaks. Teflon gaskets were evaluated, but ablated too easily. Viton rubber gaskets are being employed presently. While the ablation of viton is still expected to be a significant source of impurities, viton gaskets are sufficient to seal both bore locations for present 30 - 50 kJ accelerator energy levels.

Linear plasma railguns place extreme demands on their insulators, as they must be an electrically insulating, plasma-facing vacuum component which can withstand both thermal and mechanical shocks from the PFN discharge. Two types of insulators were tested, boron nitride (BN) [118] and Zirconia Toughened Alumina (ZTA) [119]. Boron nitride insulators were used in initial testing ($<$ 250 kA), but proved insufficient for higher current operation as surface layers would flake off chips when PFN bank energy was increased. BN insulators would also occasionally crack and need to be replaced. ZTA proved significantly more durable for operation at currents between 250 and 500 kA, yielding only some chipping at the corners of the block. No flaking of the bulk ZTA surface was observed. Insulator selection is important as ablated rail and insulator materials are expected to be the dominant source of impurities due to the high power densities in the bore of the railgun. The effects of plasma mass accumulation due to ablation can be estimated using a one dimensional model which considers ablation of bore materials.

6.6 Railgun Model with Ablation

The Electromagnetic Gun Circuit Analysis Code (EGCAC) was developed to analyze solid projectile railguns [120]. However, the physics model employed in the EGCAC can be adapted to approximate plasma railgun performance. A plasma slug traveling the length of a railgun bore experiences a change in momentum determined by the Lorentz force, $F_{J\times B}$ from the acceleration current, the ablative drag force, F_a, from energy ablating the walls of the bore, and viscous drag F_d force created by the plasma projectile/armature sliding on the bore walls.

$$m\frac{\partial v_p}{\partial t} = F_{J\times B} - F_a - F_d \tag{13}$$

Given a railgun with rail dimensions of length l, width w, and height h and also rail separation s the driver force $F_{J\times B}$ can be expressed :

$$F_{J\times B} = \frac{1}{2}L'I^2 \tag{14}$$

If $h \ll w$,the inductance per unit length can be modeled as a thin parallel plate wave guide, $L' = \mu_0 s/w$

Next viscous drag is a result of the frictional forces of the plasma sliding in contact with the walls. F_d can be expressed as:

$$F_d = \frac{1}{2}C_f v_p^2 \langle\rho\rangle A_s \tag{15}$$

The area over which a plasma slug of length $\tilde{l}$ is in contact with the wall is $A_s = w\tilde{l} + s\tilde{l}$, and the average density of the plasma is $\langle\rho\rangle = m_p/(ws\tilde{l})$, where m_p is the mass of the plasma projectile. The coefficient of friction has been experimentally determined for a free arc railgun to be C_f=0.003 [121, 122, 123].

Finally the ablative drag can be modeled as the change in total projectile momentum due to mass ablated from the walls m_a of the bore,

$$F_a = v_p\frac{\partial m_a}{\partial t} \tag{16}$$

where the rate of mass ablation was modeled as a linear function of the power dissipated in the bore walls from the acceleration current discharge and from viscous drag.

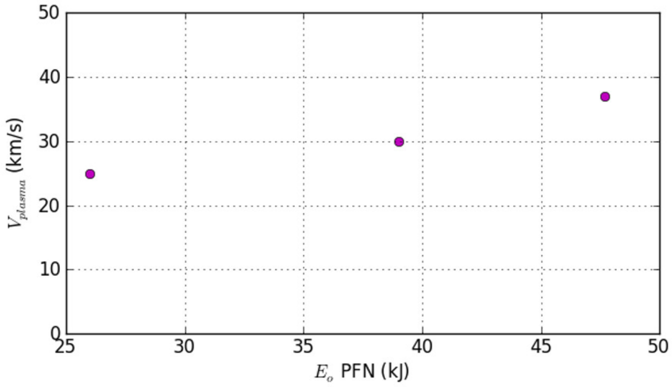

Figure 76 *Accelerator bank energies of 26 kJ, 39 kJ, and 48 kJ were tested. Since PFN inductance was held constant, accelerator pulse duration was also lengthen with each iteration. As PFN banks approach design energy, plasma jet velocity increased.*

$$\frac{\partial m_a}{\partial t} = \frac{k_i + k_r}{2}(2IV + C_f v_p^3 \langle\rho\rangle A_s) \tag{17}$$

k is the ratio of power imparted to the bore walls to mass ejected. k is set by the material properties of the insulator and the rail and k_i from the insulator is not necessarily equal to k_r from the rails.

Combining the above equations, the change momentum of the plasma accelerated by a railgun can be expressed:

$$m\frac{\partial v_p}{\partial t} = \frac{\mu_0}{2}\frac{w}{s}I^2 - 2kIVv_p - \frac{s+w}{sw}2m_pC_f(\frac{v_p^2}{2} + kv_p^4) \tag{18}$$

Eq.(18) implies that any acceleration comes as a result of the driver current, and when the driver current is zero, a non-zero plasma armature velocity will cause the armature to decelerate.

This model predicts a rail bore of our suggested dimensions comprised of boron nitride (k$=.11 \times 10^{11} kg/W$ and HD -17 (k$=.26 \times 10^{11}$ kg/W) driving a 8 mg plasma with 48 kJ should contribute about 0.154 mg of ejected material or a 2% bore impurity contribution. An alternative vector for impurities is ablation of either the viton seals or plastic housing or nozzle which are not considered in this model.

6.7 Railgun Testing

By using different PFN bank capacitances, it was possible to evaluate early versions of the rail gun at lower energies, and then observe railgun performance as accelerator energy was gradually increased. Accelerator bank energies of 26 kJ, 39 kJ, and 48 kJ were tested. Since PFN inductance was held constant, accelerator pulse duration was also lengthened with each iteration. As demonstrated in Figure 76, as PFN banks approach design energy, plasma jet velocity increased.

To test the entire plasma railgun, the complete assembly was mounted and operated so that measurements of plasma jet properties both inside and emerging from the bore could be conducted with various diagnostics. A HyperV plasma railgun, with a LGV3 gas valve, is shown in Figure 78 was mounted on a ~2 meter long cylindrical tank with a radius of about half a meter. This ensured any produced plasma jets would have sufficient volume for free space propagation. As shown in Figure 77, a pair of collimated photodiodes [124] were mounted normal to the axis of travel to

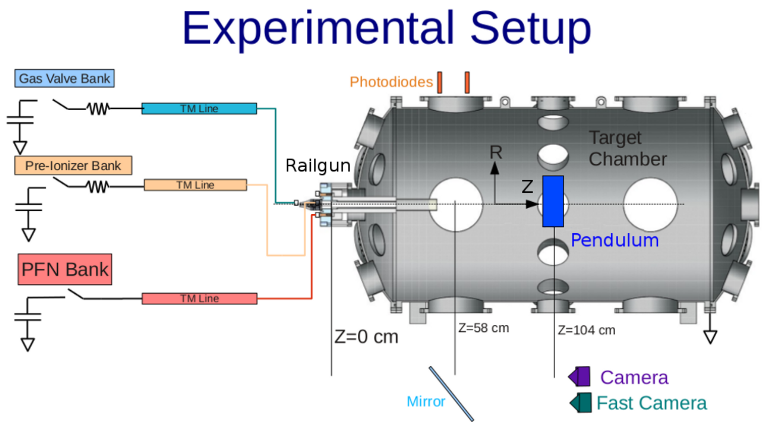

Figure 77 *A 1 cm*^{2} *bore cross-section plasma railgun with 30 cm long rails was fed with a plasma capillary. An array of magnetic field probes recorded the acceleration of the plasma armature. Photodiodes, interferometry spectroscopy and a ballistic pendulum were also used to measure expelled plasma slug*

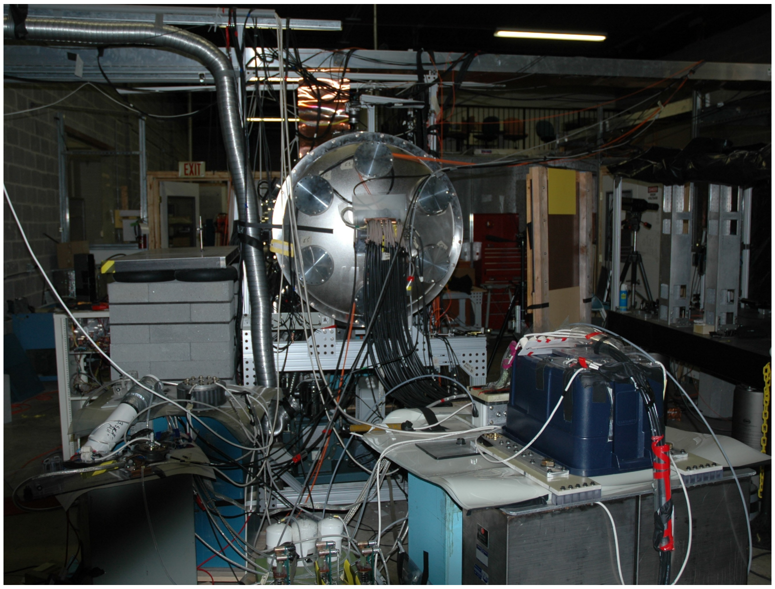

Figure 78 *A HyperV plasma railgun, with a LGV3 gas valve, is shown mounted on an ∼2 meter long cylindrical tank with a radius of about half a meter*

Table 3 *A series RLC lumped element model of HyperV driver circuits can be used to model driver currents. Two gas valve designs were used for testing, LGV3 and LGV5*

System	C(μF)	L(nH)	R(Ω)
LGV3	28	42000	1.4
LGV5	14	15000	1.2
Pre-ionizer	6	3100	1.4
Accelerator	36-141	200-300	0.005-0.010

determine plasma jet emission profile and velocity. An additional set of collimated optics were also deployed to glean spectroscopic measurements of the jet at z$\sim$55 cm, just after it emerges from the railgun nozzle . Fast and slow imaging of plasma jets was recorded with a Princeton Instruments PIMax ICCD camera and Nikon D70s digital SLR. At the center of the chamber, a heterodyne interferometer [71] for measuring line integrated density was used interchangeably with a ballistic pendulum (L_{pend}= 40.6 cm and an effective mass of 0.58 kg) [125] for estimating plasma mass and momentum. By storing the ballistic pendulum on the bottom of the vacuum chamber, the plasma jet flow could be cleared of objects for interferometric measurements. For the railgun itself, a set of magnetic gradient probes were constructed and deployed along the length of the bore to measure the rail current as the armature traversed the accelerator [126]. Rogowski coils were used to measure bank currents. Bank voltage measurements were achieved by placing high wattage resistors in parallel with railgun components and monitoring the resultant currents with Pearson probes.

6.8 Railgun Driver Circuits

Railgun gas valve and pre-ionizer driver circuits were designed to be nearly critically damped LRC circuits to reduce any spurious contributions to armature structure from banks ringing. Both systems are low enough power that high wattage resistor networks [127] can be employed for damping. Power transmission lines for these systems were constructed from RG-8/U cable. A single cable was sufficient for each because each system's inductance was already significantly larger then the contribution from the cable.

Present HyperV railgun designs call for peak accelerator currents of 250 kA to 500 kA and pulse widths as long as 15 μs. As HyperV railguns are primarily an inductive load of 200 - 300 nH, it is necessary to minimize inductance of PFN switches, transmission lines, and the railgun breach itself in order to maximize peak PFN current.

Initial PFN testing was conducted using an annular gas dielectric switch with a single current channel[128], however as PFN driver currents were increased, it became necessary to service these switches more often due to ablation of the switch electrode and switch materials. These single channel switches were also a large contributor to PFN inductance because of their geometry. In order to repeatably generate large currents from a single PFN capacitor bank, a robust, low jitter, low inductance Linear Arrayed Switch (LASW) was designed and constructed for high repeatability and high mean-time-to-repair. The LASW, described in more detail elsewhere, is a compact array of 7 spark gap switch electrode pairs in a single switch housing. By carrying the PFN current on seven current channels in parallel, both the current density on each electrode pair and the inductance contribution from the switch are reduced.

At the quarter and half mega-amp level, PFN circuits are too energetic to provide efficient resistive damping, so as a temporary measure, crowbar switches were employed to shape PFN pulses when necessary. As the railgun is primarily an inductive load, a crowbar switch in parallel with the railgun will act as the dominant channel in the resultant inductive current divider. Thus the inductance of the crowbar circuit must be much less than the inductance of the railgun to be effective. For PFN transmission lines, YK-198 coaxial cable [129] is an ideal choice, but is no longer commercially manufactured. It was possible to build a comparable solution comprised of 30 RG-8/u coaxial lines in parallel. This produced a PFN transmission line with 2.2 nH/m (the equivalent of about 10 YK-198 cables in parallel). Wider arrays are possible, but there exists a limit to the number of cables that can physically be terminated on the back of the plasma railgun. Plus, transmission line cost will scale with both the length and number of cables.

6.9 Experimental Results

Control of the railgun was achieved by varying the delays between the three driver bank triggers, $t_{pi} - t_{gv}$ and $t_{pfn} - t_{pi}$, setting the the argon gas feed pressure p_{feed}, and controlling the three bank voltages V_{gv}, V_{pi}, and V_{pfn}. High purity (Grade 5) Argon was used to feed the gas valve. Gas valve voltages were ranged from 5.0 kV to 5.8 kV and Argon feed pressures were ranged from 300 kPa to 500 kPa to control ejected armature mass. Pre-ionizer delay was used to vary the gas load present in the PI at time of trigger. Similarly, pre-ionizer energy and PFN delay were used to vary the mass of plasma injected into the accelerator. Finally accelerator bank energy was tuned to attempt to eject massive, high velocity plasma jets.

It is necessary to employ a nozzle to collimate the ejected plasma jet [105]. We expect this is because of the fringing field effects at the end of the railgun bore. If the armature current sheet "balloons" while emerging from the bore due to fringing fields, the resultant JxB acceleration from the curved field would amplify the jet expansion angle beyond the normal thermal expansion angle. A straight 19 cm long cylindrical nozzle with an inner diameter of 5 cm was added to improve jet properties. Ejected plasma jets are shown in Figure 79 with and without the nozzle. Both quartz and acrylic nozzles were tested. While quartz nozzle produce cleaner spectroscopic signals, presumably due to less material ablation, the forces produced by operating at the railgun at high power eventually cause present quartz nozzle designs to fail.

A comparison of plasma jet mass, velocity, and momentum achieved for six independent railgun inputs is shown in Figure 80. For these tests, railgun bank capacitance was held at 141 μF in order to increase PFN energy. As shown in Figure 80A, initial tests of the railgun used GV to PI delays as long as 800 μs to achieve high mass armatures via snow plow accumulation of density performed by accelerating the armature though a cloud of neutrals similar to Howard et al. [104] However, while masses well in excess of 8 mg were achieved, velocities remained less then 42 km/s. Presumably this is because in snowplow mode, as the armature traverses the bore, accelerator energy is being spent to ionize argon, while at the same time the remaining length of the bore available for accelerating the armature is decreasing while armature mass is also increasing. Initial experiments also employed high feed pressures to ensure high armature mass. Momentum, mass and velocity were improved considerably (shown in solid red markers) by reducing gas pressure to $\sim$410 kPa and reducing the gas valve trigger delay to allow argon to diffuse no further than about 1 cm into the bore. This combined with increase pre-ionizer energy and PI trigger time resulted in less variance of plasma jet mass as shown in Figure 80(E) and (B). Also as expected, plasma jet momentum increases with peak accelerator current. Early versions of the gas valve were only capable of injecting a few milligrams of gas into the railgun. When the gas valve designs were modified to increase injected mass, it was necessary to increase the pre-ionizer energy as well, in order to minimize the use of accelerator energy to ionize the armature plasma. While the accelerator has significantly more energy than the pre-ionizer banks, the pre-ionizer has higher resistance due to its geometry, and thus couples energy into the plasma more efficiently than the accelerator section. As a result, plasma jet mass and velocity were improved with increased pre-ionizer energy.

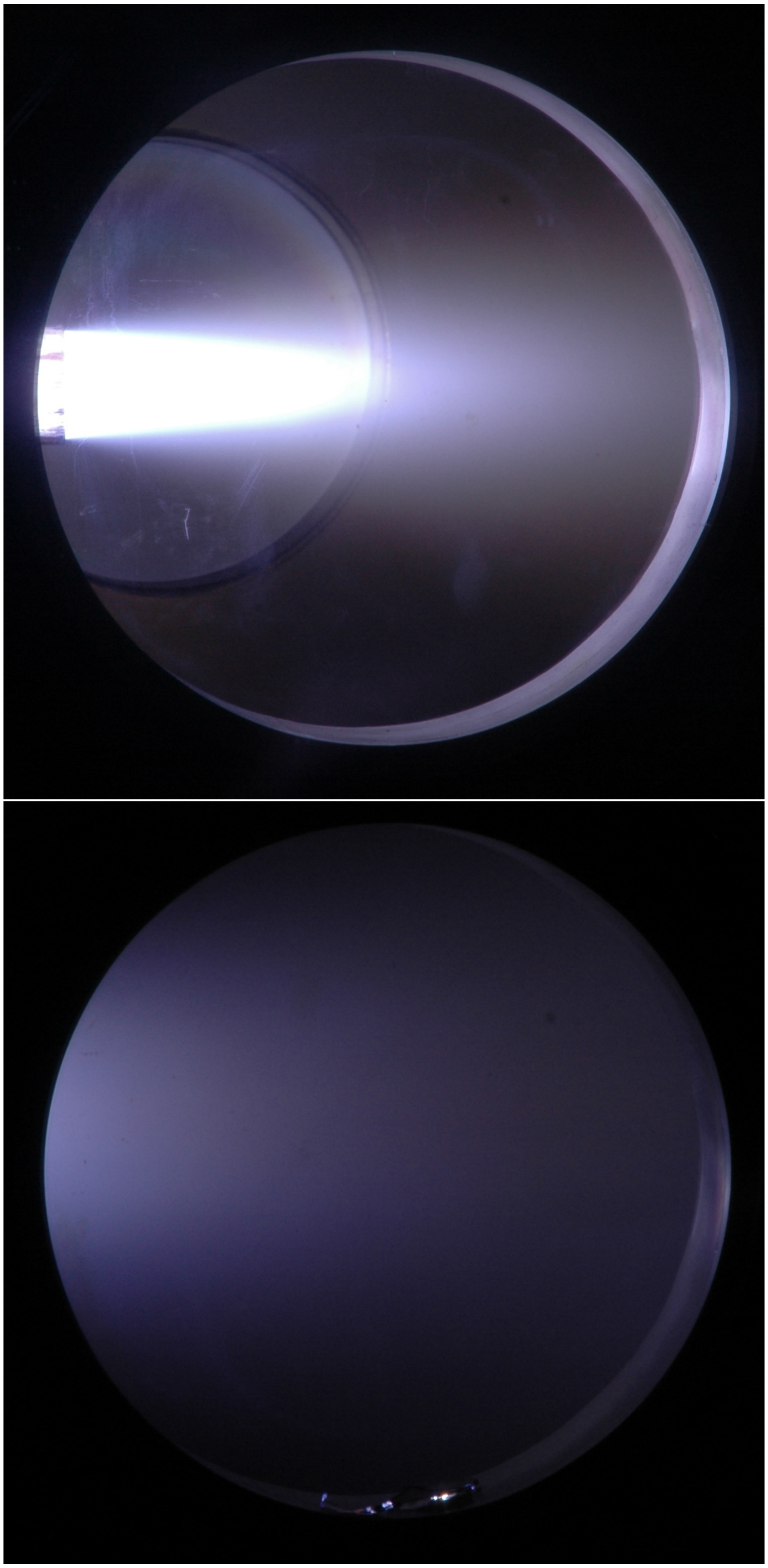

Figure 79 *A straight 19 cm long cylindrical nozzle with an inner diameter of 5 cm was added to improve jet properties. Ejected plasma jets are shown with (A) and without (B) the nozzle. It should be noted that removal of the nozzle moves the point of plume divergence back 19 cm along z (left in the images).*

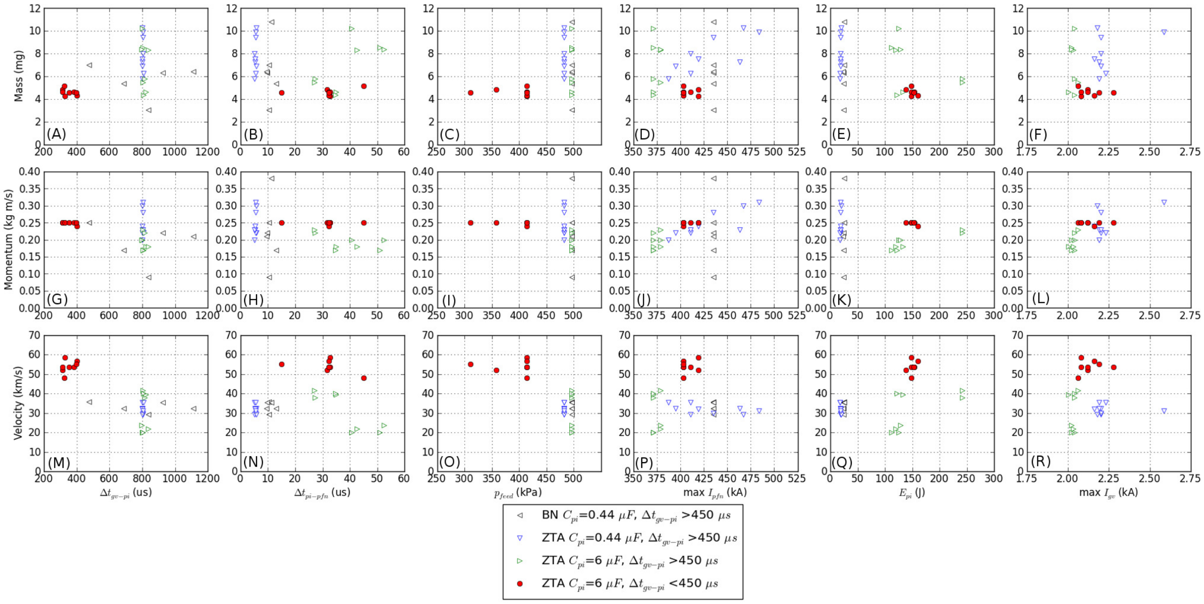

Figure 80 *Initial tests of the railgun used GV to PI delays as long as 800 μs to achieve high mass armatures via snow plow accumulation of density performed by accelerating the armature though a cloud of neutrals similar to Howard et al. [104] Momentum, mass and velocity were improved considerably (shown in solid red markers) by reducing gas pressure to ∼410 kPa and reducing the gas valve trigger delay to allow argon to diffuse no further than about 1 cm into the bore. This combined with increase pre-ionizer energy and PI trigger time resulted in less variance of plasma jet mass (E and B). Plasma jet momentum increases with peak accelerator current. Plasma jet mass and velocity were improved with increased pre-ionizer energy.*

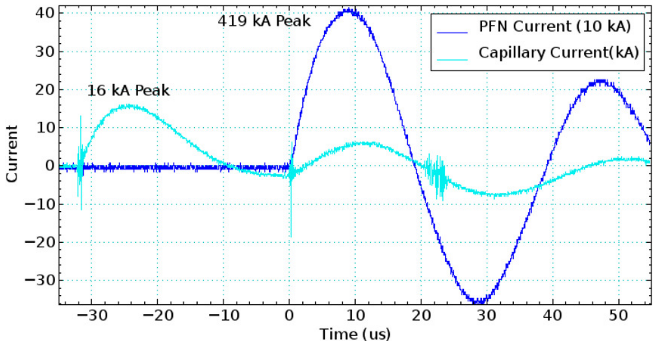

Figure 81 *A PFN voltage of 24 kV produced a 18.5 μs long pulse with a peak current of 419 kA. A 1.6 kJ pre-ionizer pulse was employed. Gas valve (not shown) was driven at 5 kV with a feed pressure of ∼359 kPa*

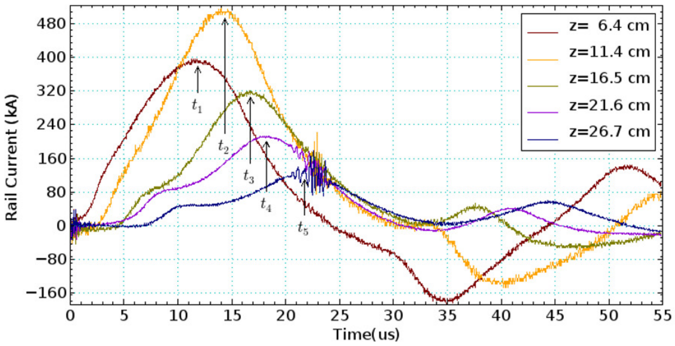

Figure 82 *Magnetic field traces indicate the propagation of an armature*

Sample Railgun driver currents are shown in Figure 81 for a 141 μF PFN driver bank. A PFN voltage of 24 kV produced a 18.5 μs long pulse with a peak current of 419 kA. A 1.6 kJ pre-ionizer pulse was employed, and gas valve was driven at 5 kV with a feed pressure of ∼359 kPa.

Magnetic field traces indicate the propagation of an armature.

Plasma emission profiles were recorded with collimated photodiodes as the plasma emerge form the nozzle. Plasma velocity was measure to be 52 km/s for this shot.

Peak density recorded by interferometry was measured to be $1.8\times10^{17} cm^{-3}$ at z=104 cm based on an estimated path length of 10 cm. Using an assumed top-hat radial density profile, this estimates plasmas mass to be about 4.7 mg. Ejected plasma emission profiles have been observed to be similar to line integrated plasma density profiles.

This is similar to peak density recorded by spectroscopy was measured to be $9.6\times10^{16} cm^{-3}$ at z∼55 cm. Ion temperature of the jet was estimate to be 2-5 eV from spectroscopy as well.

Plasma emission profiles was recorded with collimated photodiodes as the plasma emerge form the nozzle. Plasma velocity was measure to be 58.5 km/s for this shot.

Plasma momentum was measured by a ballistic pendulum to be 0.25 kgm/s for this shot. The two measurements combined allow plasma mass to be estimated as 4.9 mg.

Estimated plasma mass versus velocity for the shot series is shown in Figure 88 The highest mass achieved was 10.7 mg with a velocity of 35.3 km/s. This was also the highest momentum ejected at 0.38 kgm/s.The fastest plasma ejected was **4.3 mg at 58.5 km/s**. The largest mass moving faster than 50 km/s was estimated to be **4.9 mg at 55 km/s**. This was achieved by with

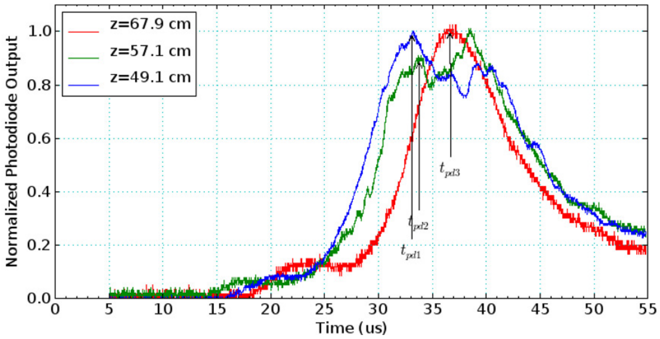

Figure 83 *Photodiode signals of the plasmoid were recorded at two positions. Ejected plasma emission profiles have been observed to be similar to line integrated plasma density profiles.*

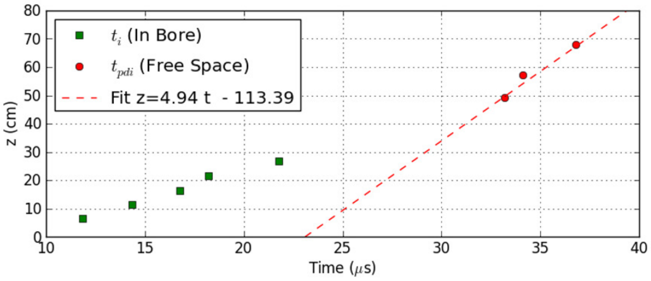

Figure 84 *Time of peak for magnetic and optical signals are shown. fitting optical signals of the plasmoid in free space estimate the velocity as* ~ 49 *km/s.*

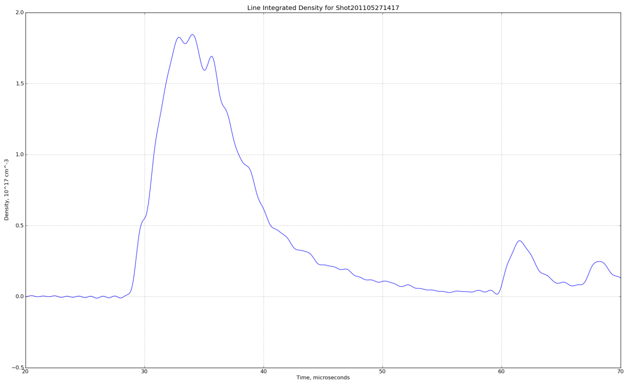

Figure 85 *Peak density recorded by interferometry was measured to be* $1.8{\times}10^{17}\mathrm{cm}^{-3}$ *at z=104 cm based on an estimated path length of 10 cm. Using an assumed top-hat radial density profile, this estimates plasma mass to be about 4.7 mg.*

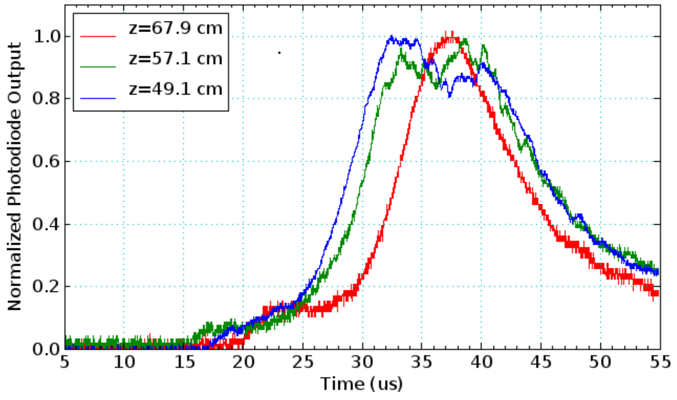

Figure 86 *Plasma emission profiles was recorded with collimated photodiodes as the plasma emerge form the nozzle. Plasma velocity was measure to be 58.5 km/s for this shot*

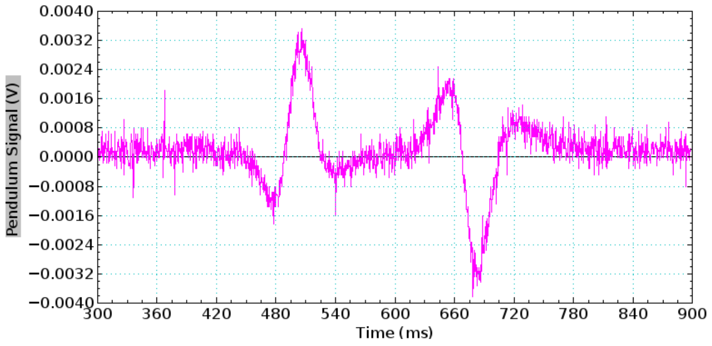

Figure 87 *Plasma momentum was measured a ballistic pendulum to be 0.25 kgm/s for this shot. A plasma with velocity of 58.5 km/s thus yields an estimated plasma mass of 4.9 mg.*

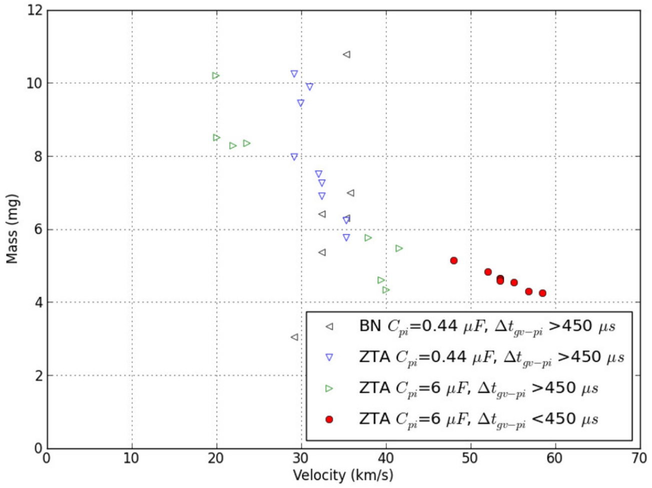

Figure 88 *Estimated plasma mass versus velocity for the shot series. The largest mass moving faster than 50 km/s was estimated to be 4.9 mg at 55 km/s*

parameters V_{gv} = 5.8 kV, V_{pi} = 23.5 kV, V_{pfn} = 25 kV, t_{gv} = -410 μs,t_{pi} = -15 μs, p_{feed} = 331 kPa C_{pi} = 6 and C_{pfn} = 141 μF.

6.10 Conclusions

To summarize, HyperV linear plasma rail guns are already regularly operating with PFN currents of 350-450 kA, and are achieving plasma jets with momentums of 0.38 kgm/s, masses of 4.3 mg to 10.7. and velocities of 35.3 km/s to 58.5 km/s. While additional control refinement is desirable, ejected plasma mass and velocity can already be augmented by adjusting railgun input parameters. The approximated axial location of the lead edge of the neutral gas pulse,and thus the mass of plasma to be ejected, can be adjusted by controlling both the gas pressure and valve driver voltage, or by changing the delay time between gas valve opening and pre-ionizer triggering. The mass, ionization and initial velocity of the plasma armature can be determined by the pre-ionizer settings. Finally the momentum of the ejected plasma jet is controlled by the PFN current profile. So as the gas valve parameters and delay determine the distribution of neutral gas at the time pre-ionizer trigger, similarly the pre-ionizer pulse characteristics and delay between pre-ionizer determine the distribution of plasma armature at the onset of acceleration current.

Testing has determined that refractory rails and advanced ceramics are essential because of the current densities required in the present design to accelerate plasmas. ZTA insulators were demonstrated to be a significantly better choice of material for 500 kA operation. Nozzles were also determined to be essential to produce the desired jet properties.

Present linear gas valve designs use a weak return spring for closing. Employing a stiffer spring may improve gas valve characteristics. The present design also has a large of portion of spurious inductance in the breach/gas valve area. Reducing the inductance contribution from this region should also improve plasma jet performance as PFN current is increased.

7 PLX Experiment

7.1 Introduction

The Plasma Liner Experiment (PLX) was originally a four-year collaborative project to generate and study cm-, μs-, and Mbar-scale plasmas formed by spherically imploding plasma liners. The liners were to be formed by merging 30 high velocity plasma jets launched from the periphery of a nine foot diameter spherical vacuum chamber (see Figure 89). The other collaborators were Los Alamos National Laboratory, University of Alabama at Huntsville, and the University of New Mexico. This project was a new start for the other collaborators, but was a renewal effort for HyperV. Los Alamos National Laboratory acted as the lead team member and hosted the PLX facility. There were some significant delays in getting funding started due to a requirement to go through peer review of the proposal a second time after the initial award was announced. The original award was subsequently confirmed after this re-review and the program work began. However, a year and a half into the four year project, the team was required to recompete the effort in mid-stream due to changes in the timing and frequency of OFES solicitation funding cycles. Unfortunately, this time the recompeted proposal was not selected for award and project funding was terminated after only two years. Despite the loss of funding, the team was able to accomplish a great deal. The HyperV part of that effort is detailed in this report.

7.2 Motivations

Two key motivations for this project are to: (1) enable a unique, cost-effective approach for generating cm-, μs-, and Mbar-scale plasmas suitable for fundamental HEDLP studies, and (2) form spherically imploding plasma liners suitable as a standoff driver [Thio, 1999] for magneto-inertial fusion (MIF) [Lindemuth, 1983]. This project was concerned mainly with exploring and establishing the performance scaling of a converging array of plasma jets for reaching Mbar pressures, and developing a predictive understanding of scientific issues underlying imploding liner formation, convergence, stagnation, and disassembly.

As it becomes evident that achieving ignition on the National Ignition Facility (NIF) is very difficult, a compelling case can be made to bolster our understanding of HEDLP which underlies inertial fusion energy (IFE) science. At present, HEDLP studies are conducted in the U.S. mostly on intermediate and large scale laser (*e.g.*, Jupiter, Trident, Omega) and pulsed power (*e.g.*, ZEBRA, COBRA, Z) facilities. Our hope and intention was to add a unique and complementary facility (PLX) for investigating fundamental HEDLP science. PLX offers a unique, cost-effective method for repetitively generating HED plasmas with larger spatial (order 1–10 cm) and longer temporal (order 1–10 μs) scales by a factor of 10–1000 over those generated by other HEDLP facilities. This increases the possibility for more detailed diagnosis of more physical quantities, which is needed for constraining and validating computer codes and ultimately for advancing HEDLP and IFE science. In addition, based on the first month of PLX experimental operations with one gun, it was found that more than 50 shots could be fired per run-day. Although this number would likely decrease for larger numbers of guns, PLX would still nevertheless be able to generate many more shots and data than most if not all other HEDLP facilities. A large number of shots providing plentiful statistics for data analysis is extremely valuable and essential for maturing the knowledge base of HEDLP and IFE.

PLX was also originally motivated by a desire to explore a standoff driver concept [Thio, 1999] for magneto-inertial fusion (MIF) [Lindemuth, 1983], which is a class of pulsed fusion approaches that utilizes a strong magnetic field in the fusing fuel to reduce thermal transport and enhance α-particle energy deposition. The strong field enables a reduced ρR threshold for fusion ignition

[Basko, 2000] and therefore requires lower implosion velocities (10–100 km/s) compared to pure inertial confinement fusion (ICF) (> 300 km/s). Recently, a magnetized laser-driven ICF target showed evidence of increased temperature and neutron yield [Chang, 2011]. At reduced ρR, lower required implosion velocity enables the use of efficient pulsed power drivers, in our case pulsed plasma jets. The high electrical to jet-kinetic-energy conversion efficiency (~ 0.5) allows the fusion energy gain for MIF to be as low as 20 and still be a viable IFE concept (requiring gain-efficiency product > 10). Eloquent arguments are made in support of exploring MIF as a relatively low-cost approach to fusion in [Lindemuth, 2009]. The PJMIF standoff driver concept uses a spherically imploding plasma liner formed via merging plasma jets to compress magnetized plasmas to fusion conditions [Thio, 1999; Hsu, 2011]. Most other MIF approaches such as Magnetized Target Fusion (MTF) [Kirkpatrick, 1995; Intrator, 2008] and MagLIF [Slutz, 2010] use pulsed power facilities to compress solid cylindrical liners which in turn compress magnetized plasma to fusion conditions. The use of solid material liners necessitate the repetitive destruction of both the liner and parts of the pulsed power transmission line, something that plasma liner driven MIF avoids. Privately funded General Fusion’s proposed MIF scheme attempts to solve the standoff problem by using spherically convergent acoustic shocks in a liquid metal to accomplish the compression of the magnetized plasma target [Laberge, 2009]. The liquid metal then doubles as the neutron shield and the tritium breeding

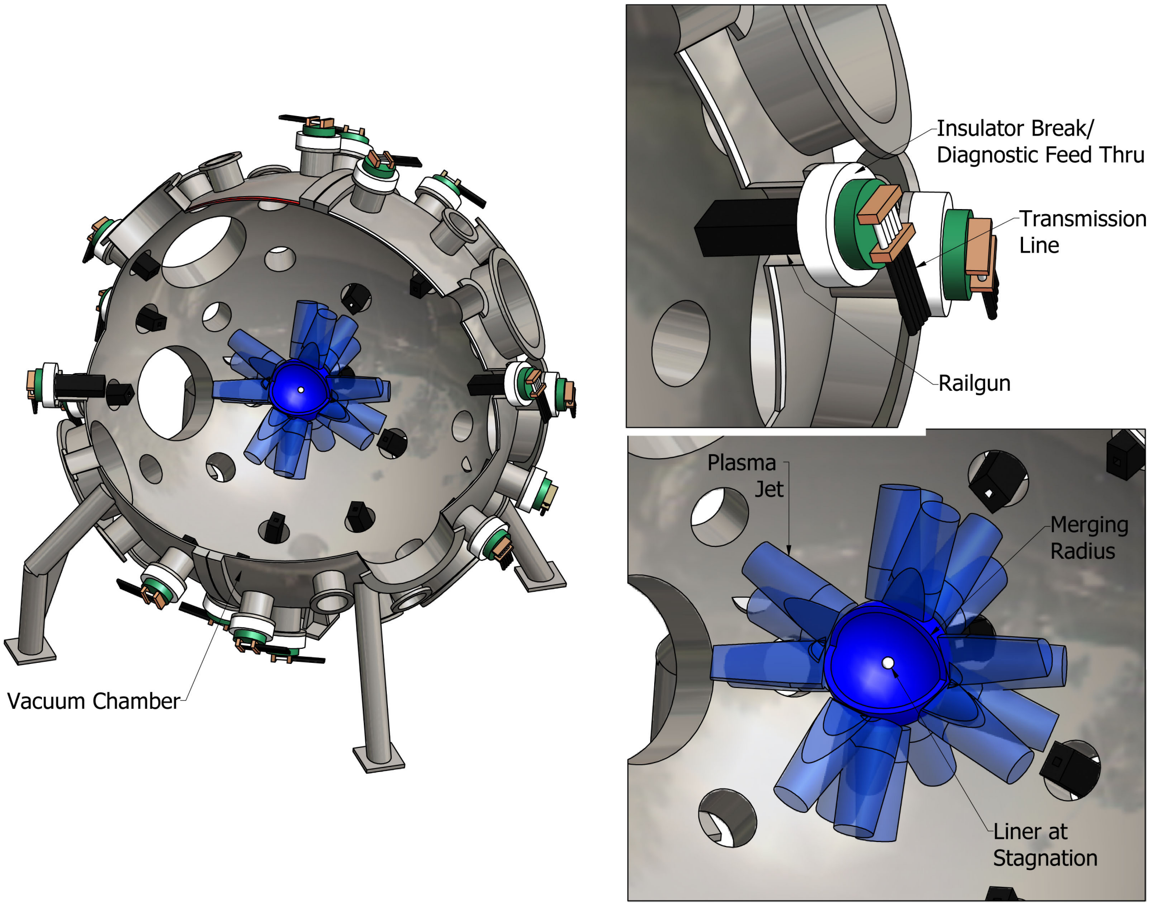

Figure 89 *Schematic of spherically imploding plasma liner formed by merging plasma jets: (left) 30 plasma guns arranged around a 9’ diameter vacuum chamber; (right, top) plasma railguns and transmission lines; and (right, bottom) jets merging and, later in time, the stagnated liner resulting in a cm-, μs-, and Mbar scale plasma.*

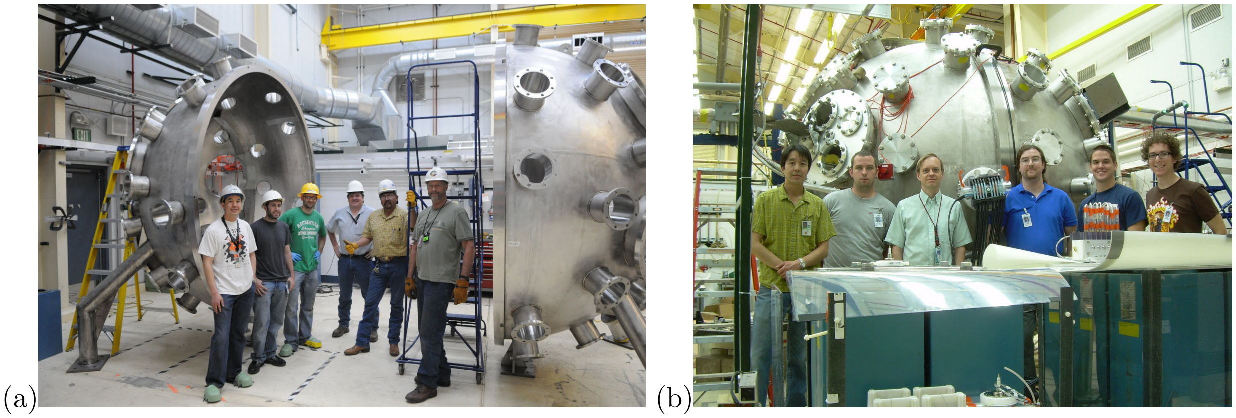

Figure 90 *(a) Photo (taken 5/26/10) of cleaned chamber halves just prior to assembly back into a sphere; (b) photo (taken 7/13/11) of capacitor banks (foreground) and the first installed gun (center, between team members).*

blanket. We envision plasma liner driven MIF to also use a liquid first wall and blanket.

7.3 PLX facility construction at LANL

Starting in Sep. 2009 (with the benefit of ∼\$60k of LANL funds), LANL personnel transformed a 5000 sq.ft. high bay from being filled with unused equipment into the operational PLX facility (see Figure 91), where first plasma gun firing occurred on Sep. 13, 2011. Riggers moved out a 6000 lb. vacuum chamber (used for CTX spheromak experiments in the 1980's) and many magnet coils weighing 2000 lb. apiece to make way for the arrival (Apr. 2010) of the 9' diameter spherical vacuum chamber (also around 6000 lb.) that is being loaned to the project from NASA Marshall Space Flight Center (MSFC). The vacuum chamber, worth \$2M (and fortunately made of stainless steel), had been sitting outside in a field at MSFC for many years. It was quite dirty with remnants of a bee hive inside. It was disassembled into its two hemi-spherical halves for shipping, which made it easier to scrub and clean. All the flanges were missing, requiring us to design/procure ∼ 100 separate flanges and windows.

Much of the spring/summer of 2010 was spent specifying, designing, and procuring hardware including vacuum components and pumps, high-voltage power supplies, and computer and control hardware. Starting in Aug. 2010 LANL began building all the supporting hardware/software systems needed for the operation of a complex plasma physics experiment, including: (1) a Labview-based control system using software and FPGA (field programmable gate array) to control shot sequence operations, send precise timing triggers, monitor all hardware systems, and operate engineered safety interlocks, (2) an oil-free vacuum pumping system anchored by a 3200 liter/sec turbomolecular pump with remote pressure monitoring and control, (3) an electromagnetically shielded "screen cage" for housing all the control and data acquisition electronics, (4) electronics for sending and receiving optical and electrical signals for control and instrument triggering, (5) diagnostic systems including an eight-chord interferometer, a survey spectroscopy system, a mount for a fast framing camera, and a photodiode array, (6) a CAMAC based digital data acquisition system with 100+ 1 MHz-10 bit and 64 40 Mhz-12 bit channels, and (7) an MDSplus (`http://mdsplus.org`) based data storage/server system. HyperV assisted in many of these tasks by providing CAD design and layout of facility systems, and advice on various hardware subsystems.

LANL achieved a base vacuum pressure in the high μTorr range on their first pump-down in Feb. 2011, and ran routinely with base pressures in the mid-10^{-7} Torr range (surpassing the goal

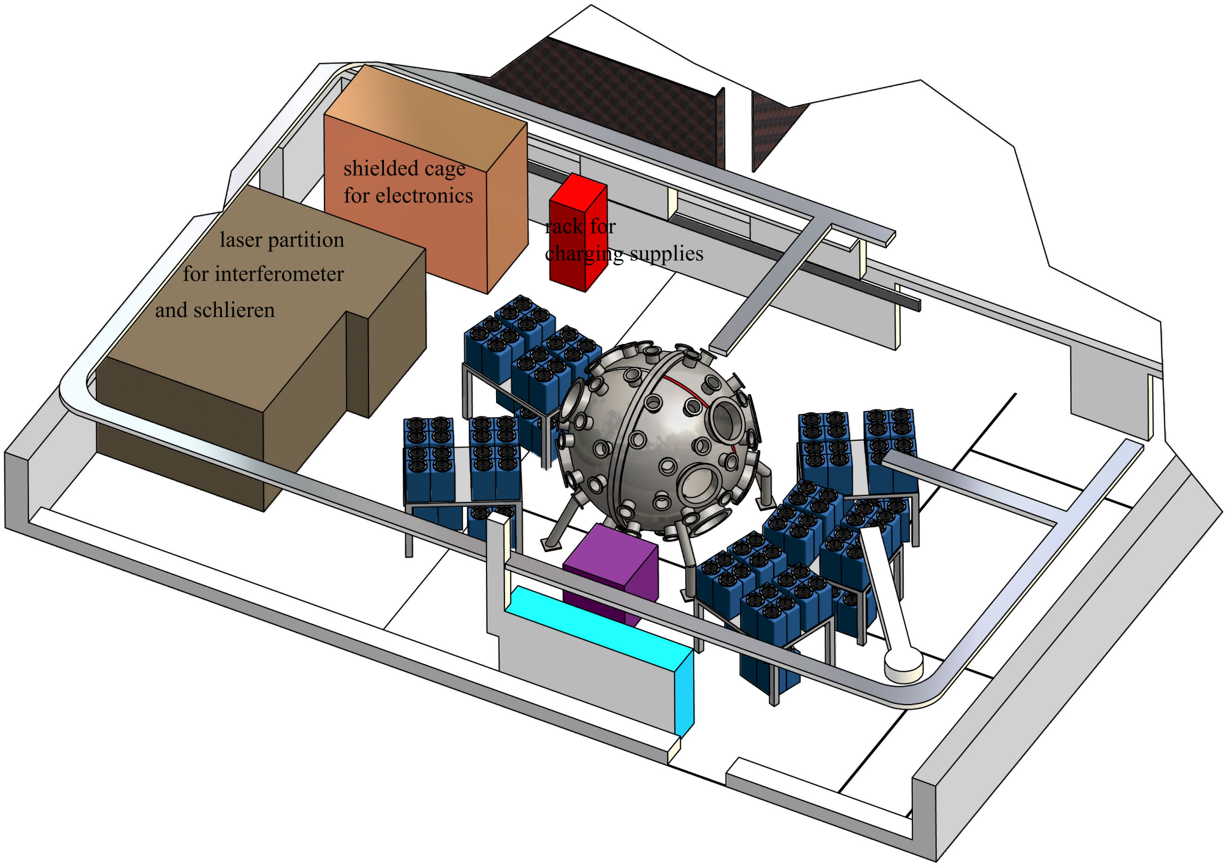

Figure 91 *Layout of the PLX facility showing planned capacitor banks for 30 guns.*

of low μTorr). With assistance from HyperV, LANL completed assembly of the capacitor banks, main bank (36 μF, 60 kV), gas valve bank (24 μF, 20 kV), pre-ionization (PI) bank (0.8 μF, 30 kV), for the first plasma gun in Jun. 2011, installed the first plasma gun in Jul. 2011, and fired it for the first time on Sep. 13, 2011, with several operational diagnostics including gun voltage and current, an eight-chord interferometer, a survey spectroscopy system, a fast-framing CCD camera, and a photodiode array. The plasma guns, switches, triggering, and pfn hardware were supplied by HypeerV and installed and tested with our assistance on site.

Two HyperV Mark1 plasma guns were eventually installed on the PLX chamber. Figure 96 further below shows one of the Mark1 guns viewed from inside the vacuum chamber. Figure 97 shows the gun from outside the chamber. These guns were used for single jet and two jet experiments. Detailed discussions of the single jet and two jet propagation experiments on the PLX experiment have been presented elsewhere and are not repeated here. We refer the reader to a number of publications in the literature [130, 131, 132, 133].

7.4 Single jet propagation experiments on PLX

The key practical issues in forming a plasma liner from many jets are (1) developing a validated predictive capability for modeling the evolution of the jet's density, temperature, velocity, and ionization state as it propagates from the chamber wall to the merging radius R_m, (2) evaluating the jet's radial and axial profiles to allow for more accurate simulations and to determine the importance of profile effects, and (3) determining whether any unforeseen phenomena (*e.g.*, filamentation or other jet structure/dynamics) could adversely affect plasma liner formation and implosion.

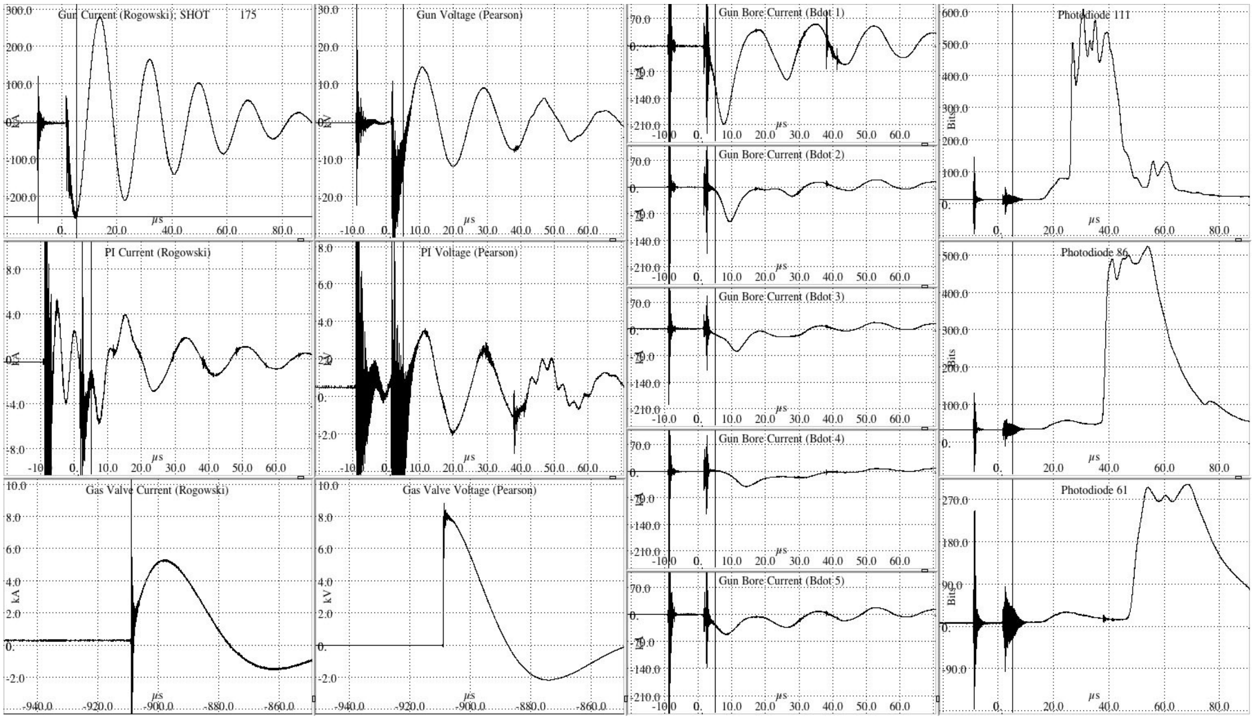

Figure 92 *Representative shot data for Shot 175 (taken 10/26/11). Voltages (kV) and currents (kA) for the capacitor banks, 5 B-dot signals yielding gun current (kA) along the gun rails, and three photodiode signals (counts) are monitored to evaluate gun performance on every shot. (Data courtesy of Scott Hsu, LANL.)*

Many hundreds of shots were fired on PLX during the course of two years. The main experimental diagnostics, including gun/bank measurements (Figure 92), multi-chord interferometry [Merritt, 2011] (Figure 93a), photodiode array (Figure 93b), spectroscopy (Figure 93c), and a fast-framing CCD camera (Figure 94), are all yielding good data. Shot-to-shot reproducibility is excellent. The primary strategy was to make detailed comparisons between experimental and simulated diagnostic data from numerical modeling. Independently funded colllaborators Far-Tech, Prism Computational Sciences, Tech-X Corp., and Voss Scientific generated simulated interferometer and spectral data. The LSP [Thoma, 2011] and Nautilus [Loverich, 2010] codes were used to simulate single jet propagation and two jet merging using a two-fluid model, and Spect3D from Prism (`http://prism-cs.com`) was used to post-process the simulation output to generate simulated atomic spectra.

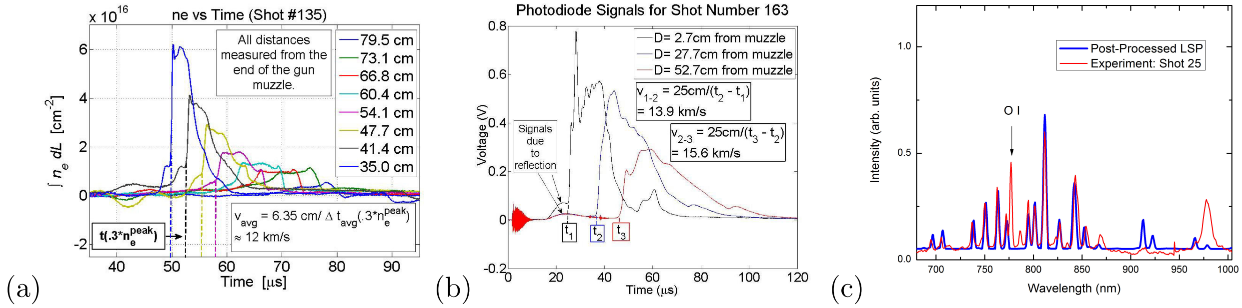

Figure 93 *(a) Line-integrated (across plasma jet) electron density from all eight channels of the interferometer, showing density decay during jet propagation and estimated jet velocity of 12 km/s. (b) Photodiode array data (looking perpendicular to the jet propagation direction at the distances indicated) yielding jet velocity of 14–15 km/s. (c) Preliminary comparison of experimental spectroscopy data against simulated spectra obtained by using Spect3D to post-process an LSP simulation of jet propagation with expected jet parameters. (Simulated spectral data courtesy of J. MacFarlane of Prism Computational Sciences and C. Thoma of Voss Scientific.)*

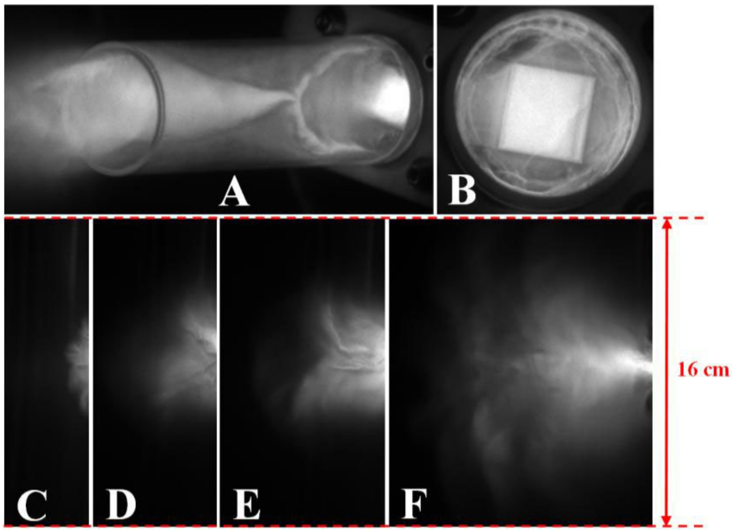

Figure 94 *Gated visible light images of argon/impurity plasma jets on PLX obtained with a DiCam PRO iCCD w/70–300 mm lens. (A) view through gun nozzle ($t = 38.7$ μs, 20 ns gate); (B) view down gun bore ($t = 16.5$ μs, 3 ns gate); (C)–(F) jet propagating beyond nozzle, which is to right of fields-of-view; (C) $t = 29$ μs, 20 ns gate, $v_{jet} \sim 11$ km/s; (D) $t = 29$ μs, 20 ns gate, $v_{jet} \sim 19$ km/s; (E) $t = 28.7$ μs, $v_{jet} \sim 21$ km/s; (F) $t = 39$ μs, $v_{\rm jet} \sim 11$ km/s (all times relative to gun current initiation, and v_{jet} derived from photodiode array data). (Photos courtesy of Scott Hsu, LANL.)*

7.5 Plasma gun and pulsed power development

We largely met the gun milestones of the first two years of our original project. We built and tested a series of plasma guns at HyperV, including improved fast gas valves, pre-ionizers (PI), high current sparkgap switches, and control and triggering systems. We also fabricated, tested, and delivered the first one inch bore gun and its associated hardware to LANL, and subsequently assisted installing the gun on PLX and successfully performing the first test firings. A second gun was installed in 2011.

7.6 Plasma gun design

The rails are constructed from a machinable 90% tungsten alloy. The rails are brazed to a copper electrode for connection to the capacitor bank circuit. The insulators are currently acquired as one inch square boron nitride (BN) rods 12” long. Although these have worked fine at lower currents and pressures, we have seen some breakage and surface degradation of the BN above about 400 kA. We are therefore transitioned to much stronger ceramic insulators for the 30 gun array. We have just started testing zirconium strengthened aluminum oxide, and plan to test high purity aluminum oxide and silicon nitride in the future. Silicon nitride is the best, but more expensive, so we hope to use the less expensive ceramics first. The body of the railgun structure was originally fabricated using Delrin plastic. As the currents and forces increased, we have since transitioned to using Noryl which is a stronger plastic, and we have also incorporated various stress reducing machining features to avoid breakage at high current. We may ultimately use G-10, but are trying to avoid the higher cost of that unless necessary.

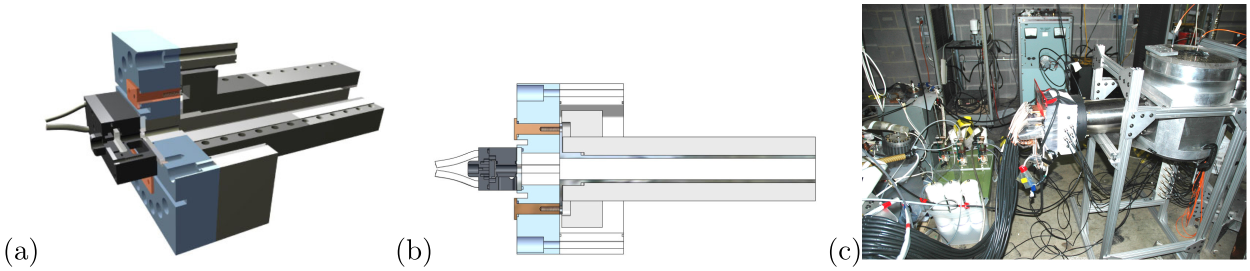
(a) (b) (c)

Figure 95 *(a) 3D drawing of the one inch square bore minirailgun. (b) Side view of the gun shows internal structure, gas valve, and pre-ionizer capillary. (c) Side photo of the gun mounted on the octagon vacuum facility for testing, with > 400 kA current fed via a bundle of RG-8 coaxial cables.*

The minirailgun barrel structure is mounted to a (white) breech block which contains all the necessary features for holding leads and the PI and gas valve assemblies. There is also an integral insulator standoff locally isolating the gun ground from the vacuum tank to avoid ground loops. The insulator also provides a mount for B-dot probes (Figure 95c). The fast gas valve has evolved from a single coaxially-mounted coil design with a circular disk flyer plate [Witherspoon, 2009; Witherspoon, 2010] to a double coil and rectangular flyer plate design (Figure 98a). The change in design approach was driven by the need for more robust operation, easier assembly, longer life, and better performance. The present design will be further improved in lifetime and reliability.

Argon gas under few atm pressure is admitted by the gas valve in a few hundred μs through the PI, which consists of a thick-walled BN tube with electrodes at each end. Once admitted, a short current pulse through the gas in the PI heats and ionizes the gas which is then injected as a plasma into the railgun bore at 1–2 km/s. After a short adjustable delay, the main bank fires to accelerate the plasma armature out the end of the gun. We typically use a tubular transparent plastic nozzle at the gun exit to help confine/direct the plasma jet Figure 96. The gun ground rail also acts as one electrode of the PI.

All of the PLX experiments were performed with the Mark1 plasma gun. Figure 96 shows an inside view of one of the Mark1 guns mounted on the PLX vacuum chamber. Figure 97 shows the corresponding outside views of the same gun. The RG/8 current feed cables can be seen with the light blue insulation.

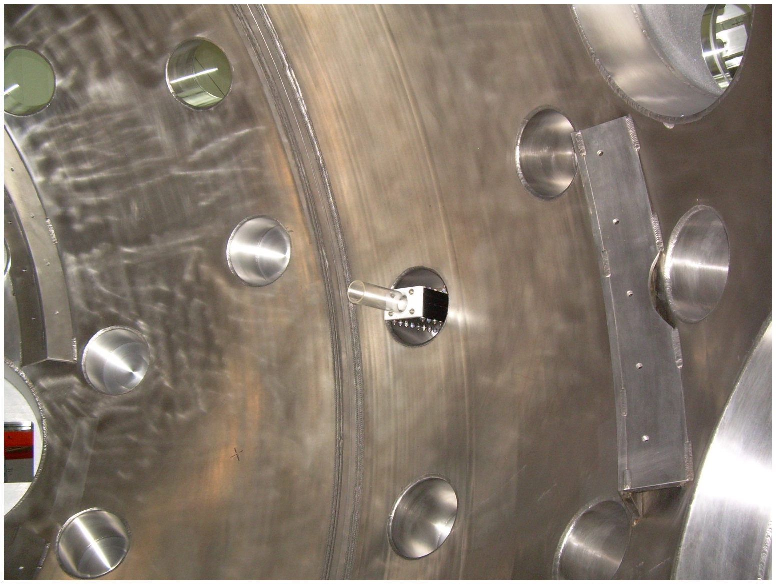

Figure 96 *Inside view of a Mark1 plasma gun installed on the PLX nine foot diameter vacuum tank.*

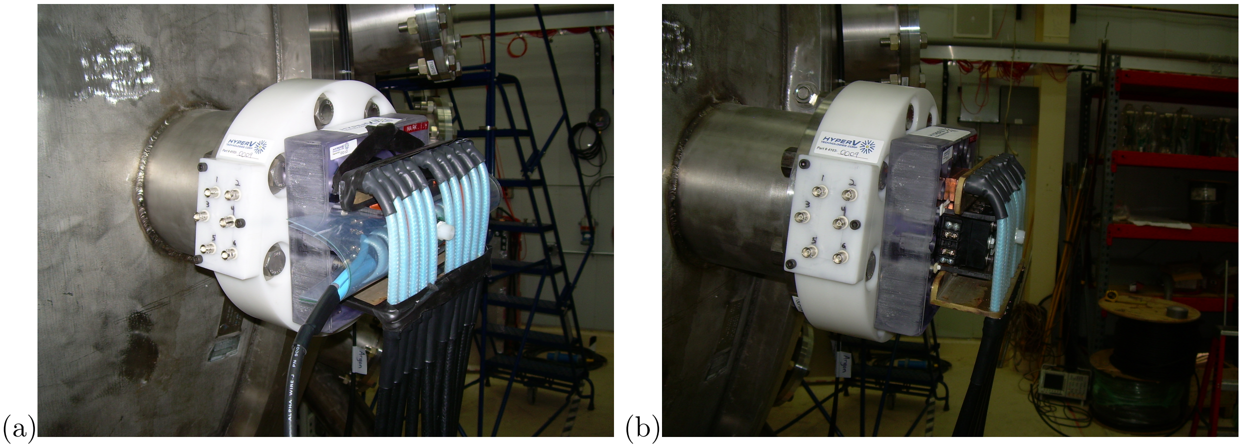

(a) (b)

Figure 97 *Two ouside views of a Mark1 plasma gun installed on the PLX nine foot diameter vacuum tank.*

7.7 Pulsed power components

Pulse forming network (pfn): The baseline design (Figure 98b) consists of six 6 μF, 60 kV capacitors lumped together as one single effective capacitance connected to the switch and gun load.

Linear spark gap switch: The sparkgap switch designs have also gone through several iterations as we learned how to make sparkgap switches that could survive the several hundred kA current pulses, and still be sufficiently inexpensive to fabricate for the 30 gun experiment. We began with a coaxial switch design [Brockington, 2010] which was successfully tested all the way to 1 MA, and which then evolved into the linear array sparkgap switch shown in Figs. 98b and 98c. The linear switch turns out to be more robust mechanically, is considerably cheaper to fabricate, is much more easily integrated into the pfn plate and transmission line structures, and provides lower inductance. The latter is critical for minimizing the operating voltage and current ringing.

Transmission lines: We used bundles of coaxial cables for the transmission lines from the pfn to the gun. This provides a flexible low inductance solution at modest cost. Although we use RG-8 cable bundles for all current testing, we planned to transition to even lower inductance custom made cables for the 30 gun array on PLX to allow us to locate the capacitor banks a little farther away from the chamber for easier access to guns and diagnostics.

High voltage circuit: The high voltage circuit has been simplified from the original concept. We now operate all the gas valve coils off of a single pfn and switch per group. We also operate the PIs from a single switch and pfn per group. This approach reduces the number of switches and pfn's required for a 30 gun system, thus reducing cost and complexity.

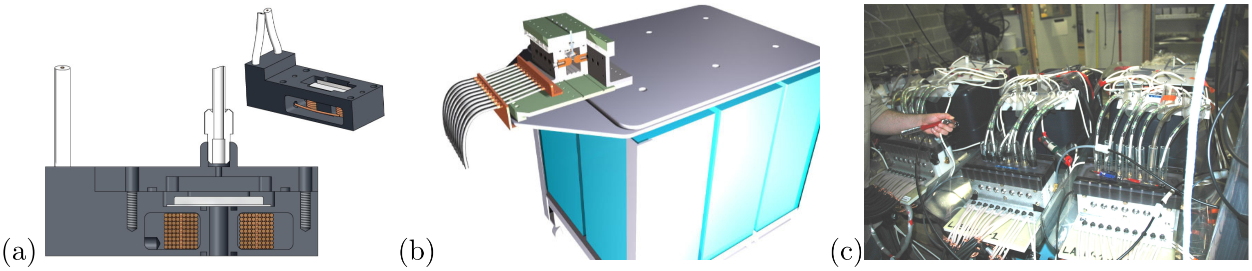

Figure 98 *(a) Fast gas valve which is mounted at the entrance to the PI as shown earlier in Figure 95a. (b) LANL's 36 μF capacitor bank and cutaway view of the linear sparkgap (insulating mylar between plates not shown for clarity). (c) Three linear sparkgap switches for the three gun merge tests at HyperV. Bottom cables are the transmission lines, and top cables are for switch triggering.*

8 Plasma Jet Merge Experiments at HyperV

8.1 Recap of Three Jet Merging Experiments

The merging of high speed plasma jets is of interest both for fundamental physics studies such as laboratory models of astrophysical jets and for better understanding of the dynamics of plasma liners as compression drivers for magneto-inertial fusion[1, 6, 13, 134, 135, 8]. HyperV Technologies is developing devices capable of generating supersonic plasma jets, both advanced coaxial accelerators[48] and Minirailguns [105] capable of accelerating large plasma masses to velocities of tens of kilometers per second. The devices used in this series of experiments are one centimeter bore Minirailguns operating at reduced capacity compared to what can be achieved. This was done in order to guarantee large numbers of shots without significant stress on system components.

Experimental Arrangement The experimental arrangement is shown in Figure 99. The port geometry of the end flanges of the vacuum chamber replicates the port geometry of a portion of the spherical PLX vacuum chamber[13]. Three Minirailguns are placed at the corners of an equilateral triangle, aimed at the center of the chamber. The angle between any pair of guns is 37.9 degrees. The Minirailguns were aligned using a small laser held in a fixture which fit tightly in the nozzle of the gun. A target was placed at the intended convergence point and the laser was aimed at it. The guns were aligned so that the laser spot lay within a 1 cm diameter spot on the center of the vacuum chamber.

The Minirailguns are variants of those described in reference [105], with a 1 cm square bore instead of 2.54 cm. The operating regime chosen was well below the maximum performance of the guns in order to ease stresses on the guns, switches, and capacitor banks. The MiniRailgun consists of three subsystems: a fast gas valve, a pre-ionizer, and a pair of tungsten alloy rails with boron nitride insulators holding them at 1 cm separation. An arc is drawn between the rails to drive a plasma armature down the length of the gun and into the nozzle. The gas valves are a custom design which permits large masses ($\gg$ 10 mg) of gas to be dispensed in a short time ($\approx 400\ \mu s$). All three gas valves are driven in parallel by a single 84 μF capacitor bank operating at 8.5 kV and driving a current of 8 kA per valve. A ballast resistance of 0.6 Ω damped the current so as to avoid multiple openings of the valve. The pre-ionizers were driven in parallel by a 1.2 μF bank charged to 30 kV, with 2.2 Ω ballast resistance per pre-ionizer. The Minirailguns were each driven by a 51 μF capacitor bank switched by a low inductance custom switch consisting of seven pairs of electrode knobs in a linear array. Each pair of electrodes was triggered independently by a separate trigger pin. The pins were switched using a trigger fanout that triggered all pins on all switches simultaneously using a Titan 40264 spark gap switch. The Rail PFNs were charged to 22 kV and typically drove a peak current of 180 kA.

A pair of fiber coupled photodiodes is used to measure initial plasma velocity by focusing collimating optics on the nozzle of one of the guns. An interferometer chord passes transversely through the chamber on center. Two spectrometer chords view the center of the chamber, one at a right angle to the axis, and one at 22 degrees off-axis, looking towards the guns. In addition, there is a 12 channel fast photodiode array viewing the merge region at the center of the chamber. This array consists of a line of fibers at the focal plane of an SLR camera, coupled to fast detection electronics in the screened control room.

In order to characterize individual gun performance the pulse forming networks of two guns were disconnected and the remaining single gun fired while being monitored by the diagnostics. The main parameter of interest was the arrival time of the plasmoid at the center of the tank. This varied by about 1 μs per gun, compared to a total plasmoid transit time through the merge point

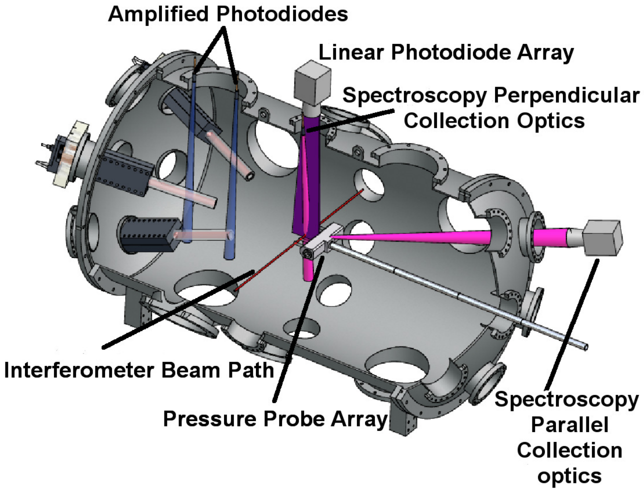

Figure 99 *Layout of the Mini Railguns and diagnostics on the vacuum chamber*

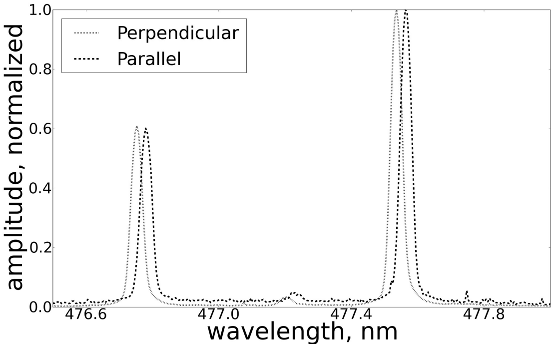

Figure 100 *Spectra taken parallel and perpendicular to the merge axis. The blue shift of the parallel spectrum corresponds to a velocity of 22 km/s. Line widths are within experimental uncertainty of the instrumental line width, indicating temperatures below 1.5 eV.*

of approximately 15 μs as measured by interferometry. In addition, interferometry showed close resemblance between the traces of all three individual Minirailguns.

The final set of parameters chosen for the merging experiments provided a plasmoid velocity of 22 ± 2 km/s as shown by spectroscopy (Figure 100) and fast photodiode measurements, and a plasmoid mass of $\sim$ 0.5 mg. The jet temperature estimated from ionization balance[136] is approximately 1.5 eV, and the electron density is 10^{15}cm^{-3}. Because the guns were operated in off-nominal conditions there was a small fast "prepulse" leading the main plasmoid. This does not affect the results as it has passed by the time the main plasmoid arrives at the point of convergence.

The initial tests used the array of five pressure probes at three positions, at the chamber center and 12.5 cm in front of and behind center. The coordinates used are positive in the direction of plasmoid propagation. Three shots were taken at each of these positions. The probe array was then moved back, well away from the center, in order to avoid interference with interferometer and spectroscopic measurements. Finally the probe was removed altogether and its feedthrough flange replaced with a window for axial fast imaging of the merge process.

Results A series of axial images of the merging process is shown in Figure 101. The bright inverted "Y" structure may be due to shocks (discussed further in the next section) at the location where the jets meet. With a convergence angle of 37.9 degrees the jets meet with a relative velocity perpendicular to the direction of propagation of 13.5 km/s. This corresponds to a Mach number of 5.5 in the plasma frame, which is in addition to the free expansion velocity perpendicular to the jet of $2c_s/(\gamma - 1)$. The nozzle diameter (35 mm) provides a length scale reference indicating that the thickness of the bright structures is on the order of 5 mm.

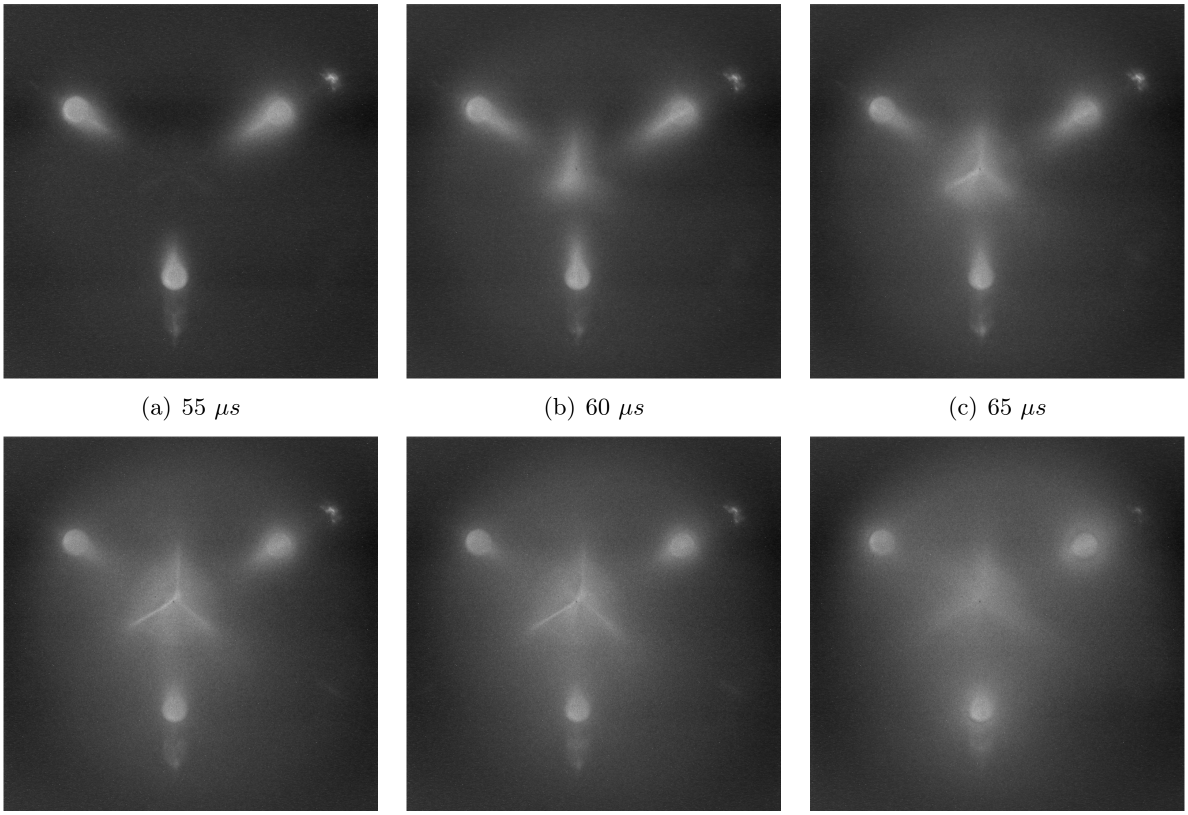

(a) 55 μs

(b) 60 μs

(c) 65 μs

(d) 70 μs

(e) 75 μs

(f) 80 μs

Figure 101 *Axial images of the merging process. In images c,d, and e the circular feature behind the inverted 'Y' structure is caused by reflections off the center flange on the vacuum chamber. This leads to the structure appearing slightly fuzzier than it actually is. Using the nozzle exit for scale, the width of the arms of the structure is on the order of 5 mm. Exposure time is 5 ns.*

The interferometer trace for both a single jet and the merged jets is shown in Figure 102. Note that the single jet trace is magnified by a factor of ten for better visibility. It is evident from the large difference in line integrated density that the merged jets form a high plasma density region at the point of convergence. The negative swings on the interferometer trace are due to the presence of neutrals and ions. There is a detailed analysis of this effect in reference [130]. The data in the figure is plotted in terms of line integrated density, but the single jet case is almost certain to be partially ionized. Neutrals cause a phase shift in the opposite direction from the electrons, reducing the measured density and even causing it to swing negative as seen in the single gun case in Figure 102. Therefore the single gun trace in its positive swing must be considered a lower bound on electron density, and in the negative portion to be dominated by neutrals. According to reference [130], the zero crossing of the interferometer signal occurs at an ionization fraction of approximately 0.07. To

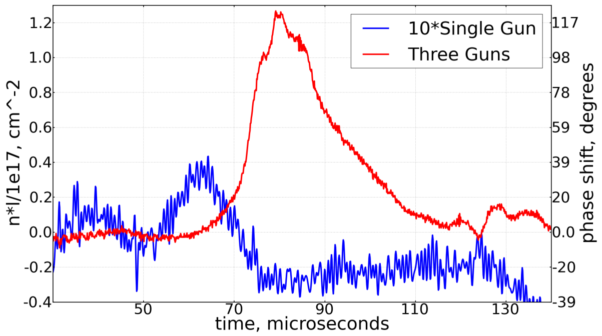

Figure 102 *Merged plasma line integrated density is far higher than single jet line integrated density, indicating compression of plasma into a compact structure at the point of convergence. Negative swings are due to neutral argon and ions. The very large electron density in the three gun case is in part due to formation of argon III as is seen in simulations as well as to collisional ionization of neutrals as seen in the unmerged jet case.*

disambiguate the signal into a neutral contribution and an electron contribution would require a two color interferometer.

In order to produce the large density peak seen in the three gun case we must assume that there is ionization of the neutrals seen in the single gun case. The center of mass merge velocity in excess of 13 km/s is sufficient to ionize argon through collisions. For this reason we expect the peak in the three jet case to be almost fully ionized. Another factor contributing to the later peak in the three gun case is the flow of plasma into the merge region that would in the single gun case have passed on the 'inside' (gun side) of the merge point. This plasma is deflected by impact with the other jets and flows into the center via a longer path than the plasma traveling directly from the nozzle. The high line integrated density in the three gun case is most likely due to to formation of a compact high density structure at the point of convergence. Imaging suggests that the width of this structure is approximately one centimeter. This implies a density of $\sim 1.2 \times 10^{17}$ cm^{-3} in this region.

Figure 103 shows the peak pressures measured at three locations using the five fast pressure probe array. Only the center probe measured any appreciable signal though there were small signals sometimes seen on one of the off-center probes. The relatively large signal seen on the far side of the merge point is due to the impact of a collimated jet of plasma that emerges from the merge region after the jets pass through. This jet is clearly seen in images taken off the chamber axis through one of the off-axis end cap ports. Figure 104 shows such an image, taken through a port looking 22 degrees off the chamber axis.

Discussion All diagnostics indicate the formation of a compact high pressure region at the point of convergence of the three jets. As expected there is a significant pressure spike at the point of convergence of the jets. The formation of a well collimated jet emerging from the convergence point suggests that the plasma is fairly cold even at convergence. This is consistent with the spectroscopic results and suggests that formation of a cold, dense plasma liner for MTF applications is possible using the MiniRailgun plasma accelerators.

The supersonic convergence of the jets suggests that there may be a shock at the point of intersection (the arms of the Y-shaped structure seen in Figure 101). The existing set of measurements do not at present provide sufficient data to test this hypothesis.

Simulation[137] using the LSP 3D hybrid PIC code shows the presence of narrow high density

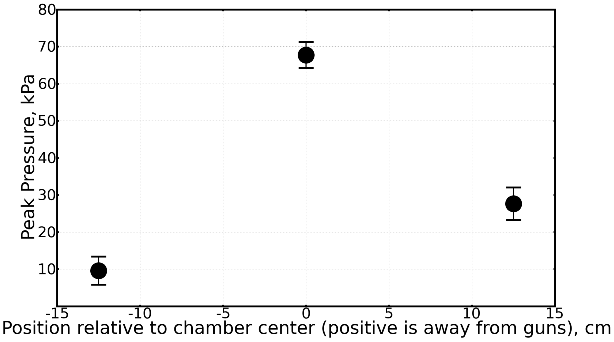

Figure 103 *Peak pressures measured at three locations, with approximate uncertainties*

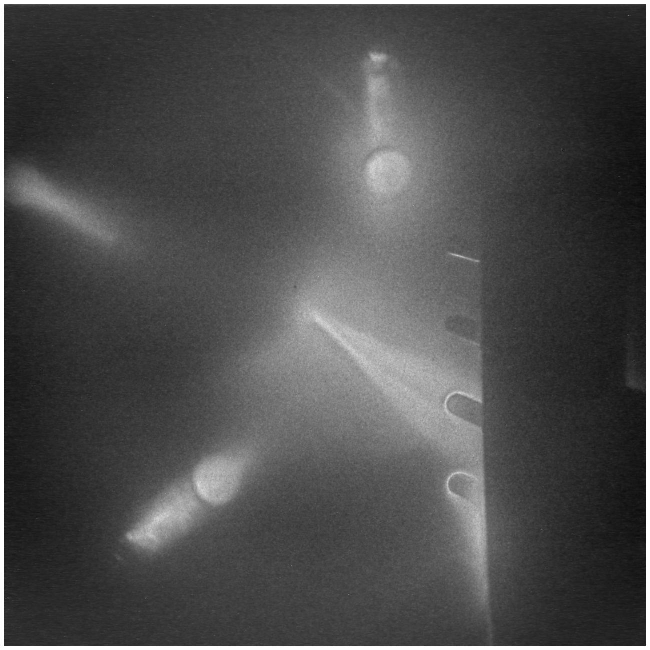

Figure 104 *Imaging off axis late in time (after peak density at merge point) shows formation of a collimated jet. The pressure probe array is seen on the right side of the image. The image is taken through the same port as the spectroscopy parallel collection optics in Figure 99.*

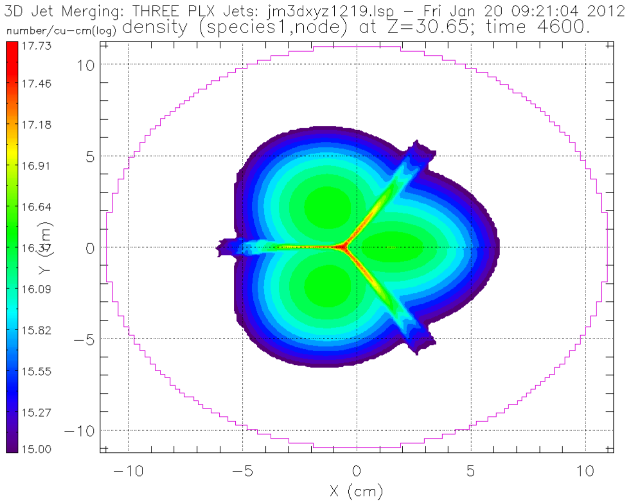

Figure 105 *A slice through an LSP simulation of three jets merging, in the plane perpendicular to the average direction of propagation of the three jets*

structures along the line of contact between the plasmoids as shown in Figure 105. These structures have an elevated temperature (2 eV vs 1 eV in the main plasmoid), though it must be emphasized that the simulation is of the higher performance railgun plasmoids of PLX as opposed to the lower density and lower velocity plasmoids produced by the de-rated railguns used in the present experiment. The highest temperatures measured in the current experiment are below 1.5 eV, a difference most likely due to the lower convergence velocity in this case, the PLX guns having 2.5 times the velocity. The width of the contact line structures is just under 1 cm, consistent with that seen in the images. For comparison, the ion-electron and ion-ion collision lengths are 1.5 and 0.8 cm respectively, and the electron-ion collision length is 0.005 cm.

Conclusions We have merged three plasma jets in a configuration related to that of the PLX experiment, in a parameter range lower than the PLX jets but still relevant to that experiment. We find that a compact ($\sim$ 1 cm transverse scale length), high density ($\sim 1.2 \times 10^{17}\mathrm{cm}^{-3}$), high pressure ($\sim$ 70 kPA), low temperature ($\sim$ 1.5 eV) region is formed at the point of convergence of the jets. The collision of the jets appears to result in ionization of the neutrals carried along with the plasma jet. In addition a well collimated secondary jet emerges from the point of convergence. The line of contact between adjacent jets forms a structure which may be a shock, though further research is required to confirm this.

8.2 Recap of Six Jet Merging Experiments

Following the three jet merging experiments the next logical step was to place three guns on the other side of the experimental chamber and fire them directly at each other. The resulting arrangement of six guns partially replicates the desired geometry of the PLX experiment.

Experimental Arrangement One end of the experimental chamber is shown in Figure 106. Three one cm bore minirailguns are arranged in a triangular formation aiming at the center of the chamber. The other end of the chamber has the same arrangement of minirailguns, but rotated through 180 degrees, so that each gun is firing directly at another gun on the opposite side of the chamber.

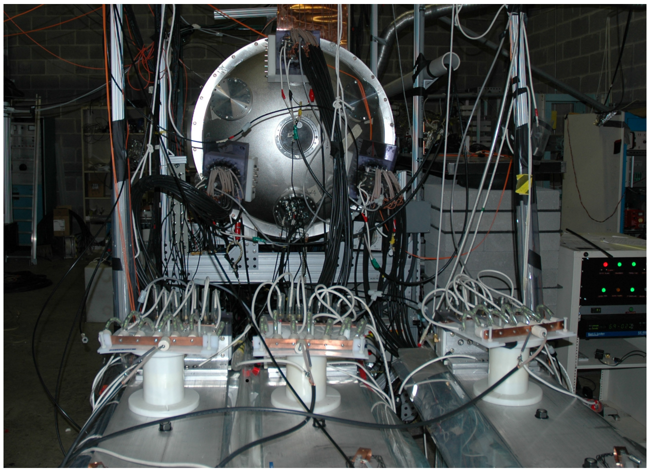

Figure 106 *East End of Chamber, showing PFNs and Railgun Breeches*

The high voltage banks were set up as follows: All six fast gas valves were driven by a single bank of 6 capacitors of 14 μF each. Ballast resistance was 0.3 ohms. Charge voltage was 5.6 kV and the typical current was 2 kA. The pre-ionizer bank was 6×6 μF capacitors in parallel fired by a custom switch designed by HyperV. The ballast resistance for each pre-ionizer was 2.6 Ohms and the charge voltage of 22 kV drove a peak current of 7.5 kA per pre-ionizer. Three of the minirailgun PFNs were the same as for the three gun merge experiment, namely 3×17 μF capacitors per gun, charged to 23 kV, providing a rail current of 250 kA, matched within 15% The remaining three PFNS consisted of a 46 μF and a 6 μF capacitor, charged to 23 kV and driving a peak current of 250 kA, matched within 15%. Four of the PFN switches were seven-knob linear switches designed by HyperV, while the remaining two were four-knob spark plug triggered switches, also designed by HyperV.

The PFN linear switches were triggered by a single switch fanned out to all six PFN switches so as to ensure simultaneous firing. The timing sequence was: (1) fire fast gas valve, (2) after $475\mu s$ fire the pre-ionizer, and (3) after $15\mu s$ fire the main PFN. This sequence has been shown in previous experiments to produce a good balance between jet velocity and jet mass. Jitter between PFNs was typically below 1 μs but occasionally reached as high as $2.7\mu s$.

The first step in preparing for the experiment is firing single guns to check that they are performing similarly. This was done simply by disconnecting the PFNs for all but one gun at a time, leaving the Puff Valve and PreIonizer banks to fire as usual. Emphasis was on having the peak of the plasmoid density arrive on center at the same time (matching velocities) rather than matching mass. This was done using the intensified photodiodes and the photodiode array for timing measurements. Plasmoid arrival times varied by about 1 μs.

Once individual gun performance had been verified, shots were taken using all six guns. Similarity of performance was monitored by looking at Gas Valve, Pre-ionizer, and PFN currents. Seven shots in all were taken, the experiment being prematurely terminated by the failure of one of the $46\mu F$ capacitors.

The diagnostic suite for this set of experiments is a subset of that used for the three gun merging experiments, namely fast imaging using a PIMax II camera, time integrated imaging using a Nikon SLR, Spectroscopy, fast photodiodes, and Rogowski’s and Pearsons for monitoring the high voltage systems.

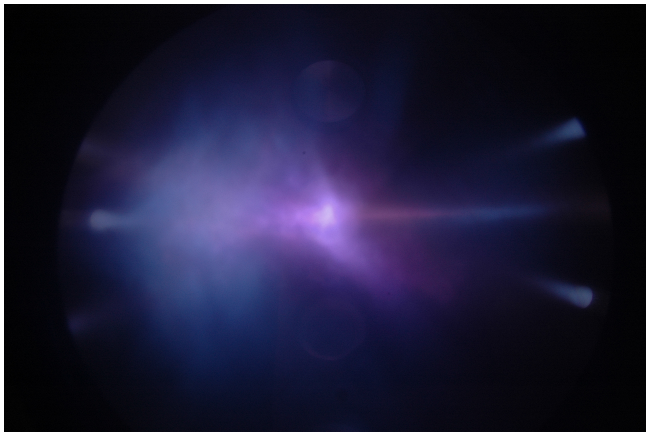

Figure 107 *Nikon SLR camera Image taken with shutter open for 2 seconds spanning the entire shot. Neutral density filters reduce intensity to minimize saturation.*

Results An open-shutter image of the central region of the experimental chamber is shown in Figure 107. Plumes from the six minirailguns are visible at the edges of the frame, and a bright central spot can be seen. Figure 108 shows an image taken using the PIMax II high speed camera. The image is taken at 56 microseconds after the PFN switches fire, shortly before the expected time of peak compression. For comparison, the transit time of a plasmoid from a single gun to the center of the chamber is $62\mu s$.

Three individual fast photodiodes were used to track the progress of a single plasmoid from one of the guns to the chamber center. Traces from these photodiodes can be seen in Figure 109. The velocity inferred from the photodiode traces is 26 km/s, slightly faster than in the three gun merge experiments. The small "foot" seen in the third photodiode trace (pointed at the chamber center) may be due to a fast prepulse occasionally seen in some gun experiments, or may be due to chamber wall reflections.

The spectroscopy timing was shifted between shots, so we have spectra perpendicular and parallel to the machine axis for times of 52, 56, 60, 64, and $68\mu s$ from PFN switch firing. The parallel view data is shown in Figure 110. The viewing volume includes the jets, so translation into temperature is unreliable, but it is worth noting that the greatest line width is seen in the spectrum for 64 μs, right after the peak light emission on the photodiodes. This implies either a (relatively) high temperature or large velocity spread (10.75 km/s).

The perpendicular view spectroscopy data show dramatic differences depending on the timing, as seen in Figure 111. The data for 64 μs after PFN firing shows a velocity spread of 39 km/s suggesting that right after peak light emission on the photodiodes there is a strong radial jet formed as the plasma rebounds from peak compression. The fact that the line broadening is anisotropic indicates that it is not due to temperature alone, but must be due to bulk flows. Assuming the bulk flows are driven by thermal expansion, and working from the peak perpendicular direction expansion velocity, which is the free expansion velocity $v_f = 2c_s/(\gamma - 1)$, and using $\gamma = 1.4$, we can back out a peak temperature of between 9 and 18 eV, depending on the charge state of the ions.

In addition to the high resolution Acton spectrometer we used a Ocean Optics survey spectrometer to try to get an overview of all the lines present in the plasma. Unfortunately most of the spectrum was saturated, but the near UV end of the spectrum was not. Shown in Figure 112, it is possible to distinguish three lines which might be either Ar III or W II. We expect that there will be trace amounts of tungsten in the plasma due to rail erosion, but the operating point for the guns was chosen in part to minimize rail erosion, so the total contribution of Tungsten to the spectrum

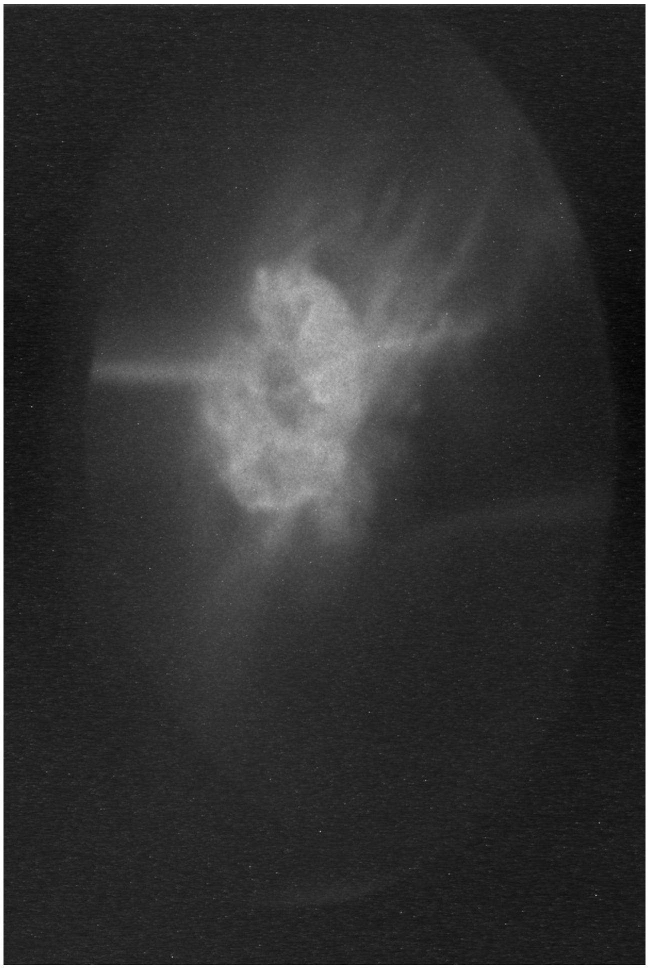

Figure 108 *High speed image taken using PIMax II camera. The image is taken 56μs after firing the rails, just before the expected peak compression. Gate width is 5 ns.*

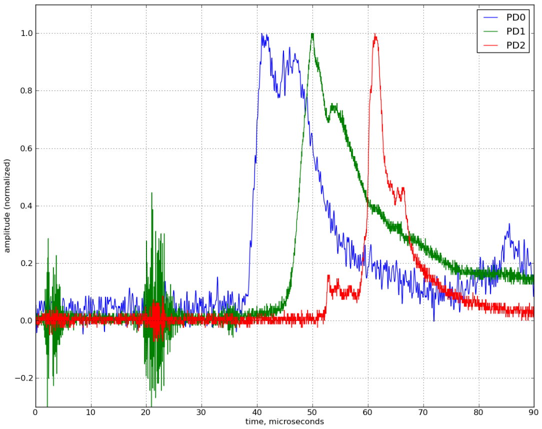

Figure 109 *Photodiodes indicate a jet velocity of 26 km/s with arrival time at center of the chamber at 62 μs.*

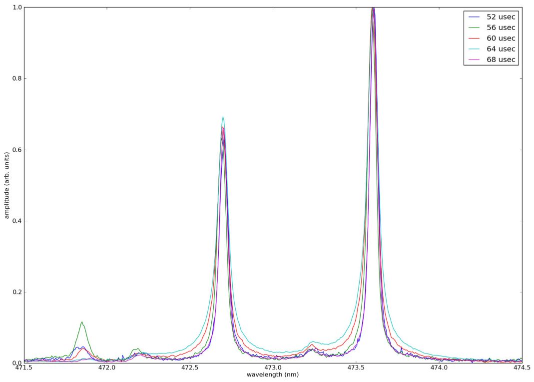

Figure 110 *View parallel to machine axis gives velocity spread of 4.75 to 10.75 km/s. Viewing volume includes jets, so translation into temperature is not reliable.*

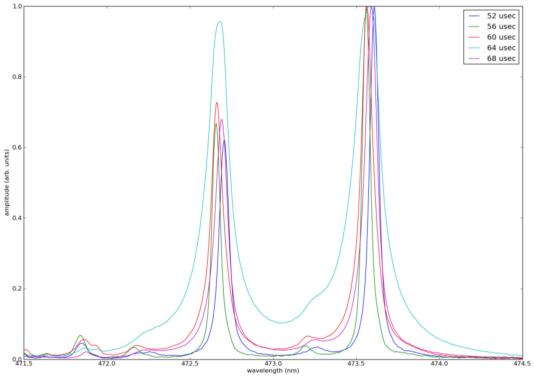

Figure 111 *View perpendicular to machine axis gives velocity spread of 14 to 39 km/s. Peak velocity spread occurs right after peak light emission on photodiodes, and suggests formation of a jet perpendicular to the machine axis.*

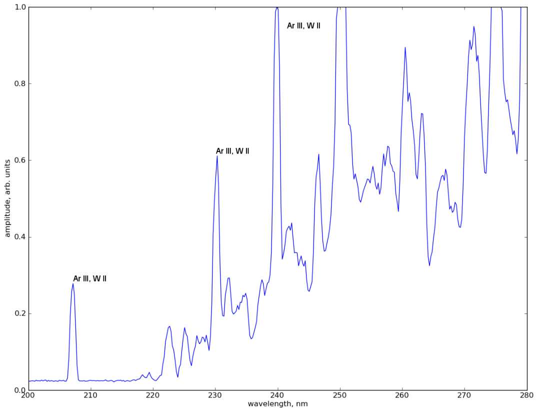

Figure 112 *Survey spectrometer has indications of Ar III, but higher resolution is needed to distinguish from W II lines close by. Tungsten is expected in the jet in small amounts due to rail erosion.*

should be small. We know we have Ar II in the central region in large quantities since that is the overwhelming primary component of the jets. In addition, the jet kinetic energy is well above the threshold for secondary ionization. These considerations lead us to suggest that the lines seen in the survey spectrum are Argon III, present due to collisional ionization of Ar II from the jets.

Conclusions We have demonstrated the ability to successfully synchronize and fire six plasma minirailguns in a manner that is scalable to much larger numbers of guns such as those needed for the PLX experiment. We have shown that we can match gun parameters within approximately 15% across six guns utilizing two different PFN configurations and two different switch types.

Based on the results presented above we conclude that the six jet merging results in the formation of a compact high density structure with a temperature in the range 9-18 eV. The structure probably contains some Argon III due to impact ionization. Shortly after peak light emission (interpreted as the arrival on center of the highest density portion of the jet plasmoids) a strong radial flow is seen as plasma expands out of the point of convergence.

9 Mark 2 MiniRailgun - PLX Gun Performance Goal Achieved

While the Mark 1 was being tested on PLX, HyperV continued development of the Mark 2 gun in order to achieve the stated performance goals required for the full 30 gun array planned to be deployed on PLX later.

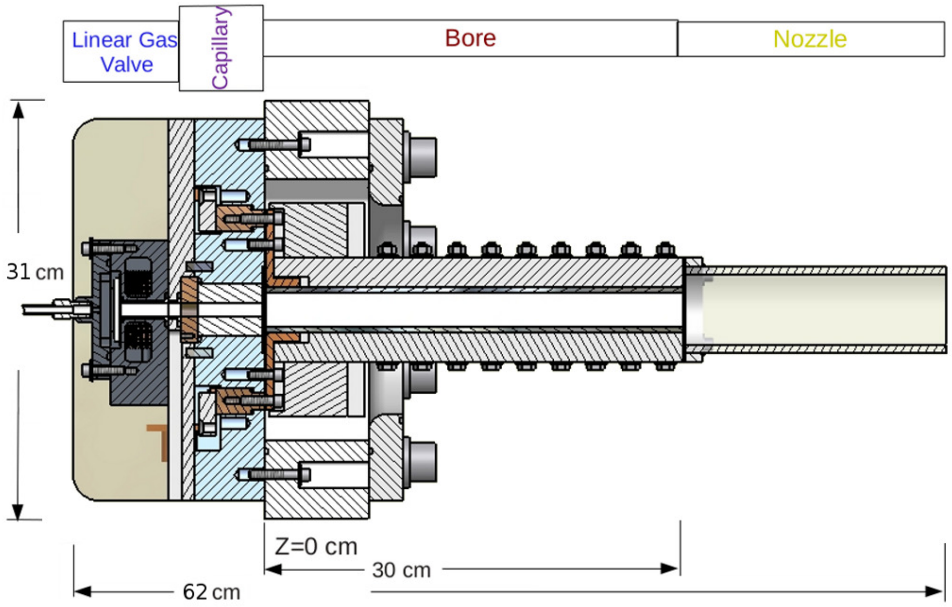

Figure 113 *HyperV plasma railguns are three stage linear plasma accelerators. First, neutral gas is injected with an electromechanical fast gas valve (GV). Next, the pre-ionization stage (PI) ionizes the gas electrothermally using a capillary discharge channel. This injects a plasma armature into the final railgun acceleration stage. There the plasma armature is accelerated via a Lorentz force, generated by current from a Pulse Forming Network (PFN), and ejected as a high velocity plasma jet.*

HyperV linear plasma railguns, illustrated in Figure 113, are three stage linear plasma accelerators. In the first stage, or gas injection stage, neutral gas is injection into the rear of an electrothermal capillary channel via an electromechanical fast gas valve (GV). In the next stage or pre-ionization stage (PI), a current of tens of kiloamps is discharged though the capillary channel. This pre-ionizes the injected gas which will form the plasma armature, and injects this plasma into the breech of the railgun electrode gap. Finally, the acceleration stage employs a Pulse Forming Network (PFN) to drive a large current (as much as 660 kA in these tests) through the armature via the rail electrodes. As the armature current moving through the plasma is also moving normal to its self-generated magnetic field, the plasma armature experiences a Lorentz force, accelerating it down the length of the bore to be ejected as a high velocity plasma jet. Since the goal of this design was to meet or exceed the PLX plasma jet specifications, these specifications determined the performance requirements for the various subsections of the railgun. The gas valve needed to be fast opening, and inject sufficient gas to produce the required 8 mg plasma jet mass as described in earlier sections. The pre-ionizer needed to not only ionize the gas, but also inject a localized plasma pulse with some initial velocity to reduce the dwell time of the armature at the breech of the accelerator. Finally, the accelerator section was required to supply the necessary energy and withstand the forces required to repeatedly accelerate the plasma to 50 km/s. Since the desired plasma jet kinetic energy for PLX is about 10 kJ, a railgun operating with an assumed efficiency of

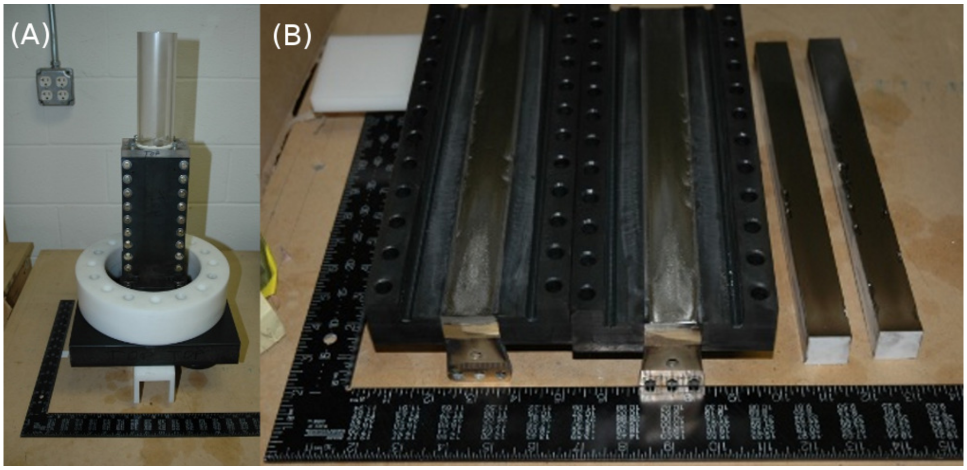

Figure 114 *The present 2.5 cm square-bore plasma railgun forms a plasma armature from high density neutral gas, pre-ionizes it electro-thermally, and accelerates this plasma armature with 30 cm long parallel-plate railgun electrodes driven by a pulse forming network (PFN)*

20% was estimated to require a PFN bank energy of about 50 kJ.

9.1 Railgun and Driver Circuit Changes

Previous experiments with HyperV railguns using a 44 kJ acceleration bank successfully generated plasma jets with 4900 μg at 55 km/s, as described in the previous section, However additional upgrades to the driver circuits and the railgun itself were necessary to meet the PLX specification for performance. The chief difficultly arose from having to insert both gas and high voltage into the breech of the railgun, while still maintaining electrical standoff and vacuum seals in the space provided. Because of the size and proximity of components, early solutions to these requirements forced the PFN transmission line to have large inductances because of how the PFN was routed through the space available, thus leaching power from the railgun inductive load. Several changes were necessary to reduce inductive losses. First, dimensions of the railgun breech flange were increased from 20 x 20 cm to 30 x 30 cm. This allowed wider bus connections and wider high-current vacuum penetrations to be used to provide PFN current. Plus it allowed the railgun to mate directly to flanges at PLX and still be adapted down to the 8 inch flanges available at HyperV. Second, rotating the gas valve so that PFN transmission lines could be routed to the sides instead of over the gas valve decreased the cross-sectional area of the TM line coupling. A parallel plate model can be used to approximate many sections of the PFN high current feeds. Thus, inductance was reduce by maximizing the width of conductors while minimizing conductor loop area.

The largest changes in railgun driver circuits occurred in the PFN system. Present HyperV railgun designs call for peak accelerator currents of 0.5 MA to 1.0 MA and pulse widths as long as 15 μs. As HyperV railguns are primarily an inductive load of 200-300 nH, it is necessary to minimize inductance of PFN switches and transmission lines in order to maximize peak PFN current for a given pfn. In order to repeatably generate large currents from a single PFN capacitor bank, a robust, low jitter, low inductance switch had to be designed for high repeatability and high mean-time-to-repair. Some success was achieved with a 30 cm wide linear arrayed switch consisting of 7 sparkgap electrode pairs in a single housing. However, by moving to a 60 cm wide, 8 electrode pair linear spark gap switch, it was possible to increase peak currents further due to increased switch robustness, and reduced switch inductance. Increased interior volume in the switch also mitigated the acoustic shock to the switch components because energy imparted to the switch gas had a larger volume to pressurize. A second 60 cm arrayed spark gap switch was added to the accelerator pulse forming network to act as a current crowbar for pulse shaping. Finally, the accelerator bank transmission line connections were also redesigned to reduce inductance. The net result was a decrease in total system inductance of about 53 nH or ∼ 19% improvement over our previous designs.

Railgun Gas valve and pre-ionizer systems were also upgraded. The return spring on the flyer plate was stiffened to force the gas valve to close faster. Pre-ionizer systems were modified to use large bulk ceramic disk resistors to increase system robustness. Previously employed resistor arrays were prone to cascade failure from component fatigue. These disc resistors had much improved voltage standoff and pulse withstanding characteristics, allowing a more consistent pre-ionization current pulse to be produced.

Previous linear gas valve designs used a weak return spring for closing. This slowed valve closing time, resulting in plasmoids with masses in excess of the 8000 μg target. By employing a stiffer return spring to assist in closing the valve, gas valve closing times were improved resulting in greater control over ejected mass.

While the present design still uses large amounts of plastic, this is a design choice to reduce the cost of manufacturing parts so that larger arrays of railguns could be deployed. The total mass of the railgun, without PFN cables, is about 15.4 kg, allowing railgun units to be lifted and mounted into position by hand if necessary. This railgun was also design with 4 interfaces, to make nozzles, bores, breeches and gas valves standardized parts that could be interchanged or replaced in order to minimize downtime from equipment failure or maintenance.

9.2 Experimental Results

With these design upgrades in place, an improved HyperV 2.5 cm square-bore Linear Plasma Railgun was mounted on a large stainless steel vacuum vessel for performance measurements. A Cartesian coordinate system is used to describe railgun features. Axes are defined as x being the lateral axis of the railgun across the electrode face, y being changes in height, and z being locations along the length of the railgun. The foot of the accelerator rail is defined as z=0. Unless indicated otherwise, time events are referenced from the time of accelerator current onset at t=0.

The improved linear plasma railgun, shown earlier in Figure 114, was mounted on the end-cap of a large steel tank 115, allowing ample volume for the free space propagation of the plasma jets. A pair of collimated photodiodes were mounted normal to the direction of travel to measure the velocity of ejected plasmas, along with additional spectroscopic and interferometric measuring apparatus. A removable ballistic pendulum was also mounted in the chamber, allowing measurements of imparted plasma momentum to be recorded.

Sample railgun driver currents are shown in Figure 116 for a 141 μF PFN driver bank. A PFN voltage of 26 kV produced a 17.6 μs long pulse with a peak current of ∼480 kA. A 1.6 kJ pre-ionizer pulse was employed. Gas valve (not shown) was driven at 7.1 kV with a feed pressure of ∼207 kPa of Argon.

Magnetic field probes were installed along the length of the bore at ∼5 cm intervals. Location and orientation of the probe was determined to maximize signals from the propagation of the plasma armature current. Normalized magnetic field traces, shown in Figure 117 indicated the propagation of the armature.

Peak density recorded by interferometry was measured to be $5\times10^{16} cm^{-3}$ at z=104 cm based on an estimated path length of 10 cm. Using an assumed top-hat radial density profile, this estimates plasmas mass to be about 5.5 mg depending on assumptions of plasma shape and neutral presence. Neutrals reduce plasma interferometer signals leading to depressed line density measurements [130].

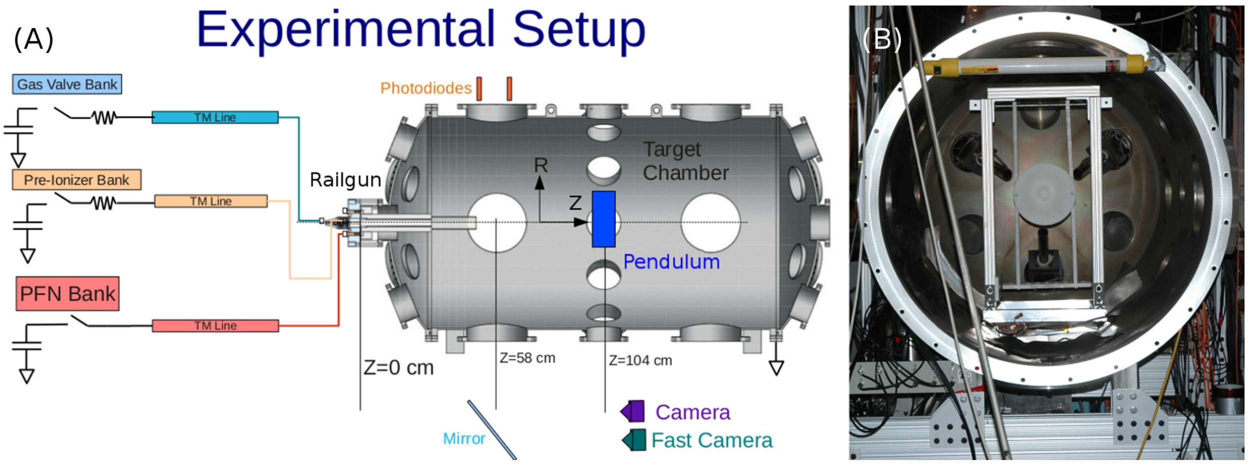

Figure 115 *(A) A 2.5 cm square-bore, linear plasma railgun was fired at a ballistic pendulum of* $L=40.6$ *cm and* $M_{eff}=0.58$ *kg mounted on center at* $Z=104$ *cm or about 55 cm from the end of the nozzle. A* $\sim$ *20 cm diameter white Delrin plastic strike plate was used. A pair of photodiodes normal to the path of travel were used to measure plasma velocity. (B) The Ballistic Pendulum is shown mounted in the chamber with the end cap removed.*

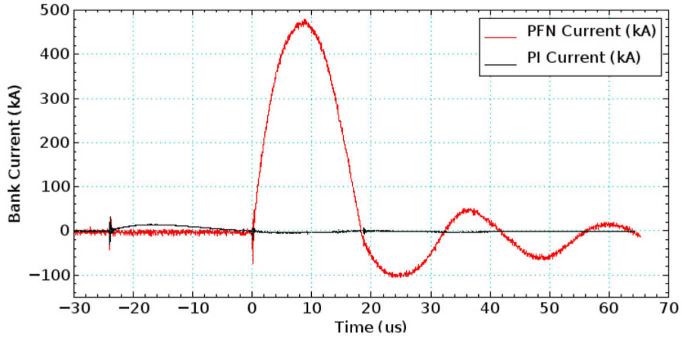

Figure 116 *A PFN voltage of 26 kV produced a 17.6 μs long pulse with a peak current of ∼480 kA. A 1.6 kJ pre-ionizer pulse was employed. Gas valve (not shown) was driven at 7.1 kV with a feed pressure of ∼207 kPa*

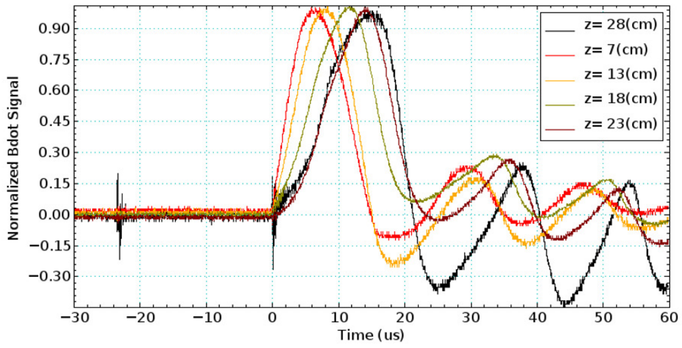

Figure 117 *Magnetic field traces indicate the propagation of the armature*

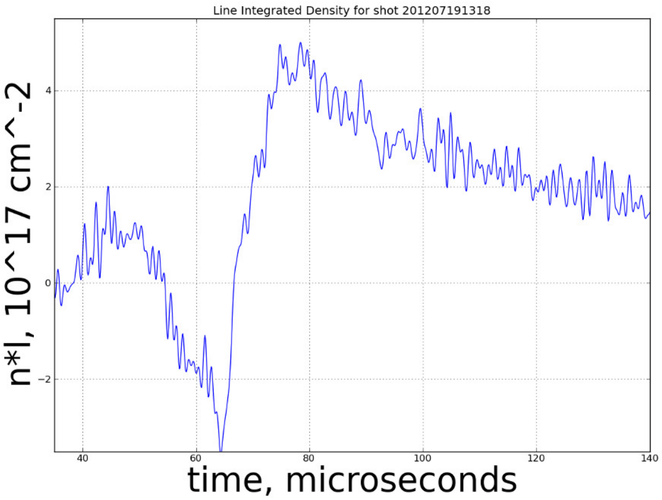

Figure 118 *Line density from interferometry of an ejected plasma at z=104 cm. Peak density calculated with an estimated path length of 10 cm was determined to be* $5{\times}10^{16}cm^{-3}$*. Using an assumed top-hat radial density profile, this estimates plasma mass to be about 5.5 mg depending on assumptions of plasma shape and neutral presence.*

Spectroscopic measurements indicated high levels of impurities at regions of interest, but that was to be expected here. The introduction of these impurities is a result of using an acrylic nozzle instead of a lower strength, quartz nozzle employed in lower power experiments to reduce nozzle ablation. Additional nozzle development is necessary. An acrylic nozzle was used for testing of the improved railgun. While Acrylic was able to withstand the forces produced by the exiting plasma jet, spectroscopic readings experienced obfuscation not present when quartz nozzles were employed, This is presumed to be from ablation of nozzle material contaminating the jet, and will need to be corrected in future designs.

Plasma emission profiles were recorded with collimated photodiodes as the plasma emerged from the nozzle. Plasma velocity was measured to be 53.5 km/s km/s for this shot.

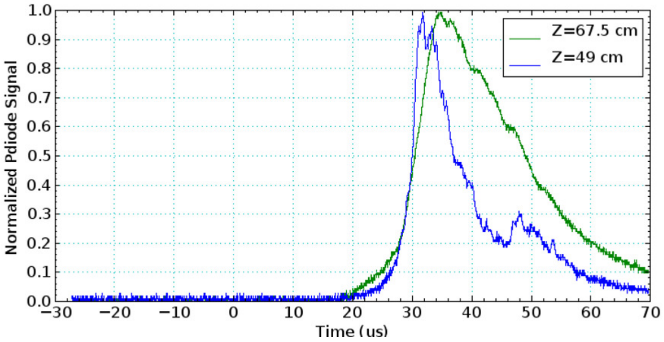

Figure 119 *Plasma emission profiles was recorded with collimated photodiodes as the plasma emerge form the nozzle. Plasma velocity was measure to be 53.5 km/s for this shot*

A ballistic pendulum was used to determine plasma momentum and estimate plasma mass. The pendulum design, consists of two assemblies, a heavy rigid support frame, and a rigid rotating pendulum arm with strike plate. The foot of the pendulum arm contains two rare earth permanent

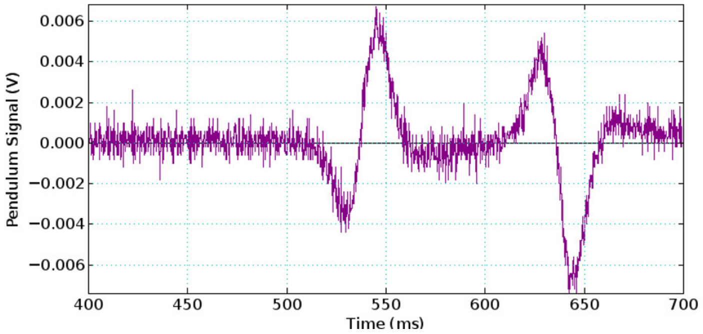

Figure 120 *Plasma momentum was measured a ballistic pendulum to be .455 kgm/s for this shot. A plasma with velocity of 53.5 km/s thus yields an estimated plasma mass of 8.5 mg.*

magnets oriented to face outward in opposite polarities away from the strike plate (See appendix for further dtails). Signals generated by the motion of the pendulum arm magnets are then recorded by a 100 turn pick-up coil mounted on the support frame. The collision of the plasma "projectile" with the target plate imparts momentum. The pendulum swings backwards and upward with the velocity of the pendulum arm read out by the pickup coil on the return swing. The motion of the pendulum produces a characteristic pair of up/down signals whose order changes based on the direction of motion. The time between the signals comprising the pairs is then used to determine the velocity of the pendulum from which the momentum imparted to the pendulum can be calculated from angular momentum. Plasma momentum was measured with a ballistic pendulum to be .455 kgm/s for this shot. Plasma velocity and momentum measurements combined to allow plasma mass to be estimated as 8.5 mg for this shot.

Estimated plasma mass versus velocity for the shot series is shown in Figure 121. The highest mass achieved was ∼13.7 mg with a velocity of 34 km/s. the highest momentum ejected was at 0.58 kgm/s. The fastest plasma ejected was **7.5mg at 62.4 km/s**. The largest mass moving faster than 50 km/s was estimated to be **10.8 mg at 52.8 km/s**. This was achieved with the parameters V_{gv}=7.1 kV, V_{pi}=23 kV, V_{pfn}=26 kV, t_{gv}=-341μs, t_{pi}=-16 μs, t_{pfc}=+16.5 μs,p_{feed}=207 kPa C_{pi}=6μF and C_{pfn}=141 μF.

Another observation of key interest is that pulse shaping offers a chance to dramatically improve ejected plasma momentum. As indicated in Figure 122, two types of crowbarred current signal were recorded based on the exact time of the PFN circuit closing: "returning crowbar currents" where PFN current peaked to some value and then returned to a local minimum at or near zero creating a short current pulse, and "non-returning" crowbar currents where local minimum is elevated about a hundred kiloamps, effectively more than doubling the width of the current pulse. Non-returning crowbar currents were seen to increase plasma momentum, indicating a more detailed study of acceleration pulse shaping could still yield significant momentum improvements.

9.3 Mark2 Summary

To summarize, the Mark2 plasma railgun driver meets the design specifications for the original PLX experiment of 8 mg at 50 km/s. HyperV linear plasma rail guns are regularly operating with PFN currents of 475 to 665 kA, and are generating plasma jets with momentum as high as 0.58 kgm/s, masses as large as ∼13.7 mg (at lower velocity), and velocities as high as ∼79.2 km/s (at smaller mass). In specific combinations we achieved **7.5mg at 62.4 km/s** and **10.8 mg at 52.8 km/s**. The ejected plasma jet structures have been observed to be cold and dense as well as steep and fast,

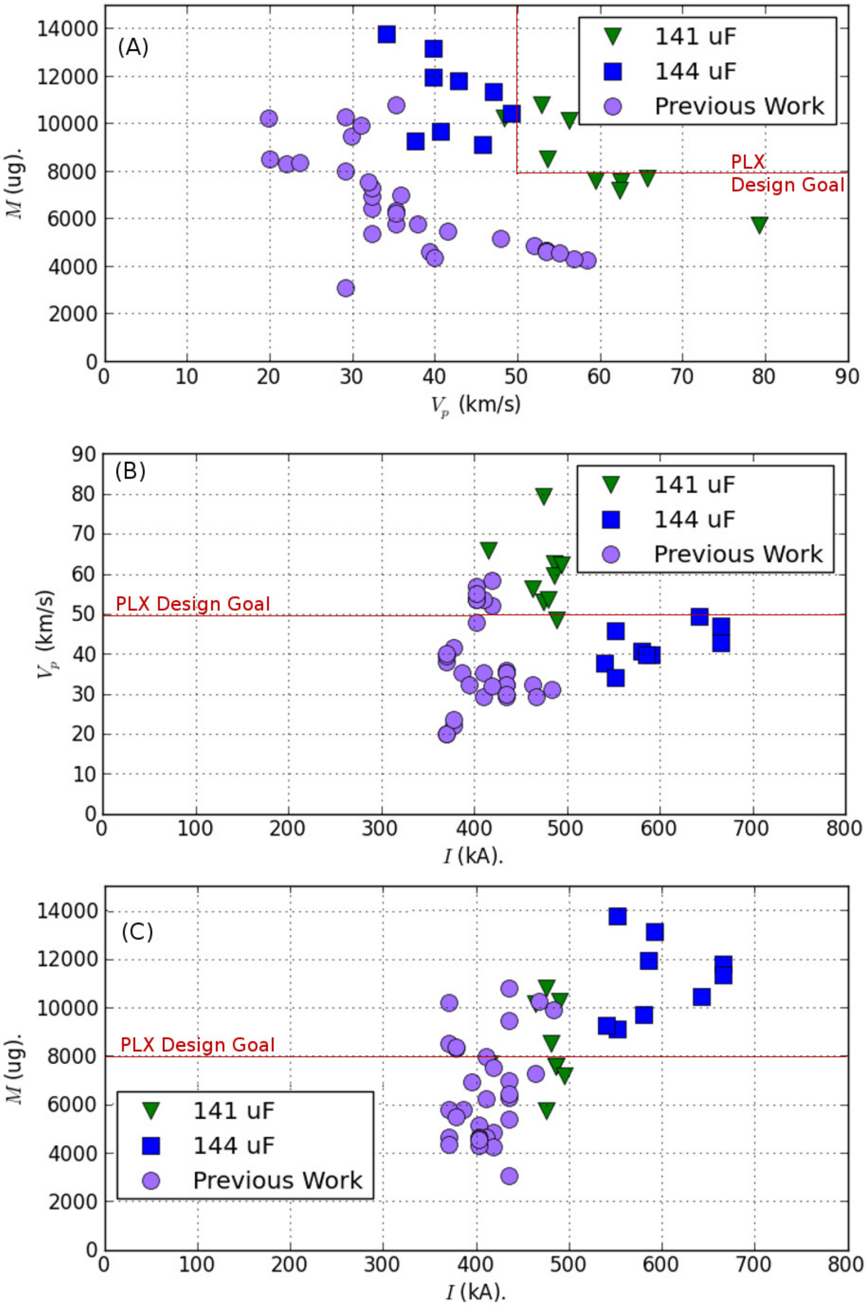

Figure 121 *Estimated plasma mass versus velocity for the shot series. The largest mass moving faster than 50 km/s was estimated to be 10.8 mg at 52.8 km/s*

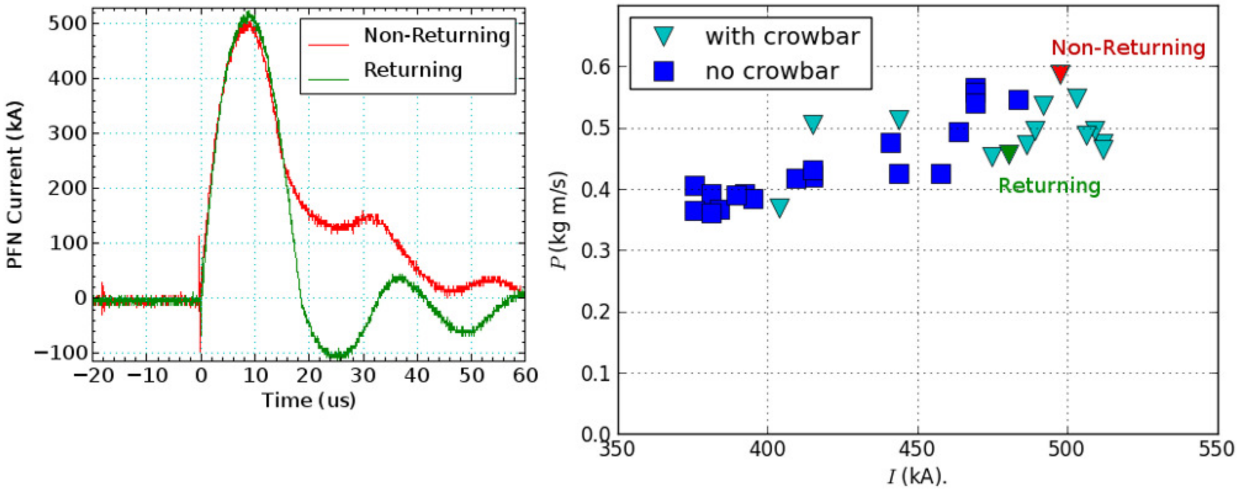

Figure 122 *Comparison of performance with returning and non-returning crowbar currents.*

and further performance increases appear to be possible through optimization of PFN current pulse shaping. While the present design still uses large amounts of plastic, this is a design choice to reduce the cost of manufacturing parts so that larger arrays of railguns could be deployed. The total mass of the railgun, without PFN cables, is about 15.4 kg, allowing railgun units to be lifted and mounted into position by hand if necessary. This railgun was also designed with four interfaces, to make nozzles, bores, breeches and gas valves standardized parts that could be interchanged or replaced in order to minimize downtime from equipment failure or maintenance. An acrylic nozzle was used for testing of the improved railgun. While Acrylic was able to withstand the forces produced by the exiting plasma jet, spectroscopic readings experienced obfuscation not present when quartz nozzles were employed. This is presumed to be due to ablation of nozzle material contaminating the jet, and will need to be corrected in future designs.

10 Directions for Future Experiments

10.1 Coaxial vs. MiniRailguns

Future plans call for returning to the coaxial gun for future plasma liner experiments. There are a number of important reasons for this. There are two key issues associated with the coax gun relative to a PLX style experiment. First, it will require substantially more current than the minirailgun for the same mass and velocity due to the inherently smaller L' of coax guns. And secondly, it will require a more complex injection system due to the annular geometry of the injection region. These two issues originally drove us to select the Minirailgun as the baseline plasma gun for PLX, because it would be much easier to achieve the desired performance parameters within the funding profile projected at the time. But future PLX-type experiments would greatly benefit from coaxial systems if funding allowed it.

Structure and Symmetry The natural symmetry of the coax gun gives it distinct advantages over the parallel-plate railgun. This is a natural result of the rotational symmetry about its long axis. Such symmetry does not exist in the parallel-plate railgun. As a result of the geometry, the coax gun does not require an insulator separating the electrodes along the length of travel, as does a railgun. It does require an insulator at the breech, but that is relatively easy to deal with for modest size coax guns. This has major advantages in cost and complexity, and in the methods by which the electrodes are connected to external capacitors. Eliminating the linear insulator eliminates viscous drag and loss of plasma along insulating surfaces, an unavoidable problem for parallel-plate railguns. This reduces restrike issues somewhat, but mainly eliminates a major source of drag and plasma loss along the surface.

The coaxial geometry has closed field lines that do not intersect an insulator wall, as is the case for a railgun. This is definitely an important advantage for low to modest density operation, and may also be so for high density operation.

An additional practical advantage of the coax is that the outer electrode can act as its own vacuum vessel, thus eliminating high current, high voltage vacuum feedthroughs that are necessary for the MiniRailgun.

Enhanced Jet Shape Control Although the MiniRailguns appear to have the edge for near-term performance potential in terms of mass and velocity, the coax gun has a clear edge in terms of flexibility of structuring that jet to the desired "hockey-puck" or pancake-like configuration. Modeling performed by Cassibry [138] showed that the natural hole in the toroidal structure of a coax jet does not appear to be as detrimental as might first be thought. In addition, the toroidal structure will evolve in flight so that the hole is at least partially filled in by the time the plasmoids merge, so that the toroidal jet structure actually seems to be pretty close to the desired final jet structure. Achieving similar pancake-like structures from the MiniRailgun is problematical.

The Coax has the potential for jet nozzle controls that are inherently "built-in" to the nozzle electrode structure, rather than added on, as is necessary for the MiniRailgun. The preferred circular jet shape does not have to be forced by external tubes, as for the MiniRailgun, thus eliminating a potential source of shock heating of the plasma.

Flexibility in Parameters The Coax gun is much more flexible than the railgun in terms of the parameter space it can access. This is especially true for very high velocity operation at any density level. A parallel-plate railgun cannot easily achieve velocities above about 100 km/s the way a coax gun can.

Injection Injection of the gas or plasma into the annular region of the coax gun is a bit trickier than it is for the MiniRailgun, where a single simple injector can be used at the breech. The MiniRailgun was, in fact, originally conceived as an even smaller device that could be used to inject high speed plasma into a full-scale coax gun using an array of MiniRailguns mounted around the periphery of the injection annulus. However, if the coax gun can be made small enough, then injection becomes much less of an issue. We describe further below some straightforward adaptations of our MiniRailgun fast gas valve which would allow injection of high-Z gases into a MiniCoax gun.

Performance A significant advantage that parallel-plate railguns have over coax (other than simpler injection), is their larger L'. However, this can be compensated for in large part by the ability to make much lower inductance connections to a coax geometry compared to parallel-plate. This in turn reduces the total capacitance that would otherwise be required and also reduces the peak operating voltage, both of which reduce cost and physical size. In addition, the current density at the electrode surface can be significantly lower than for parallel-plate leading to lower erosion and lower impurities.

The coax gun is more susceptible to the blow-by instability, while railguns are more susceptible to current sheet canting. The blow-by instability is addressed by using the contoured-gap electrode profiles as shown in Figure 123, whereas current sheet canting seems to be partially ameliorated by very high density operation.

MiniRailgun seems to have an edge at modest velocities (50 to perhaps 80 km/s) for high mass plasmoids, which is why MiniRailguns were chosen as the baseline configuration for the PLX experiment, which needed 8000 μg at only 50 km/s. On the other hand, coax guns have a well known and long history of outperforming railguns at higher velocity than this, having demonstrated velocities even in excess of 1000 km/s, far beyond what railguns can realistically achieve. The Coax should have a much higher performance potential in the longer run, in addition to its better and more flexible jet shaping.

Scaling to smaller size appears to be feasible, although at the expense of larger drive currents. As the physical size is reduced the effective J and B both increase in proportion. Since L' scales as $\log\left(r_{outer}/r_{inner}\right)$, as long as the radius ratio is maintained constant you should obtain the same performance (at least, in principle, for the same length gun). But since we want to shorten the gun at the same time that we reduce the cross section size, that means we will need to increase the radius ratio, and increase the drive current somewhat. This appears feasible by proper tailoring of the electrode profile to avoid the blow-by instability, which becomes more prevalent at larger radius ratio. There should, in principle, be a family of solutions for a given mass/velocity combination, although the current drive requirement will be unacceptable for many of those solutions. The parameter space is large, so effective high physics content modeling is key to reducing the number of hardware geometries fabricated for testing.

10.2 Coax Gun

A Coax gun will look similar to something like that shown in Figure 123. We have begun exploring various configurations, mostly concentrating on how to do the fast gas injection into the annular breech region, since this is the most critical engineering issue. For large, i.e. full-scale coax guns, getting an annular gas injection system to work with low jitter is challenging, but achievable, and the task becomes easier the smaller one can make the coax gun for a given performance. The challenge here is going to be to operate with small size (10's cm), extremely small inductance (10's nH) transmission lines, high current ($sim1$ MA), high mass (1000's μg), careful injection, and carefully tailored electrode profiles [1, 6, 7, 48].

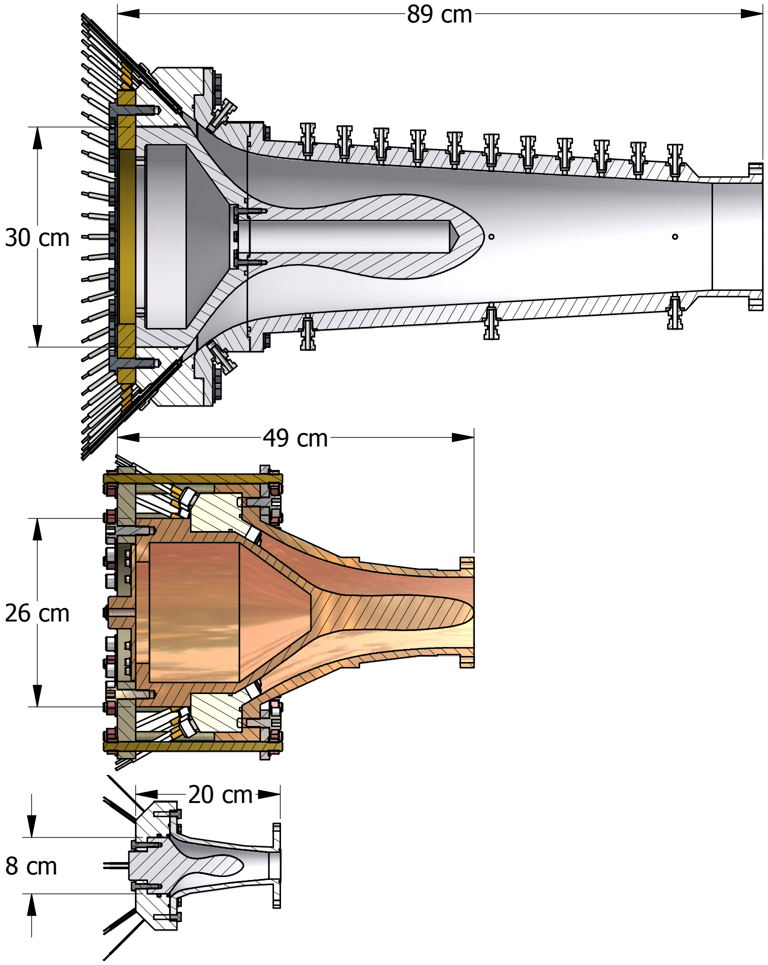

Figure 123 *Full-scale (top), half-scale (middle), and quarter-scale (bottom) coax guns built and tested at HyperV.*

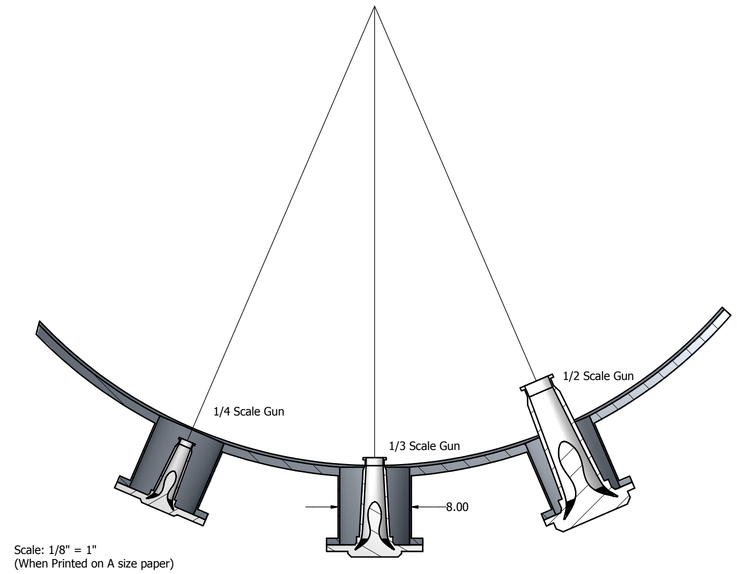

Figure 124 *Quarter-, Third-, and Half-Scale coax guns mounted on the standard 8 inch PLX ports as an illustration of possible layouts. The mounts shown are reentrant, which minimize hardware sticking out of the vacuum tank and extends the muzzle closer to the center. The different sizes are simple scalings of the full scale gun. In reality, the electrode profiles would be different for each gun size, since the profiles don't just scale directly.*

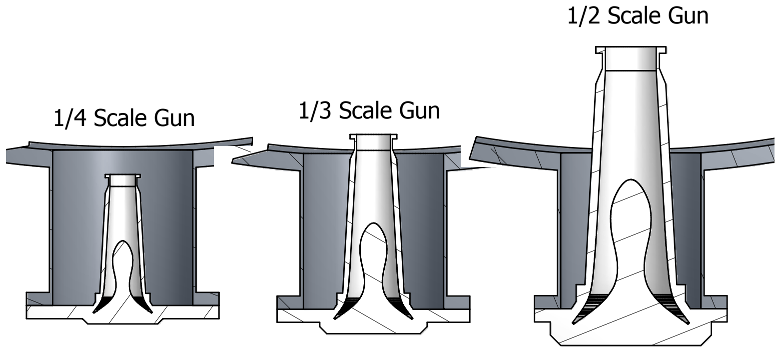

Figure 125 *A larger comparison of Quarter-, Third-, and Half-Scale coax gun sizes mounted on 8 inch PLX ports. The mounts shown are reentrant. The mounting flange would be an integral part of the back end of the gun and forms the vacuum seal alnong with the outer electrode. The guns could also be mounted directly at the gun muzzle for an even simpler vacuum seal.*

10.3 The Full Scale Coax Gun

The full-scale coax gun was constructed to allow high energy testing of low molecular weight plasmas at very high velocity (>200 km/s) and with better diagnostic access. It uses 64 small ablative capillary plasma injectors identical to those used in the half-scale coax gun as described in detail in [48]. This gun incorporated numerous diagnostic ports for Bdot and photodiode detectors along the barrel to study plasma armature dynamics. However, funding was terminated before we could do much testing with this gun.

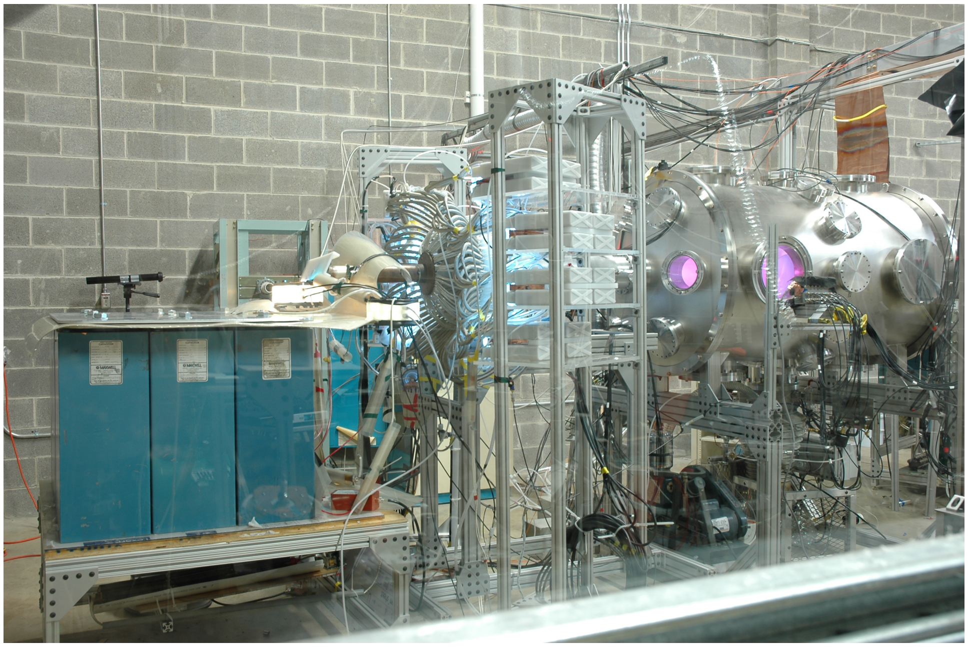

(a) The full-scale coax gun firing at low energy. The gun is mostly hidden by the towers in the center which hold the capacitors for driving the 64 capillary injector units. The large vacuum chamber (3ft dia by 6 ft long) is on the right.

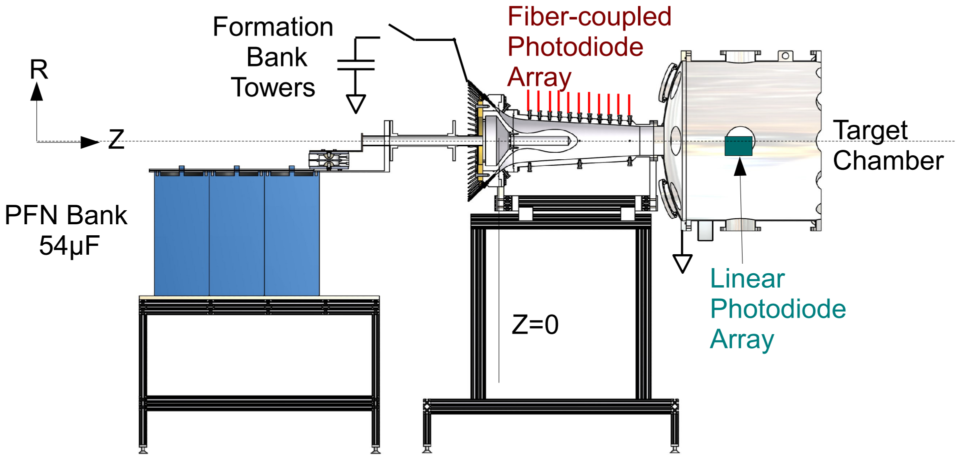

(b) Layout of full-scale gun hardware

Figure 126 *Full-scale coax gun firing into target vacuum tank.*

MACH2 simulations of the full-scale gun show that it should be capable of accelerating 500 μg to over 200 km/s. The plot in Figure 127 shows that it could also accelerate 8000 μg of plasma to 50 km/s (with a high-Z gas injection system), providing a useful baseline design point for Coax gun development.

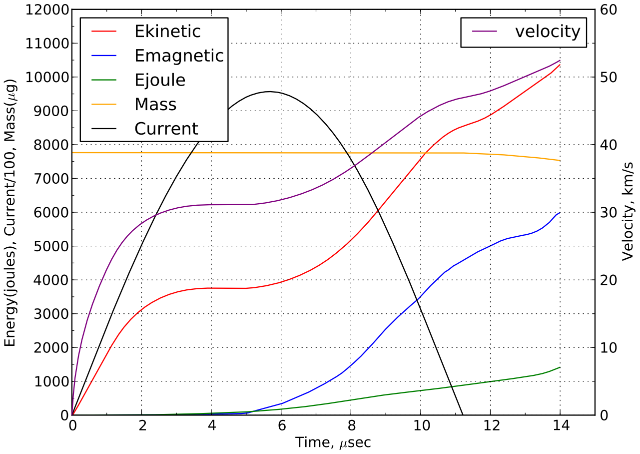

Figure 127 *MACH2 simulation of full scale gun shows that it can achieve the desired 8000 μg at 50 km/s. This provides a starting point from which to scale to smaller sizes.*

The effect of nozzle shaping in the coax gun is illustrated in Figure 128, which shows electron density profiles at 7.8 and 8.0 μs for three different outer electrode profiles from MACH2 simulations. The middle and right case illustrate how simple shaping of the outer electrode can lead to smoother better shaped plasmoids. It is clear that we will have a very strong and flexible tool to control the plasma topology by shaping the electrodes.

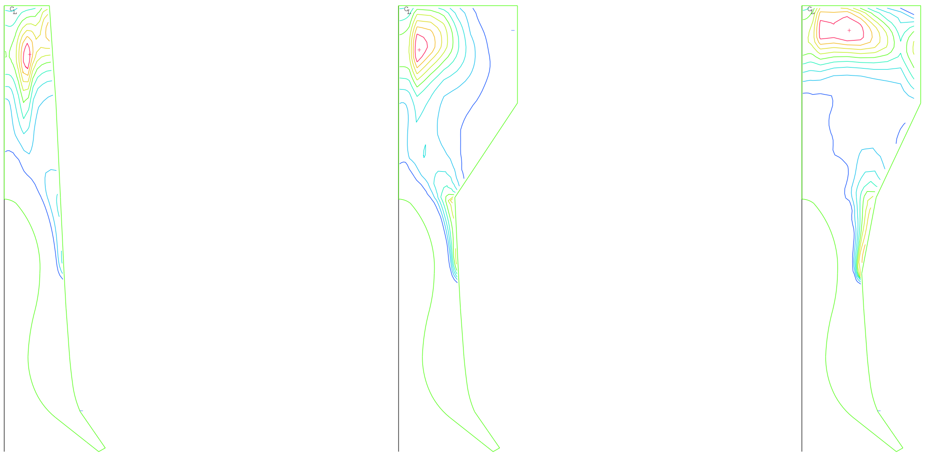

(a) 7.8 μs, $4.3{\times}10^{16}$ cm^{-3}, 190 k/s.

(b) 7.8 μs, $2.15{\times}10^{16}$ cm^{-3}, 195 k/s.

(c) 7.8 μs, $1.11{\times}10^{16}$ cm^{-3}, 205 k/s.

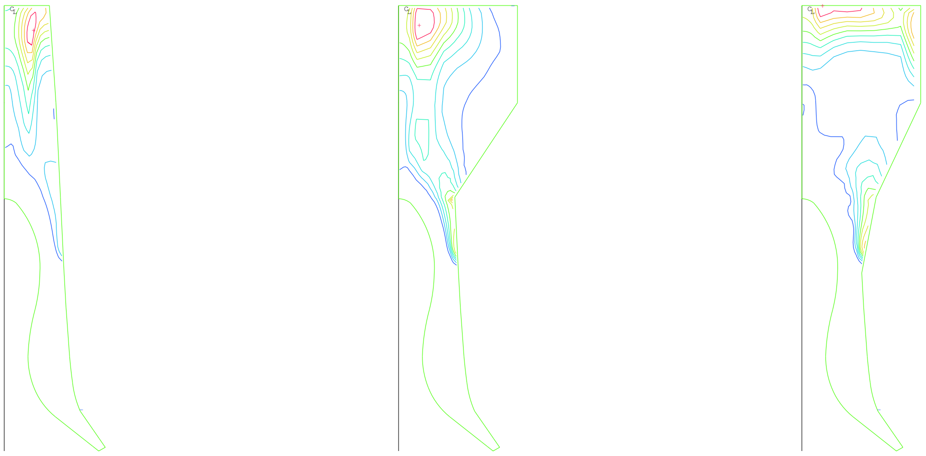

(d) 8.0 μs, $4.09{\times}10^{16}$ cm^{-3}, 180 k/s.

(e) 8.0 μs, $1.63{\times}10^{16}$ cm^{-3}, 180 k/s.

(f) 8.0 μs, $0.93{\times}10^{16}$ cm^{-3}, 190 k/s.

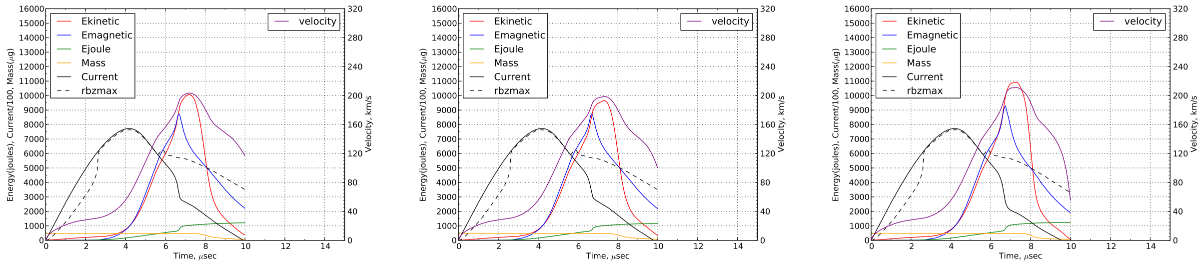

(g) (h) (i)

Figure 128 *Electron density contours form* M*ACH*2 *simulations of full-scale coax gun. Density listed is peak density inside inner red contour. Nozzle shape, along with the contoured accelerator electrode profile, provides a key tool that is much more effective at controlling plasma jet topology than is the case for parallel-plate railguns. Plots at the bottom show time history plots of current, bulk plasma velocity, total mass, and various energies.*

10.4 Injection Approaches

Any gas armature injection system requires at least one gas valve that can be opened on a timescale short compared to the time it takes gas to flow into the breech of the gun. For high-Z gases, this constraint is less of a problem than for low molecular weight gases like hydrogen with much higher sound speeds. For our guns, it is desirable to be able to open in 50-100 μs. It is possible to construct electro-magnetically driven valves on such time scales. Previous coaxial railguns have employed both a single fast valve and arrays of fast valves to inject gas. The Ring Accelerator Experiment (RACE) employed an annular array of fast gas valves to inject target gas [21]. The Compact Toroid Injection Experiment (CTIX) uses a single annular gas valve [22]. The chief aspects of design to consider are: the flow rate and uniformity of the injected gas pulse into the breech because this will affect the armature. The volume of gas plenum not in the gun breech, because this determines the amount of residual plasma exhausted by the gun, and the kilo-Amp-turns (kA-turns) necessary to open the gas valve on the required time scale. Several options exist for constructing a fast gas valve for a future HyperV coaxial railgun - 1) the present minirail gas valve can be adapted to the coaxial geometry, 2) a single-coil annular gas valve can be created, ans 3) a multi-coil annular gas valve could also be engineered.

10.4.1 Central Gas Valve

An operational fast-gas valve, shown earlier in Figure 38, has already been created for the minirailgun. The minirail gun gas valve can deliver 4.8 cm^3 of target gas at pressures up to 60 psig in 25 μs. The valve has a throat diameter of 20 mm and requires 160 kA-turns to move a 3.8 g aluminum plate. The present experimental minirailgun gas valve shows consistent performance with a present mean time to failure of ~50 shots. A gas valve of this design could be mated with the coaxial electrodes as shown in Figure 129. A central plenum can disperse gas through a series of parallel perforations in the center electrode. The chief advantages of this technique are that it leverages an existing gas valve design and requires only a single gas valve per coaxial gun.

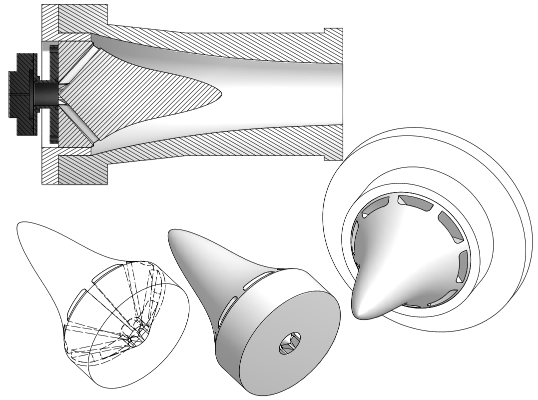

Figure 129 *An existing fast gas valve could be mated to coaxial electrodes to inject gas from a central plenum. We will try this first just to get the research started quickly.*

10.4.2 Single-Coil Annular Gas Valve

In order to improve the annular uniformity of the injected gas pulse, an annular gas valve can be engineered into the breech of the coaxial gun. As shown in Figure 130(a), an annular flyer plate can be driven by a single large coil that has been designed to allow orifices, through which to inject gas into the breech of the gun. This design not only reduces the center electrode complexity from the central gas valve design, but also reduces the volume of gas plenum which drains into the breech of the gun after the shot. Furthermore, it provides the ability to add a pre-ionization system to the coaxial gun. An annular array of the formation electrodes can be placed into the breech of the gun, and used to pre-ionize the plasma before the acceleration pulse is fired.

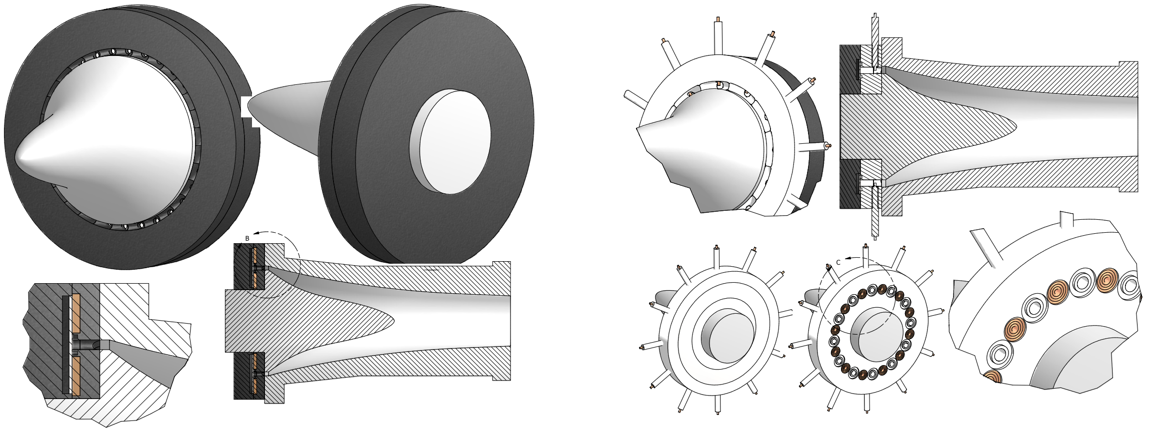

(a) An annular flyer plate can be driven by a single large coil which injects gas into the breech of the gun through an array of orifices.

(b) An annular flyer plate which injects gas into the breech of the gun through an array of offices can also be driven by an array of small coils.

Figure 130 *Short compact jets have been achieved with the MiniRailguns*

10.4.3 Multi-Coil Annular Gas Valve

A variation on the annular gas valve illustrated in Figure 130(b) would be to use an array of small coils to drive the flyer plate. This design retains the advantages of the single coil valve design, but also prevents the gas valve driver coil from having to fill the entire center region of the gun with flux. This reduces the kA-turns necessary to drive the flyer plate.

10.4.4 Multiple Small Gas Valves

We built and tested two smaller gas valves, about half the size of the earlier 1 cm version. Preliminary testing showed a jitter of 1-2 μs in the arrival time of the pressure front in a minirailgun using a pressure probe located up in the bore. This is very encouraging, since we typically have a 100-150 μs delay before firing the gun. This was a first attempt, and we should be able to get that jitter in the gas valve opening below 1 μs with further effort. This would be accomplished with more exacting tolerances on the parts, and by hitting the drive coil harder. Figure 131 shows a concept that would incorporate several of these smaller gas valves into the breech of a coax gun.

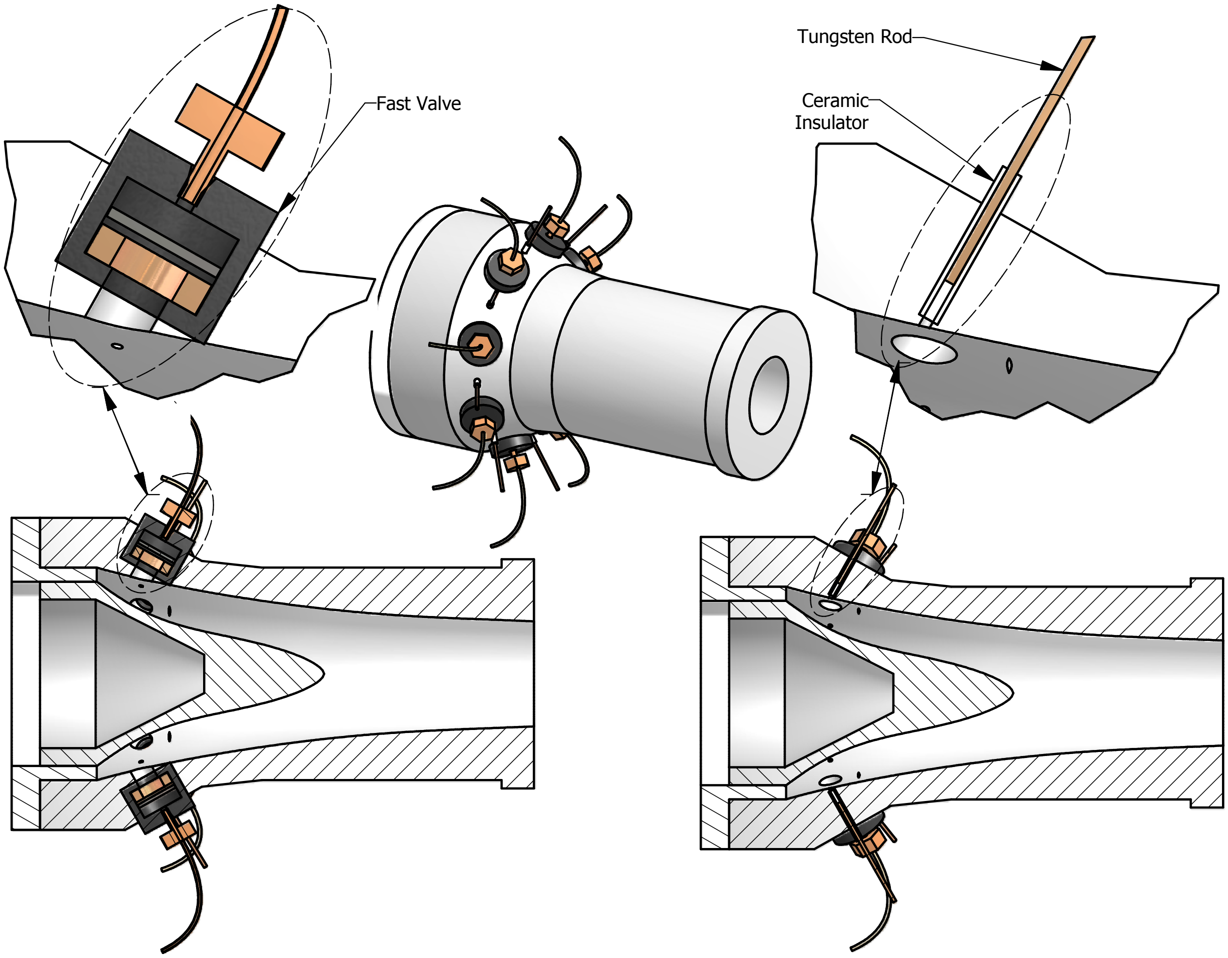

Figure 131 *Multiple small fast gas valves and miniET ignitor.*

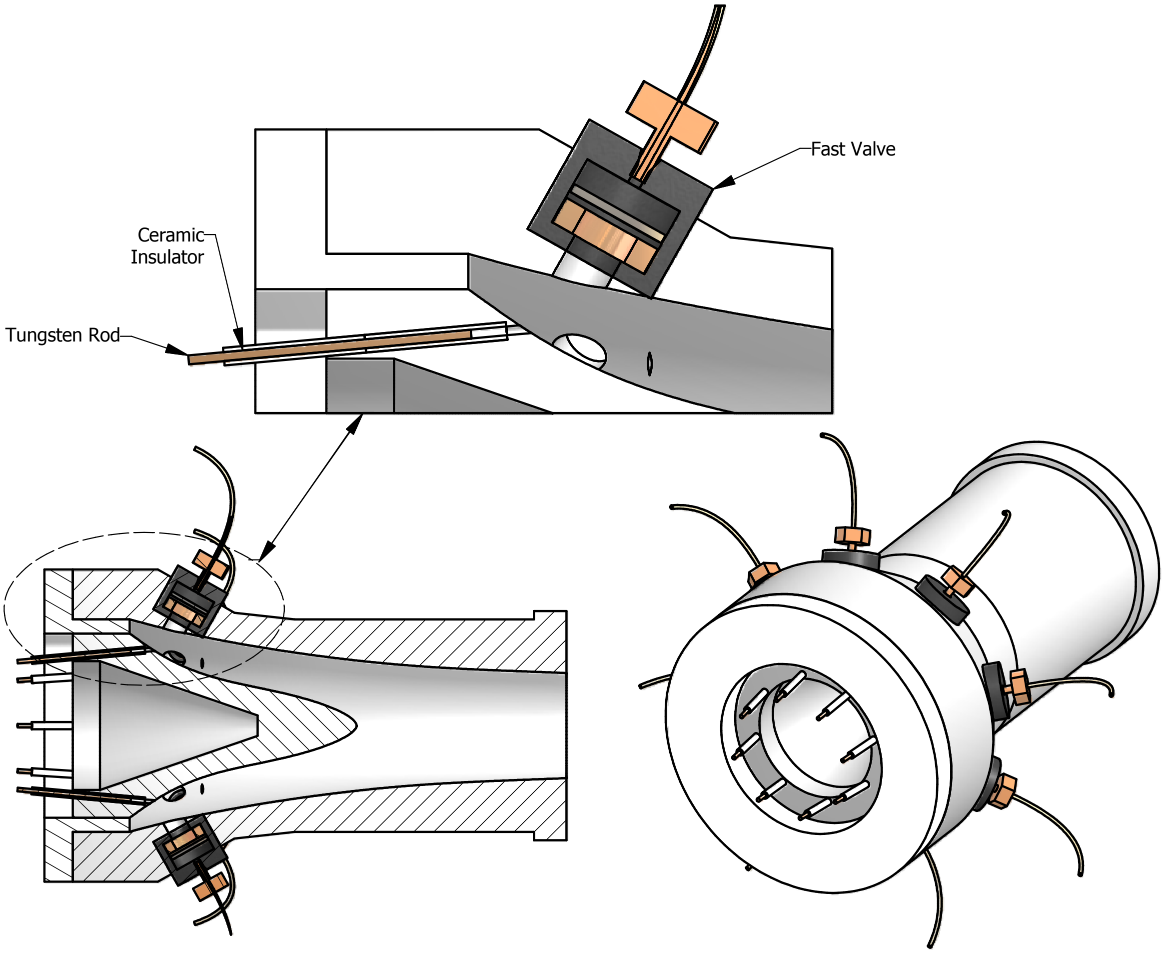

Figure 132 *Multiple small fast gas valves and miniET ignitor.*

11 Acknowledgments

The authors gratefully acknowledge the excellent electromechanical design and CAD work of Dave van Doren at HyperV. Thanks also go to Tom York for assistance with pressure probes and donation of some equipment, to Tim Barrett for design and construction of much electronic controls, to Mike Freese for help with Mach2 modeling, to Snezhana Abarzhi for theoretical analysis, and to Jason Cassibry and Bruno Bauer for modeling and analytical support. Additional thanks goes to Scott Hsu, Jason Cassibry, Mark Gilmore and the rest of the PLX Team for helping make this project possible and for many stimulating discussions. We also acknowledge and thank the U.S. Department of Energy Office of Fusion Energy Sciences for its funding support. A final special thanks to Francis Thio for many useful technical and scientific discussions, for originating the PJMIF concept and the contoured gap coaxial plasma gun approach, and for his support of this project.

References

[1] Y.C.F. Thio, C.E. Knapp, R.C. Kirkpatrick, R.E. Siemon, and P.J. Turchi, Journal of Fusion Energy, **20**, Nos. 1/2, 1-11, June (2002).

[2] R. E. Siemon, I. R. Lindemuth, and K. F. Schoenberg, Comments on Plasma Physics and Controlled Fusion, **18**, 363 (1999).

[3] R. E. Siemon, P. J. Turchi, D. C. Barnes, J. H. Degnan, P. Parks, D. Ryutov, and Y. C. F. Thio, Proc. of the Joint Conference of the 12th International Toki Conference and the 3rd General Scientific Assembly of Asia Plasma & Fusion Association, Toki, Japan, December 11-14 (2001).

[4] I. R. Lindemuth and R. C. Kirkpatrick, Nuclear Fusion, **23**, 263 (1983).

[5] R. C. Kirkpatrick, I. R. Lindemuth, and M. S. Ward, Fusion Technology, **27**, 201 (1995).

[6] Y. C. F. Thio, E. Panarella, R. C. Kirkpatrick, C. E. Knapp, and F. Wysocki, Current Trends in International Fusion Research, Proceedings of the 2nd Symposium, E. Panarella, ed. (NRC Press, National Research Council of Canada, Ottawa, Canada, 1999).

[7] Y.C.F. Thio, First U.S. Plasma Jet Workshop, Los Alamos National Laboratory, January 24-25 (2008).

[8] J. H. Degnan, W. L. Baker, M. Cowan Jr, J. D. Graham, J. L. Holmes, E. A. Lopez, D. W. Price, Dale Ralph, and N. F. Roderick, “Operation of a Cylindrical Array of Plasma Guns,” *Fusion Technology* **35** pp. 354-360 (May 1999).

[9] J. H. Degnan, M. L. Alme, B. S. Austin, J. D. Beason, S. K. Coffey, D. G. Gale, J. D. Graham, J. J. Havranek, T. W. Hussey, G. F. Kiuttu, B. B. Kreh, F. M. Lehr, R. A. Lewis, D. E. Lileikis, D. Morgan, C. A. Outten, R. E. Peterkin, D. Platts, N. F. Roderick, E. L. Ruden, U. Shumlak, G. A. Smith, W. Sommars, and P. J. Turchi, “Compression of Plasma To Megabar Range using Imploding Liner,” Phys. Rev. Lett. 82, 2681 (1999).

[10] S. C. Hsu, “Technical Summary of the First U.S. Plasma Jet Workshop,” J. Fusion Energy Vol 28, 3, (2009).

[11] J. Cassibry, S. Thompson, S. Hsu, D. Witherspoon, Bull. Amer. Phys. Soc., **53**, (4), p.155 (2008).

[12] J.T. Cassibry, R. J. Cortez, S. C. Hsu and F. D. Witherspoon, ”Estimates of confinement time and energy gain for plasma liner driven magnetoinertial fusion using an analytic self-similar converging shock model,” Physics of Plasmas, 16, 112707 (2009).

[13] S. C. Hsu, T. J. Awe, S. Brockington, A. Case, J. T. Cassibry, G. Kagan, S. J. Messer, M. Stanic, X. Tang, D. R. Welch, and F. D. Witherspoon “Spherically Imploding Plasma Liners as a Standoff Driver for Magneto-Inertial fusion” *IEEE Transactions on Plasma Science* **40**, 5 pp. 1287 (2012).

[14] Y.C.F. Thio - private communication (2004).

[15] K.L. Baker, D.Q. Hwang, R.W. Evans, R.D. Horton, H.S. McLean, S.D. Terry, S. Howard, and C.J. DiCaprio, Nucl. Fusion **42**, pp. 94-99 (2002).

[16] K.L. Baker, R.D. Horton, D.Q. Hwang, R.W. Evans and S. Howard, IEEE Trans. Plasma Sci. **30**, 48 (2002).

[17] J.T. Cassibry, Y.C.F. Thio, and S.T. Wu, Phys. of Plasmas, **13**, 053101 (2006).

[18] R.G. Jahn, *Physics of Electric Propulsion*, 1st ed., New York, McGraw-Hill, pp. 272-275, 288-297 (1968).

[19] J. Marshall, Phys. Fluids, **3**, p. 134 (1960).

[20] J.H. Degnan, R.E. Peterkin, Jr., G.P. Baca, J.D. Beason, D.E. Bell, M.E. Dearborn, D. Dietz, M.R. Douglas, S.E. Englert, T.J. Englert, K.E. Hackett, J.H. Holmes, T.W. Hussey, G.F. Kiuttu, F.M. Lehr, G.J. Marklin, B.W. Mullins, D.W. Price, N.F. Roderick, E.L. Ruden, C.R. Sovinec, P.J. Turchi, G. Bird, S.K. Coffey, S.W. Seiler, Y.G. Chen, D. Gale, J.D. Graham, M. Scott, and W. Sommars, Phys. Fluids B **5** (8), pp. 2938-2958, August (1993).

[21] J.H. Hammer, C.W. Hartman, J.L. Eddleman, and H.S. McLean, Phys. Rev. Lett. **61**, 25 Dec (1988).

[22] H.S. McLean, D.Q. Hwang, R.D. Horton, R.W. Evans, S.D. Terry, J.C. Thomas, R. Raman, Fusion Science & Technology **33**, (3) May (1998).

[23] M. Rosenbluth, Los Alamos Sci. Tech. Rept. LA-1850, Los Alamos, NM (1954).

[24] P.J. Hart, Phys. Fluids **5**, 38 (1962).

[25] Y.C.F. Thio, J.T. Cassibry, and T.E. Markusic, "Pulsed Electromagnetic Acceleration of Plasmas," AIAA Joint Prop. Conf., Indianapolis, IN, Paper AIAA-2002-3803, July (2002).

[26] O. V. Gotchev et al., "Magneto-inertial Approach to Direct-drive Laser Fusion," J. Fusion Energy **27**, 25 (2008).

[27] G. A. Wurden, T. P. Intrator, P. E. Sieck, L. Dorf, S. C. Hsu, R. Renneke, W. J. Waganaar, Z. Wang, J. H. Degnan, E. L. Ruden, M. Domonkos, P. Adamson, C. Grabowski, D. G. Gale, M. Kostora, W. Sommars, M. H. Frese, S. D. Frese, J. F. Camacho, S. K. Coffey, N. F. Roderick, D. J. Amdahl, P. Parks, R. E. Siemon, T. Awe, and A. G. Lynn, "FRCHX Magnetized Target Fusion HEDLP Experiments," Los Alamos Technical Report LA-UR-080796, presented at the IAEA Fusion Energy Conference (2008).

[28] P. B. Parks, "On the efficacy of imploding plasma liners for magnetized fusion target compression," Phys. Plasmas **15**, 062506 (2008).

[29] D. D. Ryutov and Y. C. F. Thio, "Plasma Liner with an Intermediate Heavy Shell and Thermal Pressure Drive," Fusion Sci. Tech. **49**, 39 (2006).

[30] S. Kohno, Y. Teramoto, I.V. Lisitsyn, S. Katsuki, and H. Akiyama, IEEE Trans. on Plasma Sci., **27**, No. 3, pp. 778-785, June (1999).

[31] D.A. Tidman, Y.C. Thio, S.A. Goldstein, and D.S. Spicer, GT-Devices Tech Note GTD 86-7, November (1986).

[32] R.L. Burton, S.A. Goldstein, D.A. Tidman, S.Y. Wang, N.K. Winsor, and F.D. Witherspoon, IEEE Trans. on Magnetics, **Mag-22**, pp. 1410-1415, November (1986).

[33] Burton, R. L., D. Fleischer, S.A. Goldstein, D.A. Tidman, J. Propulsion and Power, **6**, No. 2, p. 139 (1990).

[34] M. Levin, A. Pukhov, R.F. Hubbard, D. Kaganovich, D.F. Gordon, P. Sprangle, A. Ting, B. Hafizi, and A. Zigler, App. Phys. Lett. **87**, 261501 (2005).

[35] B.H.P. Broks, W. Van Dijk, J.J.W. van der Mullen, A.J. Gonsalves, T.P. Rowlands-Rees, and S.M. Hooker, Phys. of Plasmas **14**, 023501 (2007).

[36] D.J. Spence, P.D.S. Burnett, and S.M. Hooker, Optics Letters, Vol. **24**, p. 993 (1999).

[37] Y. Ehrlich, C. Cohen, D. Kaganovich, A. Zigler, R.F. Hubbard, P. Sprangle, and E. Esarey, J. Opt. Soc. Am. B **15**, 2416 (1998).

[38] D.J. Spence and S.M. Hooker, Phys. Rev. E **63**, 015401(R) (2000).

[39] C.D. Macchietto, B.R. Benware, and J.J. Rocca, Optics Lett. **24**, No. 16, 1115 (1999).

[40] B.R. Benware, C.D. Macchietto, C.H. Moreno, and J.J. Rocca, Phys. Rev. Lett. **81**, 5804 (1998).

[41] J.J. Rocca, D.P. Clark, J.L.A. Chilla, and V.N. Shlyaptsev, Phys. Rev. Lett. **77**, 1476 (1996).

[42] F.D. Witherspoon, R.L. Kincaid, and D.W. Massey, Jour. of Thermal Spray Tech., **11**, No. 1, pp.119-128, March (2002).

[43] J.T. Cassibry, PhD dissertation, University of Alabama in Huntsville, (2004).

[44] R. E. Peterkin, M. H. Frese, and C.R. Sovinc, J. Comp. Phys. **140**, 148 (1998).

[45] R. E. Peterkin, Jr. and M. H. Frese, Air Force Research Laboratory, Kirkland AFB, NM (2000).

[46] S. P. Lyon, and J. D. Johnson, "SESAME: The Los Alamos National Laboratory Equation of State Database," LANL Technical Report LA-UR-92-3407, Los Alamos National Laboratory, Los Alamos, NM (1992).

[47] I. Uzun-Kaymak, S. Messer, R. Bomgardner, A. Case, R. Clary, R. Ellis, R. Elton, C. Teodorescu, F. D. Witherspoon, and W. Young. "Cross-Field Plasma Injection into Mirror Geometry." *Plasma Phys. and Controlled Fusion*, **51**, 9, 095007 (Summer 2009).

[48] F. D. Witherspoon A. Case, S. J. Messer, R. Bomgardner III, M. W. Phillips, S. Brockington, and R. Elton. "A Contoured Gap Coaxial Plasma Gun with Injected Plasma Armature." *Rev. Sci. Inst.* **80**, 083506 (2009).

[49] J.D. Cobine, "Gaseous Conductors, Theory and Engineering Applications," Dover Publications, New York, 1958.

[50] W.J. Sarjeant, R.E. Dollinger, "High-Power Electronics," TAB Books, Blue Ridge Summit, PA, 1989.

[51] http://www.ohmite.com

[52] http:/www.caddock.com

[53] http:/www.hvrint.com

[54] P. Mazzotta, G. Mazzitelli, S. Colafrancesco and N. Vittorio, Aston. Astrophys. Suppl. Ser. **133**, pp. 403-409 (1998).

[55] M.A. Gigosos and V. Cardenoso, J. Phys. B **29**, pp. 4795-4838 (1996).

[56] D.E. Johnson, D.P. Bauer, IEEE Transactions on Magnetics **25**(1) pp. 271-276, January (1989).

[57] R.H. Lovberg, C.L. Dailey, AIAA Journal. **20** (7) 971-7, July (1981).

[58] A. Keshtkar, S. Bayati and A. Keshtkar, "Derivation of a Formula for Inductance Gradient Using Intelligent Estimation Method," IEEE Trans. on Magnetics, Vol. 45, No. 1, pp. 305-308, January, 2009.

[59] J.V. Parler, "Muzzle Shunt Augmentation of Conventional Railguns," IEEE Trans. on Magetics, Vol. 27, No. 1 pp. 80-84, January, 1991.

[60] R.L. Burton, F.D. Witherspoon, S.A. Goldstein, "Self-Augmented Railgun Experiments", Journal of Applied Physics, Vol. 70, pp. 3907-3911, October 1, 1991.

[61] F. D. Witherspoon, R. L. Burton and S. A. Goldstein, "Physics Experiments on the EMET Launcher Facility," IEEE Trans. Magnetics **25**, 605 (1989).

[62] F. D. Witherspoon, R. L. Burton and S. A. Goldstein, "Railgun Experiments with Lexan Insulators," IEEE Trans. Magnetics **17**, 353 (1989).

[63] F. D. Witherspoon and R. L. Burton, "GEDI EMET Railgun Experiments at GT-Devices," Final Report, AMCCOM Contract DAAA21-85-C-0228, November, 1991.

[64] F. D. Witherspoon, R. L. Burton and S. A. Goldstein, "A Second Generation EMET Railgun for Secondary Arc Studies," IEEE Trans. Magnetics **27**, 91 (1991).

[65] T. E. Markusic, "Current Sheet Canting in Pulsed Electromagnetic Accelerators," Ph.D. dissertation, Princeton University (2002).

[66] Bellan, Paul C., "Spheromaks - A Practical Application of Magnetohydrodynamic Dynamos and Plasma Self-organization," Imperial College Press London, 2000.

[67] Thomas J.C., Hwang D. Q., Horton R. D., Rodgers J.H., Raman R., "A Simple Fast Pulse Gas Valve using Dynamic Pressure as the Primary Closing Mechanism," Rev. Sci. Instrum. 64 (6), June, 1993.

[68] Horton, Robert; Howard, Stephen; Hwang, David; Brockington, Sam; Graf, Alex; Evans, Russell; Rogers, Michael "Density Buildup by Accelerator-Region Gas Puffing on CTIX," American Physical Society, 46th Annual Meeting of the Division of Plasma Physics, ÂăSavannah, GA. November, 2004.

[69] R. Horton, S. Howard, S. Brockington, R. Evans, D. Hwang, "Accelerator-Region Gas Puffing Experiments on CTIX," 2005 47th Annual Meeting of the Division of Plasma Physics, Denver, Colorado, October 2005.

[70] K.L. Baker, D.Q. Hwang, R.W. Evans, R.D. Horton, H.S. McLean, S.D. Terry, S. Howard and C.J. DiCaprio "Compact toroid dynamics in the Compact Toroid Injection Experiment" *Nucl. Fusion* **42**, 1, pp. 94-99 (2002).

[71] A. Case, S. Messer, R. Bomgardner, and F. D. Witherspoon. "Interferometer Density Measurements of a High-Velocity Plasmoid," Phys. Plasmas Vol. 17 No. 1 (2010).

[72] A. MacPhee, S. MacGregor, and S. Turnbull, IEEE Pulsed Power Conference 2, 781 (1995).

[73] H.G. Hammon III, G. Frazier, I. Roth, J. Naff, and P. Sincerny, "High-Coulomb spark gap for electric guns [pulsed power supply]," IEEE Trans. Magentics 27 pp. 356-358 (1991).

[74] J. Woodworth et al., "Optical and pressure diagnostics of 4-MV water switches in the Z-20 test Facility," IEEE Trans. Plas. Sci. 32 pp. 1778-1789 (2004).

[75] J. Schien, IEEE Conf. Pulsed Power Plas. Sci (2001).

[76] S. Roche, Physique and Industrie (2004).

[77] Parallel Operation of Dynex IGBT Modules, Dynex Semiconductor, Doddington Road ,Lincoln, Lincolnshire. LN6 3LF. United Kingdom (2002).

[78] W. Nunnally, R. Neurath, C. Holmes, S. Sampayan, and G. Casporaso, Pulsed Power Conference (2003).

[79] T. Kanabe, K. Yoshida, Y. Kato, M. Nakatsuka, and C. Yamanaka, Rev. Sci. Instrum. 57, 2 (1985).

[80] Switch Model SG-103M, R.E.Beverly III and Assoc., P.O.Box 198, Lewis Center, OH 43035 (2002).

[81] K. LeChien et al., 11 (2008).

[82] W. Weisser, K. Frank, and G. Schroder, IEEE Trans. Plas. Sci. 29 (2001).

[83] J. M. Lehr, M. D. Abdalla, F. R. Grunner, B. C. Cockreham, M. C. Skipper, S. M. Ahern, and W. D. Prather, IEEE Trans. Plas. Sci. 28 (2000).

[84] S. Hussain and M. Zakaullah, Plasma Sci. Tech. 9, 504 (2007).

[85] L. H. Bowen, E. G. Farr, J. Elizondo, and J. Lehr, Switching Notes. (1999).

[86] J. Niedbalski, J. Phys. D: Appl. Phys. 29, 789 (1996).

[87] Model SG-111M-75C Spark Gap Switch, R.E.Beverly III and Assoc., P.O. Box 198, Lewis Center, OH 43035 (2009).

[88] D. Denissov, H. Rebholz, W. Khler, and S. Tenbohlen, University of Stuttgart IEH (2005).

[89] A. R. Dick, S. J. MacGregor, M. Buttram, R. Pate, L.F.RineHart, and K. Prestwich, IEEE Trans. Plas. Sci. 28 (2000).

[90] Operation and Maintenance Manual, Titan Systems Corperation-Pulse Siences Division, 2700 Merced St, San Leandro, CA 94577 (1996).

[91] Technical Description and Specifications PG-103D Trigger Generator, R.E.Beverly III and Assoc., P.O.Box 198, Lewis Center, OH 43035 (2008).

[92] D. Meeker, Finite Element Method Magnetics User's Manual (2010).

[93] "High-Density Tungsten Based Metals," Mi-Tech Metals Inc., 4701 Massachusetts Ave, Indianapolis, Indiana 46218.

[94] MAKROLON GP (Polycarbonate), Plastics International, 7600 Anagram Drive Eden Prairie, MN 55344 (2004).

[95] Delrin (Acetal Homopolymer), Plastics International, 7600 Anagram Drive Eden Prairie, MN 55344 (2004).

[96] http://www.code-aster.org

[97] M. Keidar, I. Boyd, and I. Beilis, J. Prop. Power (2003).

[98] J. Powell and A. Zielinski, IEE. Trans Mag. 29 (1993).

[99] Delrin Acetal resins: Design Information, Dupont, Barley Mill Plaza, Building 22, P.O. Box 80022, Wilmington, Delaware 19880 (2003).

[100] R. Raman and P. Gierszewski, Fusion Engin. Design 39- 40 (1998).

[101] W. Liu and S. Hsu, Nucl. Fusion 51 (2011).

[102] I. Bogatu, J. Kim, and S. Galkin, IEEE ICOPS (2009).

[103] I. Uzun-Kaymak, S. Messer, R. Bomgardner, A. Case, R. Clary, R. Ellis, R. Elton, A. Hassam, C. Teodorescu, D. Witherspoon, et al., Journal Fusion Energy 28 (2012).

[104] S. Howard, M. Laberge, L. McIlwraith, D. Richardson, J. Gregson, "Development of Merged Compact Toroids for Use as a Magnetized Target Fusion Plasma," Journal of Fusion Energy 28 (2008).

[105] F. D. Witherspoon, A. Case, S. J. Messer, R. B. II, M. W. Phillips, S. Brockington, and R. Elton, "Minirailgun plasma jet accelerators for high energy density laboratory plasmas (HEDLP) and fusion applications," to be submitted to *Rev. Sci. Instrum.*

[106] K. Baker, R. Horton, D. Hwang, R. Evans, and S. Howard, IEEE Trans. Plas. Sci. 30 (2002).

[107] J. Kotas, C. Guderjahn, and F. Littman, IEEE Trans. Mag. 22 (1986).

[108] Fisher, A., Mako, F., and Shiloh, J., *Rev. Sci. Instrum.* **49**, 872 (1978).

[109] Lowder, R. S. *Rev. Sci. Instrum.* **11**, 1236 (1962).

[110] Wetstone, D. M. *Rev. Sci. Instrum.* **32** 1209 (1961).

[111] Thomas, J. C., Hwang, D. Q., Horton, R. D., Rogers, J. H., and Raman, R. *Rev. Sci. Instrum.* **64**, 1410 (1993).

[112] S. Brockington, *Profiling Compact Toroid Plasma Density on CTIX with Laser Deflection*, Thesis, University of California Davis (2007).

[113] A. Case, S. Brockington, S. Messer, R. Bomgardner, and F. D. Witherspoon, "A High Speed High Mass Flow Low Profile Magnetically Actuated Gas Valve," to be submitted to Rev. Sci. Instrum.

[114] J. Thomas, D. Hwang, R. Horton, J. Rogers, and R. Raman, Rev. Sci. Instrum. 64 (1993).

[115] S. Bozhenkov, K. Finken, M. Lehnen, and R. Wolf, Rev.Sci. Instrum. 78 (2007).

[116] R. Weast, M. Astle, and W. Beyer, CRC handbook of Chemistry and Physics (Boca Raton, FL, 1984).

[117] Brockington, S. et al., "Plasma Density Gradient Measurement Using Laser Deflection," Rev. Sci. Instrum. 76, 1 (2005).

[118] "More about Glass and ceramics," McMasterCarr Supply Co. (2012).

[119] ZTA-96 Zirconia Toughened Alumina Ceramic, AstroMet Inc., 9974 Springfield Pike, Cincinnati, OH 45215 (2013).

[120] G. E. Rolader, L. D. Thornhill, J. H. Batteh, and J. J. S. III, IEEE Trans. Mag. 29, 499 (1993).

[121] J. Parker, 14th IEEE conf. on Plasma Sci. (1987).

[122] J. Parker, W. Parsons, C. Cummings, and W. Fox, AIAA Fluid Dynamics and Plasma Dynamics and Lasers Conference Paper AIAA-85-1575 (1985).

[123] L. Thornhill, J. Batteh, and D. Littrell, Final Report for Period October 1987-September 1988 (1988).

[124] PDA100A Operating Manual - Switchable Gain, Ampli- fied Silicon Detector, PO Box 366, 435 Route 206N, Newton, NJ 07860 (2011).

[125] S. Brockington, A. Case, S. Messer, R. Bomgardner, and F. D. Witherspoon, "Plasma Railgun Momentum Measurements with Ballistic Pendulum," to be submitted to Rev. Sci. Instrum.

[126] J.V. Parker, "Magnetic probe Diagnostics for Railgun Plasma Armatures," IEEE Trans. Plas. Sci. **17** 3, pg. 487-500 (1989).

[127] HVP Advance Power Components High Energy Disk Resistors, 2250 Military, Road Tonawanda, NY, 14150 (2011).

[128] S. Brockington, A. Case, S. Messer, R. Bomgardner, and F. D. Witherspoon, "A High-Voltage, High-Current Switch for Plasma Pulsed Power Applications," to be submitted to Rev. Sci. Instrum.

[129] L. K. Tully, D. A. Goerz, R. D. Speer, and T. J. Ferriera, IEEE Itnl Power Mod. Conf. Las Vegas, NV, United States (2008).

[130] E. C. Merrit, A. G. Lynn, M. A. Gilmore, C. Thoma, J. Loverich, and S. Hsu, "Multi-chord fiber-coupled interferometry of supersonic plasma jets (invited)" *Rev. Sci. Instrum.* **83** 10D523 (2012).

[131] E. C. Merrit, A. L. Moser, S. C. Hsu, J. Loverich, and M. A. Gilmore, "Experimental Characterization of the Stagnation Layer between Two Obliquely Merging Supersonic Plasma Jets," *Phys. Rev. Letters* **111** 085003 (2013).

[132] E. C. Merrit, A. L. Moser, S. C. Hsu, C. S. Adams, J. P. Dunn, A. M. Holgado, and M. A. Gilmore, "Experimental evidence for collisional shock formation via two obliquely merging supersonic plasma jets," *Phys. Plasmas* **21** 055703 (2014).

[133] S. C. Hsu, A. L. Moser, E. C. Merritt, C. S. Adams, J. P. Dunn, S. Brockington, A. Case, M. Gilmore, A. Lynn, S. J. Messer, and F. D. Witherspoon, "Laboratory plasma physics experiments using merging supersonic plasma jets," submitted to J. Plasma Physics, (2014).

[134] J. Loverich and A. Hakim, "Two-Dimensional Modeling of Ideal Merging Plasma Jets," *J. Fusion Energy* **29** pp. 532-539 (2010).

[135] S. A. Galkin, I. N. Bogatu, and J. S. Kim, "High Density High Velocity Plasma Jet Interaction," *Proc. 16th IEEE International Pulsed Power Conference* pp.947-950, 2007.

[136] H.-K. Chung, M.H. Chen, W.L. Morgan, Y. Ralchenko, R.W. Lee, *High Energy Density Physics* **1**, pp 3-12 (2005).

[137] L. Wu, M. Phillips, F. D. Witherspoon, "Numerical Simulation of Merging Plasma Jets Using High-Z Gases" submitted to *IEEE Transactions on Plasma Science* April 2012.

[138] Jason Cassibry - private communication (2011).

[139] B. Longmeir, E. B. III, J. Squire, T. Glover, F. Chang-Diaz, and M. Brukardt, 47th AIAA Aero. Sci. Meeting. (2009).

[140] S.F. Goncharov, P. Pashinin, V. Perov, R. Serov, and V. Yanovsky, Rev. Sci. Instrum. **59** (1988).

[141] J. Grun and B.H. Ripin, Rev. Sci. Instrum. **53** (1982).

[142] W. Schall, H. Eckel, and S. Walther, "Lightcraft impulse measurements under vacuum," AFRL Report Contract EOARD FA8655-02-M4017 (2002).

[143] W. Schall, H. Eckel, J. Tegel, F. Waiblinger, and S. Walther, "Properties of laser ablation products of delrin with CO2 laser," EOARD Grant FA8655-03-1-3061 Final Report May 2004.

[144] D.A. Reilly, "Laser Propulsion Experiments - Final Report", AVCO Research Lab, Inc., Everett, Maine 02149, Subcontract B116822 for University of California Livermore National Laboratory, Jordan Kare, Program Manager, 1991.

APPENDIX

A Ballistic Pendulum

The Ballistic Pendulum is a very simple but powerful diagnostic based on allowing complete transfer of plasmoid momentum to a light polyethylene cup suspended by lightweight fibers. The subsequent deflection of the cup (measured using the PIMax camera multiple exposure feature) allows us to back out the plasmoid momentum with a small (20%) error introduced by ablation of material from the surface of the cup.

Plasma jet railguns under development at HyperV can be considered two-stage accelerators. The first stage, or formation stage, pre-forms a plasma armature and injects it into the bore of a linear parallel-plate or coaxial railgun. The second stage, or acceleration stage, drives a large current through the plasma armature, accelerating the ejected plasma jet to high velocity via the JxB Lorentz force. Plasma railguns have been proposed, or employed, as solutions for applications in tokamak refueling, ELM pacing, and disruption mitigation [100, 101, 102]. Plasma railguns are also being considered as rotation drivers for magnetically confined plasma [103], implosion liner drivers for plasma-jet magneto-inertia fusion reactors [13], and fuel injectors for magnetized target fusion generators [104]. These are in addition to their applications in laboratory astrophysics and satellite electric propulsion. While the topologies of these plasma railguns show vast similarities, what differs greatly are their required regions of performance. Regardless of the method used for armature formation and rail geometry, determining the momentum of the ejected plasma armature is critical to evaluating railgun performance and targeting rail gun design to specific applications. Additionally, once the armature plasma velocity is known, measurements of plasma momentum can be used to estimate the total mass ejected, also a critical performance metric.

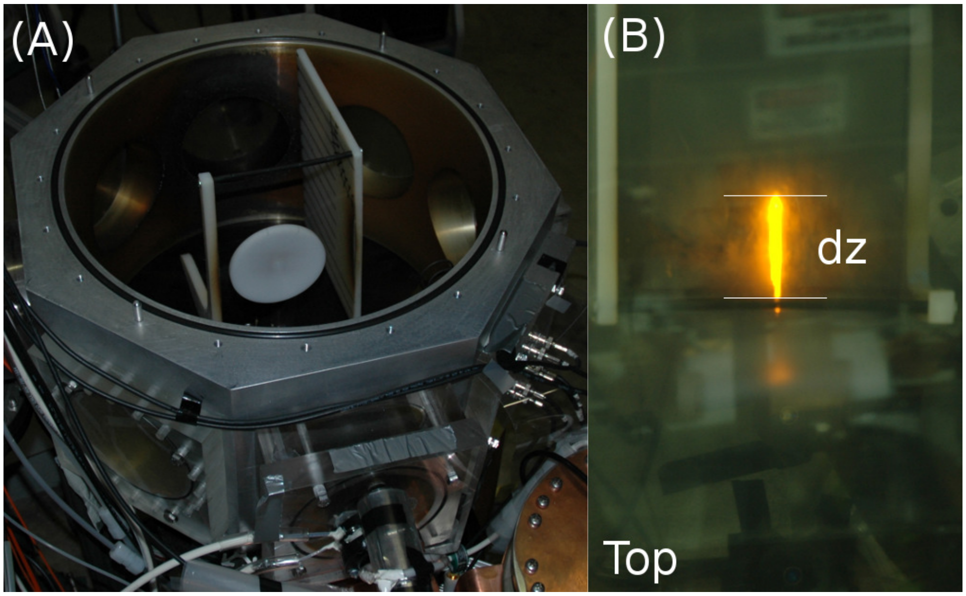

Figure 133 *Previous ballistic pendulums employed a LED mounted on the rear of the target plate (A). Pendulum motion was resolved by determining the distance of translation of LED in pixels via with a long exposure image (B), seen here in a top-down view. Image processing can be further complicated if the pendulum experiences torsion.*

Previous ballistic pendulum implementations at HyperV [48] used a LED on the pendulum target plate, whose motion was acquired with a long exposure Nikon camera. When resolved with 2-3 s exposure time, displacement of the pendulum resulted in an image with a faint streak of light denoting the apex of the pendulum arc. This design, while effective, was constrained by

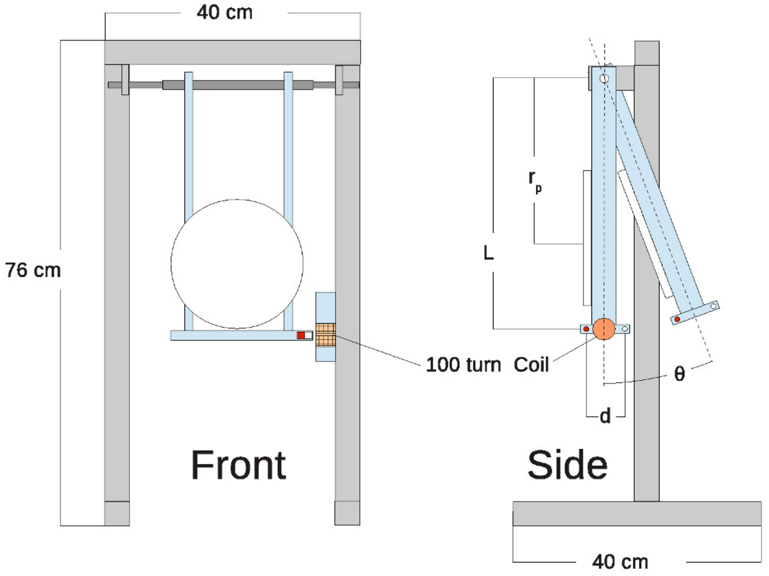

Figure 134 *The pendulum consists of two assemblies, a heavy rigid support frame, and a rigid rotating pendulum arm with strike plate. The arm assembly base contains two rare earth permanent magnets oriented to face a 100 turn pick-up coil mounted in the support in order to record pendulum velocity.*

the battery LED system on the pendulum strike plate. The LED had to be left on continuously and had limited battery life. The chamber would have to be cycled often to replace the battery. Additionally, resolving the light streak from the LED motion required image processing, often by hand, which was time consuming, not always obvious, and became harder to resolve as the intensity of plasma emission increased, especially after the use of neutral density filters became necessary to avoid saturating the camera CCD. This technique also required a pre-trigger of several seconds to allow the camera shutter time to open. Chip based accelerometers exist which could be used to resolve pendulum motion [139]. However, the chip has to be affixed to the moving pendulum arm in a low mass manner, and sufficient thermal management has to be provided for the chip, as well as electrical isolation from inbound plasma. Accelerometer IC's also require multiple in-vacuum signal lines, adding more complexity. Laser shadow-graphs have also been used for pendulum motion detection [140], but the laser usually needs to be placed outside of the vacuum chamber for cooling.

An alternative approach is to use a magnet and pickup coil to determine the velocity of the pendulum arm [141]. A magnetically sensed pendulum design records recoil motion without complicated trigger setups or cameras, thus allowing straightforward measurements of momentum. The pendulum then consists of a single unit that limits the exposure of electronics to plasma so that unambiguous, clearly resolved signals are generated. This expedites post-processing of the data, and facilitates automation of processing.

Pendulum Design

The pendulum design, shown in Figure 134, consists of two assemblies, a heavy rigid support frame, and a rigid rotating pendulum arm with strike plate. The support frame is of post and lintel construction with a stainless tube for the hinge axle. The pendulum arm is supported by this axle. The pendulum arm assembly consists of a larger stainless tube at the top creating the hinge, two plastic leg struts each of length L, and a plastic base plate containing two rare earth permanent

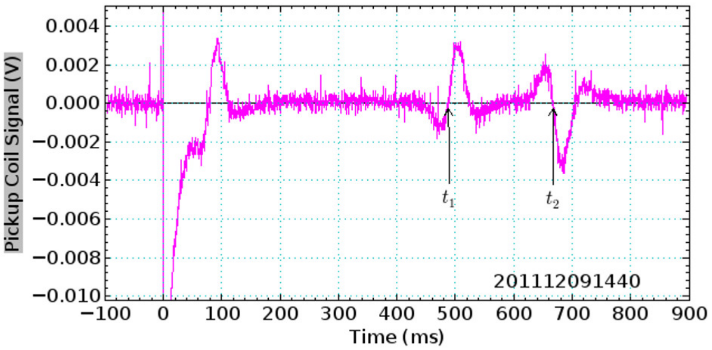

Figure 135 *When the return swing is large enough to send both magnets past the detector, a minimum and maximum induced current are generated at t_1 and t_2 which can be used to calculate the velocity of the pendulum.*

magnets[2] oriented to face outward in opposite polarities.

Signals generated by the motion of the pendulum arm magnets are then recorded by a 100 turn pick-up coil mounted on the support frame. The collision of the plasma “projectile” with the target plate imparts momentum. The pendulum swings backwards and upward with the velocity of the pendulum arm read out by the pickup coil on the return swing. The motion of the pendulum produces a characteristic pair of up/down signals whose order changes based on the direction of motion. The time separation between signal pairs provides the period of the pendulum. The time between the signals comprising the pairs is then used to determine the velocity of the pendulum from which the momentum imparted to the pendulum can be calculated from angular momentum.

Consider a plasma “projectile” of mass m_p and velocity v_p traveling along a path at a height r_p which strikes a pendulum with a target plate centered at r_p and a magnet array separation d affixed at a radius L from the hinge. The inertial moment of the pendulum can be calculated from its components: the sum of the moments of the tube at the hinge, the long rectangular bars radiating from the hinge to the sensor and target plates, and finally the sensor and target plates themselves. For an inelastic collision where the final momentum of the plasma is negligible, conservation of momentum states:

$$r_p m_p v_p = \dot{\theta}\Sigma I_i = \frac{v_d}{\sqrt{L^2 + d^2/4}}\Sigma I_i \tag{19}$$

where $\Sigma I_i = 2I_{leg} + I_{plate} + I_{base}$ is the sum of the moments of the components of the pendulum arm. The momentum of the plasma can then be calculated,

$$m_p v_p = \frac{v}{\sqrt{L^2 + d^2/4}\; r_p}\Sigma I_i \tag{20}$$

where v is the velocity of the end of the pendulum arm. Since the magnets on the pendulum base are separated by a known distance d, v can be calculated. When the return swing is large enough to send both magnets past the detector, a minimum and maximum induced current are generated at t_1 and t_2 as shown in Figure 135:

$$v = \frac{d}{t_2 - t_1} \tag{21}$$

---

[2] Ultra-High-Pull (2.3 lb) Nickel plated Neodymium Ring Magnet

From this an effective pendulum mass can be calculated for the radius at which the velocity measurement is acquired:

$$m_{eff} = \frac{\Sigma I_i}{L^2 + d^2/4} \tag{22}$$

This also implies that the minimum resolvable momentum is that which lifts the first magnet across the detector head, namely

$$p_{min} = \frac{d\sqrt{g}}{\sqrt[4]{4L^2 + d^2}}\ m_{eff} \tag{23}$$

where g is the gravitational acceleration constant. Similarly, the maximum resolvable momentum occurs when the pendulum is lifted to a height equal to half the length of the moment arm, namely

$$p_{max} = \sqrt{Lg}\ m_{eff}. \tag{24}$$

Larger motions of the arm may be discernible, but excessive motion of the pendulum arm increases the possibility of shifting the position of the base, which would likely invalidate the measurement.

The pendulum designed as shown in Figure 134 has an effective mass of ∼0.6 kg and a period of ∼1.2 s. A rigid object of mass 5 mg traveling at a velocity of 50 km/s is expected to produce a pendulum velocity of 0.51 m/s. At this velocity, a 100-turn pickup coil of inner diameter 4.8 mm produces signals of several millivolts. While these signals are small, EMF produced from firing a plasma railgun only lasts at most hundreds of microseconds, compared to the pendulum return swing requiring hundreds of milliseconds to occur. Because the pendulum motion is now acquired as a scope trace instead of as a camera image, bulk computer processing of pendulum data is greatly simplified. By making the striker plate interchangeable, a clean plate of the appropriate mass can be installed to measure the required momentum range of an experiment.

While the resistance of the hinge joint is low, the frictional losses in the pendulum are evident by the amount of time necessary to bring the pendulum to rest after perturbation. The hinge joint of the pendulum is composed of a stainless steel tube turning on a stainless steel shaft so as to minimize the coefficient of friction. Since the measurement of velocity is not recorded until the return swing of the pendulum, the amount of energy lost can be quantified by examining the Q factor of the pendulum. Since Q is the ratio of stored energy to energy lost per cycle, (or about twice the energy lost per half cycle), the initial velocity at impact, v_0, can be given by the measured pendulum velocity v by :

$$Q = 2\pi \frac{m{v_i}^2}{2(1/2m{v_i}^2 - 1/2m{v_{i+1}}^2)} \tag{25}$$

$$v_0 = \frac{v_1}{\sqrt{1 - \frac{\pi}{Q}}} \tag{26}$$

This implies a correction factor of 1.021 to the measured velocity for a pendulum of Q=77.0. The pendulum with a period of 1.175 s experiences about -35 dB reduction in motion in ∼107 s, so as long as the time between shots is reasonably greater, the pendulum is assured to come to rest before the next shot.

An additional correction factor can be applied to pendulum arm velocity as the v measured is the average velocity over the transit time past the detector and not the instantaneous velocity when $\theta = 0$. Consider the frictionless pendulum where position is give by $\theta(t) = \theta_0 \cos\sigma t$. The average angular velocity $\langle\dot{\theta}\rangle$ is

$$\langle\dot{\theta}\rangle = \frac{\theta(t_2) - \theta(t_1)}{t_2 - t_1} = \frac{\theta_0}{t_2 - t_1} 2\sin\sigma\frac{t_2 + t_1}{2}\sin\sigma\frac{t_2 - t_1}{2} \tag{27}$$

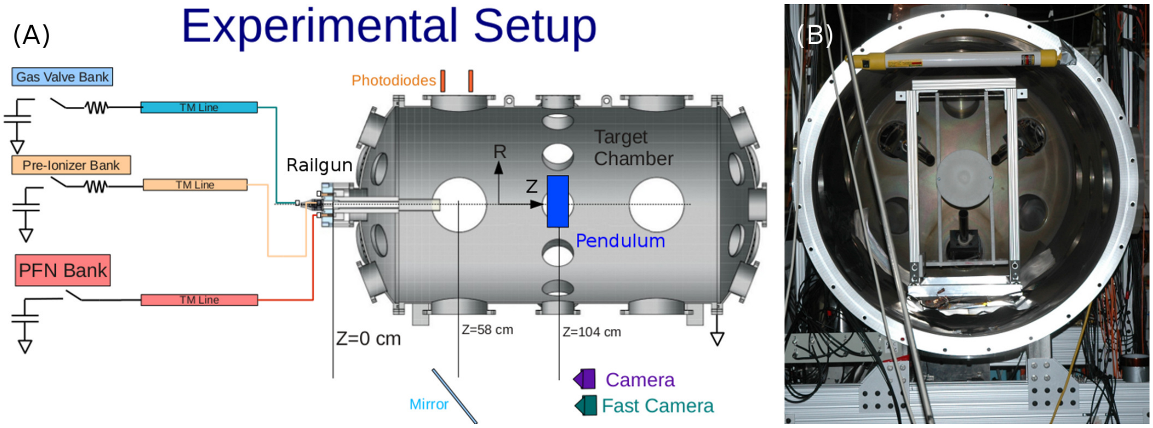

Figure 136 *(A) A 2.5 cm square-bore, linear plasma railgun was fired at a ballistic pendulum of L=40.6 cm and* M_{eff}*=0.58 kg mounted on center at Z=104 cm or about 55 cm from the end of the nozzle. A ∼ 20 cm diameter white Delrin plastic strike plate was used. A pair of photodiodes normal to the path of travel were used to measure plasma velocity. (B) The Ballistic Pendulum is shown mounted in the chamber with the end cap removed.*

where t_1 and t_2 are the time of arrival at the two equidistant positions on either side of the $\theta = 0$ position. This implies that the maximum angular velocity ω occurs at the average of the two times.

$$\omega = \theta_0 \sigma \sin \sigma \frac{t_2 + t_1}{2} \tag{28}$$

This allows the ratio of the average to the instantaneous angular velocities to be expressed as a function of the $\Delta t = t_2 - t_1$ recorded by the pendulum.

$$\frac{\omega}{\langle \dot{\theta} \rangle} = \frac{\sigma \Delta t}{2 \sin \sigma \delta t / 2} \tag{29}$$

For a pendulum with period $T = 2\pi/\sigma$ of 1.175 s, measuring an impulse resulting in a Δt of 0.099 s, $\omega/\langle \dot{\theta} \rangle$ is about 1.01 or 1% correction factor.

Linear Plasma Railgun Results

A ballistic pendulum with L=40.6 cm and M_{eff}=0.58 kg was constructed and used to measure the momentum produced by a 2.5 cm square-bore linear plasma railgun [105]. As shown in Figure 136, a plasma railgun was mounted with breech at Z = 0 cm. The pendulum was mounted on center at Z = 104 cm, or about 55 cm from the end of the railgun nozzle. A ∼ 20 cm diameter white Delrin plastic pendulum strike plate was used. A pair of neutral density filtered photodiodes separated by ΔZ = 18.4 cm were placed at normal chords along the axis of travel in order to measure the velocity of the ejected plasma. It was necessary to place black-wrap or mat black painted aluminum foil on the floor and wall of the chamber to eliminate chamber wall reflections of plasma emission. The rail gun pulsed gas valve was fed at 37 psig argon and employed a 1.6 kJ capillary pre-ionizer. The railgun PFN consisted of 141 μF charged to voltages of 24-25 kV. Driver currents for the railgun shot displayed are shown in Figure 137. This yielded a pendulum output as shown in Figure 135. As seen, the transit time of the pendulum magnets is measured to be 177.6 ms. Knowing the effective mass of the pendulum, this allows the momentum imparted to the pendulum to be calculated at ∼0.25 kg·m/s.

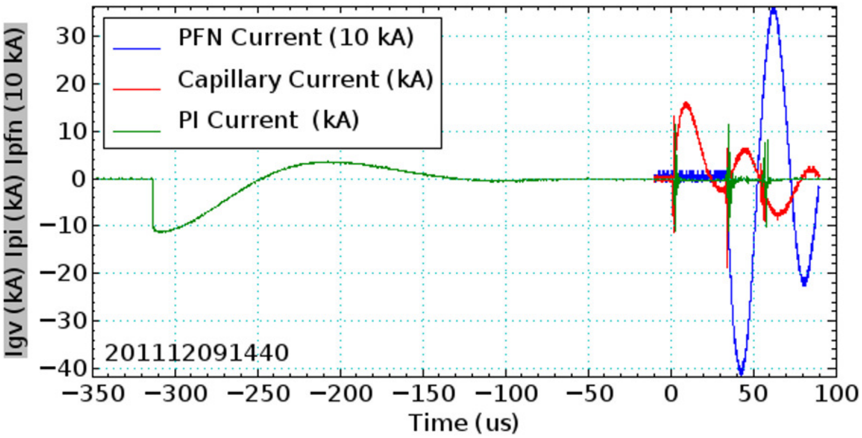

Figure 137 *Railgun driver current pulses are shown for the gas valve, pre-ionizer, and PFN of the railgun under test. A peak current of 419 kA was used to drive the PFN.*

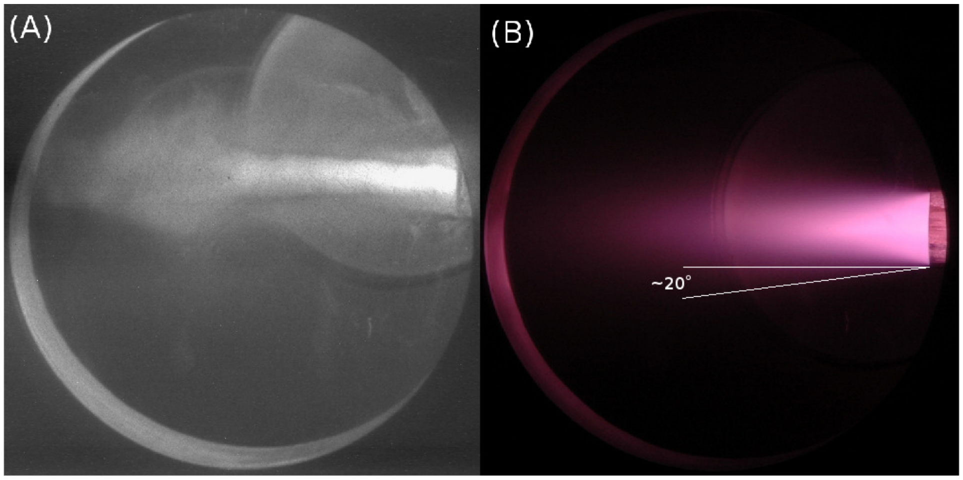

Figure 138 *Short and long exposure images of a collimated argon plasma armature emerging from the rail gun traversing toward the pendulum target. PIMax ICCD (A) and Nikon (B). Expansion angle estimated from imaging is ∼ 20°.*

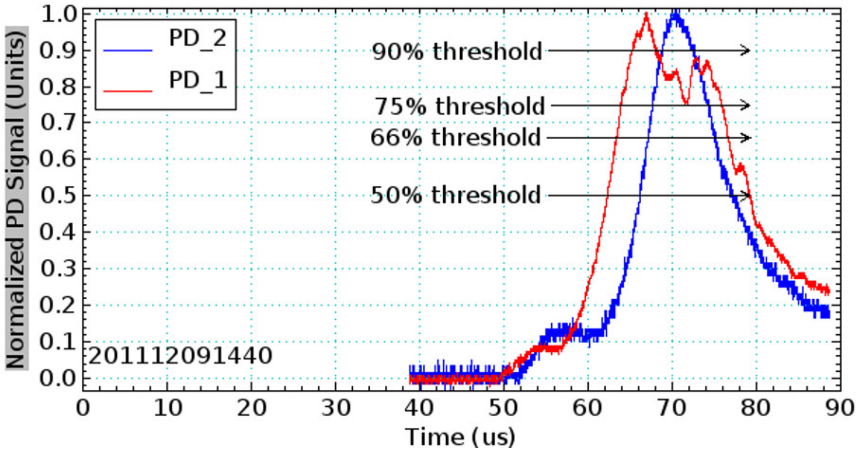

Figure 139 *Two collimated photodiodes were mounted normal to the transit of the plasma slug. By comparing the time of arrival of the centroid of plasma emission greater then a given threshold, the velocity of the plasma slug can be estimated. A time delay of 3.8 μs implies a plasma velocity of 49.4 km/s.*

The principle obstacles in interpreting pendulum measurements are in the dynamics of the plasma-target interaction. First, we must estimate the amount of plasma intercepted by the target plate. Next, plasma velocity must be determined so that plasma mass can be estimated. Finally, we must consider what kind of momentum contribution a reflected argon pulse or target sputtering would produce in order to verify that the argon armature is the principle source of momentum.

First, in order to impart momentum to the pendulum, the target plate should cover the cross-section of the expanding plasma slug. A 20 cm diameter white Delrin strike plate is expected to be of sufficient size to completely intercept plasma emerging from a 5 cm nozzle with ratios of v_p/v_{th} of at least 7.333. Below this threshold, the pendulum will underestimate momentum, as plasma will have expanded to a larger radius than the target plate. As shown in Figure 138, accelerated plasmas emerged collimated by the railgun nozzle at an angle of $\sim$ 10-20^o. This implies the exhaust plume diameter expands to as much as 25-44 cm when it reaches the pendulum plate.

Plasma mass can be estimated from momentum, if the plasma velocity is known. Collimated photodiode traces of ejected plasma emission are shown in Figure 139. While photodiodes measure plasma emission, which is related to, but not completely determined by, plasma density, measurements of line integrated plasma density from interferometry have tended to exhibit profiles similar to photodiode signals on previous experiments with these railguns [71]. Thus, plasma emission is a reasonable indicator of argon plasma line integrated density, and estimates of plasma velocity can be determined from two photodiode signals separated by a distance d by comparing the time of arrival of the thresholded centroid, where time of arrival is determined by the centroid of the signal f(t) exceeding a threshold of k % of maximum.

$$g_i(t) = f_i(t) \cdot (f_i(t) > k \cdot \max(f_i(t))) \tag{30}$$

$$c_i = \frac{\int t g_i(t) dt}{\int g_i(t)} \tag{31}$$

$$v = \frac{d}{c_1 - c_0} \tag{32}$$

Table 4 *Mass measurements for plasma velocities calculated using threshold values.*

Threshold %	V_p (km/s)	m_p (mg)
0	311	0.8
50	159	1.6
66	130	1.9
75	103	2.4
90	49	5.0
100	54	4.6

Plasma masses for various threshold levels are shown in Table 4, as well as the ratio of the considered integral to the discarded integral of each metric. A threshold of 90% of peak emission measures plasma velocity to be 49.4 km/s and plasma mass to be 5.0 mg for this shot.

Finally, there are two mechanisms which could cause the pendulum to over-estimate the momentum in the ejected plasma slug, a reflected plasma pulse, and sputtering from the target plate. It is possible to observe backward traveling signals with the photodiodes measuring velocity. We added 10 nm band pass filters at $\lambda = 470\ nm$ to the photodiode in order to further isolate the contributions from argon emission versus any impurities produced by ablation of bore materials. When operated at full power, however, filtered photodiodes produced measurements of negative velocity. This implies that emission in the bandpass region is as great as, or increased after the collision with the pendulum plate. Negative velocities were determined to be about –18.4 km/s. These signals are likely the thermal expansion of the plasma armature after being heated by the collision with the target plate. A velocity of 18.4 km/s would imply a temperature of 47 eV. If a reflected plasma was traveling backward at this velocity, it would have to contain a mass of 0.13 mg to effect 1% changes in pendulum momentum readings.

Sputtering of the target plate material would also inflate pendulum momentum measurements. A per particle energy of 517 eV is expected to be the sputtering threshold of Delrin. Coupling of energy is reduced because the plasma slug is normally incident to the target plate [139]. A target mass of 2.6 g was ablated over ∼89 shots, or ∼29.2 mg per shot. This implies that sputtered particles would have to be ejected at a velocity of only 84.2 m/s to effect 1% changes in pendulum momentum readings, but a velocity of 8420 m/s is necessary to account for the entire momentum measurement. Similarly, laser ablation of Delrin [142, 143, 144] has produced rocketing with energy depositions on the order of 30 MW/cm^2, considerably more than the 0.69 MW/cm^2 produced by a 5 mg plasma traveling at 49.4 km/s and colliding over ∼28 μs. However, the highest velocity of ablated material in those experiments was determined to be ∼2 km/s. This implies 1.2 mg of sputtered material would have to be ejected at this velocity to effect 1% changes in pendulum momentum readings, but 123 mg would have to be ejected at 2 km/s to account for all momentum measured. This implies it would be advantageous to move to a target plate material which reduces sputtering.

Conclusions

A ballistic pendulum is a useful tool for measuring the momentum and mass of plasma armatures ejected by plasma railguns. Because pendulum motions are so slow compared to plasma motion, signals are recorded hundreds of milliseconds after the plasma discharge for very high noise immunity. By using a two magnet, inductive pendulum velocity measurement system, unambiguous momentum measurements could be cleanly recorded and processed automatically. Despite the strength of this technique, however, these ballistic pendulums could still be further improved. An optical position sensing technique could allow for continuous position or velocity measurements by counting hashes. Also, moving to materials such as graphite or alumina would further reduce errors from target plate material ejection though sputtering.